



The cusp-core problem in dwarf galaxies : new solutions

Pierre Boldrini

► To cite this version:

Pierre Boldrini. The cusp-core problem in dwarf galaxies : new solutions. Galactic Astrophysics [astro-ph.GA]. Sorbonne Université, 2020. English. NNT : 2020SORUS082 . tel-03191290

HAL Id: tel-03191290

<https://theses.hal.science/tel-03191290>

Submitted on 7 Apr 2021

HAL is a multi-disciplinary open access archive for the deposit and dissemination of scientific research documents, whether they are published or not. The documents may come from teaching and research institutions in France or abroad, or from public or private research centers.

L'archive ouverte pluridisciplinaire **HAL**, est destinée au dépôt et à la diffusion de documents scientifiques de niveau recherche, publiés ou non, émanant des établissements d'enseignement et de recherche français ou étrangers, des laboratoires publics ou privés.

École doctorale n° 127 :
Astronomie et Astrophysique d'Île de France

Doctorat à l'Institut d'Astrophysique de Paris

THÈSE

pour obtenir le grade de docteur délivré par

Sorbonne Université

Spécialité doctorale "Astrophysics"

présentée et soutenue publiquement par

Pierre Boldrini

le 18 Septembre 2020

The cusp-core problem in dwarf galaxies: New solutions

Directeur de thèse : **Roya Mohayaee**

Co-directeur de thèse : **Joe Silk**

Jury

M. Marco Cirelli,

M. Volker Springel,

M. Jorge Peñarrubia,

M. Mark Vogelsberger,

M. Pierre Salati,

Mme. Lia Athanassoula,

M. David Valls-Gabaud,

Directeur de recherche, Sorbonne Université

Professeur, Max-Planck-Institute for Astrophysics

Chercheur, Royal Observatory, Edinburgh

Professeur, Massachusetts Institute of Technology

Professeur, Université Savoie Mont Blanc

Professeure, Université d'Aix-Marseille

Directeur de recherche, Observatoire de Paris

Président

Rapporteur

Rapporteur

Examineur

Examineur

Examinatrice

Membre invité

Institut d'Astrophysique de Paris

UMR CNRS 7095, PARIS, France

Publications related to this thesis

This thesis has used material from the following first-authored publications:

- *“Fornax globular cluster distributions: implications for the cusp-core problem,”*
P. Boldrini, R. Mohayaee, J. Silk, 2019, MNRAS, ([arXiv:1903.00354](#))
- *“Cusp-to-core transition in low-mass dwarf galaxies induced by dynamical heating of cold dark matter by primordial black holes,”*
P. Boldrini, Y. Miki, A. Wagner, R. Mohayaee, J. Silk, A. Arbey, 2020a, MNRAS, ([arXiv:1909.07395](#))
- *“Embedding globular clusters in dark matter minihalos solves the cusp-core and timing problems in the Fornax dwarf galaxy,”*
P. Boldrini, R. Mohayaee, J. Silk, 2020b, MNRAS, ([arXiv:1909.07404](#))
- *“Subhalo sinking and off-center IMBHs in dwarf galaxies,”*
P. Boldrini, R. Mohayaee, J. Silk, 2020c, MNRAS letters, ([arXiv:2003.02611](#))
- *“The origin of the black hole offset in M31,”*
P. Boldrini, 2020d, MNRAS letters, ([arXiv:2007.03010](#))
- *“A dark matter core in M31”*
P. Boldrini, R. Mohayaee, J. Silk, 2020e, MNRAS, submitted, ([arXiv:2002.12192](#))

Résumé

Cette thèse porte sur la nature de la matière noire (MN) et plus particulièrement sur le problème de la disparité des profils de densité interne de MN dans les galaxies naines, connu sous le nom du problème "cusp-core". Nous avons trouvé de nouvelles solutions à ce problème en utilisant des simulations à haute résolution avec le code N-corps GOTHIC uniquement avec des GPUs. Nous avons commencé par avons réétudier le problème "cusp-core" pour une galaxie naine, Fornax, en utilisant la distributions spatiale et de masse des amas globulaires que nous donnaient les observations afin de contraindre le profil de MN. Ensuite, nous avons démontré au moyen de simulations N-corps sur GPUs que les minihalos de MN, en tant que nouvelle composante des amas globulaires, résolvent à la fois le "timing problem" et le problème "cusp-core" dans Fornax — dans le cas où les amas globulaires ont été récemment accrétés par Fornax. Par ailleurs, nous avons examinés si les candidats de MN sous la forme de trous noirs primordiaux (TNP) peuvent résoudre le problème "cusp-core" dans les galaxies naines de faible masse. Ce mécanisme fonctionne pour les TNPs entre 25 et 100 M_{\odot} mais nécessite que la masse de la population de TNPs soit plus de 1% de la masse totale de MN dans les galaxies naines. Ensuite, nous avons démontré pour la première fois qu'en chutant, les sous-halos de MN transfèrent de l'énergie par friction dynamique dans les centres des galaxies naines. Ce chauffage dynamique éjecte alors le trou noir central à des dizaines de parsecs, à $z=1,5-3$. Enfin, nous démontrons que l'accrétion d'un satellite sur une orbite très excentrique provoque la formation d'un coeur de MN et explique également que le trou noir central soit décentré dans M31.

Abstract

This doctoral research focuses on the nature of the dark matter (DM) and more particularly on the inconsistency of inner DM density profiles in dwarf galaxies, known as the cusp-core problem. We perform simulations with the high performance collisionless N-body code GOTHIC. We provided different solutions invoking globular clusters embedded in DM minihalos, primordial black holes (PBHs) as DM candidates and DM subhalos sinking for this cold dark matter challenge at small scales using high resolution fully GPU N-body simulations. We have found new resolutions of the core-cusp problem for dwarf galaxies.

First, we have re-investigated the Fornax cusp-core problem using observational results on the spatial and mass distributions of globular clusters in order to put constraints on the dark matter profile. We model Fornax using high resolution N-body simulations with entirely live systems, i.e. self-gravitating systems composed of stars and dark matter, which account correctly for dynamical friction and tidal effects between Fornax and the globular clusters. We test two alternative hypotheses, which are a cored and a cuspy halo for Fornax by exploring a reasonable range of initial conditions on globular clusters. For Fornax cored dark matter halo, we derive a lower limit on the core size of $r_c \gtrsim 0.5$ kpc. Contrary to many previous works, we show also that for different initial conditions, a cuspy halo is not ruled out in our simulations based on observations of Fornax globular clusters. Then, fully GPU N-body simulations were designed to demonstrate that dark matter minihalos, as a new component of globular clusters, resolve both the timing and cusp-core problems in Fornax if the five (or six) globular clusters were recently accreted (≤ 3 Gyr ago) by Fornax. Under these assumptions, infall of these globular clusters does not occur and no star clusters form in the centre of Fornax in accordance with observations. We find that crossings of globular clusters that have DM minihalos near the Fornax centre induce a cusp-to-core transition of the dark matter halo and hence resolve the cusp-core problem in this dwarf galaxy. The dark matter core size depends on the frequency of globular cluster crossings. Our simulations clearly demonstrate also that between the passages, the dark matter halo can regenerate its cusp. Moreover, our models are in good agreement with constraints on the dark matter masses of globular clusters as our clusters lose a large fraction of their initial dark matter minihalos. These results provide circumstantial evidence for the universal existence of dark matter halos in globular clusters.

Secondly, we have examined whether dark matter candidates in the form of PBHs can solve the cusp-core problem in low-mass dwarf galaxies through high-resolution N-body simulations. If some fraction of the dark matter in low-mass dwarf galaxies consists of PBHs and the rest is cold dark matter, dynamical heating of the cold dark matter by the PBHs induces a cusp-to-core transition in the total dark matter profile. The mechanism works for PBHs in the 25-100 M_\odot mass window, consistent with the LIGO detections, but requires a lower limit on the PBH mass fraction of 1% of the total dwarf galaxy dark matter content. The cusp-to-core transition time-scale is between 1 and 8 Gyr. This time-scale is also a constant multiple of the relaxation time between cold dark matter particles and PBHs, which depends on the mass, the mass fraction and the scale radius of the initial density profile of PBHs. We conclude that dark matter cores occur naturally in halos comprised of

cold dark matter and PBHs, without the need to invoke baryonic processes.

Then, we have demonstrated for the first time that subhalos sink and transfer energy via dynamical friction into the centres of dwarf galaxies using N-body simulations. This dynamical heating kicks any central intermediate massive black hole out to tens of parsecs, especially at early epochs ($z=1.5-3$). This mechanism helps explain the observed off-center BHs in dwarf galaxies and also predicts that off-center BHs are more common in higher mass dwarf galaxies since dynamical friction becomes significantly weaker and BHs take more time to sink back towards the centres of their host galaxies. One consequence of off-center BHs during early epochs of dwarf galaxies is to quench any BH feedback.

Finally, we show that M31 harbours a dark matter core. Observational data provide stringent constraints on the initial conditions of our simulations. We demonstrate that accretion of a satellite on a highly eccentric orbit heats up the central parts of M31, causes an outward migration of dark matter particles, flattens the central cusp over more than a decade in scale and generates a model-independent new dark matter profile that is well-fitted by a core. Our results imply that cores could be a common feature of galaxies that have been initially cuspy but have accreted satellites on eccentric orbits. We show also that the infall of a dark matter rich satellite naturally explains a present black hole offset by sub-parsecs in M31. The heating of the central region of M31 by the satellite via dynamical friction entails a significant black hole offset after the first pericentric passage. After having reached its maximum offset, the massive black hole sinks towards the M31 centre due to dynamical friction and it is determined to be offset by sub-parsecs as derived by observations.

Acknowledgments

Contents

Contents	xi
1 Introduction	3
1.1 Distribution of dark matter	4
1.2 Structure of this thesis	9
1.3 References	9
2 The cusp-core problem	11
2.1 The discrepancy between Λ CDM and observations	12
2.2 Solutions	19
2.3 References	36
3 Fully GPU and pure gravitational N-body simulations of collisionless systems	45
3.1 N-body technique	46
3.2 Accelerating N-body simulations	48
3.3 GOTHIC	50
3.4 Simulation analysis	51
3.5 References	51
4 Our solution to the Fornax cusp-core problem	53
4.1 The Fornax timing problem	54
4.2 Constraints from globular cluster distribution	55
4.3 Embedding GC in DM minihalos	69
4.4 References	87
5 Primordial black holes as dark matter candidates: a new solution to the cusp-core problem	91
5.1 Primordial black holes as dark matter candidates	92
5.2 N-body modelling	92
5.3 Results	94
5.4 References	101
6 Quenching any BH feedback: one consequence of off-center massive black holes	103
6.1 Off-center massive black holes	104
6.2 Dark matter subhalos and off-center massive black holes	104
6.3 References	111

7	Andromeda galaxy (M31): a test case	113
7.1	A dark matter core in M31	114
7.2	The origin of the black hole offset in M31	123
7.3	References	128
8	Conclusion & Prospects	131
8.1	References	135

Chapter 1

Introduction

Contents

1.1	Distribution of dark matter	4
1.2	Structure of this thesis	9
1.3	References	9

Dark matter (hereafter DM) spans our entire Universe. This dominant component is traditionally referred to as a medium that manifests itself only through gravitational interaction with itself and baryonic matter. However, the nature of DM is currently one of the most fundamental and elusive mysteries in physics.

As the gravity of the baryonic matter is not sufficient to explain the evolution of the Universe with its observed structures, cosmological models predict the existence of a collisionless and non-relativistic matter, the so-called cold dark matter (CDM) [Peebles, 1982]. Lambda Cold Dark Matter (Λ CDM) model describes a universe comprised primarily of CDM and a cosmological constant Λ [Blumenthal et al., 1984] and has emerged as the prevailing cosmological theory. Within the framework of general relativity, the CDM paradigm can provide a quantitative description of the Universe at present and is extremely successful at explaining the Universe on large scales [Croft et al., 2002; Spergel et al., 2003].

1.1 Distribution of dark matter

Our Universe constitutes of a large collection of potential wells, more or less deep, created by gravitationally bound DM particles, namely halos. In the Λ CDM model, spherical infall models link small density fluctuations in the early Universe to the final equilibrium configurations of DM halos [Gott, 1975; Gunn & Gott, 1972]. Small perturbations in the DM density field are the first to decouple from the Hubble flow and collapse. Surrounding collisionless DM is aggregated and falls on to the cosmic structure until its mass greatly exceeds that of the originally overdense region, resulting in the formation of a gravitationally self-bound structure, a virialized DM halo. The DM structure with its total mass M_{vir} is bounded by the virial radius, r_{vir} .

The spherically averaged radial distribution of mass within a DM halo is called the DM density profile. The main prediction of these models is that the inner part of the first halos is described asymptotically by a power-law density profile, namely cusp:

$$\rho \propto r^\alpha. \quad (1.1)$$

The predicted slope of the inner profile, illustrated by the orange region in Figure 1.1, varies between $\alpha = -2$ and -2.25 [Bertschinger, 1985; Fillmore & Goldreich, 1984]. These analytical studies restricted their models to collisionless DM collapsing on purely radial orbits. By regarding a virialized DM halo as a fluid with pressure, we can predict the limit of purely radial orbits delimited by the asymptotic central density structure with $\alpha = -2$. The pressure equilibrium equation is written as:

$$\frac{dp}{dr} = -\frac{GM(r)}{r^2}\rho, \quad (1.2)$$

where

$$M(r) = 4\pi \int_0^r \rho(u)u^2 du, \quad (1.3)$$

and

$$p = \frac{\rho}{m} kT, \quad (1.4)$$

with m being the DM particle mass. Assuming that the temperature $T = \text{constant}$, we obtain

$$\frac{d}{dr} \left(r^2 \frac{d \ln(\rho)}{dr} \right) = -\frac{4\pi Gm}{kT} r^2 \rho. \quad (1.5)$$

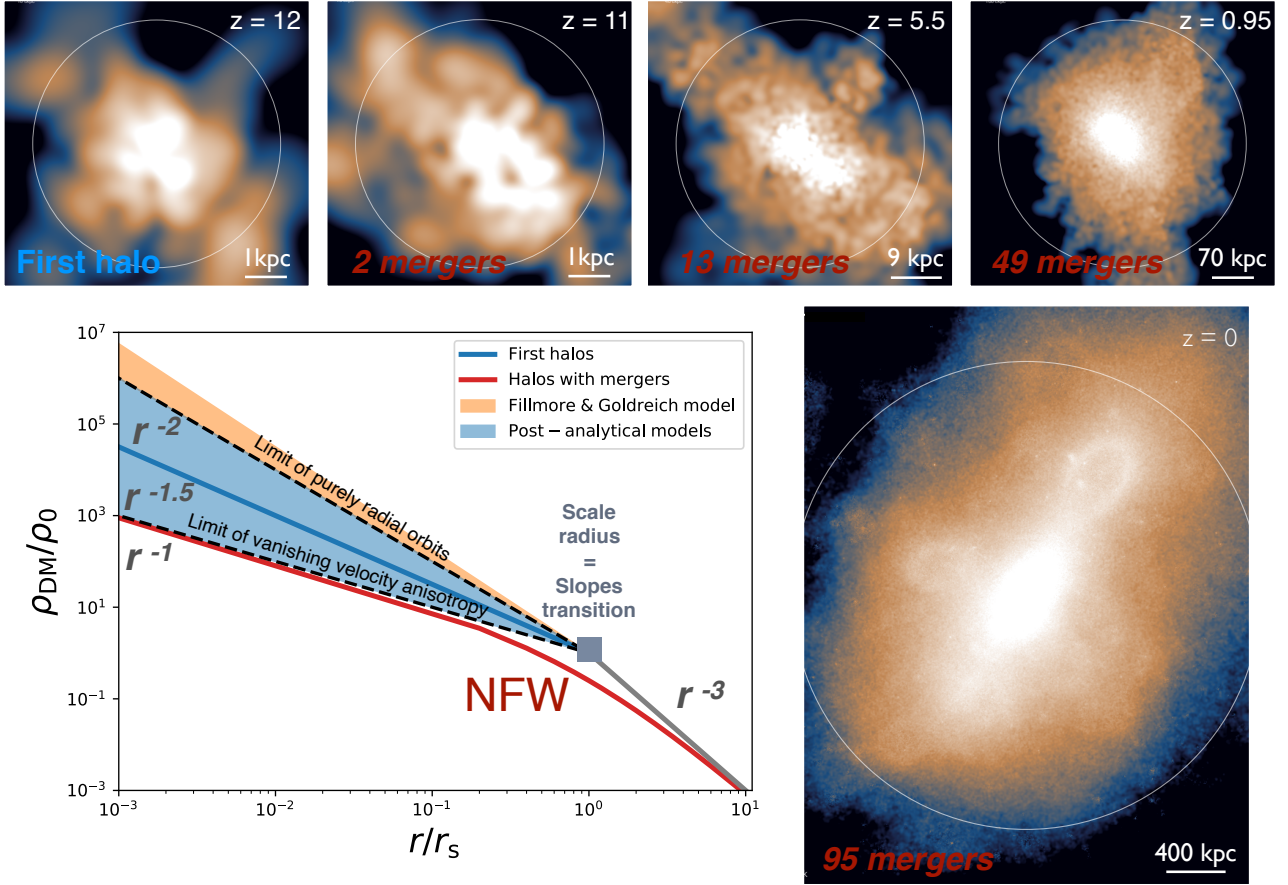


Figure 1.1 – **DM distribution in the central region:** Mean DM volume density across time for a Milky Way-like halo from the Illustris TNG simulation [Nelson et al., 2019] and normalized density profiles as a function of the radius normalized by the DM half mass radius r_m of DM halos over their evolution. We specified the number of mergers undergone by the first halo. The predicted slope of the inner profile, depicted by the orange region, varies between $\alpha = -2$ and -2.25 .

One solution to this equation is $\rho \propto r^\alpha$ with $\alpha = -2$. As the mass of this sphere diverges at large radii, this model can only describe the central part of halos.

Subsequent analytical and numerical studies extended the prediction of the asymptotic behaviour of first halos to a power-law density distribution with $\alpha = -1.5$ by including non-radial orbits [Nusser, 2001; Sikivie et al., 1997]. N-body simulations confirmed these analytical predictions [MacMillan et al., 2006; Vogelsberger et al., 2011; White & Zaritsky, 1992; Williams et al., 2004]. Moreover, the assumption of isotropic velocity dispersion for the collapsed system entails the formation of inner structures with $\alpha = -1$ [Lapi & Cavaliere, 2011; Lu et al., 2006; Subramanian, 2000; Teyssier et al., 1997]. The range of α predicted by these post-analytical models is represented by the blue region in Figure 1.1.

However, N-body simulations showed that these first DM halos possess a markedly different density profile that asymptotes to a power-law density distribution with $\alpha = -1.5$ in the inner regions [Anderhalden & Diemand, 2013; Angulo et al., 2017; Ishiyama, 2014; Ishiyama et al., 2010; Ogiya & Hahn, 2018; Polisensky & Ricotti, 2015]. This cuspy profile is stable in the absence of halo mergers (cf. blue line in Figure 1.1).

It is now established that a cuspy profile with $\alpha = -1.5$ for the first halos emerges some time after their formation. Larger halos form in a hierarchical manner. They are subsequently formed

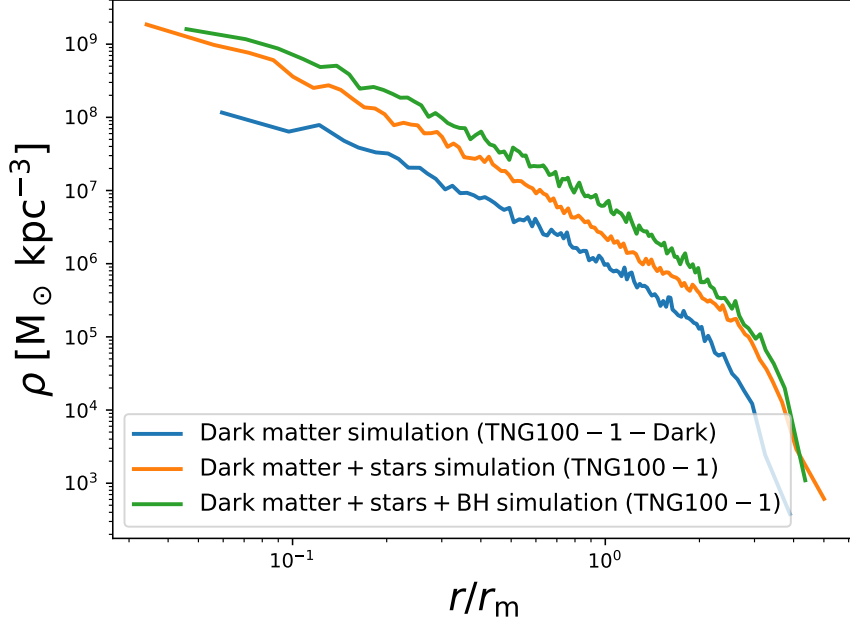


Figure 1.2 – **Baryon impact:** DM density profiles as a function of the radius normalized by the DM half mass radius r_m for a $10^{11} M_\odot$ halo from the Illustris TNG simulation [Nelson et al., 2019] with and without baryonic physics. The DM profile becomes slightly steeper due to the presence of stars and the black hole at the galaxy centre.

by mergers of pre-existing halos and by accretion of diffuse and unbound DM. It was found that the dynamical impact of consecutive mergers weakens as the logarithmic central density slope, α , approaches unity [Angulo et al., 2017; Ogiya et al., 2016]. Indeed, the density profile becomes increasingly shallower as the halo mass grows. In Figure 1.1, the snapshots of a halo from the Illustris TNG-100 simulation at different redshifts illustrates the formation of a halo by the accretion of unbound DM matter and hierarchical clustering of smaller halos. We specified the number of mergers undergone by the first halo. The halo at $z = 0$ is similar to the Milky Way (MW) halo with a mass of $\sim 10^{12} M_\odot$.

In cosmological simulations, halo mergers gradually drive the halo density profiles towards a central density cusp, which behaves as r^{-1} , with a sharp decline towards their outskirts [Dubinski & Carlberg, 1991; Frenk et al., 1988; Gelb & Bertschinger, 1994]. Their density profiles, which are almost independent of halo mass, cosmological parameters and the power spectrum of initial fluctuations, appeared to be well-described by the following form [Navarro et al., 1996, 1997, hereafter NFW]:

$$\rho_{\text{NFW}}(r) = \frac{\rho_0}{\left(\frac{r}{r_s}\right) \left(1 + \frac{r}{r_s}\right)^2}, \quad (1.6)$$

where r is the distance from the centre of the DM halo, and ρ_0 and r_s represent the central density and scale radius, respectively. Figure 1.1 depicts the universal NFW profile (red curve), which is a double power-law that transitions from r^{-1} at small radii to r^{-3} at large radii. The scale radius marks the transition between the two slopes in the NFW profile (cf. the grey square in Figure 1.1). As the NFW profile appears to be the generic consequence of halo mergers and becomes more resilient, this might explain why this density profile is universally observed in most cosmological simulations.

The formation and evolution of structures in the Universe ranging in size from dwarf galaxies all the way up to galaxy clusters is driven by the dynamics of DM. Potential wells created by virialized

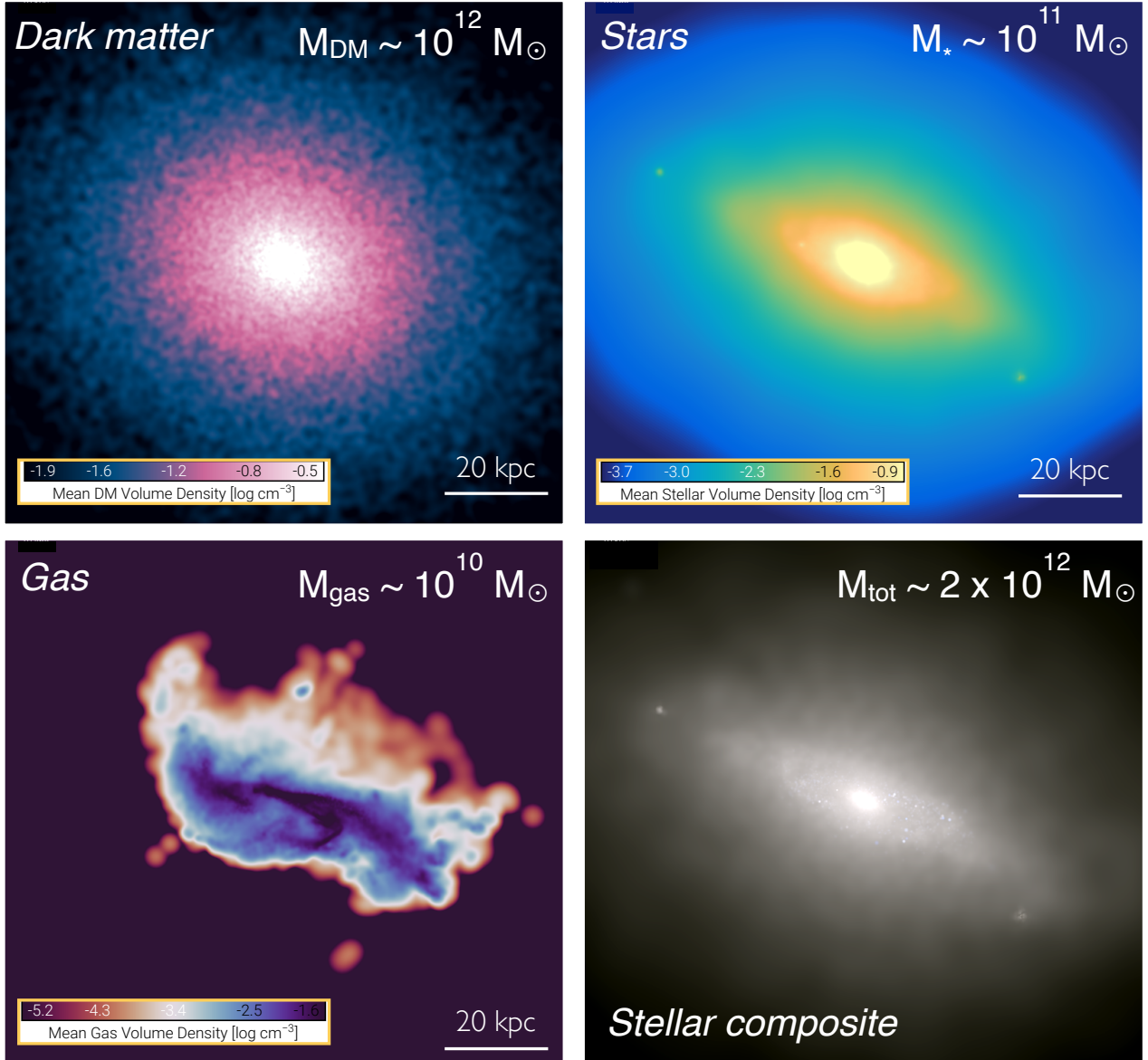


Figure 1.3 – **Galaxy components:** Mean volume density of DM, stars and gas for a Milky Way-like galaxy at $z = 0$ from the Illustris TNG-100 simulations [Nelson et al., 2019]. The most important constituent is the DM because it is dominating the gravitational potential as the most massive part. The second most dominant constituent is the stellar component. The lower right panel shows a stellar composite image of stars in common filters on the James Webb Space Telescope [Gardner et al., 2006].

DM halos drive the formation and evolution of galaxies by attracting gas into their centres. Thus, galaxies are believed to form from gas condensing at the centres of massive DM halos, where stars form [White & Rees, 1978]. Then, galaxies consist of three constituents: DM, gas, and stars. The DM is thus not only the dominant gravitational component but also the dominant factor in determining the distribution of matter. In the Λ CDM model, cusps appear naturally in the inner parts of halos with its most adequate description given by the NFW profile. Nevertheless, the DM profile becomes slightly steeper due to the presence of stars and the black hole at the galaxy centre. As depicted in Figure 1.2, this behaviour is confirmed in the Illustris-TNG simulations. The density of the inner parts of the halos is higher due to the stars and a central black hole (BH). Figure 1.3 shows that the most important constituent is the DM because it is dominating the gravitational potential as the most massive part. The second most dominant constituent is the stellar component.

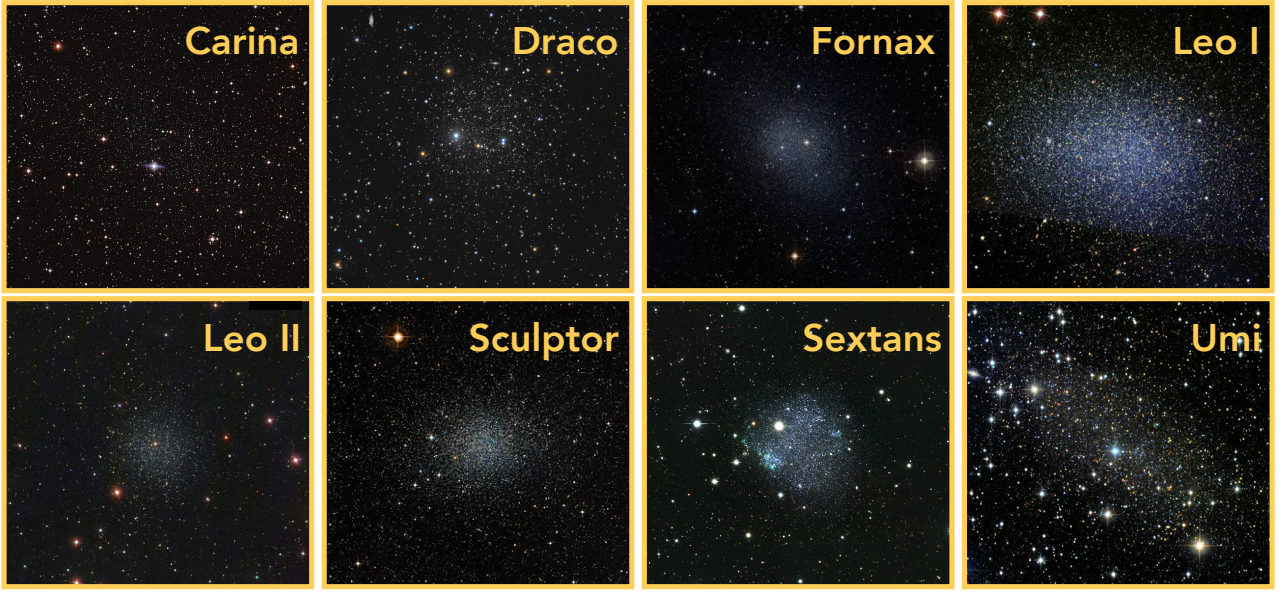


Figure 1.4 – **Dwarf galaxies of the local group:** Images of the luminous matter of the eight most common dwarf spheroidal galaxies orbiting around the MW. These systems are among the most DM-dominated galaxies in the Universe. Their DM mass is predicted to be between 10^9 and $10^{10} M_{\odot}$ [Read et al., 2019].

About forty dwarf galaxies have been discovered in the Local Group, which encompasses our MW galaxy and Andromeda galaxy [Mateo, 1998]. These dwarf galaxies are more than 100 times less massive than the MW. The dwarf galaxy population of the MW exhibits various different morphological types. Dwarfs can be divided into roughly two groups: dwarf spheroidals and dwarf irregulars [McConnachie, 2012]. In this work, we focus on dwarf spheroidals only. They have characteristically old stellar populations and are generally devoid of gas [Carraro, 2015]. Close to the MW and Andromeda, one finds predominantly dwarf spheroidals. These dwarfs are among the most DM-dominated galaxies in the Universe [Battaglia et al., 2013; Walker, 2013]. In some dwarf spheroidals, DM constitutes 90% or more of the total mass, even at the centre of the galaxy, so the dynamics are determined entirely by the gravitational field of the DM. Therefore, these systems provide an excellent laboratory to study DM distribution at small scales. The eight most common dwarf spheroidal galaxies orbiting around the MW are represented in Figure 1.4.

1.2 Structure of this thesis

The purpose of this work is to provide new solutions to the cusp-core problem, especially in dwarf galaxies. This doctoral thesis is written in seven chapters, organized as follows. The introduction is followed by Chapter 2, which focuses on the inconsistency of inner DM density profiles in dwarf galaxies, known as the cusp-core problem. Our numerical approach based on high-resolution N-body simulations on GPU is provided in Chapter 3. Our solution to the Fornax cusp-core problem is illustrated in Chapter 4. Chapter 5 provides a second solution by invoking primordial black holes as DM candidates. The sinking of DM subhalos in dwarf galaxies, which contributes to explain observed off-centre BHs in dwarf galaxies, is outlined in Chapter 6 within the context of the cusp-core problem. Chapter 7 describes our recent investigations on the shape of the DM profile and the fate of the central black hole in Andromeda galaxy (M31) due to the infalling satellite, as the origin of the tidal features of M31. Finally, in Chapter 8, we summarize the key aspects of the work presented in this thesis.

1.3 References

- Anderhalden D., Diemand J., 2013, *J. Cosmology Astropart. Phys.*, 2013, 009 5
- Angulo R. E., Hahn O., Ludlow A. D., Bonoli S., 2017, *MNRAS*, 471, 4687 5, 6
- Battaglia G., Helmi A., Breddels M., 2013, *New Astron. Rev.*, 57, 52 8
- Bertschinger E., 1985, *ApJS*, 58, 39 4
- Blumenthal G. R., Faber S. M., Primack J. R., Rees M. J., 1984, *Nature*, 311, 517 4
- Carraro G., 2015, Morphological Transformations of Dwarf Galaxies in the Local Group. p. 253, doi:10.1007/978-3-319-10614-4_21 8
- Croft R. A. C., Weinberg D. H., Bolte M., Burles S., Hernquist L., Katz N., Kirkman D., Tytler D., 2002, *ApJ*, 581, 20 4
- Dubinski J., Carlberg R. G., 1991, *ApJ*, 378, 496 6
- Fillmore J. A., Goldreich P., 1984, *ApJ*, 281, 1 4
- Frenk C. S., White S. D. M., Davis M., Efstathiou G., 1988, *ApJ*, 327, 507 6
- Gardner J. P., et al., 2006, *Space Sci. Rev.*, 123, 485 7
- Gelb J. M., Bertschinger E., 1994, *ApJ*, 436, 467 6
- Gott J. Richard I., 1975, *ApJ*, 201, 296 4
- Gunn J. E., Gott J. Richard I., 1972, *ApJ*, 176, 1 4
- Ishiyama T., 2014, *ApJ*, 788, 27 5
- Ishiyama T., Makino J., Ebisuzaki T., 2010, *ApJ*, 723, L195 5
- Lapi A., Cavaliere A., 2011, *ApJ*, 743, 127 5

- Lu Y., Mo H. J., Katz N., Weinberg M. D., 2006, *MNRAS*, 368, 1931 5
- MacMillan J. D., Widrow L. M., Henriksen R. N., 2006, *ApJ*, 653, 43 5
- Mateo M., 1998, in *Magellanic Clouds and Other Dwarf Galaxies*. pp 53–66 8
- McConnachie A. W., 2012, *AJ*, 144, 4 8
- Navarro J. F., Frenk C. S., White S. D. M., 1996, *ApJ*, 462, 563 6
- Navarro J. F., Frenk C. S., White S. D. M., 1997, *ApJ*, 490, 493 6
- Nelson D., et al., 2019, *Computational Astrophysics and Cosmology*, 6, 2 5, 6, 7
- Nusser A., 2001, *MNRAS*, 325, 1397 5
- Ogiya G., Hahn O., 2018, *MNRAS*, 473, 4339 5
- Ogiya G., Nagai D., Ishiyama T., 2016, *MNRAS*, 461, 3385 6
- Peebles P. J. E., 1982, *ApJ*, 263, L1 4
- Polisensky E., Ricotti M., 2015, *MNRAS*, 450, 2172 5
- Read J. I., Walker M. G., Steger P., 2019, *MNRAS*, 484, 1401 8
- Sikivie P., Tkachev I. I., Wang Y., 1997, *Phys. Rev. D*, 56, 1863 5
- Spergel D. N., et al., 2003, *ApJS*, 148, 175 4
- Subramanian K., 2000, *ApJ*, 538, 517 5
- Teyssier R., Chièze J.-P., Alimi J.-M., 1997, *ApJ*, 480, 36 5
- Vogelsberger M., Mohayaee R., White S. D. M., 2011, *MNRAS*, 414, 3044 5
- Walker M., 2013, *Dark Matter in the Galactic Dwarf Spheroidal Satellites*. p. 1039, doi:10.1007/978-94-007-5612-0_20 8
- White S. D. M., Rees M. J., 1978, *MNRAS*, 183, 341 7
- White S. D. M., Zaritsky D., 1992, *ApJ*, 394, 1 5
- Williams L. L. R., Babul A., Dalcanton J. J., 2004, *ApJ*, 604, 18 5

Chapter 2

The cusp-core problem

Contents

2.1 The discrepancy between ΛCDM and observations	12
2.1.1 Observed rotation curves	12
2.1.2 Dynamical models	14
2.1.3 The diversity problem	17
2.2 Solutions	19
2.2.1 Baryonic physics	19
2.2.2 Alternative theories of dark matter	25
2.3 References	36

The theory of the formation of our Universe dominated by the DM is established, and the Λ CDM model can now be confronted with observations. This chapter is intended to give an overview of the current observational and theoretical status of the DM distribution at small scales. Small scales refer to galactic or sub-galactic scales, which correspond to the inner few kpc.

2.1 The discrepancy between Λ CDM and observations

Λ CDM model is extremely successful in explaining the DM distribution of the Universe on large scales [Tegmark et al., 2004] but also many important aspects of galaxy formation [Springel et al., 2006; Trujillo-Gomez et al., 2011]. As shown previously, CDM simulations including only DM particles predict that DM halos should have density profiles that behave as r^{-1} at small radii. These early simulations of structure formation found the universal cuspy NFW density profile in halos ranging from dwarf galaxies to galaxy clusters [Navarro et al., 1996b]. This important result was obtained from N-body simulations and is independent of initial conditions and cosmological parameters [Navarro et al., 1997]. Nevertheless, later studies show that the DM density profile does not seem to be universal. Indeed, DM density profiles rise steeply at small radius more like $\rho(r) \propto r^{-\alpha}$ with $\alpha = 0.8 - 1.4$ [Fukushige & Makino, 1997; Moore et al., 1998; Navarro et al., 2010]. In order to find good probes of the DM distribution, it is essential that the dynamics of selected galaxies are dominated by DM. The mass regime, which has been studied most extensively, is at the dwarf galaxy scale.

2.1.1 Observed rotation curves

The DM density profile of these galaxies can be inferred by measuring the rotation of either the gas with HI or using the stellar H α emission line. Early measurements of the HI rotation curves of gas-rich dwarf galaxies highlighted, for the first time, a large discrepancy between the observed rotation velocities and those predicted by Λ CDM simulations, especially in the inner parts [Burkert, 1995; Flores & Primack, 1994; Moore, 1994]. The rotation curve $V_c(R)$ is derived from the observed line-of-sight velocity at any position (x, y) in the galaxy velocity field:

$$V(x, y) = V_0 + V_c(R) \sin i \cos \theta + V_{\text{exp}}(R) \sin i \sin \theta, \quad (2.1)$$

where V_0 , R , $V_{\text{exp}}(R)$ and i are the systemic velocity, the radius in the plane of the galaxy, the expansion velocity describing non-circular motions and the inclination, respectively. Assuming spherical symmetry, the rotation curve is defined as

$$V_c(R) = \sqrt{\frac{GM(R)}{R}}, \quad (2.2)$$

where G is the gravitational constant and $M(r)$ corresponds to the mass within the radius R . By inverting the previous equation, we can determine the mass inside a radial distance R . As the interior mass $M(R)$ is directly related to the density $\rho(r)$ according to the following equation:

$$M(R) = 4\pi \int_0^R r^2 \rho(r) dr, \quad (2.3)$$

it is, therefore, possible to establish the DM density profile in galaxies. For instance, the NFW mass distribution gives rise to a DM rotation curve:

$$V_c(R) = V_{200} \left(\frac{\ln(1 + cx) - cx/(1 + cx)}{x(\ln(1 + cx) - c/(1 + c))} \right), \quad (2.4)$$

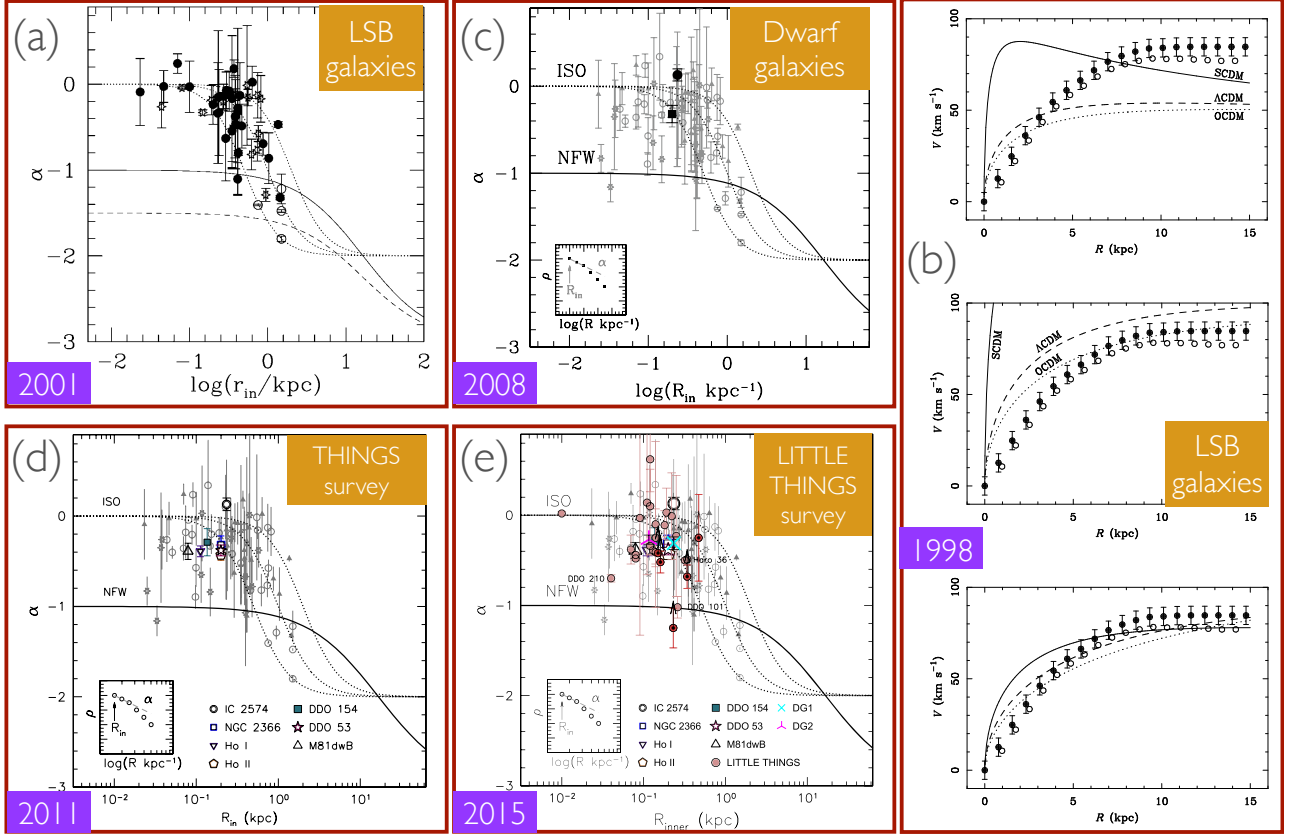


Figure 2.1 – **Cusp-core problem:** Comparison between cores inferred from observations and NFW form predicted by simulations over the last twenty years with their new observational data specified by orange boxes. (a),(c),(d),(e): Inner slope α of the density profiles as a function of the radius of the innermost point, within which α is measured. Main data are taken from Oh et al. [2011, 2015]; Swaters et al. [2003]; de Blok & Bosma [2002]; de Blok et al. [2001]. The theoretical slopes of a pseudo-isothermal halo is over-plotted with dotted lines for a core size of 0.5 (leftmost), 1 (centre), and 2 (rightmost) kpc. The solid line represents an NFW model [Navarro et al., 1996b]. The pseudo-isothermal model is preferred over the NFW model to explain the observational data. (b): Rotation curve of F583-1 galaxy as a function of the radius. The solid and open points are the observed rotation curve and the rotation curve of the DM with the baryonic component subtracted from the total, respectively. Even for various cosmologies and assuming both c and V_{200} as free parameters, CDM predictions do not fit observations. The figure is taken from McGaugh & de Blok [1998]; Oh et al. [2008, 2011, 2015]; de Blok et al. [2001].

where $x = R/R_{200}$ with the virial radius R_{200} . The circular velocity is only characterized by the concentration c and the virial velocity $V_{200} = V_c(R_{200})$ [Navarro et al., 1996b]. Given the halo mass and redshift, both halo concentrations c_{200} can be estimated from cosmological N-body simulations. Indeed, the mass and concentration of halos at redshift $z = 0$ in Λ CDM are correlated:

$$\log_{10}(c_{200}) = 0.905 - 0.101 \log_{10}(M_{200} h - 12), \quad (2.5)$$

with a scatter $\Delta \log_{10}(c_{200}) = 0.1$, where h is the Hubble parameter [Dutton & Macciò, 2014]. After the data analysis, the central DM distributions in this DM-dominated galaxies were found to be inconsistent with $1/r$ behavior of cuspy profiles and indicate the presence of a constant-density core. These latter implies $\rho(r) \propto r^{-\alpha}$ with $\alpha = 0$ in the inner regions. This discrepancy between observations and simulations led to the original small-scale problem, which has now become known as the cusp/core problem [Flores & Primack, 1994; Moore, 1994].

Nevertheless, it was argued that baryonic processes could explain the observed cores in these

galaxies [Navarro et al., 1996a]. As a proof of concept, numerous studies investigated more massive DM dominated galaxies such as Low Surface Brightness (LSB) galaxies as the baryonic processes were declared to be only effective in dwarf galaxies. Moreover, the stellar component yields only a small contribution to the observed rotation curves of these DM-dominated galaxies. As shown in Figure 2.1, the measurements in LSB galaxies eventually confirmed that the observations were still consistent with the existence of DM cores [Côté et al., 2000; McGaugh & de Blok, 1998; de Blok & McGaugh, 1996, 1997; de Blok et al., 1996]. Subsequent observations in the H α line supported the existence of DM cores in LSB galaxies [Borriello & Salucci, 2001; Marchesini et al., 2002; Salucci, 2001; Swaters et al., 2000; de Blok, 2005; de Blok & Bosma, 2002; de Blok et al., 2001]. However, it was argued that systematic effects could be responsible of the core signature in the rotation curve [Marchesini et al., 2002; Rhee et al., 2004; de Blok & Bosma, 2002; de Blok et al., 2003]. The absence of a comprehensive and satisfactory resolution has also led to a wide range of different conclusions concerning the DM inner profile [de Blok & McGaugh, 1996; van den Bosch & Swaters, 2001; van den Bosch et al., 2000]. As a consequence, the NFW form cannot be ruled out [Spekkens et al., 2005; Swaters et al., 2003]. More recently, high-resolution velocity fields were used to derive stronger constraints on the DM distributions in galaxies [Gentile et al., 2004; Kuzio de Naray et al., 2008, 2009; Oh et al., 2008; Trachternach et al., 2008; Zackrisson et al., 2006; de Blok et al., 2008]. Indeed, a core profile represented by the pseudo-isothermal model is preferred over the NFW profile to explain the observational data (see Figure 2.1). The mass distribution of the pseudo-isothermal sphere is given by:

$$\rho(r) = \frac{\rho_0}{1 + (r/R_c)^2}. \quad (2.6)$$

This density distribution leads to a circular velocity, which can be written as

$$V_c(R) = \sqrt{\frac{4\pi G \rho_0 R_c^3}{r} \left(\frac{r}{R_c} - \tan^{-1} \left(\frac{r}{R_c} \right) \right)}, \quad (2.7)$$

where ρ_0 and R_c are the central density and the core radius of the DM halo, respectively. Another density profile that appears to fit also the observed rotation curves is the so-called Burkert profile [Burkert, 1995]. This latter, which is similar to the pseudol-isothermal form, is defined as:

$$\rho(r) = \frac{\rho_0}{(1 + r/r_c)(1 + (r/r_c)^2)}, \quad (2.8)$$

where ρ_0 and r_c are the central density and the core radius of the DM halo, respectively. In a nutshell, measurements of galaxy rotation curves have revealed that the density profile of the DM halos are not consistent with Λ CDM predictions and suggest that LSB galaxies contain DM cores with a size of kiloparsecs. Recent surveys of nearby dwarf galaxies, THINGS and LITTLE THINGS have offered ultra-high resolution rotation curve data [Hunter et al., 2012; Walter et al., 2008]. By reaching the necessary resolution to alleviate some systematic effects, the logarithmic inner slopes α of their DM halo densities were found to be high $\alpha = -0.32 \pm 0.24$ [Oh et al., 2011, 2015]. These recent measurement reinforced the disagreement with the prediction of cuspy NFW halos (see Figure 2.1).

2.1.2 Dynamical models

As most of the dwarf galaxies are devoid of gas, the kinematics of their stars must be also used to probe their DM inner region. However, only line-of-sight velocities of stars are observable. The line-of-sight velocity dispersion of these stars from the spherical Jeans equation [Binney, 1980; Binney & Tremaine, 2008] can be written as [Binney & Mamon, 1982]:

$$\sigma_{\text{los}}^2 = \frac{2}{\Sigma_*(R)} \int_R^\infty \left(1 - \beta \frac{R^2}{r^2} \right) \frac{v(r) \sigma_r^2(r) r}{\sqrt{r^2 - R^2}} dr, \quad (2.9)$$

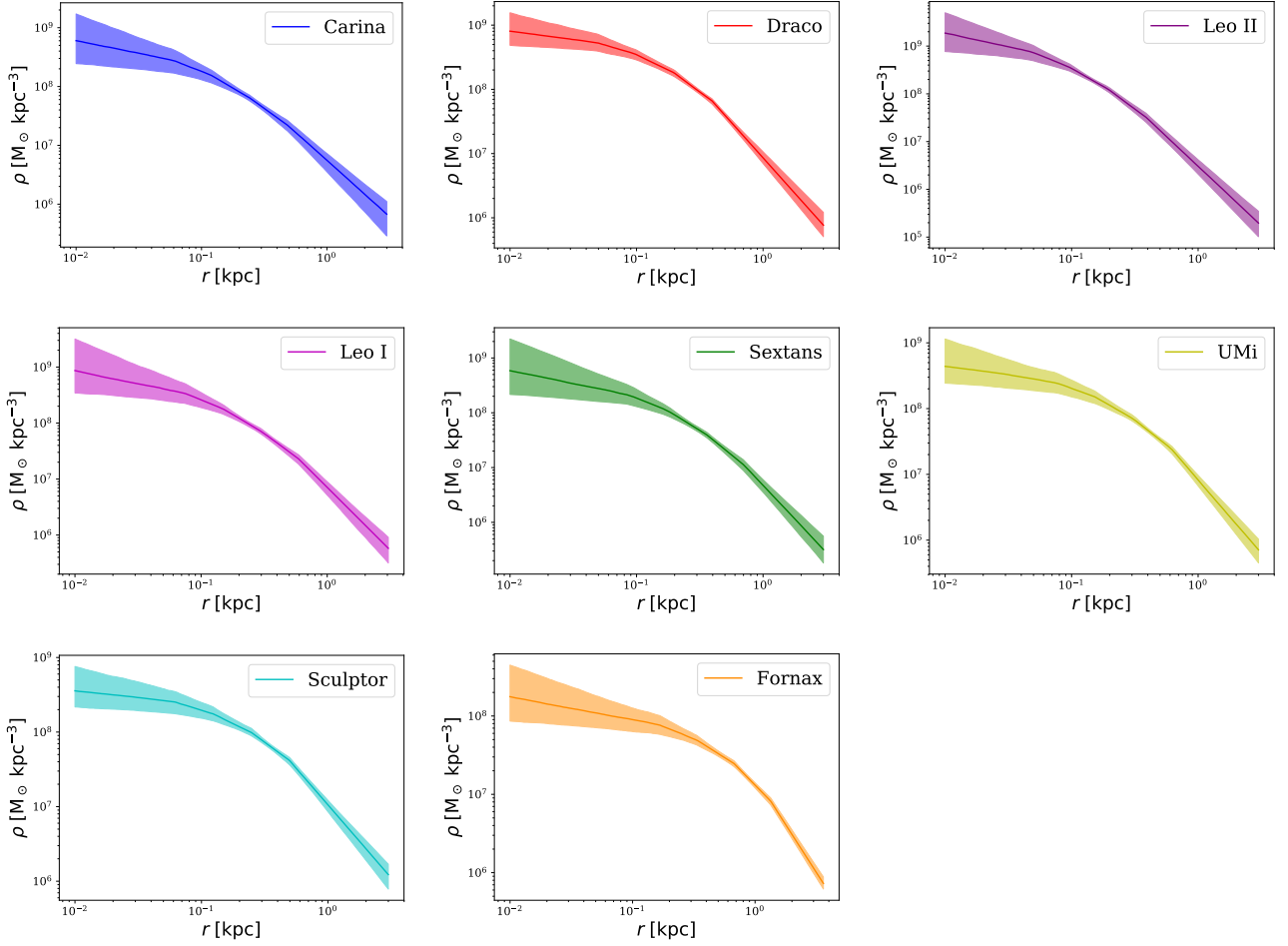


Figure 2.2 – **Dynamical modelling:** DM density profiles of the eight MW classical dwarf galaxies derived from the stellar kinematics [Read et al., 2019]. The shaded regions mark the 68% confidence intervals of the model. In this interval, it is hard to distinguish between cusp and core for the MW satellites according to GravSphere fits. As their profile is better constrained at a radius of 150 pc, it was established that seven dwarfs have a central DM density $\rho(150 \text{ pc})$ consistent with a cusp and only Fornax had a $\rho(150 \text{ pc})$ consistent with a DM core [Read et al., 2019].

where $\Sigma_*(R)$ is the surface mass density at projected radius R and the radial velocity dispersion $\sigma_r^2(r)$ is defined as:

$$\sigma_r^2(r) = \frac{1}{v(r)g(r)} \int_r^\infty \frac{GM(u)v(u)}{u^2} g(u) du, \quad (2.10)$$

with

$$g(r) = \exp\left(2 \int \frac{\beta(r)}{r} dr\right), \quad (2.11)$$

where $v(r)$ and $\beta(r)$ are the radial density profile and the velocity anisotropy, which describes the orbital structure of the stellar system, respectively. $\beta = 0, 1$ and $-\infty$ correspond to an isotropic, fully radial and fully tangential distributions, respectively. This technique allows the measurement of the central DM density profile in galaxies as the line-of-sight velocity dispersion of stars depends on the mass profile $M(r)$. However, there is a degeneracy between the radial density profile of DM, $\rho(r)$, and the unknown orbit distribution of the stars. This latter is typically characterized by the velocity anisotropy parameter β which is hard to constrain with only line-of-sight velocities [Binney & Mamon, 1982; Evans et al., 2009; Merrifield & Kent, 1990; Read & Steger, 2017]. That is the reason why analyses of the line-of-sight velocities in dwarf galaxies have led to contradictory conclusions. Some authors conclude that the kinematic data require DM core [Agnello & Evans, 2012; Gilmore

et al., 2007; Walker & Peñarrubia, 2011], while others found that the data are also consistent with the NFW form [Breddels et al., 2013; Richardson & Fairbairn, 2014; Strigari et al., 2010]. For the brighter MW dwarfs, this degeneracy can be broken by using metallicity or colour to split the stars into distinct components [Agnello & Evans, 2012; Battaglia et al., 2008; Walker & Peñarrubia, 2011]. Other methods have been proposed to break this degeneracy by using higher-order velocity moments [Łokas, 2009], Schwarzschild methods [Breddels et al., 2013; Jardel et al., 2013], and proper motions [Massari et al., 2018; Strigari et al., 2007; Wilkinson et al., 2002]. Indeed, together with line-of-sight velocities and positions on the sky, stellar proper motions, which are the two additional transverse velocity components, provide five out of the six phase-space coordinates of the stars. The degeneracy may be also broken by including the fourth-order projected virial theorem [Merrifield & Kent, 1990]. A non-parametric Jeans method, namely GravSphere, employs the additional constraints from the virial shape parameters in their analysis [Read & Steger, 2017]. This higher-order Jeans analysis method has been shown to successfully recover DM density distributions of simulated dwarfs [Genina et al., 2019; Read & Steger, 2017]. In Figure 2.2, the DM density profile of eight dwarf spheroidal galaxies was estimated by using stellar kinematics [Read et al., 2019]. In the 68% confidence interval, it is hard to distinguish between cusp and core for the MW satellites according to GravSphere fits (see Figure 2.2). As their profile is better constrained at radius of 150 pc, it was established that seven dwarfs have a central DM density $\rho(150 \text{ pc})$ consistent with a cusp and only Fornax had a $\rho(150 \text{ pc})$ consistent with a DM core [Read et al., 2019]. It was found that the spherically averaged DM profile evolution of the MW dSphs is well characterized by a modified NFW functional form. The coreNFW profile is a fitting function, which captures the cusp-core transformation [Read et al., 2016a]. For this model, the cumulative mass profile is given by:

$$M_{\text{cNFW}}(< r) = M_{\text{NFW}}(< r) f^n, \quad (2.12)$$

where M_{NFW} is the NFW mass profile and f^n generates a shallower density profile below a core radius r_c :

$$f^n = \left[\tanh\left(\frac{r}{r_c}\right) \right]^n, \quad (2.13)$$

where the parameter $0 < n \leq 1$ controls how shallow the core becomes and corresponds to the transition region between cusp and core. Indeed, $n = 0$ ($n = 1$) corresponds to a fully cuspy (core) halo. The density profile of the coreNFW model is given by:

$$\rho_{\text{cNFW}} = f^n \rho_{\text{NFW}} + \frac{n f^{n-1} (1 - f^2)}{4\pi r^2 r_c} M_{\text{NFW}}. \quad (2.14)$$

Despite the complexity of the Jeans analysis, dynamical models are often claimed to require shallower density profile slopes that are consistent with a core at their centre [Adams et al., 2014; Agnello & Evans, 2012; Amorisco & Evans, 2012; Read et al., 2019; Walker & Peñarrubia, 2011]. Figure 2.3, taken from Wetzel et al. [2016], shows the circular velocity of 19 subhalos in the DM-only simulation at $z = 0$. Only five subhalos from the GIZMO cosmological simulation are consistent with Ursa Minor, Draco, Sculptor, Leo I, and Leo II. As a result, the other subhalos are too dense. One way to reduce the inner DM density of halos is core formation. Thus, dark-matter-only simulation suffers from the cusp-core problem.

Although the CDM paradigm can successfully explain various observations at different scales, this discrepancy remains one of the greatest challenges faced by the CDM paradigm (see de Blok [2010] for a detailed review on the observational challenges and see Bullock & Boylan-Kolchin [2017]; Genina et al. [2018] for global reviews related to the cusp-core problem). Even if we focus only on the cusp-core problem in this thesis, there are other tensions of the Λ CDM model at small scales, which

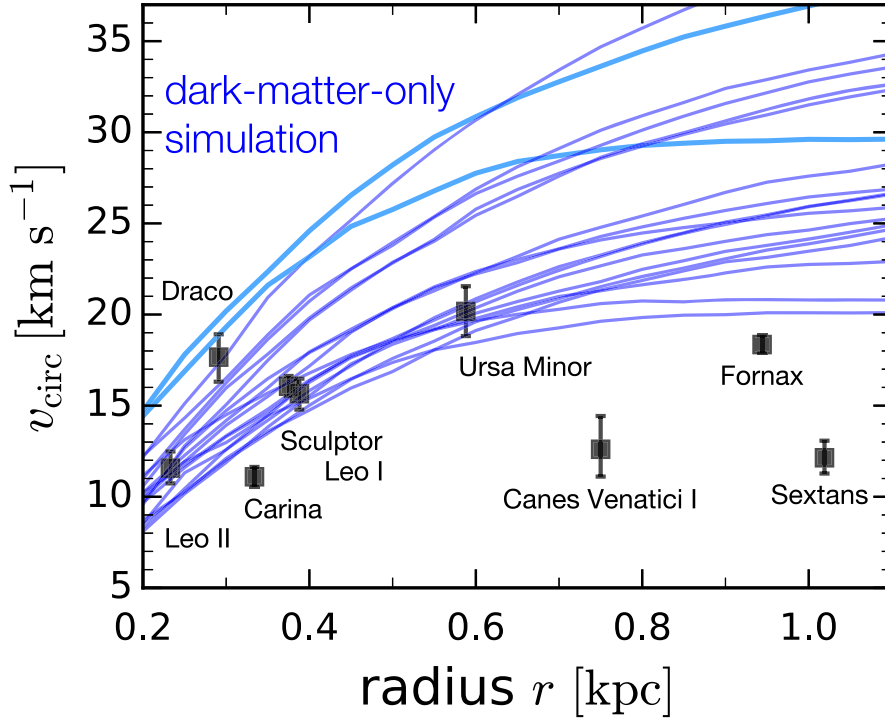


Figure 2.3 – **Rotation curves of classical dwarfs:** Circular velocity of 19 subhalos in the dark-matter-only simulation at $z = 0$. Black points show observed satellites of the MW [Wolf et al., 2010]. Only five subhalos from the GIZMO cosmological simulation are consistent with Ursa Minor, Draco, Sculptor, Leo I, and Leo II. As a result, the other subhalos are too dense. One way to reduce the inner DM density of halos is core formation. Thus, dark-matter-only simulation suffers from the cusp-core problem. This figure is taken from Wetzel et al. [2016].

are the missing satellites problem, the too big to fail problem and the alignment of the substructures in the Galactic halo [Boylan-Kolchin et al., 2011; Bullock & Boylan-Kolchin, 2017; Klypin et al., 1999; Schneider et al., 2012b].

2.1.3 The diversity problem

As shown previously, a key observable related to the inner mass distribution of galaxies is their rotation curve. The circular velocity curves of simulated galaxies vary systematically as a function of their maximum circular velocity V_{\max} with a marginal uncertainty for a given V_{\max} . On the other hand, observed galaxies show a large diversity of rotation curve shapes, even at fixed maximum rotation velocity, especially for dwarf galaxies. This is at odds with the expectation for CDM halos, where V_{\max} fully determines $V_{\text{circ}}(2 \text{ kpc})$ and has been termed the diversity problem [Oman et al., 2015]. The origin of this diversity is still not well understood.

Figure 2.4 shows the circular velocity $V_{\text{circ}}(2 \text{ kpc})$ versus V_{\max} for observed galaxies. We also used the coreNFW model in order to characterize the inner DM density from these observed circular velocities. The lines trace the mean of the circular velocity at $r = 2 \text{ kpc}$ as a function of V_{\max} described by ΛCDM (red), coreNFW model (see Equation.(2.14)) for $n = 0.25$ (magenta), $n = 0.5$ (purple), $n = 0.75$ (violet) and $n = 1$ (blue), where the width of the bands correspond to the 1σ scatter in DM halo concentrations (see Equation.(2.5)). Observed galaxies with their observation type such as HI (black square), H α (black circle), and HI+H α (black triangle) were taken from the compilation by Oman et al. [2015]. Galaxies below the red band are those with less mass within 2 kpc than expected from the predicted ΛCDM model. This is evidence for the presence of cores in

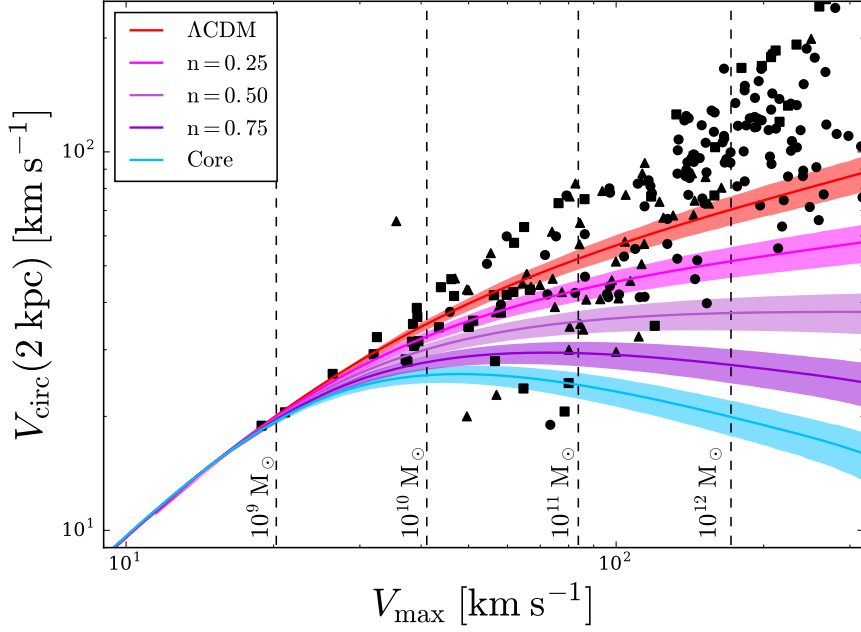


Figure 2.4 – **Diversity problem:** Circular velocity at $r = 2$ kpc versus the maximum circular velocity, V_{\max} for observed galaxies. The lines trace the mean $V_{\text{circ}}(2 \text{ kpc})$ as a function of V_{\max} described by ΛCDM (red), coreNFW model (see Equation (2.14)) for $n = 0.25$ (magenta), $n = 0.5$ (purple), $n = 0.75$ (violet) and $n = 1$ (blue), where the width of the bands correspond to the 1σ scatter in DM halo concentrations (see Equation (2.5)). Observed galaxies with their observation type such as HI (black square), H α (black circle), and HI+H α (black triangle) were taken from the compilation by [Oman et al. \[2015\]](#). Galaxies below the red band are those with less mass within 2 kpc than expected from the predicted ΛCDM model. This is evidence for the presence of cores in such galaxies. However, galaxies at large masses tend to have a higher circular velocity at $r = 2$ kpc than expected from ΛCDM . This is explained by the non-negligible contribution of the baryons to the inner rotation curve in massive galaxies. We also note also that the scatter in the circular velocity at 2 kpc is reduced for galaxies below the red band as well as the mass increase.

such galaxies (see Figure. 2.4). However, galaxies at large masses tend to have a higher circular velocity at $r = 2$ kpc than expected from ΛCDM . This is explained by the non-negligible contribution of the baryons to the inner rotation curve in massive galaxies. We also note that the scatter in the circular velocity at 2 kpc is reduced for galaxies below the red band as well as the mass increase (see Figure 2.4).

Explaining this observed diversity demands a mechanism that creates cores of various sizes in only some galaxies, but not in others, over a wide range of V_{\max} . Nevertheless, these galaxies, formed in similar halos, have approximately the same baryonic mass, and similar morphologies. Some diversity induced by differences in the distribution of the baryonic component was expected, but clearly the observed diversity is much greater than in simulations [[Brook et al., 2012](#); [Governato et al., 2010](#); [Madau et al., 2014](#); [Oh et al., 2011](#); [Teyssier et al., 2013](#)]. Further, we would expect that the DM is most affected in systems where baryons play a more important role such as high-surface brightness galaxies, whereas observations seem to suggest the opposite trend [[Benítez-Llambay et al., 2019](#)]. From a suite of very high-resolution simulations, the observed diversity can be explained from the starburst cycles of galaxies and their influence on the dynamical state of the galaxy [[Read et al., 2016b](#)].

2.2 Solutions

There are two main approaches that could solve this discrepancy between Λ CDM and observations. Cosmological solutions invoke a different spectrum at small scales [Zentner & Bullock, 2003], different nature for DM particles, such as fuzzy and self-interacting DM [Colín et al., 2000; Goodman, 2000; Hu et al., 2000; Kaplinghat et al., 2000; Peebles, 2000; Sommer-Larsen & Dolgov, 2001], modified gravity theories [Bengochea & Ferraro, 2009; Buchdahl, 1970; Dent et al., 2011; Godani & Samanta, 2020; Linder, 2010; Zheng & Huang, 2011] or Modified Newtonian dynamics [Milgrom, 1983]. On the contrary, astrophysical solutions invoke sub-galactic baryonic physics within the Λ CDM paradigm. A common aspect of these two broad categories of solutions is that core creation has been identified as their main mechanism. In this section, we explore some of the most popular and promising solutions to the cusp-core problem discussed above.

2.2.1 Baryonic physics

One of the key predictions of the Λ CDM paradigm is that DM assembles into halos that develop cuspy density profiles following the NFW form in the absence of baryonic effects. Indeed, the cusp-core problem was established without the inclusion of baryons. That is the reason why baryonic physics appeared as a natural solution within the Λ CDM framework. Moreover, the size of a galactic core is typically on the order of a few kpc, where baryons start to play an important role. Since DM interacts only gravitationally, baryons can affect it through the gravitational potential.

Stellar and black hole feedback

First, two feedback processes were designated to explain this discrepancy: stellar and black hole feedback. Stellar feedback consists of all interactions of stars with the interstellar medium. This space between stars is mostly filled with gas. Throughout the life of a star, its feedback injects energy and momentum to the surrounding gas through mechanisms such as photo-heating, radiation pressure, supernovae, and stellar winds [Dekel & Silk, 1986; Larson, 1974; White & Frenk, 1991; White & Rees, 1978]. As massive black holes harbour the centre of most of the galaxies [Ferrarese & Merritt, 2000; Gebhardt et al., 2000], the accretion of matter by them also provides feedback with energy that is of orders of magnitudes higher than that of stellar feedback [Churazov et al., 2005; Fabian, 2012]. It was established that at high halo masses, effective feedback is provided by black holes, but at lower masses, stellar feedback dominates, mainly from high mass stars.

Even if baryons steepen the DM potential well when they cool and accumulate at their centre [Abadi et al., 2010; Blumenthal et al., 1986; Gnedin et al., 2004; Schaller et al., 2015], feedback mechanisms are able to alter the DM distribution. Both powerful feedback processes showed their ability to generate significant movements of the gas. Indeed, gas gathers in DM halos and feedback can expel large amounts of gas from the bottom of their potential well [Brooks & Zolotov, 2014; Freundlich et al., 2020; Gnedin & Zhao, 2002; Macciò et al., 2012b; Madau & Dickinson, 2014; Martizzi et al., 2013; Mashchenko et al., 2008; Navarro et al., 1996a; Pontzen & Governato, 2012, 2014; Read & Gilmore, 2005; Silk, 2017]. A fraction of this gas then cools and returns to the centre, generating repeated cycles of significant gas outflows which, in turn, cause rapid fluctuations of the gravitational potential. These potential fluctuations dynamically heat the DM and lead to the formation of a core. As a result, baryonic processes transform a central DM cusp $\alpha = -1$ into a core $\alpha = 0$. The gradual dispersion of the DM particles away from the centre of the halo is ultimately responsible for core creation. More precisely, these fluctuations in the potential transfer energy into DM particles, thus expanding the DM distribution. Thus, one solution to the cusp-core problem is

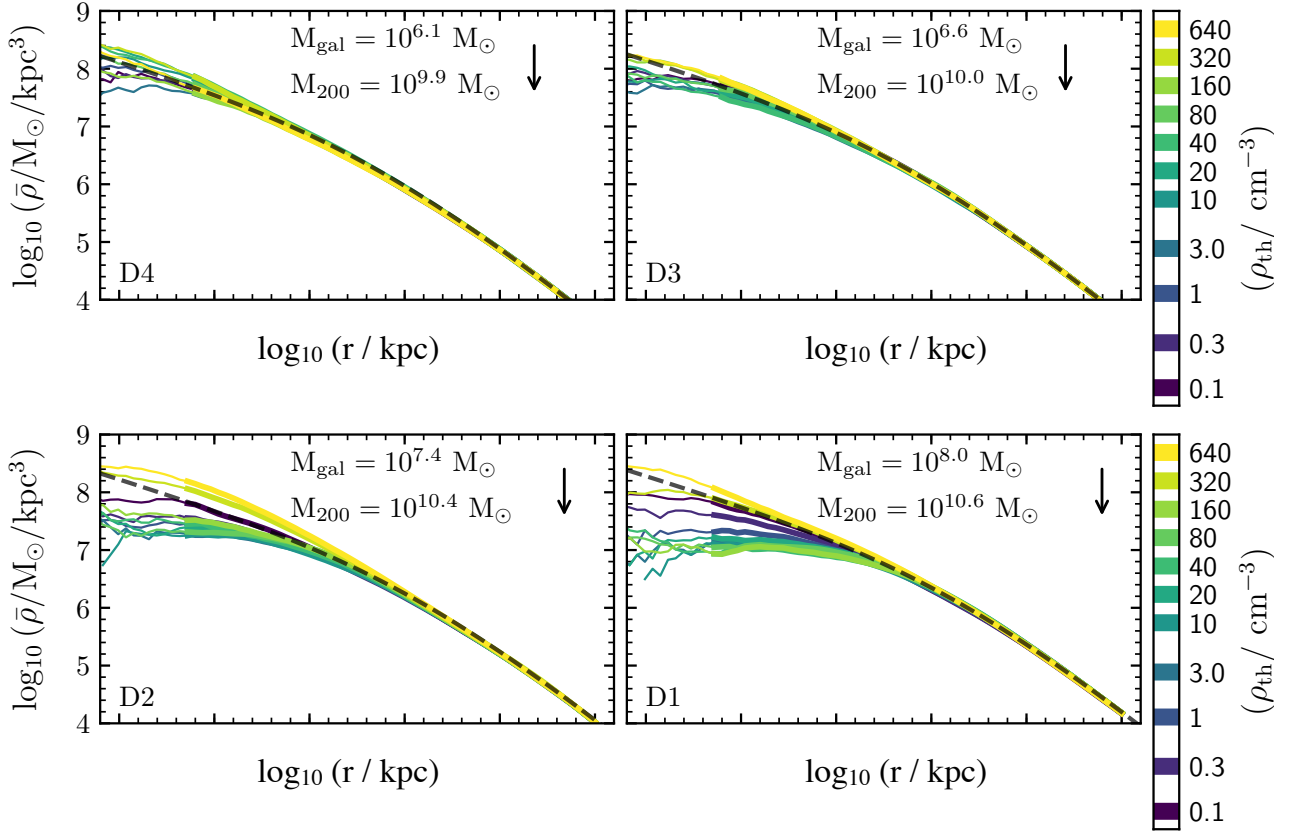


Figure 2.5 – **Cusp-to-core transition:** Mean enclosed DM density profiles at $z = 0$ of our four dwarf galaxies for different gas density threshold for star formation, ρ_{th} compared to the NFW profile (dashed curve). The virial radius of the halos is indicated by black arrows. The value of ρ_{th} varies from 0.1 to 640 cm^{-3} . For $\rho_{\text{th}} = 0.1 \text{ cm}^{-3}$, the DM profiles are all consistent with NFW form above the convergence radius defined by [Power et al. \[2003\]](#). This radius indicates the region within which numerical convergence is not achieved because of two-body relaxation. For higher values of ρ_{th} , the density profiles depart systematically from NFW in some cases. The dependence of the core radius on the halo mass is highlighted over a wide range of the gas density threshold. This confirms that very low-mass dwarfs do not exhibit large DM cores as in earlier works [[Bullock & Boylan-Kolchin, 2017](#); [Di Cintio et al., 2014](#); [Tollet et al., 2016](#)]. Moreover, it is also demonstrated that the particular choice of ρ_{th} determines the size of the core. This figure is taken from [Benítez-Llambay et al. \[2019\]](#).

that a DM heating through feedback processes from stars or black hole generates a cusp-to-core transition for the DM halo within the paradigm of CDM.

Cosmological hydrodynamical simulations performed with different codes such as GASOLINE [[Di Cintio et al., 2014](#); [Governato et al., 2010](#); [Tollet et al., 2016](#); [Zolotov et al., 2012](#)], FIRE [[Chan et al., 2015](#); [Fitts et al., 2017](#); [Garrison-Kimmel et al., 2017](#); [Hopkins et al., 2018](#); [Oñorbe et al., 2015](#); [Wetzel et al., 2016](#)], RAMSES [[Peirani et al., 2017](#)] and GADGET [[Benítez-Llambay et al., 2019](#); [Bose et al., 2019](#); [Duffy et al., 2010](#); [Fattahi et al., 2016](#); [Sawala et al., 2016](#); [Schaye et al., 2010](#)] have proved the efficiency of these feedback mechanisms for core creation. Many of these most advanced hydrodynamic simulations with different feedback implementations are able to produce core-like density profiles as inferred from rotation curves such as those shown in Figure 2.1. Figure 2.5, taken from [Benítez-Llambay et al. \[2019\]](#), illustrates the mean enclosed DM density profiles at $z = 0$ of our four dwarf galaxies for different gas density threshold for star formation, ρ_{th} , compared to the NFW profile (dashed curve). For $\rho_{\text{th}} = 0.1 \text{ cm}^{-3}$, the DM profiles are all consistent with NFW form above the convergence radius defined by [Power et al. \[2003\]](#). For higher values of

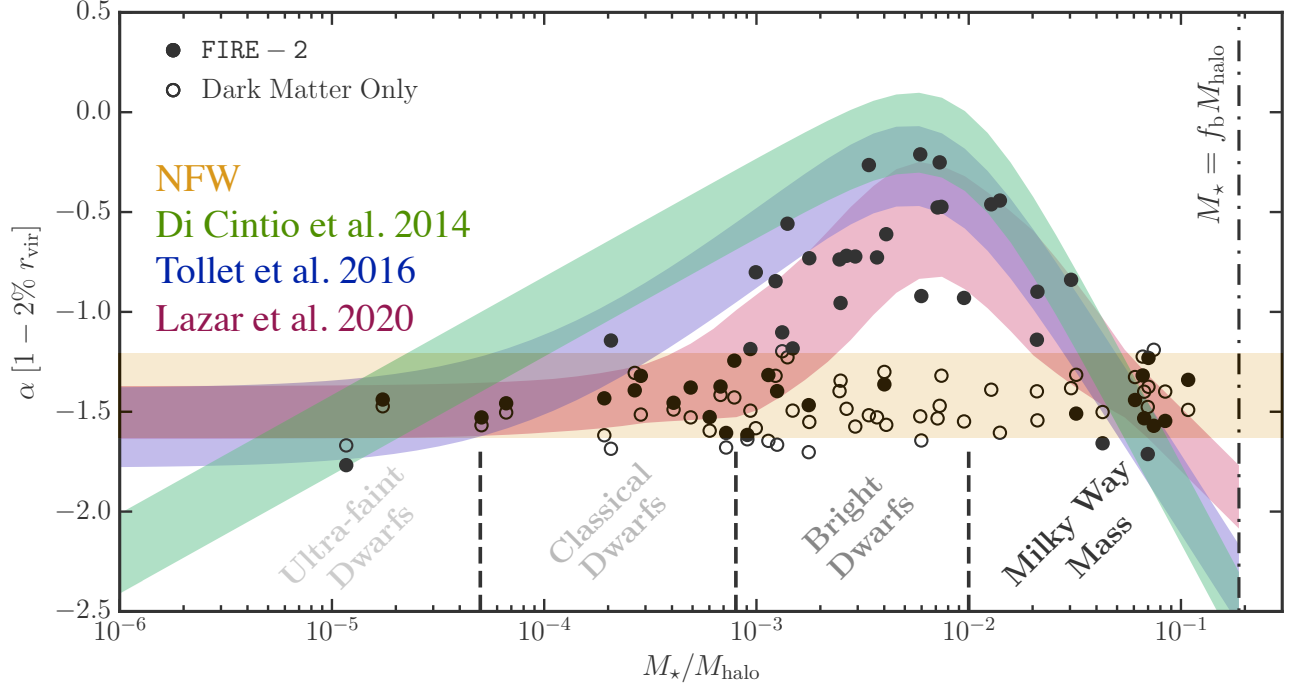


Figure 2.6 – **The impact of baryonic feedback:** Inner DM density slope α at $r = 0.015 r_{\text{vir}}$ as a function of M_*/M_{vir} for simulated galaxies at $z = 0$ from FIRE and GASOLINE cosmological hydrodynamic simulations [Chan et al., 2015; Di Cintio et al., 2014; Fitts et al., 2017; Hopkins et al., 2018; Lazar et al., 2020; Tollet et al., 2016]. The shaded orange band shows the expected range of DM profile slopes for NFW profile as derived from DM-only simulations by including concentration scatter. The filled black circles show results for hydrodynamic simulations while the open circles show results for the DM-only simulations, which all have $\alpha = -1.5$ as expected from Λ CDM without baryon effects. Core profiles are associated with $\alpha = 0$, while cuspy profiles have lower values than $\alpha = -1$. We note that there are DM core formation peaks in the regime of the brightest dwarfs ($M_*/M_{\text{vir}} = 0.005$). Furthermore, all hydrodynamical simulations find that baryonic feedback is negligible in the regime of classical and ultra-faint dwarfs ($M_*/M_{\text{vir}} < 10^{-4}$). We also notice that MW-mass halos seem to have a density structure similar to the DM-only results. However, MW-like halos have cored density profiles. The choice of a specific radius $r = 0.015 r_{\text{vir}}$ for determining the slope α is responsible for this effect. This figure is taken from Lazar et al. [2020].

ρ_{th} , the density profiles depart systematically from NFW in some cases. The dependence of the core radius on the halo mass is highlighted over a wide range of the gas density threshold. This confirms that very low-mass dwarfs do not exhibit large DM cores as in earlier works [Bullock & Boylan-Kolchin, 2017; Di Cintio et al., 2014; Tollet et al., 2016]. Moreover, it is also demonstrated that the particular choice of ρ_{th} determines the size of the core (see Figure 2.5). However, it was concluded that a value of ρ_{th} higher than the mean interstellar medium density is necessary for forming cores induced by stellar feedback [Benítez-Llambay et al., 2019; Dutton et al., 2019]. However, these simulations have shown that cores form efficiently only in a narrow range of stellar/halo mass, which corresponds to bright dwarf galaxies (see Figure 2.6). It was also suggested that the inner slope of DM halos is mass-dependent [Di Cintio et al., 2014; Pontzen & Governato, 2012]. Figure 2.6, taken from Lazar et al. [2020], depicts the impact of baryonic impact on the DM density distribution by showing the inner DM density slope α at $r = 0.015 r_{\text{vir}}$ as a function of M_*/M_{vir} for simulated galaxies at $z = 0$ from FIRE and GASOLINE cosmological hydrodynamic simulations. Indeed, a relationship was established between the slope α and the stellar/halo mass fraction, M_*/M_{vir} , of simulated galaxies [Chan et al., 2015; Di Cintio et al., 2014; Hopkins et al., 2018; Tollet et al., 2016; Wang et al., 2015]. As a result, there is a characteristic mass-ratio of $M_*/M_{\text{vir}} = 0.005$ for

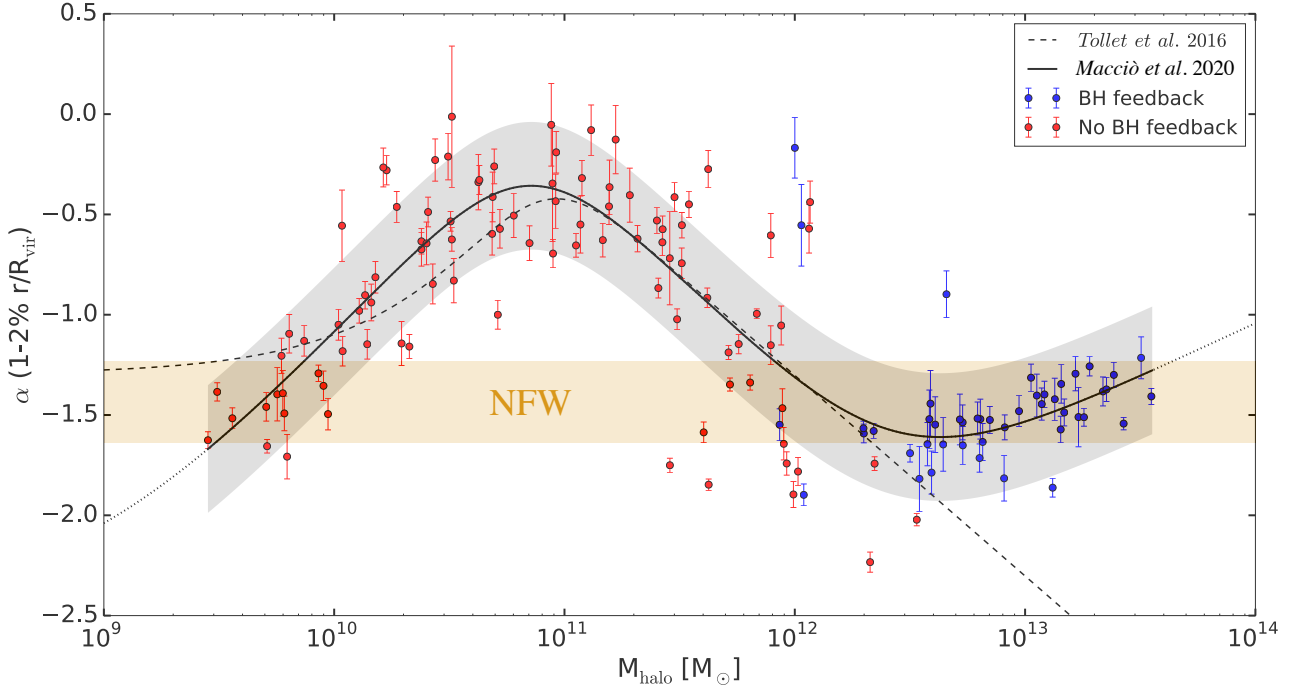


Figure 2.7 – **Black hole feedback:** Inner DM density slope α at $r=0.015r_{\text{vir}}$ as a function of the halo mass M_h at $z=0$ for galaxies without (red symbols) and with black hole feedback (blue symbols). The best fit of Macciò et al. [2020] (black solid line) is compared to the relation proposed in NIHAO-IV [Tollet et al., 2016], based on galaxies without black hole (dashed line). The gray shaded area shows the one sigma scatter for the whole sample. Gas outflows generated by black hole feedback are able to partially counteract the DM contraction due to the large central stellar component in these massive halos. As a result, the DM distribution becomes less cuspy at the transition from stellar to AGN feedback dominated systems ($M_h > 3 \times 10^{12} M_\odot$). We note that most of the final DM slopes remain similar to the NFW profile in the black hole feedback regime. This figure is taken from Macciò et al. [2020].

efficient core formation, above and below which DM halos remain similar to the cuspy NFW profile predicted by DM-only simulations. In fact, DM halos become more cored as M_*/M_{vir} increases to this characteristic mass-ratio. These halos exhibit shallow DM cusps according to their slope α . Furthermore, all hydrodynamical simulations find that baryonic feedback is negligible in the regime of classical and ultra-faint dwarfs ($M_*/M_{\text{vir}} < 10^{-4}$), as expected on energetic grounds [Garrison-Kimmel et al., 2013; Peñarrubia et al., 2012]. We notice also that MW-mass halos seem to have a density structure similar to the DM only results. However, MW-like halos have cored density profiles. The choice of a specific radius $r=0.015r_{\text{vir}}$ for determining the slope α is responsible for this effect.

More precisely, the importance of black hole feedback on DM distribution is addressed in Figure 2.7, taken from Macciò et al. [2020], but also Chan et al. [2015]; Duffy et al. [2010]; Martizzi et al. [2012, 2013]; Peirani & de Freitas Pacheco [2008]; Peirani et al. [2017]. Gas outflows generated by black hole feedback are able to partially counteract the DM distribution despite the huge quantity of baryons at the centre of these massive halos. As a result, the DM distribution becomes less cuspy at the transition from stellar to black hole feedback dominated systems ($M_h > 3 \times 10^{12} M_\odot$). We note that most of the final DM slopes remain similar to the NFW profile in the black hole feedback regime.

Even if hydrodynamical simulations alleviate this Λ CDM tension by creating cores, its significance depends on the feedback model [Benítez-Llambay et al., 2019; Bose et al., 2019; Fattahi et al., 2016; Oman et al., 2015; Sawala et al., 2016]. Indeed, galaxies without a sufficient number of stars are

unlikely to have cores due to insufficient amount of energy from feedback [Peñarrubia et al., 2012]. It was also argued that the timing of star formation relative to DM halo growth can also affect core formation. Cusps can regenerate from the core induced by the feedback as a result of DM rich mergers [Oñorbe et al., 2015]. As discussed before, the gas density threshold is a crucial feedback parameter for producing cores in galaxies. Cosmological simulations with low-density thresholds for star formation such as APOSTLE and Auriga [Bose et al., 2019] have been shown to not exhibit DM cores. Moreover, It seems unlikely that stellar feedback can remove a large amount of mass ($\sim 10^9 M_\odot$) from the inner 5 kpc as the galaxy IC 2574 according to its measured rotation curve [Oman et al., 2015].

There is a consensus that the stellar feedback can erase the central cusps as demonstrated in Figure 2.5. As baryons tend to accumulate towards the centre of galaxies, feedback processes could solve the cusp-core problem, at least, for the largest galaxies. However, DM cores tend to persist even for smaller galaxies, including those that are rather DM-dominated.

Dynamical friction via sinking objects

Chandrasekhar [1943] showed that a massive particle moving through an infinite, homogeneous and isotropic background of lighter particles experiences a force of dynamical friction given by

$$F(x, v) = 2\pi G^2 \rho(x) \ln(1 + \Lambda^2) \left(\text{erf}(X) - \frac{2X}{\sqrt{\pi}} \exp(-X^2) \right) \frac{v}{|v|^3} M, \quad (2.15)$$

where this massive particle of mass M at position x is moving at velocity v through a background density ρ . The quantity X is defined as $|v|/\sqrt{(2)\sigma_r}$ with σ_r being the radial dispersion of lighter particles. The factor Λ that goes into the Coulomb logarithm is taken to be

$$\Lambda = \frac{r/\gamma}{\max(r_{\text{hm}}, GM/|v|^2)}, \quad (2.16)$$

where r_{hm} is the half-mass radius of the massive particle and γ is the absolute value of the logarithmic slope of the density, i.e. $\gamma = |d \ln(\rho)/d \ln(r)|$ [Petts et al., 2016]. The background medium composed of lighter particles produces an overdensity region behind it due to this friction between particles. The dynamical friction is responsible for a momentum loss by the massive object due to its gravitational interaction with its own gravitationally induced wake. The surrounding background medium, which consists of a combination of collisionless matter such as DM, is heated at an equal and opposite rate to the energy lost by the massive object. The rate of energy loss by the massive object is given by El-Zant et al. [2001]:

$$\frac{d}{dt} = M \frac{dv}{dt} v. \quad (2.17)$$

Indeed, an energy exchange occurs, increasing that of the lighter particles at the expense of the perturber. Hence, this dynamical effect can modify the DM inner structure. That is the reason why the sinking of massive objects such as gas clumps, globular clusters or subhalos have also been proposed for transforming cusps into cores via from the heating by dynamical friction [Cole et al., 2011; Del Popolo & Le Delliou, 2014; El-Zant et al., 2001; Goerdt et al., 2010; Inoue & Saitoh, 2011; Nipoti & Binney, 2015]. During their infall, they transfer part of their kinetic energy to the DM background through dynamical friction causing the DM halo to expand.

Figure 2.8, taken from Goerdt et al. [2010], shows the modification of the inner DM structure after the first (upper panel) and second (lower panel) closest pericentre passage of massive objects such as gas clump or globular clusters with different masses. The perturbers were started within

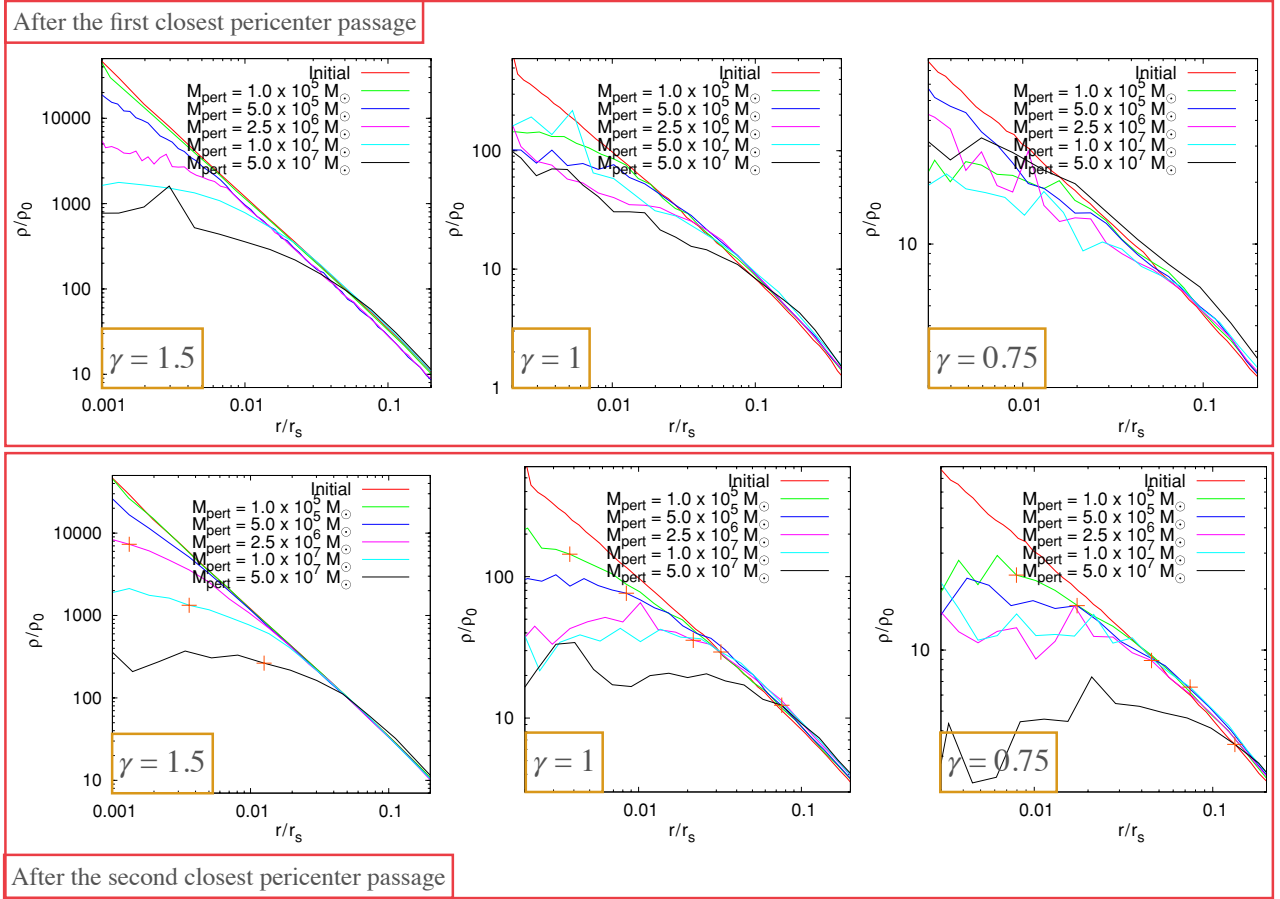


Figure 2.8 – **Sinking of massive objects:** DM density profiles of the host halo after the first (upper panel) and second (lower panel) closest pericentre passage for the different perturber masses $M_{\text{pert}} = [10^5, 5 \times 10^5, 2.5 \times 10^6, 10^7, 5 \times 10^7]$. The perturbers were started within the cusp region. From left to right, the panels show halos with different initial absolute values of the logarithmic slope of the density $\gamma = |\text{dln}(\rho)/\text{dln}(r)|$. All simulations are shown using circular orbits for the infalling objects. We note that the response of different central cusps to sinking perturbers with a range of masses using N-body simulations occurs rapidly. The DM density distribution changes significantly from cuspy to having a core. Indeed, larger perturber masses lead to larger constant density central regions. This figure is taken from [Goerdt et al. \[2010\]](#).

the cusp region. All simulations are shown using circular orbits for the infalling objects. We note that the response of different central cusps to sinking perturbers with a range of masses using N-body simulations occurs rapidly. The DM density distribution changes significantly from cuspy to having a core. Indeed, larger perturber masses lead to larger constant density central regions. It was estimated that the cusp-core transformations occur at approximately the radius where the mass of the perturber roughly matches the enclosed mass of the DM background [[Read et al., 2006](#)].

The results of these works clearly indicated, as a proof of concept, that dynamical friction heating can have an important role in DM halos on different scales and the relevance of this process depends on the properties of the massive objects and of the host halo. Such a mechanism still requires another process to then destroy the gas clumps and globular clusters at the centre of the DM halo. Otherwise, the resulting inner stellar density would be too high to be consistent with observations [[Nipoti & Binney, 2015](#)]. For the gas clumps, stellar feedback could dissolve these clumps. However, globular clusters form nuclear star clusters at the centre of galaxies but observations claimed that none of the classical dwarfs exhibit a stellar nucleus at their centre.

Less studied baryon effects have been proposed to erase the central DM cusps. DM can also

be heated from baryons by the evolution of a stellar bar [Holley-Bockelmann et al., 2005; Kataria et al., 2020; Sellwood, 2003; Weinberg & Katz, 2002], the radiation recoil by a black hole [Merritt & Milosavljević, 2005], or the transfer of angular momentum [Tonini et al., 2006].

2.2.2 Alternative theories of dark matter

The presence of the core appears to persist for dwarf galaxies that are DM dominated and baryon deficient. Thus, it is still unclear how baryonic feedback can solve this puzzle. Another possibility is that the DM is more complex and hotter than simple CDM. A wide range of alternative DM models has been proposed over the last decades. Mostly three main classes of alternative DM models have been simulated: warm dark matter (WDM) [Bode et al., 2001; Colín et al., 2000; Lovell et al., 2014; Macciò et al., 2012a; Schneider et al., 2012a; Shao et al., 2013], self-interacting dark matter (SIDM) [Burkert, 2000; Elbert et al., 2015; Kochanek & White, 2000; Miralda-Escudé, 2002; Spergel & Steinhardt, 2000; Zavala et al., 2013], and fuzzy dark matter (FDM) that fundamentally change the gravitational law [Chavanis, 2018; Goodman, 2000; Hu et al., 2000; Hui et al., 2017; Marsh & Silk, 2014; Mocz et al., 2019; Nori et al., 2019; Peebles, 2000; Schive et al., 2014a]. Many of these alternative theories have been invoked to address Λ CDM small-scale problems and more particularly, the cusp-core problem. FDM and SIDM, which are the two most recent alternatives theories, are reviewed in this chapter.

Fuzzy dark matter

As there is a current lack of evidence for any CDM particle such as weakly interacting massive particles, DM as an ultralight scalar field with no self-interaction in the non-relativistic limit was introduced under the name of Fuzzy Dark Matter (FDM) [Goodman, 2000; Hu et al., 2000]. This scalar field is assumed to be made of very light particles with a mass of $\sim 10^{-22} - 10^{-21}$ eV. One of the candidates for this alternative DM theory is the axion-like particles predicted by string theories [Marsh, 2016]. Such a scalar field is then well-described in the non-relativistic limit by the coupled Schrodinger and Poisson equations [Widrow & Kaiser, 1993]:

$$i\hbar \frac{\partial}{\partial t} \phi = -\frac{\hbar^2}{2m} \nabla^2 \phi + mU\psi, \quad (2.18)$$

$$\nabla^2 U = 4\pi G \rho_m, \quad (2.19)$$

where m is the mass of FDM particles. The mass density defines as $\rho_m = |\phi|^2$ and U is the gravitational potential. Such ultra-light DM particles have a characteristic wavelength called the de Broglie wavelength:

$$\lambda = 1.19 \left(\frac{10^{-22} \text{eV}}{m} \right) \left(\frac{100 \text{km.s}^{-1}}{v} \right) \text{kpc}, \quad (2.20)$$

where v is the characteristic velocity. Equation (2.20) shows that the wavelength of a few kpc is of astrophysical size. Indeed, the small masses of ultra-light DM particles are associated with a very large de Broglie wavelength where their quantum properties play an important role [Böhmer & Harko, 2007; Hu et al., 2000; Woo & Chiueh, 2009]. Thus, the de Broglie wavelength is of the order of the scales at which the cusp-core problem appears.

Axion-like particles are interesting DM candidates because they predict new structural and dynamical phenomena on scales of galaxies. When the de Broglie wavelength λ is on the order of or larger than the inter-particle distance d_i , quantum effects will dominate. In fact, DM particles have huge occupancy numbers at these small scales. In the non-interacting Bose gas theory, the

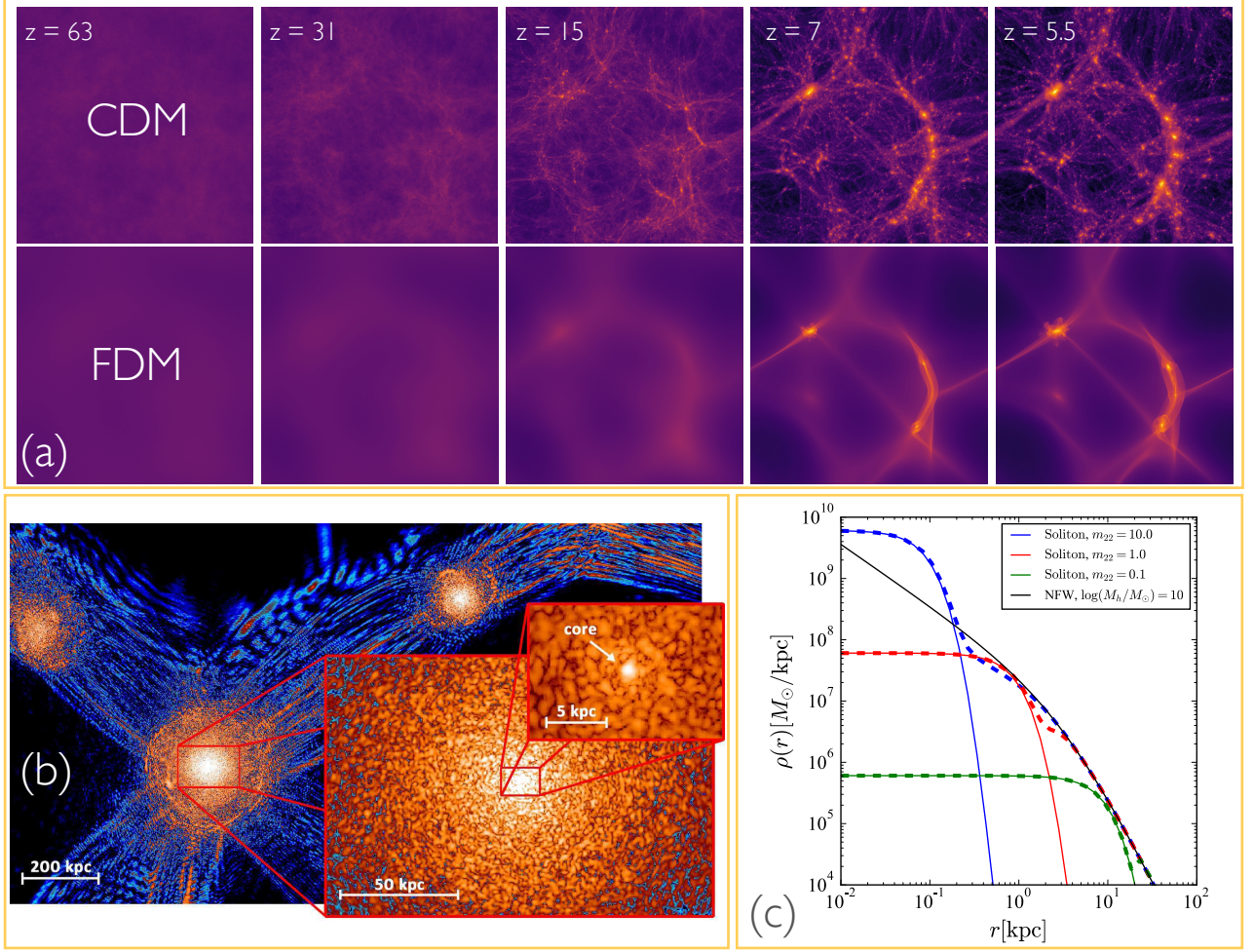


Figure 2.9 – **FDM properties:** (a) Snapshots of the DM projected densities along the line of sight at $z = 63, 31, 15, 7$, and 5.5 under the CDM (upper panel) and FDM (lower panel) cosmologies. The two cosmological simulations have led to the formation of three $\sim 10^9 - 10^{10} M_\odot$ halos. Snapshots highlight that FDM halos are connected via filaments, while CDM has filaments fragmented into subhalos. (b) Slice of density field of FDM simulation at different scales at $z = 0.1$. We can distinguish the cores with a size of $\sim 0.3 - 1.6$ kpc in each halo. These DM cores grow as particles are accreted and surrounded by virialized halos. (c) DM profiles of a $10^{10} M_\odot$ halo at $z = 0$ for different values of m_{22} . Thin solid lines show the FDM core profiles for different axion masses. The thin black line shows the NFW profile of a $10^{10} M_\odot$ halo at $z = 0$. The thick dashed lines show the full halo profile that is a combination of the FDM profile transitioning to an NFW profile around $r = 3r_c$. This figure is taken from [Mocz et al. \[2019\]](#); [Safarzadeh & Spergel \[2020\]](#); [Schive et al. \[2014a\]](#).

macroscopic occupation of the ground state is seen as condensation and this phenomenon is called Bose-Einstein condensation. In FDM, the particles form a Bose-Einstein condensate on galactic scales [[Hu et al., 2000](#)]. Figure 2.9 depicts that it results in a DM core at the halo's central region as the particles of the system are in the ground state described by a single wave function [[Böhmer & Harko, 2007](#); [Schive et al., 2014a](#)]. Cosmological simulations of light DM found that the density profile of the innermost central region of the halos at redshift $z = 0$ follows [[Schive et al., 2014a](#)]:

$$\rho(r) = \frac{\rho_0}{(1 + 0.091(r/r_c)^2)^8} 10^9 M_\odot \text{kpc}^{-3}, \quad (2.21)$$

with

$$\rho_0 = 0.019 m_{22}^{-2} r_c^{-4} 10^9 M_\odot \text{kpc}^{-3}, \quad (2.22)$$

where $m_{22} = m/10^{-22}$ eV is the DM particle mass and r_c is the radius at which the density drops to one-half its peak value for a halo at $z = 0$. The central mass density of the core is given by Robles et al. [2019]:

$$M_c = \frac{M_h^{1/3}}{4} (4.4 \times 10^7 m_{22}^{-3/2})^{2/3}, \quad (2.23)$$

and

$$r_c = \frac{1.6}{m_{22}} \left(\frac{M_h}{10^9 M_\odot} \right) \text{kpc}, \quad (2.24)$$

where M_h is the halo mass. The heating mechanism is due to quantum fluctuations arising from the uncertainty principle. Indeed, the quantum pressure stabilizes the gravitational collapse and prevents the formation of cusp by suppressing the small-scale structures [Hu et al., 2000; Lee & Lim, 2010; Woo & Chiueh, 2009]. The condensate is a stable region where no clustering takes place (see Figure 2.9). These kpc cores offer one possible solution to the cusp-core problem.

However, when $\lambda \ll d_i$, DM particles can be considered to be a classical system. Indeed, at large scales, condensation is broken and the system behaves as a system of individual massive particles [Mocz et al., 2019]. Figure 2.9 shows that the outer region of FDM halo behaves like CDM which is well approximated by the NFW [Schive et al., 2014a]. Thus, the full density profile of halos can be written as:

$$\rho(r) = \Theta(r_t - r) \rho_c + \Theta(r - r_t) \rho_{\text{NFW}}, \quad (2.25)$$

where the Θ is a step function and r_t is the transition radius, which marks the transition between the core profile and NFW profile. This specific scale is proportional to the core size as $r_t = \alpha r_c$ where $\alpha \sim 2 - 4$ [Robles et al., 2019].

FDM was introduced by the motivation to solve the core-cusp problem in DM halos of galaxies. As halo cores form naturally in FDM theory, this scenario is appealing in principle. However, some specific observations are necessary to verify this type of DM. The quantum nature of DM particles gives rise to specific density profiles and potential fluctuations that may affect delicate structures such as tidal streams and disks [El-Zant, 2019].

As illustrated above, any DM model, which sets a universal core profile cannot fit observations. As such, baryonic physics must also play a significant role in shaping the DM profiles. Figure 2.10 illustrates DM density profiles of a halo with a final virial mass of $10^{10} M_\odot$ at three different redshifts assuming FDM, FDM with baryons and CDM with baryons. At the earliest redshift $z = 5.6$, the CDM halo exhibits the highest central DM density with a cuspy profile, while the FDM halos show core profiles. The FDM halo with baryons has a lower density at the centre than the FDM-only halo because the baryon pressure delays its collapse. In contrast, at $z = 4$, the FDM central density is more than one order of magnitude higher with baryons than without, exceeding the central DM density of the CDM halo. Indeed, in the presence of baryons, the cores grow by more than a factor of two. However, the core mass does not evolve over time if baryons are absent (see Figure 2.10). As DM cores become more massive and compact in the presence of baryons, observed rotation curves are likely harder to reconcile with FDM [Veltmaat et al., 2020].

Moreover, we expect that DM distribution of centrally baryon-dominated galaxies, especially those containing supermassive black holes, are more strongly affected [Bar et al., 2019; Davies & Mocz, 2020; Davoudiasl & Denton, 2019; Desjacques & Nusser, 2019]. Figure 2.10 shows density profiles of FDM halos with masses from $10^8 M_\odot$ up to $10^{14} M_\odot$ assuming a FDM particle mass of $m = 10^{-22}$ eV. The dot-dashed (thicker) lines correspond to DM halos without (with) a central black hole. It can be seen that the black hole increases the central density only for $M_h \geq 10^{13} M_\odot$. This latter effect depends also on the FDM particle mass. Thus, black holes are most effective

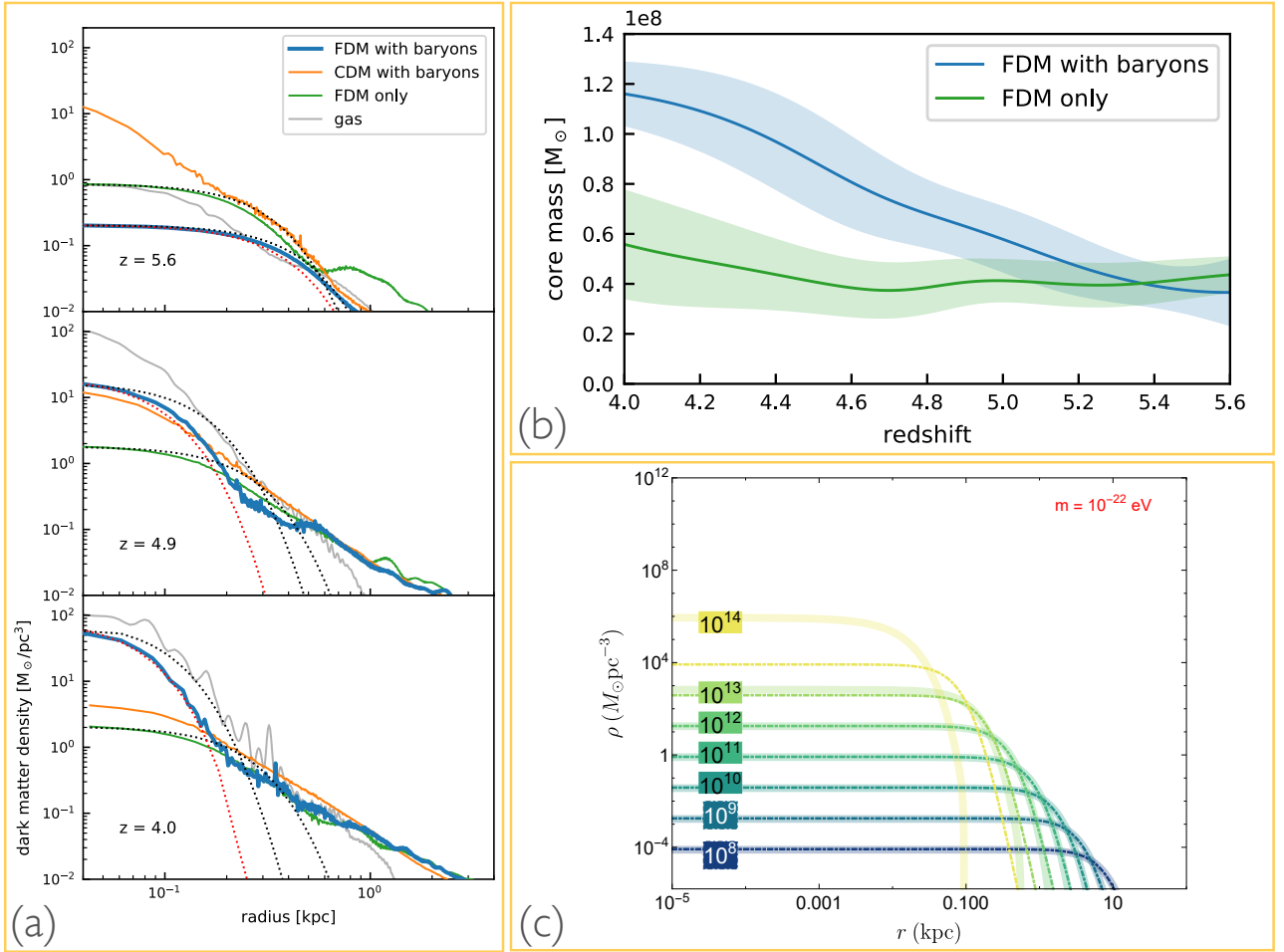


Figure 2.10 – **Adding baryons and black holes:** (a) DM density profiles of a halo with a final virial mass of $10^{10} M_\odot$ at three different redshifts assuming FDM only, FDM with baryons and CDM with baryons. At the earliest redshift of $z=5.6$, the CDM halo exhibits the highest central DM density with a cuspy profile, while the FDM halos show core profiles. The FDM halo with baryons has a lower density at the centre than the FDM-only halo because the baryon pressure delays its collapse. On the contrary, at $z=4$, the FDM central density is more than one order of magnitude higher with baryons than without, exceeding the central DM density of the CDM halo. (b) Evolution of the core mass over redshift for a FDM halo with (blue curve) and without baryons (green curve). The shaded regions represent the corresponding standard deviations. In the presence of baryons, the cores grow by more than a factor of two. However, the core mass does not evolve over time if baryons are absent. (c) Density profiles of FDM halos with masses from $10^8 M_\odot$ up to $10^{14} M_\odot$ assuming a FDM particle mass of $m = 10^{-22} \text{ eV}$. The dot-dashed (thicker) lines correspond to DM halos without (with) a central black hole. It can be seen that the black hole increases the central density only for $M_h \geq 10^{13} M_\odot$. This latter effect depends also on the FDM particle mass. Thus, black holes are most effective at modifying the DM distribution for higher halo masses, and larger FDM particle masses. By numerically solving the Schrodinger-Poisson equations, it was shown that black holes decrease the core radius and increase the central density of FDM halos. This figure is taken from [Davies & Mocz \[2020\]](#); [Veltmaat et al. \[2020\]](#).

at modifying the DM distribution for higher halo masses, and larger FDM particle masses. By numerically solving the Schrodinger-Poisson equations, it was shown that black holes decrease the core radius by increasing the central density of DM halos (see Figure 2.10).

Moreover, it not clear if FDM halos can be in line with known galaxy scaling relation [[Bar et al., 2019](#); [Deng et al., 2018](#); [Robles et al., 2019](#); [Safarzadeh & Spergel, 2020](#)]. Figure 2.11 depicts the mass profiles of FDM halos with masses from $10^9 M_\odot$ up to $10^{12} M_\odot$. Left, middle and right

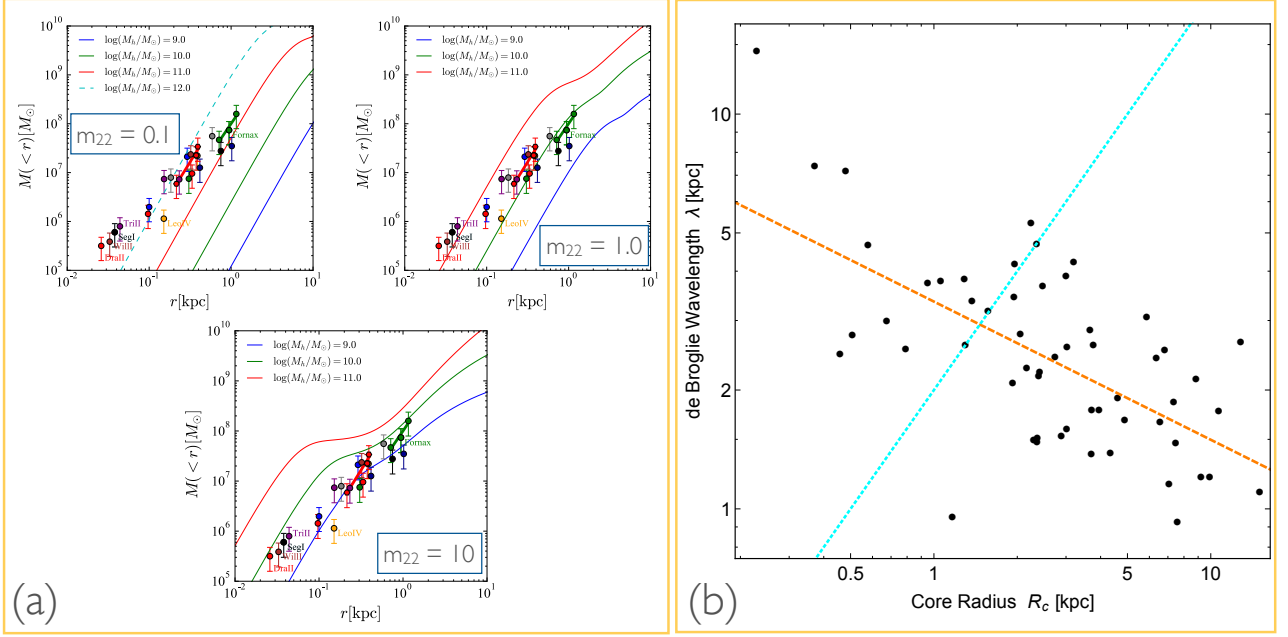


Figure 2.11 – **FDM inconsistencies:** (a) Mass profiles of FDM halos with masses from $10^9 M_\odot$ up to $10^{12} M_\odot$. Left, middle, and right panels represent the mass profiles corresponding to $m_{22} = 0.1$, 1, and 10, respectively. The individual data points for dwarf galaxies are collected from [Martin et al. \[2016\]](#); [Wolf et al. \[2010\]](#), and the slopes of Fornax and Sculptor (green and red lines) are from [Walker & Peñarrubia \[2011\]](#). The profiles show a core region parametrized by Equation (2.23) which then follow an NFW profile at $r = 3r_c$. For $m_{22} = 0.1$, the predicted halo mass of the dwarf galaxies is too high given their dynamical state in the galaxy, and higher m_{22} does not agree with the inferred slopes of Sculptor and Fornax. Low mass axions ($m_{22} = 0.1$) can explain the observed mass profile slopes in Sculptor and Fornax [[González-Morales et al., 2017](#); [Marsh & Pop, 2015](#); [Schive et al., 2014b](#)]. However, at such low masses, the predicted halo masses of the ultra-faint dwarf galaxies such as Segue I are ruled out by dynamical friction arguments. In contrast, high mass axions ($m_{22} = 10$) can explain the halo masses of the ultra-faint dwarf galaxies such as Draco II, Triangulum II, and Segue I. For this axion mass, the predicted mass profiles do not agree with the observed slope of Fornax and Sculptor. The latter highlights the tensions concerning the FDM particle mass. (b) De Broglie wavelength λ as a function of the core radius r_c for a range of galaxies assuming FDM particle mass of 10^{-22} eV. Black dots correspond to the data from [Rodrigues et al. \[2017\]](#). Dashed orange curve is the corresponding best fit power law $\lambda \propto 1/R_c^{1-\beta/2}$ with $\beta = 1.3$ for the data set. The dotted cyan curve corresponds to $\lambda = 2R_c$. We stress that the data indicates that the de Broglie wavelength is a decreasing function of the galactic core radius. However, the FDM theory seems to predict the opposite behaviour. Galaxies above the $\lambda = 2R_c$ line would have a core size that is much smaller than De Broglie wavelength λ over which the particles are localized. In contrast, galaxies below this line have a core size that is much higher than λ . Thus, it seems very difficult for FDM to reproduce the observed relationship between core density and core radius in galaxies, which obeys the rough scaling law given by $\rho_c \propto 1/R_c^\beta$ with exponent $\beta \sim 1$. This figure is taken from [Deng et al. \[2018\]](#); [Safarzadeh & Spergel \[2020\]](#).

panels represent the mass profiles corresponding to $m_{22} = 0.1$, 1, and 10 respectively. The individual data points for dwarf galaxies are collected from [Martin et al. \[2016\]](#); [Wolf et al. \[2010\]](#), and the slopes of Fornax and Sculptor (green and red lines) are from [Walker & Peñarrubia \[2011\]](#). The profiles show a core region parametrized by Equation (2.23) which then follows an NFW profile at $r = 3r_c$. For $m_{22} = 0.1$, the predicted halo mass of the dwarf galaxies is too high given their dynamical state in the galaxy, and higher m_{22} does not agree with the inferred slopes of Sculptor and Fornax. Low mass axions ($m_{22} = 0.1$) can explain the observed mass profile slopes in Sculptor and Fornax [[González-Morales et al., 2017](#); [Marsh & Pop, 2015](#); [Schive et al., 2014b](#)]. However, at

such low masses, the predicted halo masses of the ultra-faint dwarf galaxies such as Segue I are ruled out by dynamical friction arguments. In contrast, high mass axions ($m_{22}=10$) can explain the halo masses of the ultra-faint dwarf galaxies such as Draco II, Triangulum II, and Segue I. For this axion mass, the predicted mass profiles do not agree with the observed slope of Fornax and Sculptor. The latter highlights the tensions concerning the FDM particle mass (see Figure 2.11). Indeed, the MW galaxy constrained the FDM particle mass to be $m < 10^{-19}$ eV [Bar et al., 2019]. In Figure 2.11, the De Broglie wavelength λ as a function of the core radius r_c for a range of galaxies assuming FDM particle mass of 10^{-22} eV. Black dots correspond to the data from Rodrigues et al. [2017]. Dashed orange curve is the corresponding best fit power law $\lambda \propto 1/R_c^{1-\beta/2}$ with $\beta = 1.3$ for the data set. The dotted cyan curve corresponds to $\lambda = 2R_c$. We stress that the data indicate that the de Broglie wavelength is a decreasing function of the galactic core radius. However, the FDM theory seems to predict the opposite behaviour. Galaxies above the $\lambda = 2R_c$ line would have a core size that is much smaller than De Broglie wavelength λ over which the particles are localized. In contrast, galaxies below this line have a core size that is much higher than λ . Thus, it seems very difficult for FDM to reproduce the observed relationship between core density and core radius in galaxies, which obeys the rough scaling law of $\rho_c \propto 1/R_c^\beta$ with exponent $\beta \sim 1$ (see Figure 2.11). To sum up, the FDM model appears to be too predictive and seems to be in conflict with observations of galaxies [Safarzadeh & Spergel, 2020].

Self-interacting dark matter

In the Λ CDM model, DM is assumed to be collisionless. Another promising alternative is, therefore, self-interacting dark matter (SIDM) [Carlson et al., 1992; de Laix et al., 1995], proposed to solve the small scales problems, and more specifically the cusp-core problem [Spergel & Steinhardt, 2000]. In this scenario, it was initially assumed that DM interactions are isotropic elastic scatterings with an interaction cross-section that is independent of velocity. Since the mass of the DM particle is not known, self-interactions are commonly quantified in terms of the cross-section per unit particle mass, σ/m , which is an important cosmological value for SIDM theories. The total number of interactions, Γ , that occurs per unit time is given by

$$\Gamma \sim 0.1 \text{Gyr}^{-1} \times \left(\frac{\rho_{\text{dm}}}{0.1 \text{M}_\odot/\text{pc}^3} \right) \left(\frac{\sigma/m}{1 \text{cm}^2 \text{g}^{-1}} \right) \left(\frac{v_{\text{rel}}}{50 \text{kms}^{-1}} \right), \quad (2.26)$$

where m , σ and v_{rel} are the DM particle mass, the cross-section, and the relative velocity, respectively. The upper panel of Figure 2.12 compares the DM density distribution at large scales of CDM and SIDM halos with a mass of $9 \times 10^9 \text{M}_\odot$ and σ/m increasing from left to right in 100 kpc boxes. As the scattering rate Γ is proportional to the DM density, SIDM halos have the same structure as CDM halos at large scales where the DM interactions are negligible. Indeed, on the scale of their virial radius ($r_{\text{vir}} = 55 \text{kpc}$), CDM and SIDM halos are nearly identical. Moreover, the collision rate is also negligible during the early Universe when DM structures form. Therefore, SIDM is consistent with observations of large-scale structures, predicted by Λ CDM [Springel et al., 2006; Trujillo-Gomez et al., 2011]. However, self-interactions perturb the inner density structure of DM halo at late times. The upper panel of Figure 2.12 highlights that the SIDM halos at sub-galactic scales are less dense than in the CDM model due to the formation of cores.

A generic prediction for SIDM is that halos can form dense cores with size depending on the cross-section σ/m [Colín et al., 2002; Davé et al., 2001; Elbert et al., 2015; Fry et al., 2015a; Peter et al., 2013; Robertson et al., 2017; Robles et al., 2017; Rocha et al., 2013; Vogelsberger et al., 2012, 2014; Yoshida et al., 2000a,b; Zavala et al., 2013], as shown in the lower panel of Figure 2.12. The redistribution of energy and momentum by DM particle collisions decreases the central density of DM

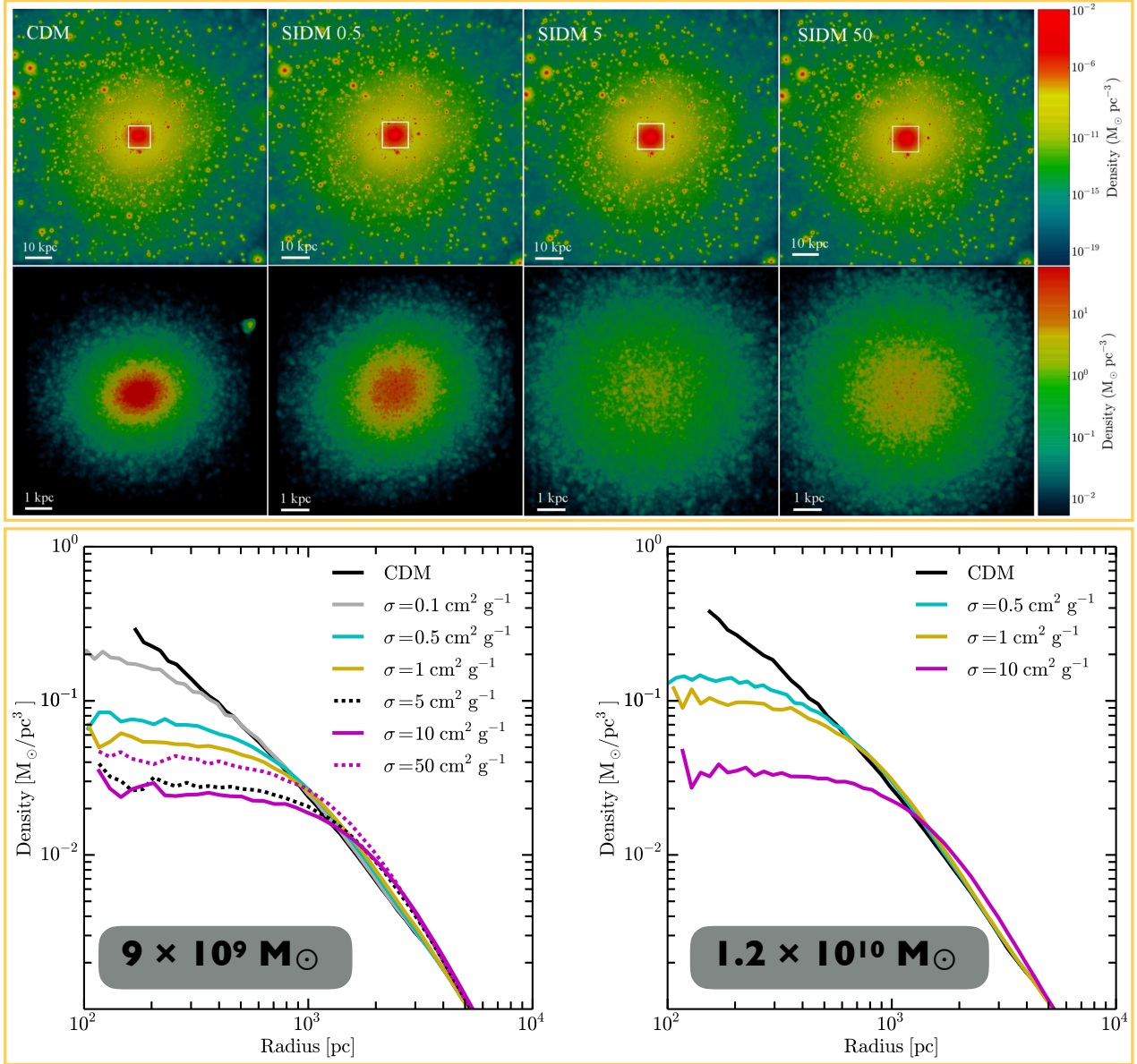


Figure 2.12 – **SIDM halo properties:** *Upper panel:* DM density maps of CDM (left) and SIDM halo with a mass of $9 \times 10^9 M_\odot$ and σ/m increasing from left to right in 100 and 10 kpc boxes. As the scattering rate Γ is proportional to the DM density, SIDM halos have the same structure as CDM halos at large scales where the DM interactions are negligible (see Equation (2.26)). Indeed, on the scale of their virial radius ($r_{\text{vir}} = 55$ kpc), CDM and SIDM halos are nearly identical. At sub-galactic scales, the SIDM halos are less dense than in CDM model due to the formation of cores. *Lower panel:* DM density profiles of 9×10^9 (left) and $1.2 \times 10^{10} M_\odot$ (right) halos in CDM and SIDM models. SIDM runs have σ/m between 0.1 and 50 $\text{cm}^2 \text{ g}^{-1}$. For $\sigma/m \geq 0.5 \text{ cm}^2 \text{ g}^{-1}$, the self-interactions between DM particles produce central cores with a size depending on σ/m . Indeed, the largest cores form for cross-sections in the range $\sigma/m = 5 - 10 \text{ cm}^2 \text{ g}^{-1}$. This figure is taken from [Elbert et al. \[2015\]](#).

halos, known as a cusp-to-core transition [[Burkert, 2000](#); [D'Onghia & Burkert, 2003](#); [Rocha et al., 2013](#); [Spergel & Steinhardt, 2000](#); [Yoshida et al., 2000a](#)]. In other words, this heat transfer alters the inner region of halos by turning cuspy profiles into a cored profile. Core formations occur only if σ/m is sufficiently large to ensure that the relatively high probability of scattering over a time T_{age} is comparable to the age of the halo: $\Gamma \times T_{\text{age}} \sim 1$. Figure 2.12 illustrates that the self-interactions between DM particles produce central cores for $\sigma/m \geq 0.5 \text{ cm}^2 \text{ g}^{-1}$ in 9×10^9 and $1.2 \times 10^{10} M_\odot$

halos. Numerous simulations have then demonstrated that models with $\sigma/m \sim 0.5 - 10 \text{ cm}^2/\text{g}^{-1}$ produce DM cores in dwarf galaxies with sizes $\sim 0.3 - 1.5 \text{ kpc}$ [Elbert et al., 2015; Fry et al., 2015a; Peter et al., 2013; Rocha et al., 2013; Vogelsberger et al., 2012; Zavala et al., 2013] that seem to alleviate the cusp-core problem. In fact, the discrepancy with observations of low surface brightness (LSB) galaxies having density cores could be avoided in SIDM theory [Spergel & Steinhardt, 2000].

The viability of DM self-interacting as a cusp-core transformation mechanism depends on whether or not this cosmological model is consistent with all observations. In other words, it remains to see if SIDM models are able to explain the observed cores from ultra-faint galaxies to galaxy clusters. SIDM model requires compromises on the cross-section, which needs to be small enough to be observationally allowed but sufficiently large to alleviate the relevant small-scale problems. The first constraint on the SIDM cross-section derives from galaxy clusters, which impose $\sigma/m < 0.02 \text{ cm}^2/\text{g}$ [Miralda-Escudé, 2002]. Later, this constraint was revised and the inferred values of $\langle \sigma v \rangle / m$ for all six clusters are consistent with a constant cross-section $\sigma/m = 0.1 \text{ cm}^2 \text{ g}^{-1}$ according to right panel of Figure 2.13 [Peter et al., 2013; Tulin & Yu, 2018]. The left panel of Figure 2.13 shows that SIDM model ($\sigma/m = 0.1 \text{ cm}^2 \text{ g}^{-1}$) allowed by cluster constraints would be very similar to the CDM predictions. While the most massive CDM subhalos are inconsistent with the kinematics of the MW dSphs, SIDM model can only alleviate this problem for $\sigma/m > 1 \text{ cm}^2 \text{ g}^{-1}$.

If the self-scattering cross-section per unit mass is $\sim 1 \text{ cm}^2 \text{ g}^{-1}$, SIDM models can solve the cusp-core problem at the scale of dwarf galaxies [Rocha et al., 2013; Vogelsberger et al., 2012;

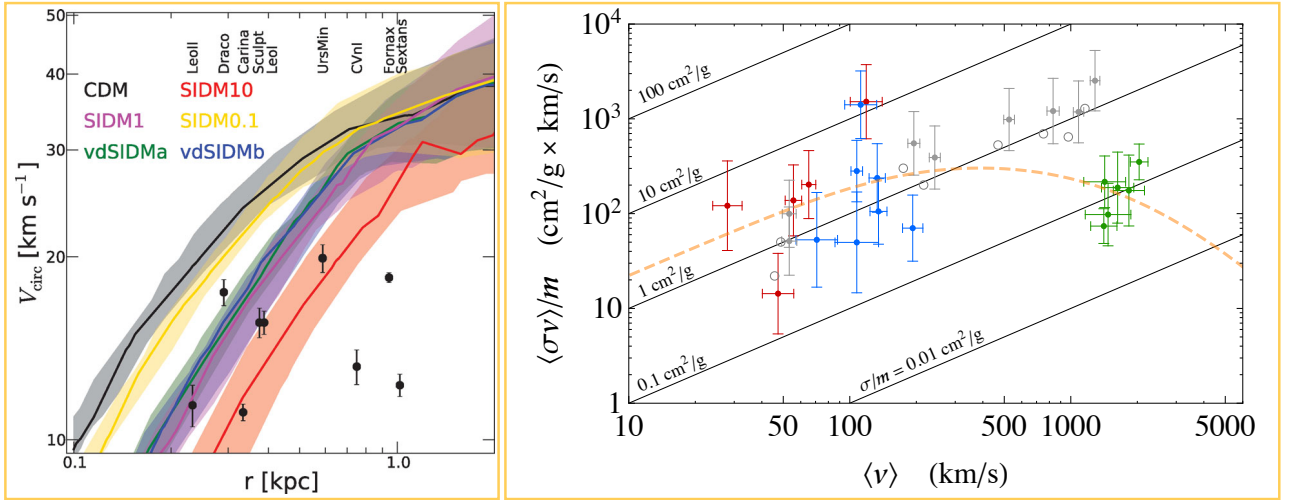


Figure 2.13 – **Constraints from observations:** Left panel: Circular velocity profiles encompassing a distribution of 15 subhalos for CDM and SIDM models with a constant cross-section between 0.1 and $10 \text{ cm}^2 \text{ g}^{-1}$. Black points with error bars correspond to the circular velocity within the half-light radii for nine MW dSphs [Walker et al., 2009; Wolf et al., 2010]. While the most massive CDM subhalos are inconsistent with the kinematics of the MW dSphs, the SIDM model with $\sigma/m > 1 \text{ cm}^2 \text{ g}^{-1}$ can alleviate this problem. Unfortunately, SIDM model ($\sigma/m = 0.1 \text{ cm}^2 \text{ g}^{-1}$) allowed by cluster constraints would be very similar to the CDM predictions. Lower mass subhalos, which could fit the observational data in the bottom right, are affected by the limited resolution of simulations. Right panel: Velocity-weighted cross-section per unit mass as a function of the mean collision velocity for dwarf galaxies (red), Low surface brightness (LSB) galaxies (blue) and galaxy clusters (green). For comparison, SIDM N-body simulations with $\sigma/m = 5 - 10 \text{ cm}^2 \text{ g}^{-1}$ are represented by grey points. Diagonal lines show the corresponding cross-section σ/m . As σ/m is not supposed to be constant in velocity, it is more convenient to invoke $\langle \sigma v \rangle / m$ rather than σ/m . The dashed curve represents the best-fit for a velocity-dependent cross-section. This figure is taken from Kaplinghat et al. [2016].

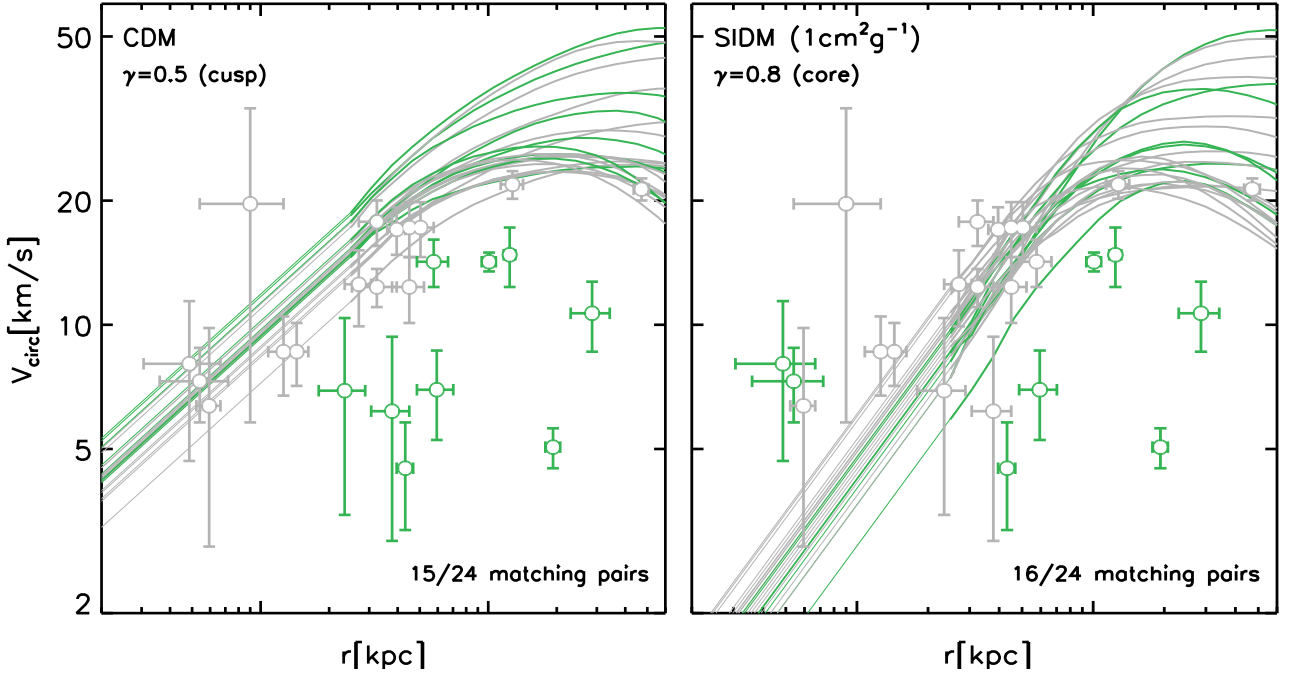


Figure 2.14 – **SIDM versus CDM**: Circular velocity profiles V_{circ} of CDM and SIDM ($\sigma/m = 1 \text{ cm}^2 \text{ g}^{-1}$) subhalos within 300 kpc from the centre of the simulated MW-like galaxies. Open symbols with error bars correspond to circular velocities at the half-light radius for 24 MW satellites [Errani et al., 2018; Torrealba et al., 2019]. Lines and symbols in gray (green) are consistent matches (mismatches) between simulated subhalos and data points. Both CDM and SIDM subhalos match only 15-16 MW satellites. Indeed, the CDM host halo has too many dense subhalos to explain the satellite distribution. It was claimed that SIDM models can solve the cusp-core problem at the scale of dwarf galaxies if the self-scattering cross-section per unit mass is $\sim 1 \text{ cm}^2 \text{ g}^{-1}$ [Rocha et al., 2013; Vogelsberger et al., 2012; Zavala et al., 2013]. But SIDM theory with $\sigma/m = 1 \text{ cm}^2 \text{ g}^{-1}$ predicts subhalos with too low densities to match the ultra-faint galaxies. This figure is taken from Zavala et al. [2019].

Zavala et al., 2013]. Figure 2.14 depicts the circular velocity profiles V_{circ} of CDM and SIDM ($\sigma/m = 1 \text{ cm}^2 \text{ g}^{-1}$) subhalos within 300 kpc from the centre of the simulated MW-like galaxies. Both CDM and SIDM subhalos match only 15-16 MW satellites. Nevertheless, SIDM theory with constant cross-section ($\sigma/m = 1 \text{ cm}^2 \text{ g}^{-1}$) predicts DM subhalos with too low densities to match the observations of ultra-faint galaxies (see Figure 2.14). Thus, a constant cross-section of $\sigma/m = 1 \text{ cm}^2 \text{ g}^{-1}$ is likely to be inconsistent with the observed halo shapes of ultra-faint galaxies and several galaxy clusters.

Figure 2.13 highlights the possible velocity dependence discernible in these data from dwarfs to clusters. As σ/m varies within a wide range, SIDM models, which assume a constant scattering cross-section, needs to be abandoned since those that could solve the cusp-core problem in dwarfs seemed to violate several astrophysical constraints. In order to alleviate the cusp-core problem and also match constraints at different scales, SIDM model needs to have a velocity-dependent cross-section $\sigma(v)$ that decreases as the relative velocity of DM particles involved from dwarfs to clusters such as in Figure 2.15 [Feng et al., 2010; Loeb & Weiner, 2011; Vogelsberger et al., 2012]. For $\sigma/m > 10 \text{ cm}^2 \text{ g}^{-1}$, self-interactions between DM particles are frequent enough to entail a core-collapse, which is a well-known mechanism in globular clusters [Lynden-Bell & Wood, 1968], within a Hubble time in halos. Then, it results in the collapse of the core into a central cusp for SIDM halos [Balberg et al., 2002; Colín et al., 2002; Koda & Shapiro, 2011; Nishikawa et al., 2020; Pollack et al., 2015]. As the vdSIDM model has cross-sections near and above the core-collapse limit according to

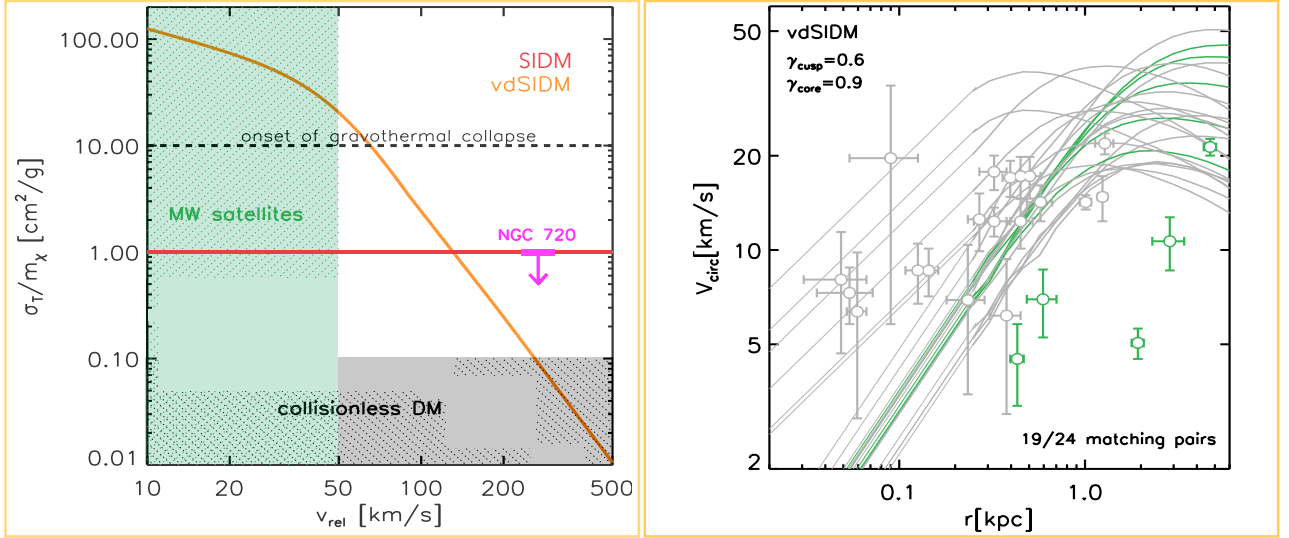


Figure 2.15 – **Velocity-dependent cross-section:** Left panel: Cross-section as a function of the relative velocity. vdSIDM model consists of a SIDM with a strong velocity-dependent cross-section (orange line). The collisionless region is delimited by the black area $\sigma/m < 0.1 \text{ cm}^2 \text{ g}^{-1}$. For $\sigma/m > 10 \text{ cm}^2 \text{ g}^{-1}$, self-interactions between DM particles are frequent enough to result in core-collapse within a Hubble time in halos. The green area represents the relevant region for MW satellites. A constraint on the cross-section from the elliptical galaxy NGC720 is represented by a magenta arrow. Right panel: Circular velocity profiles V_{circ} of vdSIDM (orange line in the left panel) subhalos within 300 kpc from the centre of the simulated MW-like galaxies. Open symbols with error bars correspond to circular velocities at the half-light radius for 24 MW satellites [Errani et al., 2018; Torrealba et al., 2019]. Lines and symbols in gray (green) are consistent matches (mismatches) between simulated subhalos and data points. As the vdSIDM model has cross-sections near and above the core-collapse limit, it produces a bimodal distribution composed of cusps and cores for MW-like subhalos. Indeed, the core collapse is responsible for this diversity, which is more consistent with cored brighter satellites and cuspy ultra-faint galaxies. This figure is taken from Zavala et al. [2019].

Figure 2.15, it produces a bimodal distribution composed of cusps and cores for MW-like subhalos. Indeed, the core collapse is responsible for this diversity, which is more consistent with cored brighter satellites and cuspy ultra-faint galaxies [Zavala et al., 2019]. Thus, core collapses can be considered as a mechanism to create a diverse population of dwarf-size haloes, some of which would be cuspy and others that would have cores in velocity-dependent SIDM models [Kahlhoefer et al., 2019; Nishikawa et al., 2020; Sameie et al., 2020; Zavala et al., 2019].

All previous works are based on SIDM simulations without taking into account baryonic physics. The inclusion of baryons into CDM simulations of dwarf galaxies has initially served to reduce the discrepancy between DM-only simulations and observations concerning the inner DM distribution. We have shown previously that baryonic feedback can reduce the central density of a cuspy DM halo. By including hydrodynamics in SIDM simulations, it was found that the DM inner region of dwarf galaxies with stellar masses $M_* < 10^6$ are nearly identical to the SIDM-only simulations [Fry et al., 2015b; Robles et al., 2017; Vogelsberger et al., 2014]. Substantial DM cores are formed in both SIDM and SIDM+baryons simulations. It appears then that SIDM is more robust to feedback than CDM at dwarf scales [Elbert et al., 2018; Robles et al., 2017]. This suggests that the faintest dwarf spheroidals provide excellent laboratories constraining SIDM models. Indeed, they are ideal targets as SIDM and CDM produce cores and cusps in these galaxies, respectively.

For high baryon concentration, it leads to a dense inner halo with a smaller core in SIDM model

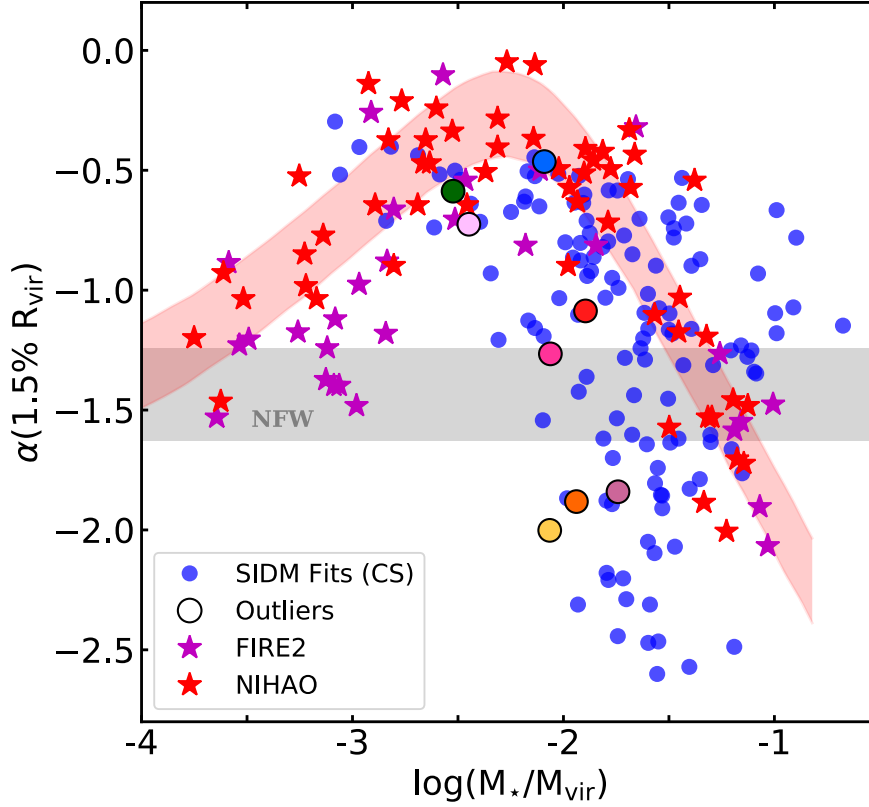


Figure 2.16 – **Baryon impact:** Inner DM density slope α at $r = 0.015 r_{\text{vir}}$ as a function of M_*/M_{vir} at $z = 0$ from SIDM fits [Ren et al., 2019], NIHAO [Tollet et al., 2016] and FIRE-2 [Fitts et al., 2019; Hopkins et al., 2018] hydrodynamical CDM simulations. The SIDM fits of the SPARC sample [Lelli et al., 2016], which contains 135 galaxies, including the impact of baryons on the halo profile and compatible with a unique cross-section of $3 \text{ cm}^2 \text{ g}^{-1}$. The shaded grey band shows the expected range of DM profile slopes for the NFW profile as derived from CDM-only simulations by including concentration scatter. The slope α of SIDM fits spans a large range from -0.5 to -2.5, indicating that the SIDM model predicts both cored and cuspy halos. It was also pointed out that this reflects different baryon distributions in galaxies, which have a large impact on SIDM halos. As a result, the SIDM model predicts cored DM density profiles in low surface brightness galaxies and cuspy density profiles in high surface brightness galaxies, and agrees best with observations. As halos that host concentrated stellar populations exhibit few differences in density profiles between CDM and SIDM models in the presence of baryons, the resulting DM core is effectively indistinguishable between CDM and SIDM. Maybe signatures in stellar kinematics could distinguish these two core formation mechanisms, one impulsive (feedback) and the other adiabatic (SIDM) [Burger & Zavala, 2019]. This figure is taken from Kaplinghat et al. [2019].

[Kaplinghat et al., 2014]. Moreover, baryons can cause SIDM halos to core-collapse and become denser than DM halos in presence of baryons [Balberg et al., 2002; Colín et al., 2002; Kochanek & White, 2000; Koda & Shapiro, 2011; Vogelsberger et al., 2012]. As long as the baryonic component dominates the central region, core-collapse can occur for $\sigma/m = 0.5 \text{ cm}^2 \text{ g}^{-1}$ [Elbert et al., 2018]. This is the reason why SIDM model predicts both cored and cuspy profiles, depending on baryon concentration. As a result, the coupling between the SIDM and baryons also provides an explanation for the uniformity of the rotation curves [Creasey et al., 2017; Kamada et al., 2017; Ren et al., 2019].

Figure 2.16 shows that the logarithmic slope of the DM density profile, at 1.5% of the virial radius inferred from the SIDM fits, is correlated with the stellar mass [Ren et al., 2019]. Then, SIDM+baryons model with an interaction cross-section of $3 \text{ cm}^2 \text{ g}^{-1}$ can reproduce galaxy rotation curves from ~ 50 to 300 km s^{-1} [Kamada et al., 2017; Kaplinghat et al., 2019; Ren et al., 2019].

The slope α of SIDM fits, which include the baryonic impact, spans a large range from -0.5 to -2.5, indicating that the SIDM model predicts both cored and cuspy halos. It was also pointed out that this reflects different baryon distributions in galaxies, which have a large impact on SIDM halos. Thus, the SIDM model predicts cored DM density profiles in low surface brightness galaxies and cuspy density profiles in high surface brightness galaxies and agrees best with observations. This coupling works because within the characteristic scale of these galaxies, the DM and baryonic masses are comparable. As halos that host concentrated stellar populations exhibit few differences in density profiles between CDM and SIDM models in the presence of baryons, the resulting DM core is effectively indistinguishable between CDM and SIDM (see Figure 2.16). Maybe signatures in stellar kinematics could distinguish between these two core formation mechanisms, one impulsive (feedback) and the other adiabatic (SIDM) [Burger & Zavala, 2019]. However, the impact of baryonic physics in ultra-faint galaxies is negligible, such that it is difficult to imagine how a population of dense ultra-faint galaxies can be accommodated with a constant cross-section of $\sigma/m = 3 \text{ cm}^2 \text{ g}^{-1}$ (see Figure 2.16) [Zavala et al., 2019].

2.3 References

- Abadi M. G., Navarro J. F., Fardal M., Babul A., Steinmetz M., 2010, *MNRAS*, **407**, 435 19
- Adams J. J., et al., 2014, *ApJ*, **789**, 63 16
- Agnello A., Evans N. W., 2012, *ApJ*, **754**, L39 15, 16
- Amorisco N. C., Evans N. W., 2012, *MNRAS*, **419**, 184 16
- Balberg S., Shapiro S. L., Inagaki S., 2002, *ApJ*, **568**, 475 33, 35
- Bar N., Blum K., Lacroix T., Panci P., 2019, *J. Cosmology Astropart. Phys.*, **2019**, 045 27, 28, 30
- Battaglia G., Helmi A., Tolstoy E., Irwin M., Hill V., Jablonka P., 2008, *ApJ*, **681**, L13 16
- Bengochea G. R., Ferraro R., 2009, *Phys. Rev. D*, **79**, 124019 19
- Benítez-Llambay A., Frenk C. S., Ludlow A. D., Navarro J. F., 2019, *MNRAS*, **488**, 2387 18, 20, 21, 22
- Binney J., 1980, *MNRAS*, **190**, 873 14
- Binney J., Mamon G. A., 1982, *MNRAS*, **200**, 361 14, 15
- Binney J., Tremaine S., 2008, *Galactic Dynamics: Second Edition* 14
- Blumenthal G. R., Faber S. M., Flores R., Primack J. R., 1986, *ApJ*, **301**, 27 19
- Bode P., Ostriker J. P., Turok N., 2001, *ApJ*, **556**, 93 25
- Böhmer C. G., Harko T., 2007, *J. Cosmology Astropart. Phys.*, **2007**, 025 25, 26
- Borriello A., Salucci P., 2001, *MNRAS*, **323**, 285 14
- Bose S., et al., 2019, *MNRAS*, **486**, 4790 20, 22, 23
- Boylan-Kolchin M., Bullock J. S., Kaplinghat M., 2011, *MNRAS*, **415**, L40 17

- Breddels M. A., Helmi A., van den Bosch R. C. E., van de Ven G., Battaglia G., 2013, *MNRAS*, **433**, 3173 16
- Brook C. B., Stinson G., Gibson B. K., Wadsley J., Quinn T., 2012, *MNRAS*, **424**, 1275 18
- Brooks A. M., Zolotov A., 2014, *ApJ*, **786**, 87 19
- Buchdahl H. A., 1970, *MNRAS*, **150**, 1 19
- Bullock J. S., Boylan-Kolchin M., 2017, *ARA&A*, **55**, 343 16, 17, 20, 21
- Burger J. D., Zavala J., 2019, *MNRAS*, **485**, 1008 35, 36
- Burkert A., 1995, *ApJ*, **447**, L25 12, 14
- Burkert A., 2000, *ApJ*, **534**, L143 25, 31
- Carlson E. D., Machacek M. E., Hall L. J., 1992, *ApJ*, **398**, 43 30
- Chan T. K., Kereš D., Oñorbe J., Hopkins P. F., Muratov A. L., Faucher-Giguère C. A., Quataert E., 2015, *MNRAS*, **454**, 2981 20, 21, 22
- Chandrasekhar S., 1943, *ApJ*, **97**, 255 23
- Chavanis P.-H., 2018, *Physics of the Dark Universe*, **22**, 80 25
- Churazov E., Sazonov S., Sunyaev R., Forman W., Jones C., Böhringer H., 2005, *MNRAS*, **363**, L91 19
- Cole D. R., Dehnen W., Wilkinson M. I., 2011, *MNRAS*, **416**, 1118 23
- Colín P., Avila-Reese V., Valenzuela O., 2000, *ApJ*, **542**, 622 19, 25
- Colín P., Avila-Reese V., Valenzuela O., Firmani C., 2002, *ApJ*, **581**, 777 30, 33, 35
- Côté S., Carignan C., Freeman K. C., 2000, *AJ*, **120**, 3027 14
- Creasey P., Sameie O., Sales L. V., Yu H.-B., Vogelsberger M., Zavala J., 2017, *MNRAS*, **468**, 2283 35
- D'Onghia E., Burkert A., 2003, *ApJ*, **586**, 12 31
- Davé R., Spergel D. N., Steinhardt P. J., Wandelt B. D., 2001, *ApJ*, **547**, 574 30
- Davies E. Y., Mocz P., 2020, *MNRAS*, **492**, 5721 27, 28
- Davoudiasl H., Denton P. B., 2019, *Phys. Rev. Lett.*, **123**, 021102 27
- Dekel A., Silk J., 1986, *ApJ*, **303**, 39 19
- Del Popolo A., Le Delliou M., 2014, *J. Cosmology Astropart. Phys.*, **2014**, 051 23
- Deng H., Hertzberg M. P., Namjoo M. H., Masoumi A., 2018, *Phys. Rev. D*, **98**, 023513 28, 29
- Dent J. B., Dutta S., Saridakis E. N., 2011, *J. Cosmology Astropart. Phys.*, **2011**, 009 19
- Desjacques V., Nusser A., 2019, *MNRAS*, **488**, 4497 27

- Di Cintio A., Brook C. B., Dutton A. A., Macciò A. V., Stinson G. S., Knebe A., 2014, *MNRAS*, **441**, 2986 20, 21
- Duffy A. R., Schaye J., Kay S. T., Dalla Vecchia C., Battye R. A., Booth C. M., 2010, *MNRAS*, **405**, 2161 20, 22
- Dutton A. A., Macciò A. V., 2014, *MNRAS*, **441**, 3359 13
- Dutton A. A., Macciò A. V., Buck T., Dixon K. L., Blank M., Obreja A., 2019, *MNRAS*, **486**, 655 21
- El-Zant A. A., 2019, in *Journal of Physics Conference Series*. p. 012007, doi:10.1088/1742-6596/1253/1/012007 27
- El-Zant A., Shlosman I., Hoffman Y., 2001, *ApJ*, **560**, 636 23
- Elbert O. D., Bullock J. S., Garrison-Kimmel S., Rocha M., Oñorbe J., Peter A. H. G., 2015, *MNRAS*, **453**, 29 25, 30, 31, 32
- Elbert O. D., Bullock J. S., Kaplinghat M., Garrison-Kimmel S., Graus A. S., Rocha M., 2018, *ApJ*, **853**, 109 34, 35
- Errani R., Peñarrubia J., Walker M. G., 2018, *MNRAS*, **481**, 5073 33, 34
- Evans N. W., An J., Walker M. G., 2009, *MNRAS*, **393**, L50 15
- Fabian A. C., 2012, *ARA&A*, **50**, 455 19
- Fattahi A., et al., 2016, *MNRAS*, **457**, 844 20, 22
- Feng J. L., Kaplinghat M., Yu H.-B., 2010, *Phys. Rev. Lett.*, **104**, 151301 33
- Ferrarese L., Merritt D., 2000, *ApJ*, **539**, L9 19
- Fitts A., et al., 2017, *MNRAS*, **471**, 3547 20, 21
- Fitts A., et al., 2019, *MNRAS*, **490**, 962 35
- Flores R. A., Primack J. R., 1994, *ApJ*, **427**, L1 12, 13
- Freundlich J., Dekel A., Jiang F., Ishai G., Cornuault N., Lapiner S., Dutton A. A., Macciò A. V., 2020, *MNRAS*, **491**, 4523 19
- Fry A. B., Governato F., Pontzen A., Quinn T. R., 2015a, in *American Astronomical Society Meeting Abstracts #225*. p. 402.05 30, 32
- Fry A. B., et al., 2015b, *MNRAS*, **452**, 1468 34
- Fukushige T., Makino J., 1997, *ApJ*, **477**, L9 12
- Garrison-Kimmel S., Rocha M., Boylan-Kolchin M., Bullock J. S., Lally J., 2013, *MNRAS*, **433**, 3539 22
- Garrison-Kimmel S., et al., 2017, *MNRAS*, **471**, 1709 20
- Gebhardt K., et al., 2000, *ApJ*, **539**, L13 19

- Genina A., et al., 2018, *MNRAS*, **474**, 1398 16
- Genina A., et al., 2019, arXiv e-prints, p. [arXiv:1911.09124](#) 16
- Gentile G., Salucci P., Klein U., Vergani D., Kalberla P., 2004, *MNRAS*, **351**, 903 14
- Gilmore G., Wilkinson M. I., Wyse R. F. G., Kleya J. T., Koch A., Evans N. W., Grebel E. K., 2007, *ApJ*, **663**, 948 15
- Gnedin O. Y., Zhao H., 2002, *MNRAS*, **333**, 299 19
- Gnedin O. Y., Kravtsov A. V., Klypin A. A., Nagai D., 2004, *ApJ*, **616**, 16 19
- Godani N., Samanta G. C., 2020, *New Astron.*, **80**, 101399 19
- Goerdt T., Moore B., Read J. I., Stadel J., 2010, *ApJ*, **725**, 1707 23, 24
- González-Morales A. X., Marsh D. J. E., Peñarrubia J., Ureña-López L. A., 2017, *MNRAS*, **472**, 1346 29
- Goodman J., 2000, *New Astron.*, **5**, 103 19, 25
- Governato F., et al., 2010, *Nature*, **463**, 203 18, 20
- Holley-Bockelmann K., Weinberg M., Katz N., 2005, *MNRAS*, **363**, 991 25
- Hopkins P. F., et al., 2018, *MNRAS*, **480**, 800 20, 21, 35
- Hu W., Barkana R., Gruzinov A., 2000, *Phys. Rev. Lett.*, **85**, 1158 19, 25, 26, 27
- Hui L., Ostriker J. P., Tremaine S., Witten E., 2017, *Phys. Rev. D*, **95**, 043541 25
- Hunter D. A., et al., 2012, *AJ*, **144**, 134 14
- Inoue S., Saitoh T. R., 2011, *MNRAS*, **418**, 2527 23
- Jardel J. R., Gebhardt K., Fabricius M. H., Drory N., Williams M. J., 2013, *ApJ*, **763**, 91 16
- Kahlhoefer F., Kaplinghat M., Slatyer T. R., Wu C.-L., 2019, *J. Cosmology Astropart. Phys.*, **2019**, 010 34
- Kamada A., Kaplinghat M., Pace A. B., Yu H.-B., 2017, *Phys. Rev. Lett.*, **119**, 111102 35
- Kaplinghat M., Knox L., Turner M. S., 2000, *Phys. Rev. Lett.*, **85**, 3335 19
- Kaplinghat M., Keeley R. E., Linden T., Yu H.-B., 2014, *Phys. Rev. Lett.*, **113**, 021302 35
- Kaplinghat M., Tulin S., Yu H.-B., 2016, *Phys. Rev. Lett.*, **116**, 041302 32
- Kaplinghat M., Ren T., Yu H.-B., 2019, arXiv e-prints, p. [arXiv:1911.00544](#) 35
- Kataria S. K., Das M., McGaugh S., 2020, arXiv e-prints, p. [arXiv:2005.03972](#) 25
- Klypin A., Kravtsov A. V., Valenzuela O., Prada F., 1999, *ApJ*, **522**, 82 17
- Kochanek C. S., White M., 2000, *ApJ*, **543**, 514 25, 35

- Koda J., Shapiro P. R., 2011, *MNRAS*, **415**, 1125 33, 35
- Kuzio de Naray R., McGaugh S. S., de Blok W. J. G., 2008, *ApJ*, **676**, 920 14
- Kuzio de Naray R., McGaugh S. S., Mihos J. C., 2009, *ApJ*, **692**, 1321 14
- Larson R. B., 1974, *MNRAS*, **169**, 229 19
- Lazar A., et al., 2020, arXiv e-prints, p. [arXiv:2004.10817](#) 21
- Lee J.-W., Lim S., 2010, *J. Cosmology Astropart. Phys.*, **2010**, 007 27
- Lelli F., McGaugh S. S., Schombert J. M., 2016, *AJ*, **152**, 157 35
- Linder E. V., 2010, *Phys. Rev. D*, **81**, 127301 19
- Loeb A., Weiner N., 2011, *Phys. Rev. Lett.*, **106**, 171302 33
- Lokas E. L., 2009, *MNRAS*, **394**, L102 16
- Lovell M. R., Frenk C. S., Eke V. R., Jenkins A., Gao L., Theuns T., 2014, *MNRAS*, **439**, 300 25
- Lynden-Bell D., Wood R., 1968, *MNRAS*, **138**, 495 33
- Macciò A. V., Paduroiu S., Anderhalden D., Schneider A., Moore B., 2012a, *MNRAS*, **424**, 1105 25
- Macciò A. V., Stinson G., Brook C. B., Wadsley J., Couchman H. M. P., Shen S., Gibson B. K., Quinn T., 2012b, *ApJ*, **744**, L9 19
- Macciò A. V., Crespi S., Blank M., Kang X., 2020, *MNRAS*, **495**, L46 22
- Madau P., Dickinson M., 2014, *ARA&A*, **52**, 415 19
- Madau P., Shen S., Governato F., 2014, *ApJ*, **789**, L17 18
- Marchesini D., D'Onghia E., Chincarini G., Firmani C., Conconi P., Molinari E., Zacchei A., 2002, *ApJ*, **575**, 801 14
- Marsh D. J. E., 2016, *Phys. Rep.*, **643**, 1 25
- Marsh D. J. E., Pop A.-R., 2015, *MNRAS*, **451**, 2479 29
- Marsh D. J. E., Silk J., 2014, *MNRAS*, **437**, 2652 25
- Martin N. F., et al., 2016, *ApJ*, **818**, 40 29
- Martizzi D., Teyssier R., Moore B., 2012, *MNRAS*, **420**, 2859 22
- Martizzi D., Teyssier R., Moore B., 2013, *MNRAS*, **432**, 1947 19, 22
- Mashchenko S., Wadsley J., Couchman H. M. P., 2008, *Science*, **319**, 174 19
- Massari D., Breddels M. A., Helmi A., Posti L., Brown A. G. A., Tolstoy E., 2018, *Nature Astronomy*, **2**, 156 16
- McGaugh S. S., de Blok W. J. G., 1998, *ApJ*, **499**, 41 13, 14

- Merrifield M. R., Kent S. M., 1990, *AJ*, **99**, 1548 15, 16
- Merritt D., Milosavljević M., 2005, *Living Reviews in Relativity*, **8**, 8 25
- Milgrom M., 1983, *ApJ*, **270**, 365 19
- Miralda-Escudé J., 2002, *ApJ*, **564**, 60 25, 32
- Mocz P., et al., 2019, *Phys. Rev. Lett.*, **123**, 141301 25, 26, 27
- Moore B., 1994, *Nature*, **370**, 629 12, 13
- Moore B., Governato F., Quinn T., Stadel J., Lake G., 1998, *ApJ*, **499**, L5 12
- Navarro J. F., Eke V. R., Frenk C. S., 1996a, *MNRAS*, **283**, L72 14, 19
- Navarro J. F., Frenk C. S., White S. D. M., 1996b, *ApJ*, **462**, 563 12, 13
- Navarro J. F., Frenk C. S., White S. D. M., 1997, *ApJ*, **490**, 493 12
- Navarro J. F., et al., 2010, *MNRAS*, **402**, 21 12
- Nipoti C., Binney J., 2015, *MNRAS*, **446**, 1820 23, 24
- Nishikawa H., Boddy K. K., Kaplinghat M., 2020, *Phys. Rev. D*, **101**, 063009 33, 34
- Nori M., Murgia R., Iršič V., Baldi M., Viel M., 2019, *MNRAS*, **482**, 3227 25
- Oñorbe J., Boylan-Kolchin M., Bullock J. S., Hopkins P. F., Kereš D., Faucher-Giguère C.-A., Quataert E., Murray N., 2015, *MNRAS*, **454**, 2092 20, 23
- Oh S.-H., de Blok W. J. G., Walter F., Brinks E., Kennicutt Robert C. J., 2008, *AJ*, **136**, 2761 13, 14
- Oh S.-H., de Blok W. J. G., Brinks E., Walter F., Kennicutt Robert C. J., 2011, *AJ*, **141**, 193 13, 14, 18
- Oh S.-H., et al., 2015, *AJ*, **149**, 180 13, 14
- Oman K. A., et al., 2015, *MNRAS*, **452**, 3650 17, 18, 22, 23
- Peñarrubia J., Pontzen A., Walker M. G., Koposov S. E., 2012, *ApJ*, **759**, L42 22, 23
- Peebles P. J. E., 2000, *ApJ*, **534**, L127 19, 25
- Peirani S., de Freitas Pacheco J. A., 2008, *Phys. Rev. D*, **77**, 064023 22
- Peirani S., et al., 2017, *MNRAS*, **472**, 2153 20, 22
- Peter A. H. G., Rocha M., Bullock J. S., Kaplinghat M., 2013, *MNRAS*, **430**, 105 30, 32
- Petts J. A., Read J. I., Gualandris A., 2016, *MNRAS*, **463**, 858 23
- Pollack J., Spergel D. N., Steinhardt P. J., 2015, *ApJ*, **804**, 131 33
- Pontzen A., Governato F., 2012, *MNRAS*, **421**, 3464 19, 21

- Pontzen A., Governato F., 2014, *Nature*, **506**, 171 19
- Power C., Navarro J. F., Jenkins A., Frenk C. S., White S. D. M., Springel V., Stadel J., Quinn T., 2003, *MNRAS*, **338**, 14 20
- Read J. I., Gilmore G., 2005, *MNRAS*, **356**, 107 19
- Read J. I., Steger P., 2017, *MNRAS*, **471**, 4541 15, 16
- Read J. I., Wilkinson M. I., Evans N. W., Gilmore G., Kleya J. T., 2006, *MNRAS*, **366**, 429 24
- Read J. I., Agertz O., Collins M. L. M., 2016a, *MNRAS*, **459**, 2573 16
- Read J. I., Iorio G., Agertz O., Fraternali F., 2016b, *MNRAS*, **462**, 3628 18
- Read J. I., Walker M. G., Steger P., 2019, *MNRAS*, **484**, 1401 15, 16
- Ren T., Kwa A., Kaplinghat M., Yu H.-B., 2019, *Physical Review X*, **9**, 031020 35
- Rhee G., Valenzuela O., Klypin A., Holtzman J., Moorthy B., 2004, *ApJ*, **617**, 1059 14
- Richardson T., Fairbairn M., 2014, *MNRAS*, **441**, 1584 16
- Robertson A., Massey R., Eke V., 2017, *MNRAS*, **465**, 569 30
- Robles V. H., et al., 2017, *MNRAS*, **472**, 2945 30, 34
- Robles V. H., Bullock J. S., Boylan-Kolchin M., 2019, *MNRAS*, **483**, 289 27, 28
- Rocha M., Peter A. H. G., Bullock J. S., Kaplinghat M., Garrison-Kimmel S., Oñorbe J., Moustakas L. A., 2013, *MNRAS*, **430**, 81 30, 31, 32, 33
- Rodrigues D. C., del Popolo A., Marra V., de Oliveira P. L. C., 2017, *MNRAS*, **470**, 2410 29, 30
- Safarzadeh M., Spergel D. N., 2020, *ApJ*, **893**, 21 26, 28, 29, 30
- Salucci P., 2001, *MNRAS*, **320**, L1 14
- Sameie O., Yu H.-B., Sales L. V., Vogelsberger M., Zavala J., 2020, *Phys. Rev. Lett.*, **124**, 141102 34
- Sawala T., et al., 2016, *MNRAS*, **457**, 1931 20, 22
- Schaller M., Robertson A., Massey R., Bower R. G., Eke V. R., 2015, *MNRAS*, **453**, L58 19
- Schaye J., et al., 2010, *MNRAS*, **402**, 1536 20
- Schive H.-Y., Chiueh T., Broadhurst T., 2014a, *Nature Physics*, **10**, 496 25, 26, 27
- Schive H.-Y., Liao M.-H., Woo T.-P., Wong S.-K., Chiueh T., Broadhurst T., Hwang W. Y. P., 2014b, *Phys. Rev. Lett.*, **113**, 261302 29
- Schneider A., Smith R. E., Macciò A. V., Moore B., 2012a, *MNRAS*, **424**, 684 25
- Schneider M. D., Frenk C. S., Cole S., 2012b, *J. Cosmology Astropart. Phys.*, **2012**, 030 17
- Sellwood J. A., 2003, *ApJ*, **587**, 638 25

- Shao S., Gao L., Theuns T., Frenk C. S., 2013, *MNRAS*, **430**, 2346 25
- Silk J., 2017, *ApJ*, **839**, L13 19
- Sommer-Larsen J., Dolgov A., 2001, *ApJ*, **551**, 608 19
- Spekkens K., Giovanelli R., Haynes M. P., 2005, *AJ*, **129**, 2119 14
- Spergel D. N., Steinhardt P. J., 2000, *Phys. Rev. Lett.*, **84**, 3760 25, 30, 31, 32
- Springel V., Frenk C. S., White S. D. M., 2006, *Nature*, **440**, 1137 12, 30
- Strigari L. E., Bullock J. S., Kaplinghat M., 2007, *ApJ*, **657**, L1 16
- Strigari L. E., Frenk C. S., White S. D. M., 2010, *MNRAS*, **408**, 2364 16
- Swaters R. A., Madore B. F., Trewella M., 2000, *ApJ*, **531**, L107 14
- Swaters R. A., Madore B. F., van den Bosch F. C., Balcells M., 2003, *ApJ*, **583**, 732 13, 14
- Tegmark M., et al., 2004, *ApJ*, **606**, 702 12
- Teyssier R., Pontzen A., Dubois Y., Read J. I., 2013, *MNRAS*, **429**, 3068 18
- Tollet E., et al., 2016, *MNRAS*, **456**, 3542 20, 21, 22, 35
- Tonini C., Lapi A., Salucci P., 2006, *ApJ*, **649**, 591 25
- Torrealba G., et al., 2019, *MNRAS*, **488**, 2743 33, 34
- Trachternach C., de Blok W. J. G., Walter F., Brinks E., Kennicutt R. C. J., 2008, *AJ*, **136**, 2720 14
- Trujillo-Gomez S., Klypin A., Primack J., Romanowsky A. J., 2011, *ApJ*, **742**, 16 12, 30
- Tulin S., Yu H.-B., 2018, *Phys. Rep.*, **730**, 1 32
- Veltmaat J., Schwabe B., Niemeyer J. C., 2020, *Phys. Rev. D*, **101**, 083518 27, 28
- Vogelsberger M., Zavala J., Loeb A., 2012, *MNRAS*, **423**, 3740 30, 32, 33, 35
- Vogelsberger M., Zavala J., Simpson C., Jenkins A., 2014, *MNRAS*, **444**, 3684 30, 34
- Walker M. G., Peñarrubia J., 2011, *ApJ*, **742**, 20 16, 29
- Walker M. G., Mateo M., Olszewski E. W., Peñarrubia J., Evans N. W., Gilmore G., 2009, *ApJ*, **704**, 1274 32
- Walter F., Brinks E., de Blok W. J. G., Bigiel F., Kennicutt Robert C. J., Thornley M. D., Leroy A., 2008, *AJ*, **136**, 2563 14
- Wang L., Dutton A. A., Stinson G. S., Macciò A. V., Penzo C., Kang X., Keller B. W., Wadsley J., 2015, *MNRAS*, **454**, 83 21
- Weinberg M. D., Katz N., 2002, *ApJ*, **580**, 627 25

- Wetzel A. R., Hopkins P. F., Kim J.-h., Faucher-Giguère C.-A., Kereš D., Quataert E., 2016, *ApJ*, **827**, L23 16, 17, 20
- White S. D. M., Frenk C. S., 1991, *ApJ*, **379**, 52 19
- White S. D. M., Rees M. J., 1978, *MNRAS*, **183**, 341 19
- Widrow L. M., Kaiser N., 1993, *ApJ*, **416**, L71 25
- Wilkinson M. I., Kleya J., Evans N. W., Gilmore G., 2002, *MNRAS*, **330**, 778 16
- Wolf J., Martinez G. D., Bullock J. S., Kaplinghat M., Geha M., Muñoz R. R., Simon J. D., Avedo F. F., 2010, *MNRAS*, **406**, 1220 17, 29, 32
- Woo T.-P., Chiueh T., 2009, *ApJ*, **697**, 850 25, 27
- Yoshida N., Springel V., White S. D. M., Tormen G., 2000a, *ApJ*, **535**, L103 30, 31
- Yoshida N., Springel V., White S. D. M., Tormen G., 2000b, *ApJ*, **544**, L87 30
- Zackrisson E., Bergvall N., Marquart T., Östlin G., 2006, *A&A*, **452**, 857 14
- Zavala J., Vogelsberger M., Walker M. G., 2013, *MNRAS*, **431**, L20 25, 30, 32, 33
- Zavala J., Lovell M. R., Vogelsberger M., Burger J. D., 2019, *Phys. Rev. D*, **100**, 063007 33, 34, 36
- Zentner A. R., Bullock J. S., 2003, *ApJ*, **598**, 49 19
- Zheng R., Huang Q.-G., 2011, *J. Cosmology Astropart. Phys.*, **2011**, 002 19
- Zolotov A., et al., 2012, *ApJ*, **761**, 71 20
- de Blok W. J. G., 2005, *ApJ*, **634**, 227 14
- de Blok W. J. G., 2010, *Advances in Astronomy*, **2010**, 789293 16
- de Blok W. J. G., Bosma A., 2002, *A&A*, **385**, 816 13, 14
- de Blok W. J. G., McGaugh S. S., 1996, *ApJ*, **469**, L89 14
- de Blok W. J. G., McGaugh S. S., 1997, *MNRAS*, **290**, 533 14
- de Blok W. J. G., McGaugh S. S., van der Hulst J. M., 1996, *MNRAS*, **283**, 18 14
- de Blok W. J. G., McGaugh S. S., Bosma A., Rubin V. C., 2001, *ApJ*, **552**, L23 13, 14
- de Blok W. J. G., Bosma A., McGaugh S., 2003, *MNRAS*, **340**, 657 14
- de Blok W. J. G., Walter F., Brinks E., Trachternach C., Oh S. H., Kennicutt R. C. J., 2008, *AJ*, **136**, 2648 14
- de Laix A. A., Scherrer R. J., Schaefer R. K., 1995, *ApJ*, **452**, 495 30
- van den Bosch F. C., Swaters R. A., 2001, *MNRAS*, **325**, 1017 14
- van den Bosch F. C., Robertson B. E., Dalcanton J. J., de Blok W. J. G., 2000, *AJ*, **119**, 1579 14

Chapter 3

Fully GPU and pure gravitational N-body simulations of collisionless systems

Contents

3.1 N-body technique	46
3.1.1 Boltzmann-Poisson system	46
3.1.2 A discrete set of N particles	46
3.1.3 Leapfrog integrator	47
3.1.4 Collisionless regime	47
3.1.5 Softening length	47
3.2 Accelerating N-body simulations	48
3.2.1 Tree-method	48
3.2.2 Block time step	50
3.2.3 GPU	50
3.3 GOTHIC	50
3.4 Simulation analysis	51
3.5 References	51

The N-body or Lagrangian methods work by following a collection of fluid elements or particles while calculating the forces acting upon them. Gravitational N-body simulations are widely used tools in astrophysics. Celestial mechanics, dense stellar systems, the sphere of influence of a massive BH, and galaxy dynamics and cosmology are the four main astrophysical domains where N-body simulations are extensively employed. In galaxy dynamics and cosmology, many computational techniques, such as the particle-mesh method, the tree algorithm, and a hybrid combination of the two, and dedicated codes such as RAMSES [Teyssier, 2002], GADGET [Springel, 2005], and PKDGRAV [Stadel, 2001] have been developed over the last decades. This chapter outlines the computer simulation techniques used in exploring the cusp-core problem in dwarf galaxies, focusing on the methods used by the non-public Gravitational Oct-Tree code accelerated by Hlerarchical time step Controlling named GOTHIC [Miki & Umemura, 2017], which served as the base code of the work in this thesis.

3.1 N-body technique

3.1.1 Boltzmann-Poisson system

Galaxies are very extended objects with typical sizes from tens to hundreds of kiloparsecs and can be described as collections of particles that evolve under their mutual gravitational interaction. As dwarf galaxies are devoid of gas, we neglect the hydrodynamical effects in the simulated galaxy dynamics. In our pure N-body simulations, we consider only spherical isolated systems such as galaxy systems. The principal components of these many-body systems relevant to this thesis are DM and stars. CDM is considered to be collisionless particles that interact only through gravity. Stars, on the other hand, are not collisionless, but their interaction cross-sections are small enough to rarely collide head-on. Hence, they can be described as collisionless fluids, which obey the collisionless Boltzmann equation:

$$\frac{df}{dt} = \frac{\partial f}{\partial t} + v \frac{\partial f}{\partial r} - \frac{\partial \Phi}{\partial r} \frac{\partial f}{\partial v} = 0, \quad (3.1)$$

where the collective gravitational potential, Φ , is a solution of Poisson's equations:

$$\nabla^2 \Phi = 4\pi G \int f dv, \quad (3.2)$$

where $f = f(r, v, t)$ corresponds to the mass density, with the positions r and velocities v , under the influence of the collective gravitational potential. However, it is highly non-trivial to solve the above two equations directly with finite difference methods.

3.1.2 A discrete set of N particles

In order to solve the previous equations, the N-body technique consists of sampling the distribution function $f(r, v, t)$ with a discrete set of N particles, each described by a mass, position and velocity. Indeed, it is not possible to resolve individual DM particles due to computational limitations. That is the reason why it is common to simulate pseudo-particles, which represent hundreds to thousands of solar masses. Thus, the Boltzmann-Poisson system is replaced with a system of N local tracers of the mass density, which evolves according to the Hamiltonian equations of motion:

$$\frac{dr_i}{dt} = v_i, \quad (3.3)$$

$$m_i \frac{dv_i}{dt} = a_i, \quad (3.4)$$

where a_i corresponds to the acceleration of the i th particle of N particles, which is given by Newton's equation of motion:

$$a_i = \sum_{j=0, j \neq i}^{N-1} \frac{Gm_j(r_j - r_i)}{(|r_j - r_i|^2 + \epsilon^2)^{3/2}}, \quad (3.5)$$

where G is the gravitational constant, r_i and m_i are, respectively, the positions and masses of the i th particle of N particles. This Monte Carlo technique is subject to Poisson noise, and high particle numbers are, therefore, required in order to reduce noise. ϵ corresponds to the gravitational softening length. Hereafter, we label the particles which both experience and induce gravitational forces as i - and j -particles, respectively, and denote their total numbers N_i or N_j .

3.1.3 Leapfrog integrator

In order to evolve the N -body system, the next step is to update the positions and velocities of each particle by integrating the equation of motion using the calculated accelerations. Several numerical integrators have been developed to solve differential equations like Equation (3.4) such as the well-known leapfrog method. The new position and velocities of a particle after a time step Δt are given by

$$v_j^{n+1/2} = v_j^{n-1/2} + \frac{\Delta t}{2} a_j^n, \quad (3.6)$$

$$r_j^{n+1} = r_j^n + v_j^{n+1/2} \Delta t, \quad (3.7)$$

where r_j^n is the position of the j th particle at the n th time step. In the standard leapfrog integrator, a single time step Δt is used for all particles and is maintained constant throughout the integration. The method is accurate to second-order and conserves energy.

3.1.4 Collisionless regime

Numerically, our many-body system can be treated as collisionless only if the simulation time is significantly smaller than the relaxation time T_r given by [Binney & Tremaine \[2008\]](#):

$$T_r(r) \simeq \frac{v^3(r)}{8\pi(\bar{n}m^2)G^2 \ln\left(\frac{a}{\epsilon}\right)}, \quad (3.8)$$

where \bar{n} and m are the number-density and mass of particles, respectively. v , ϵ , and a represent the velocity, the softening length, and the size of the system, respectively. This relaxation time represents the time after which the deviation from the original kinetic energy of a particle due to two-body encounters is of the order of its initial kinetic energy. Hence, collisionless systems are those in which two-body collisions are negligible.

3.1.5 Softening length

Introducing a softening length ϵ in the law of gravitation is an efficient solution adopted in collisionless N -body simulations to avoid unphysical two-body scattering between nearby particles [[Aarseth, 1963](#)]. Since an N -body particle is not, in reality, a point mass, this results in numerical issues when the distance $|r_j - r_i|$ between two particles approaches zero in the absence of softening. More precisely, this divergence can lead to high velocities and finally unbinding close particles. As a result, force law saturates at close distances and then the particle collection represents a smoothed density field at small scales. Softening value can be estimated using the following criterion:

$$\epsilon \sim a/N^{1/3}, \quad (3.9)$$

where N and a are the number of particles and the typical size of the smallest object in the simulation, respectively. More precisely, a corresponds to the scale (core) radius of halos (globular clusters). Convergence tests are necessary to set this value. Another benefit of the softening length is reducing the numerical errors accumulated due to larger time steps by setting a maximum acceleration of Gm/ϵ^2 during a close encounter. Moreover, the inclusion of softening can theoretically reduce two-body relaxation as the relaxation time depends on the softening length according to Equation (5.5). It was shown that relaxation effects are not substantially suppressed by softening because relaxation depends predominantly on the number of particles used in the simulation [Dehnen, 2001; Hernquist & Barnes, 1990].

In a nutshell, choosing the appropriate softening length, time step, and the number of particles is the crucial step to ensure properly converged simulations [Ludlow et al., 2019; Power et al., 2003; Zhang et al., 2019]. This procedure helps in mitigating numerical issues.

3.2 Accelerating N-body simulations

The simplest way to solve the N-body problem is via the direct application of Equation (3.5). Since this calculation must be repeated for each particle, it results in a $\mathcal{O}(N_i N_j)$ scaling in terms of the number of operations. As a consequence, this calculation is computationally expensive and usually not appropriate for galaxy and cosmological simulations. Indeed, it is only feasible for a limited number of particles where an accurate force computation is required, such as close encounters or stellar clusters. As the computational cost is too high to investigate realistic resolved astrophysical phenomena, several methods have been proposed to accelerate N-body simulations.

3.2.1 Tree-method

One way to accelerate N-body simulations while keeping a large number of particles is to reduce the number of calculations needed. Popular algorithms such as the particle-mesh, tree method, and some hybrid techniques have been developed to solve the N-body problem with acceptable accuracy and reduce the number of operations to $\mathcal{O}(N_i \log N_j)$ [Barnes & Hut, 1986; Hockney & Eastwood, 1988]. We will only focus on the tree method as it is employed in GOTHIC used for the simulations presented in the subsequent chapters of this thesis. The fundamental assumption of the tree algorithm is that the gravitational force of far-away particles can be approximated by replacing this group of distant particles with a pseudo-particle located at the centre of mass and encompassing the total mass of those bodies. A numerically efficient way to locate particles in space and gather them into groups is the oct-tree method [Barnes & Hut, 1986]. This method builds the tree in the following manner. The algorithm starts by constructing a root cube, which contains all the particles of the system. Then, the tree code divides the main cube into eight subcubes. Each subcube is then further subdivided into more subcubes by the same division scheme, and this division continues as long as the number of particles in a cube exceeds one. As such, the oct-tree strategy consists of a recursive division of the particle distribution, which leads to a tree that consists of cubes at different levels. Figure 3.1 illustrates the 2-dimensional version of the N-body problem using quadtrees instead of oct-trees. The upper right square has been recursively subdivided into 4 nodes at each level, until each cell in the tree contains at most one particle. In this case, four levels in the tree are needed to fully subdivide the upper right square.

Figure 3.1 shows that the gravitational force of the closest tree region is explored in detail while more distant regions are considered as pseudo-particles. In other words, each subcube of the main

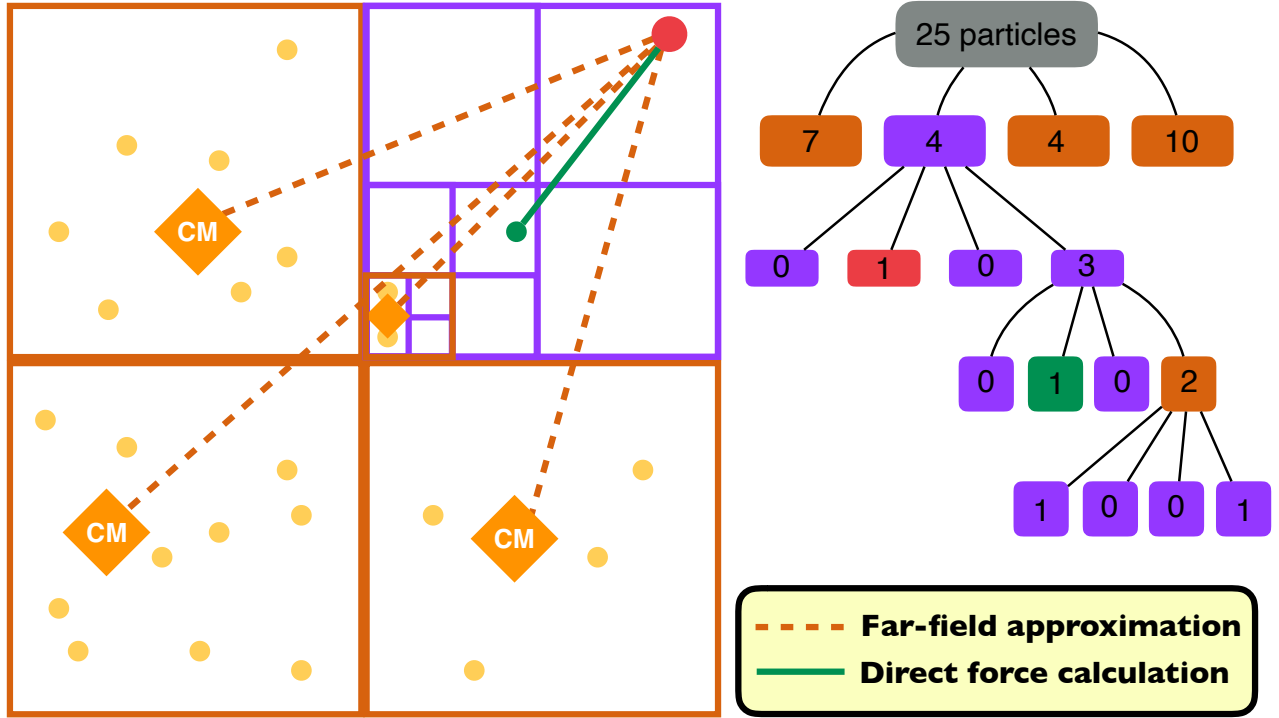


Figure 3.1 – **Oct-tree method in 2D:** The 2-dimensional version of the N-body problem using quadtrees instead of oct-trees. The upper right square has been recursively subdivided into 4 nodes at each level until each cell in the tree contains at most one particle. In this case, four levels in the tree are needed to fully subdivide the upper right square. By grouping distant particles together, the far-field approximation requires significantly fewer operations than the direct force calculation. Suppose we want to compute the force exerted on the red particle in the upper right corner, particles in orange squares are sufficiently far away from the considered particle that we can group them based on their center of mass (CM) and apply the far-field force approximation. However, the green particle is sufficiently close to the target particle such that we can apply the direct force calculation. As a result, this method requires only 5 force calculations instead of 24 using the direct force calculation.

cube is considered for direct calculation only if a specific criterion is satisfied. If a cube, at a given level, does not satisfy the criterion, the centre of mass is used for the calculation of the gravitational force. To determine whether a pseudo j -particle is near or far, the Multipole Acceptance Criterion (MAC) is employed. In GADGET-2, the acceleration MAC by [Springel \[2005\]](#) is given by

$$d_{ij} \geq \left(\frac{Gm_j b_j}{\Delta_{\text{acc}} |a_i^{\text{old}}|} \right), \quad (3.10)$$

where d_{ij} , a_i^{old} and Δ_{acc} are the distance to the particle from an i -particle, the acceleration of the i -particle in the previous time step and an accuracy controlling parameter, respectively. By grouping distant particles together, the far-field approximation requires significantly fewer operations than the direct force calculation. Suppose we want to compute the force exerted on the red particle in the upper right corner, particles in orange squares are sufficiently far away from the considered particle that we can group them based on their centre of mass and apply the far-field force approximation, as illustrated in Figure 3.1. However, the green particle is sufficiently close to the target particle such that we can apply the direct force calculation. As a result, this method required only 5 force calculations instead of 24 using the direct force calculation (cf. Figure 3.1).

3.2.2 Block time step

In the standard leapfrog integrator, a shared time step Δt is used for all particles and is constant during the integration. However, because of the large dynamic range of lengths and timescales involved in typical astrophysical systems, it causes unnecessary, additional computations to track the evolution of the system. Indeed, particles in the central region of a galaxy will have a much shorter dynamical time than one which is orbiting near the virial radius. This serves as the motivation underlying the use of block (or hierarchical) time steps by both GOTHIC and GADGET-2, in which a group of particles has the same time step [Aarseth, 1963; McMillan, 1986]. This method speeds up the execution time by reducing the number of particles N_i .

3.2.3 GPU

Most of N-body codes run using multiple central processing units (CPUs) set by the workstation or CPU nodes in clusters. Architecturally, a CPU is composed of just a few cores. As a result, a large number of CPUs, such as in CPU clusters, are required to perform galaxy simulations in a reasonable amount of time (1-30 days). In contrast, a graphics processing unit (GPU) is composed of hundreds of cores. Even if the GPU was originally developed as a processor dedicated to image processing, it is widely used as an accelerator device and is suitable for parallel computing in astrophysics. Indeed, GPUs are best suited for repetitive and highly-parallel computing tasks such as tree calculations. Recently, some of N-body codes running on CPUs were accelerated by GPUs such as PKDGRAV3 [Potter et al., 2017].

3.3 GOTHIC

In all the projects described in this thesis, we performed our simulations with the high performance collisionless N-body code GOTHIC [Miki & Umemura, 2017]. In contrast to PKDGRAV3, this gravitational oct-tree code runs entirely on GPU. For the simulations, we used a NVIDIA GeForce GTX 1080 Ti (CUDA 9.0) on Intel Xeon Silver 4114 (GCC 4.8). The N-body code is accelerated by the use of the block time step as in GADGET-2. More precisely, particles contained in a common subcube share the same time step. The latter in GOTHIC is defined as:

$$\Delta t = \eta \cdot \min\left(\frac{\epsilon}{v_{\max}}, \sqrt{\frac{\epsilon}{a_{\max}}}\right), \quad (3.11)$$

where ϵ and η are the softening length and the time-step parameter, respectively. The default value of the time-step parameter is $\eta = 0.5$. As the block time step is employed, a second-order Runge–Kutta method is adopted to integrate the particle orbit. The acceleration MAC was designated to be the optimal choice for this GPU architecture. Further details pertaining to the implementation and the performance of GOTHIC are provided in Miki & Umemura [2017] and Miki [2018].

To generate our initial conditions or live objects for simulations, we used the initial-condition generator for N-body simulations called MAGI [MAny-component Galaxy Initialiser Miki & Umemura, 2018]. Adopting a distribution-function-based method, the generator ensures that the final realization of the system is in dynamical equilibrium. The computation of the distribution functions was done with Eddington’s formula for spherically symmetric components assuming an isotropic velocity distribution. MAGI also has the functionality to represent various kinds of density profiles.

3.4 Simulation analysis

In post-processing, an important technical aspect of numerical simulations is how to extract information. We used the python module toolbox designated as pnboddy 4.0 [Revaz, 2013] to analyze our data and extract our results.

In the context of the cusp-core problem, the main purpose is to establish the spherically averaged density profile of the DM halo. Determining the halo centre is subsequently a crucial task, especially as the halos are not spherically symmetric. Throughout all our studies presented in this thesis, the centre of the stellar component or the DM halos was determined using the iterative technique suggested by Power et al. [2003]. We computed recursively the centre of mass of particles within a shrinking sphere until a convergence criterion is met. At each iteration, we calculated the mass centre within the considered sphere, which is then set as the new centre of the system. The next iteration starts with a new sphere with a radius reduced by 2.5 per cent.

During their orbits, globular clusters or DM subhalos are subjected to mass loss induced by the tidal field of the galaxy. Reconstructing accurately the mass loss history of these systems is essential for the understanding of the galaxy dynamics. We follow the iterative method of Baumgardt & Makino [2003] to determine the number of bound particles over time. First, it is assumed that all particles are bound in order to calculate the initial tidal radius r_t . Next, we calculated the mass of all particles inside r_t and used it for evaluating the new radius for the following step.

3.5 References

- Aarseth S. J., 1963, *MNRAS*, 126, 223 47, 50
- Barnes J., Hut P., 1986, *Nature*, 324, 446 48
- Baumgardt H., Makino J., 2003, *MNRAS*, 340, 227 51
- Binney J., Tremaine S., 2008, *Galactic Dynamics: Second Edition* 47
- Dehnen W., 2001, *MNRAS*, 324, 273 48
- Hernquist L., Barnes J. E., 1990, *ApJ*, 349, 562 48
- Hockney R. W., Eastwood J. W., 1988, *Computer simulation using particles* 48
- Ludlow A. D., Schaye J., Bower R., 2019, *MNRAS*, 488, 3663 48
- McMillan S. L. W., 1986, *ApJ*, 307, 126 50
- Miki Y., 2018, arXiv e-prints, p. arXiv:1811.02761 50
- Miki Y., Umemura M., 2017, *New Astron.*, 52, 65 46, 50
- Miki Y., Umemura M., 2018, *MNRAS*, 475, 2269 50
- Potter D., Stadel J., Teyssier R., 2017, *Computational Astrophysics and Cosmology*, 4, 2 50
- Power C., Navarro J. F., Jenkins A., Frenk C. S., White S. D. M., Springel V., Stadel J., Quinn T., 2003, *MNRAS*, 338, 14 48, 51

Revaz Y., 2013, pNbody: A python parallelized N-body reduction toolbox (ascl:1302.004) [51](#)

Springel V., 2005, [MNRAS](#), [364](#), [1105](#) [46](#), [49](#)

Stadel J. G., 2001, PhD thesis, UNIVERSITY OF WASHINGTON [46](#)

Teyssier R., 2002, [A&A](#), [385](#), [337](#) [46](#)

Zhang T., Liao S., Li M., Gao L., 2019, [MNRAS](#), [487](#), [1227](#) [48](#)

Chapter 4

Our solution to the Fornax cusp-core problem

The work presented in this chapter is based on Boldrini et al. (2019) ([arXiv:1903.00354](#)) and Boldrini et al. (2020b) ([arXiv:1909.07404](#))

Contents

4.1 The Fornax timing problem	54
4.2 Constraints from globular cluster distribution	55
4.2.1 Fornax-GC system	55
4.2.2 N-body simulations	58
4.2.3 Results	60
4.2.4 Appendix	68
4.3 Embedding GC in DM minihalos	69
4.3.1 Fornax-GC system	70
4.3.2 N-body simulations	73
4.3.3 Results	74
4.3.4 Appendix	83
4.4 References	87

4.1 The Fornax timing problem

Fornax, the most massive dwarf spheroidal (dSphs) of the MW, is the only one to have five (or perhaps six) globular clusters (GCs) orbiting in a dense background of DM [Wang et al., 2019] (see Figure 4.1). For instance, another major dSph, such as the Sagittarius dSph, has many GCs. Four clusters are found in its main body (M 54, Arp 2, Terzan 7 and Terzan 8) [Da Costa & Armandroff, 1995] and a few halo clusters have been associated with the stream across the sky (Sbordone et al. [2015] and references therein). The study of GC dynamics can place powerful constraints on the Fornax DM halo type.

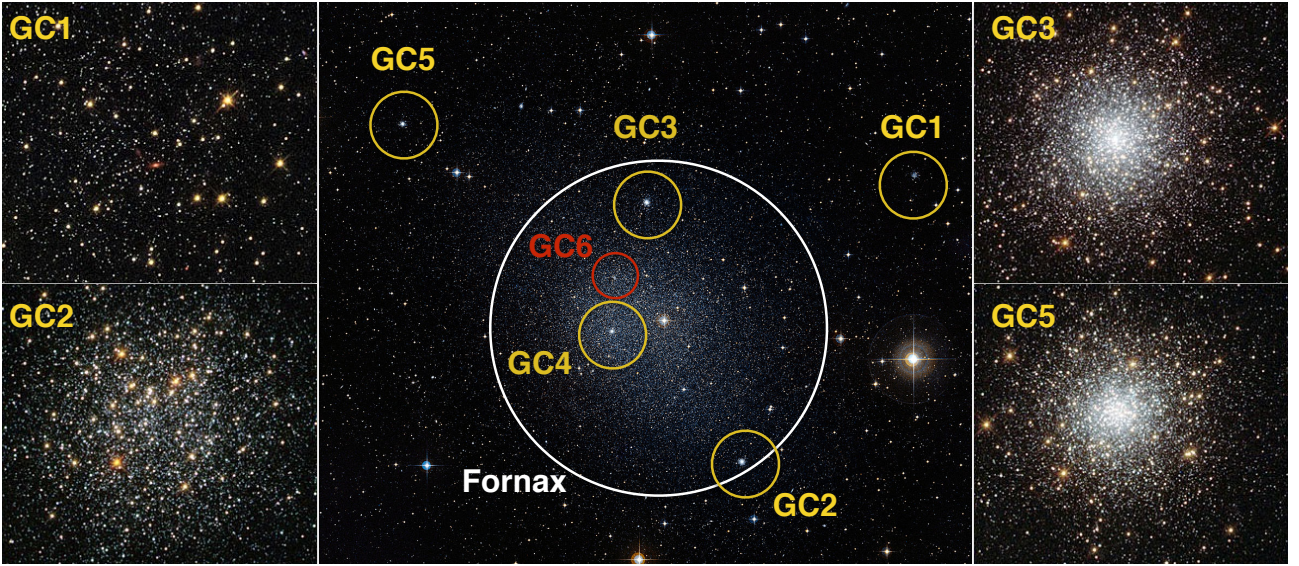


Figure 4.1 – **GC distribution:** Images of the Fornax dwarf galaxy and its five (or six) GCs with masses of about $10^5 M_{\odot}$ and the average projected distance of these clusters is about 1 kpc. Credits: ESO/Digital Sky Survey 2 and NASA, ESA, S. Larsen (Radboud University, the Netherlands).

One apparent paradox about these clusters is that we do not expect to see any of them because they should have sunk to the centre of Fornax due to dynamical friction [Chandrasekhar, 1943]. It is precisely because of this drag force that GCs are expected to sink to the centre of their host galaxy and form a nuclear star cluster [Tremaine, 1976; Tremaine et al., 1975]. However, there is no bright stellar nucleus and we are still observing GCs orbiting in Fornax (see Figure 4.2). This has become known as the Fornax timing problem [Oh et al., 2000]. Since the dynamical friction force depends directly on the density of DM halo, the timing problem could be used to probe the cusp-core problem. Changing the density profile could delay dynamical friction. Simulations agree well with Chandrasekhar’s analytic calculation for a cuspy halo such as NFW halo, which is the most commonly used model for DM halos [Goerdt et al., 2006]. Enhancement of the infall time can be achieved by changing the density profile of the DM halo.

Numerous simulations have been performed to study the timing problem [Cole et al., 2012; Goerdt et al., 2006; Oh et al., 2000; Read et al., 2006b]. A live system is necessary to capture tidal stripping and dynamical friction. Thus, Fornax has to be modelled as a live galaxy with its GCs, i.e. a self-gravitating system composed of star and DM particles. Concerning the determination of the DM density distribution, previous simulations showed that the existence of five globular clusters in Fornax is inconsistent with the hypothesis of a cuspy halo due to dynamical friction because the GCs would have sunk into the centre of Fornax in a relatively short time [Arca-Sedda & Capuzzo-Dolcetta, 2016, 2017; Goerdt et al., 2006; Sánchez-Salcedo et al., 2006]. According to Goerdt et al.

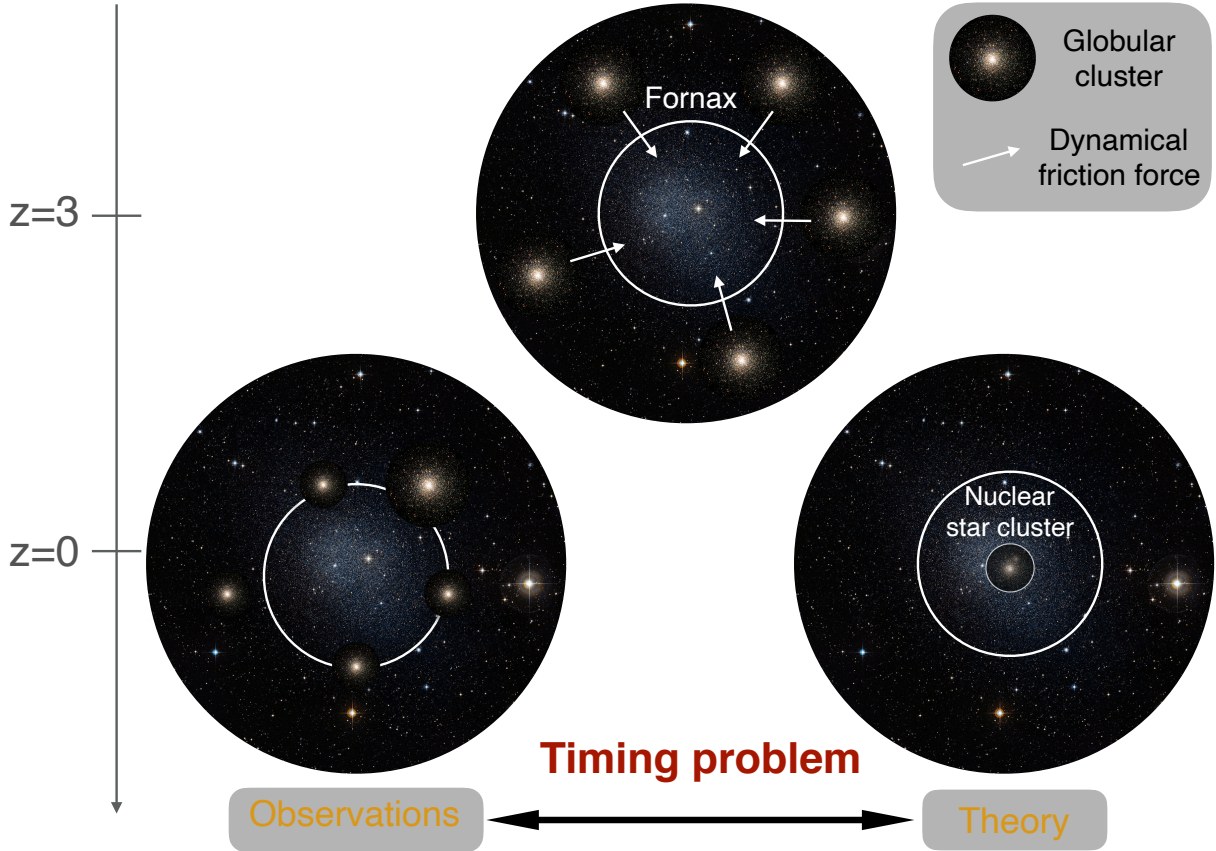


Figure 4.2 – **Fornax timing problem:** Theory predicts that the five GCs should have sunk to the centre of Fornax due to dynamical friction and form a nuclear star cluster. However, there is no bright stellar nucleus and we are still observing GCs orbiting in Fornax. This has become known as the timing problem.

[2006], a solution to the timing problem is that Fornax has a cored DM halo. In this model, GCs stop sinking at the core radius because of a resonance/scattering effect. Later work provided further support for a large DM core for Fornax [Cole et al., 2012]. The GCs did not fall to the centre because of ‘dynamical buoyancy’ created by the Fornax core. It was also proposed that GCs did not form within Fornax, but that they have been accreted by Fornax, which has a small cored halo.

In this work, we re-investigate the Fornax cusp-core problem using N-body simulations with entirely live objects i.e. fully composed of particles, in order to take into account correctly dynamical friction and tidal effects between Fornax and its GCs. The Section 4.2 is organized as follows. Section 4.2.1 provides a clear description of the Fornax system and the N-body modelling. In Section 4.2.2, we present details of our numerical simulations. In Section 4.2.3, we present our results of simulations and discuss the implications of our result on the DM halo profile of Fornax.

4.2 Constraints from globular cluster distribution

4.2.1 Fornax-GC system

The dSph galaxy Fornax is one of the most DM-rich satellites of the MW with a stellar mass of about $10^8 M_\odot$ at a distance of around 147 kpc [de Boer & Fraser, 2016]. We consider only the first five GCs with masses of about $10^5 M_\odot$ and average projected distances of about 1 kpc (see Figure 4.1). Various details are given in Table 4.1. In this subsection, we present the models for

Object	M^a [$10^5 M_\odot$]	r_c^b [pc]	$r_t^{d,e}$ [pc]	D_p^b [kpc]	D_{MW}^a [kpc]
Fornax	382 ± 12	668 ± 34^c	-	-	147 ± 4
GC1	0.42 ± 0.10	10.03 ± 0.29	59.06 ± 1.70	1.6	147.2 ± 4.1
GC2	1.54 ± 0.28	5.81 ± 0.19	108.19 ± 3.54	1.05	143.2 ± 3.3
GC3	4.98 ± 0.84	1.60 ± 0.07	108.17 ± 4.73	0.43	141.9 ± 3.9
GC4	0.76 ± 0.15	1.75 ± 0.18	115.62 ± 11.89	0.24	140.6 ± 3.2
GC5	1.86 ± 0.24	1.38 ± 0.11	25.69 ± 2.05	1.43	144.5 ± 3.3

Table 4.1 – **Observed data for the Fornax system:** r_c is the half-light radius for Fornax dwarf galaxy and the King model core radius for the GCs with their tidal radius r_t . D_p is the projected distance of the GC from the centre of Fornax. The last column is the line-of-sight distance from MW. References: (a) [de Boer & Fraser \[2016\]](#), (b) [Mackey & Gilmore \[2003\]](#), (c) [Strigari et al. \[2010\]](#), (d) [Webbink \[1985\]](#), (e) [Smith et al. \[1996\]](#).

Fornax and its GCs that provide the initial conditions for our simulations.

Fornax modelling

We construct Fornax as a live galaxy composed of stars and DM particles only, since dSph galaxies contain little or no gas today. The Fornax stellar component is modelled due to the presence of the dSph core ($r_0 = 0.668$ kpc) by a Plummer profile [[Plummer, 1911](#)]:

$$\rho(r) = \frac{3r_s^2 M_0}{4\pi} (r^2 + r_s^2)^{-5/2}, \quad (4.1)$$

where r_s and M_0 are the scale parameter and the mass, respectively.

For the DM halo of Fornax, we employ two different density profiles: NFW and Burkert profiles in order to deal with the cusp-core problem. For cuspy halos, we assume a NFW form [[Navarro et al., 1996](#)]:

$$\rho(r) = \rho_0 \left(\frac{r}{r_s} \right)^{-1} \left(1 + \frac{r}{r_s} \right)^{-2}, \quad (4.2)$$

with the central density ρ_0 and scale length r_s . For cored halos, we assume that the DM is distributed in a spherical halo with a Burkert density profile [[Burkert, 1995](#); [Salucci & Burkert, 2000](#)]:

$$\rho(r) = \frac{\rho_0 r_0^3}{(r + r_0)(r^2 + r_0^2)}, \quad (4.3)$$

where r_0 and ρ_0 are the core radius and the central density, respectively. In order to determine the halo parameters (see Table 4.2), we fitted the data of Fornax mass with a mass model that includes a stellar component and a dark halo:

$$M_{\text{model}}(r) = M_*(r) + M_h(r), \quad (4.4)$$

for all halos in Figure 4.3. The data points correspond to the mass estimates by [Walker & Peñarrubia \[2011\]](#) for two chemically distinct sub-populations. There are other mass estimators for Fornax [[Amorisco et al., 2013](#); [Errani et al., 2018](#)]. Plots of density profiles are illustrated in Figure 4.3. In order to test halo stability during the simulation, we compared our halo profiles at the beginning ($T = 0$ Gyr (solid line)) and at the end ($T = 12$ Gyr (dotted line)) of the simulation, which matches almost exactly for all radii.

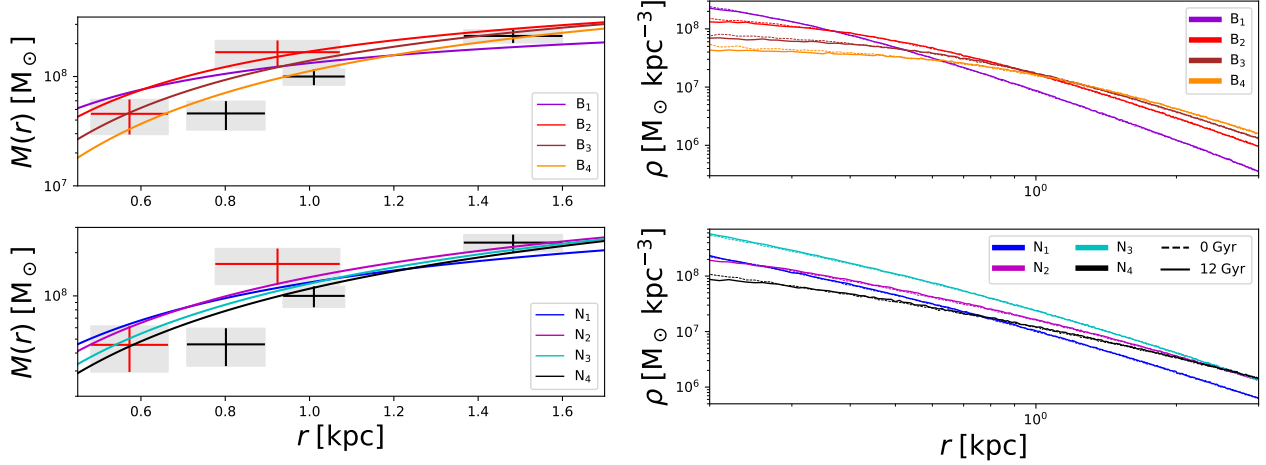


Figure 4.3 – Enclosed mass (*left panels*) and density distributions (*right panels*) for cored (*top panels*) and cuspy (*bottom panels*) DM halo models. The data points correspond to the mass estimates by Walker & Peñarrubia [2011] for two chemically distinct subpopulations and by Amorisco et al. [2013] for three distinct stellar subpopulations in the red giant branch. Radial density profiles at the beginning $T = 0$ Gyr (solid line) and at the end of the simulation $T = 12$ Gyr (dotted line), which are the same, show the stability of our halos. All halo parameters are summarized in Table 4.2.

GC modelling

There are five surviving GCs orbiting in Fornax. Our N-body realizations of GCs assume a King [1962] stellar density distribution,

$$\rho(r) = \rho_0 \left[\left(1 + \left(\frac{r}{r_k} \right)^2 \right)^{-1/2} - C \right], \quad C = \left[1 + \left(\frac{r_t}{r_k} \right)^2 \right]^{-1/2}, \quad (4.5)$$

where r_c and r_t are the King and tidal radii, respectively. For most of the simulations, we chose a King radius $r_k = 1$ pc lower than the observed radius (see Table 4.1) because it is susceptible to increase through dynamical processes such as mass loss. The projected distances for the GCs are from 0.24 to 1.6 kpc, which is the minimum distance between GCs and the Fornax centre. Based on the observed line-of-sight distance with uncertainties (see Table 4.1), as a function of the projected distance, we calculate all possible radial distances from the centre of Fornax for all GCs, which are summarized in Figure 4.4. According to this figure, the radial distance can be larger than the projected distance. We also estimate the maximum pericentre of observed GCs with eccentricity parameter $e = 0.9$ thanks to the fitted cluster tidal radius of Table 4.2 for each halo model. These radii will be used as constraints on GC final orbital radii (see Figure 4.4).

To generate the initial conditions, we use the numerical code, nbodgen [Sadoun et al., 2014]. This C++ code draws positions and velocities of each particle such that the resulting distribution follows the desired density profile $\rho(r)$. The code ensures that the final realization of the galaxy is in dynamical equilibrium.

MW tidal field

According to Gaia DR2 data [Gaia Collaboration et al., 2018], the orbit of Fornax has an eccentricity of 0.29 and its pericentre is about 85.9 kpc. We estimate the tidal radius for Fornax using the

Model	Density profile	r_s [kpc]	M_h [M_\odot]	r_t [kpc]	m_p [M_\odot]
B ₁	Burkert	0.25	0.318×10^9	2.81	89
B ₂	Burkert	0.5	0.88×10^9	3.95	230
B ₃	Burkert	0.75	1.1×10^9	4.52	285
B ₄	Burkert	1	1.28×10^9	4.98	329
N ₁	NFW	0.5	0.6×10^9	3.87	160
N ₂	NFW	1.0	1.2×10^9	4.87	310
N ₃	NFW	1.5	1.6×10^9	5.25	410
N ₄	NFW	2	2.0×10^9	5.77	510

Table 4.2 – Parameters for halo models used in the simulations. r_s and M_h are the scale radius (core radius for Burkert profile) in density profiles and mass for the halo respectively. r_t is the tidal radius for Fornax estimated from Eq (4.6). We run cored halos B_n modelled by a Burkert profile and cuspy halos N_n modelled by a NFW profile. The halo and the stellar component are represented by $N = 10^6$ particles. m_p is the mass resolution for our N-body realization.

equation of [Read et al. \[2006a\]](#):

$$r_t = r_p \left(\frac{M_s}{M_g(3+e)} \right)^{1/3}, \quad (4.6)$$

where r_p , M_s , M_g and e are the pericenter radius, the satellite mass, the galactic mass and the eccentricity respectively. We find tidal radii of 2.81-5.77 kpc, based on the range of masses for Fornax given in Table 4.2 and using a total mass for the MW of $2 \times 10^{12} M_\odot$. Within these radii, we can expect that tidal effects do not profoundly alter the structure and kinematics of Fornax. However, the MW tidal field can have a significant impact on GCs on eccentric orbits (see Appendix B). Our host galaxy potential, based on the model of [Allen & Santillan \[1991\]](#), consists of a stellar bulge as a Plummer sphere [[Plummer, 1911](#)], a disc represented by the potential from [[Miyamoto & Nagai, 1975](#)] and a spherical DM halo described by NFW profile [[Navarro et al., 1997](#)]. For this model, we used the revised parameters from [Irrgang et al. \[2013\]](#) (see their Table 1).

4.2.2 N-body simulations

Fornax is dominated by metal-rich stars whereas GCs are dominated by metal-poor stars [[de Boer & Fraser, 2016](#)]. If we compare the total mass of metal-poor ($[Fe/H] < -2$) clusters of $(8.81 \pm 0.92) \times 10^5 M_\odot$ to the metal-poor stellar mass in Fornax of $(44.9 \pm 5.3) \times 10^5 M_\odot$, this yields you a mass fraction of $19.6 \pm 3.1 \%$, which implies that a large fraction of the metal-poor stars in Fornax still belong to the GCs [[de Boer & Fraser, 2016](#)]. GC4 was excluded from this estimation because this cluster is possibly more metal-rich than the other clusters. This high mass fraction of $19.6 \pm 3.1 \%$ suggests that each of these four surviving metal-poor GCs has likely lost several times $10^5 M_\odot$ due to dynamical processes such as dynamical friction, tidal effects, and evaporation as a result of two-body relaxation. These processes act to destroy GCs on Gyr time-scales [[Fall & Zhang, 2001](#); [Jordán et al., 2007](#)]. Based on this hypothesis, we supposed that GCs were initially much more massive in the past and belonged to Fornax. Thus, the GC initial radii have to be lower than the approximate Fornax tidal radii depending on the halo mass.

We ran 75 simulations with five GCs orbiting in all our halo models. The initial parameters are orbital radii $R_i = [1.0, 1.5, 2.0, 2.5, 3.0]$ kpc and GC masses $M_i = [2.5, 5.0, 7.5, 10] \times 10^5 M_\odot$. All runs were made with eccentricity parameters $e = 0$ and $e = 0.9$. They correspond to circular and high

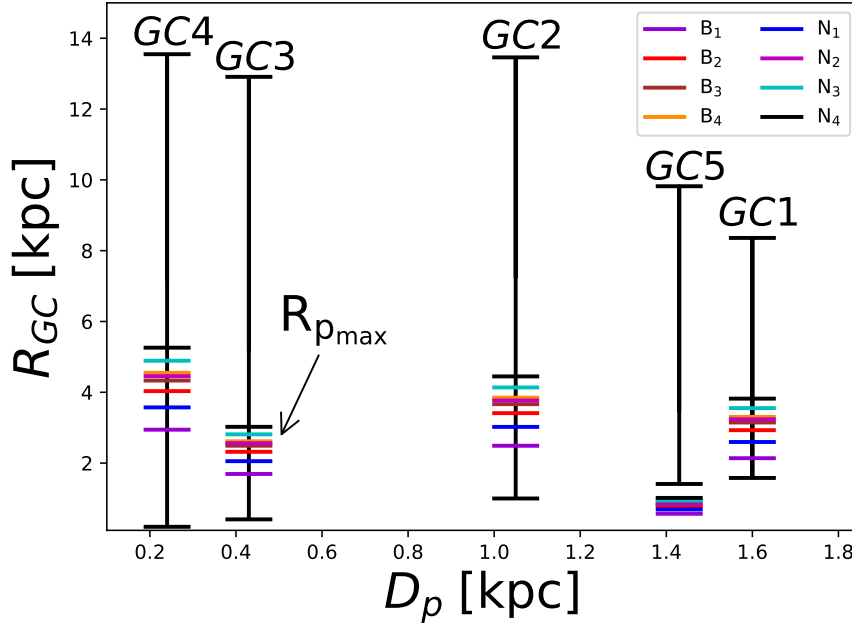


Figure 4.4 – All possible radial distances from the centre of Fornax for the five GCs, based on the observed line-of-sight distance with uncertainties, as a function of the projected distance. The minimal values correspond to the current projected distance D_p of each GC. The radial distance can be much bigger than the projected distance. The colour lines represent the maximum pericentre of observed GCs resulting from the fitted cluster tidal radius of Table 4.2 for each halo models. We applied this last constraint only for high eccentric orbit with $e = 0.9$.

eccentric orbit, respectively, with an orbital velocity which depends on the density profile of Fornax $\rho(u)$. In order to put constraints on the DM halo, we consider only these two limit cases. In fact, the lifetime of clusters can be increased on high eccentric orbit, because tidal effects decrease with eccentricity (see Equation (4.6)).

We performed our simulations with the N-body code of gadget2 (Springel [2005]). We create, for each Fornax mass model, initial conditions for the Fornax-GCs system and evolve them for 12 Gyr because the Fornax GCs are all dominated by ancient (>10 Gyr) populations of stars [de Boer & Fraser, 2016].

The halo and the stellar components are represented by $N = 4 \times 10^6$ particles. The mass ratio for these two components determines the particle number for each component. GCs are represented by about 10^3 particles depending on the halo particle mass. In fact, we impose that the particle mass of all components is set to be equal in order to reduce numerical artefacts. Based on convergence tests of decaying radial distances and mass loss of the GCs (see Appendix A), the forces between all particles are softened with the same softening length of $\epsilon = 1$ pc. The softening length is similar to the King radius in order to maintain the dynamical stability of an isolated GC. We did not use this radius as a constraint on halo models because we recognize that we do not have enough resolution in some halo models for the GC, especially with a low initial masses.

In such systems, two mechanisms are responsible for orbital decay and mass loss: tidal effects and dynamical friction induced by the DM halo. The cluster mass plays an important role in its evolution and survival and dynamical friction is responsible for the orbital decay. These two processes

compete with and regulate each other: orbital decay increases the tidal field, which reduces the GC mass and hence slows down the orbital decay. To describe cluster orbital decay, we calculated the distance between the cluster mass centre and Fornax mass centre at each snapshot, in order to get the orbital radius. In order to estimate the GC mass loss, we count only bound particles. The dissolution times were defined to be the time when 95% of the mass was lost from the GC.

4.2.3 Results

We present and discuss our simulation results. To analyze our data and extract our results, we use a python module toolbox, `pnbody` 4.0 [Revaz, 2013].

We start the discussion of our results by presenting the orbital radius as a function of mass loss for B_1 model for clusters with eccentricity parameter $e = 0$, in greater detail. The first three plots of Figure 4.5 depict the final radii and masses between 10 and 12 Gyr, due to the uncertainty on GC ages, for clusters with initial orbital radii $R_i = [0.5, 1.0, 1.5, 2.0, 2.5]$ kpc, initial masses $M_i = [2.5, 5.0, 7.5, 10] \times 10^5 M_\odot$. Final states compatible with cluster observed distributions, i.e. projected distance and mass with their uncertainties, are represented by a grey area for each GC. Cluster initial states ($T = 0$ Gyr), represented by black points, are connected by dashed lines to final states ($T = 10 - 12$ Gyr), represented by black squares and diamonds. The right bottom panel of Figure 4.5 summarizes all results for the B_1 model with eccentricity parameter $e = 0$ for the whole range of initial GC orbital radii and masses considered in this work. Blue regions represent the initial parameter range, where clusters were destroyed by the tidal field.

For instance, clusters with $2.5 \leq M_i \leq 5 \times 10^5 M_\odot$ started at $R_i \leq 2$ kpc, will suffer from Fornax tidal field and be destroyed (see left upper panel of Figure 4.5). Only clusters, initialized at $R_i > 2$ kpc, can survive. Thus, the beige regions represent the range of initial parameters, where clusters can survive over 10 - 12 Gyr. Some survival regions (beige regions) are compatible with observed GC distributions. As an example, the left upper panel shows also that clusters with $5 \leq M_i \leq 7.5 \times 10^5 M_\odot$ and $2 \leq R_i \leq 3$ kpc can reproduce the observed mass and spatial distributions of GC2. Orange regions represent the initial parameter range, where clusters have suffered from dynamical friction and have sunken to the galactic centre. For instance, clusters with $7.5 \leq M_i \leq 10 \times 10^5 M_\odot$ started at $R_i \leq 1.5$ kpc, will fall into Fornax centre (see left bottom panel).

It is important to notice there is a transition from disrupted clusters to fallen clusters due to an initial mass increase for $5 \leq M_i \leq 7.5 \times 10^5 M_\odot$ and $R_i \leq 1.5$ kpc. We did not investigate sufficiently this initial range to know precisely the transition mass and radius. For $R_i < 1$ kpc, we expect the same final state, destroyed or fallen, than GCs started at $R_i = 1$ kpc, because dynamical friction and tidal effects are stronger at lower radii. The left bottom panel indicates also the dynamical behavior of clusters with $M_i \geq 10 \times 10^5 M_\odot$. All clusters with $M_i = 10 \times 10^5 M_\odot$ will sink to the centre of Fornax. According to these results, we expect that more massive clusters will also fall due to dynamical friction at these same initial radii. We also represented the core region with green stars (see right bottom panel of Figure 4.5).

All our empirical results from our simulations can be summarized in Figures 4.6 and 4.7 for cuspy and cored halos. However, more details about GC dynamic are presented in Figures 4.8 and 4.9 for cored halos, and Figures 4.10 and 4.11 for cuspy halos in order to highlight the range of initial parameters entailing that GCs will fall towards the centre of the galaxy (orange regions), be dissolved (blue regions) and survive within 10-12 Gyr (beige regions). We marked the GCs which are

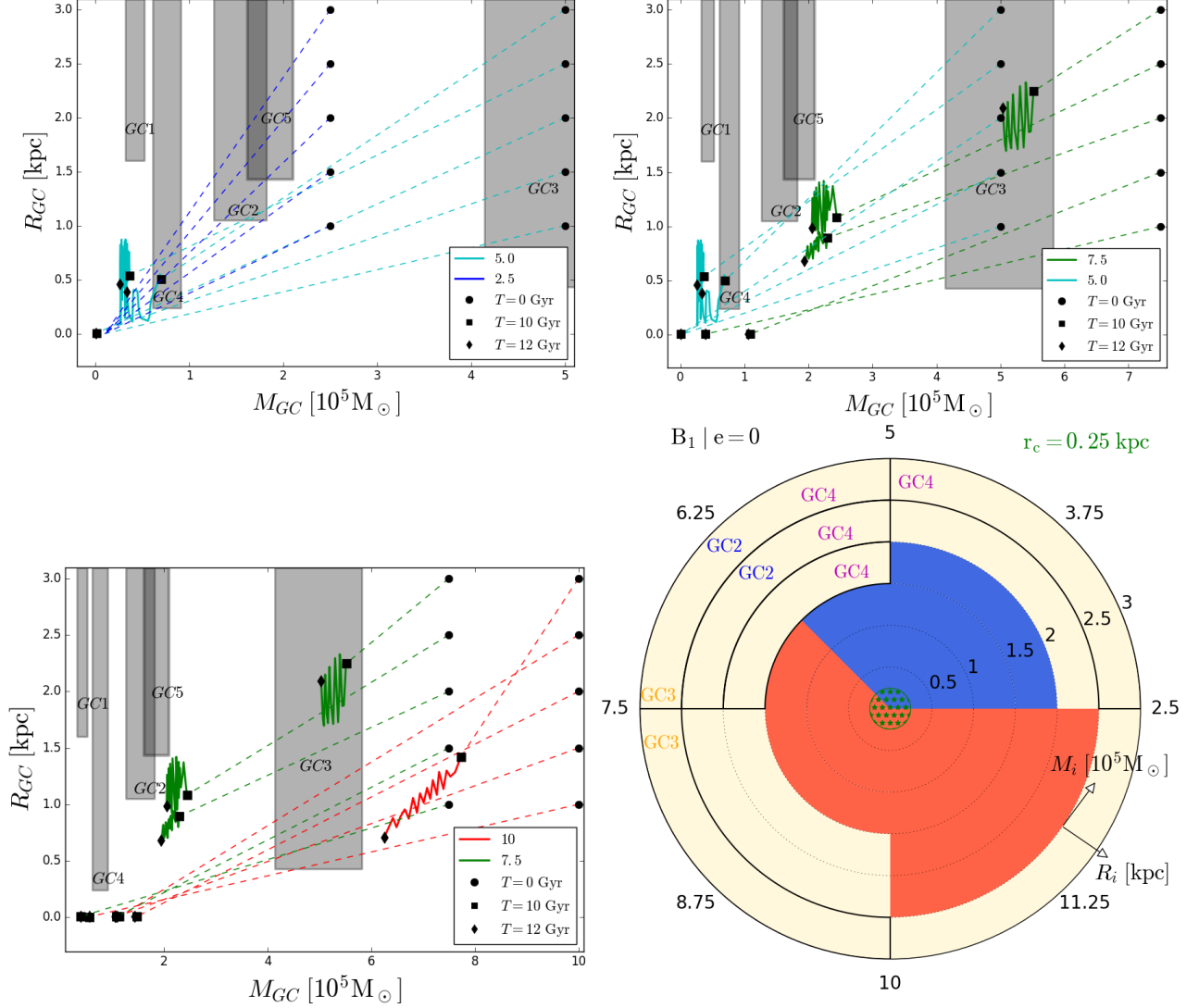


Figure 4.5 – GC orbital radius as a function of mass loss for B1 model with initial orbital radii $R_i = [0.5, 1.0, 1.5, 2.0, 2.5]$ kpc, initial masses $M_i = [2.5, 5.0, 7.5, 10] \times 10^5 M_\odot$ and eccentricity parameter $e = 0$. According to the uncertainty on GC ages, we consider the positions and masses of the GCs between $T = 10$ Gyr and $T = 12$ Gyr. Cluster initial states ($T = 0$ Gyr), represented by black points, are connected by dashed lines to final states ($T = 10 - 12$ Gyr), represented by black squares and diamonds. Final states compatible with observations, i.e. projected distance and GC mass with their uncertainties, are represented by a grey area for each GC. The bottom left panel summarizes all results for the B1 model. Blue (orange) regions represent the initial parameter range, where clusters were destroyed by the tidal field (have suffered from dynamical friction and have sunken to the galactic centre). The beige regions represent the range of initial parameters, where clusters can survive over 10-12 Gyr. Some of these regions are compatible with observed GC distributions. We also represented the core region with green stars. Observed data for GCs are summarized in Table 4.1. All halo parameters are summarized in Table 4.2.

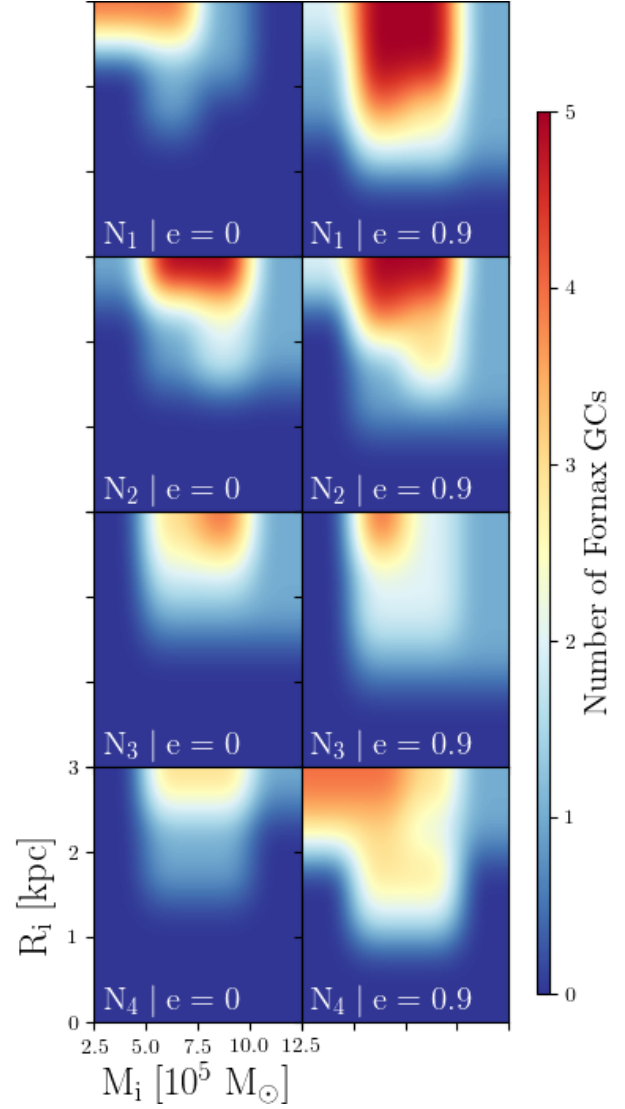
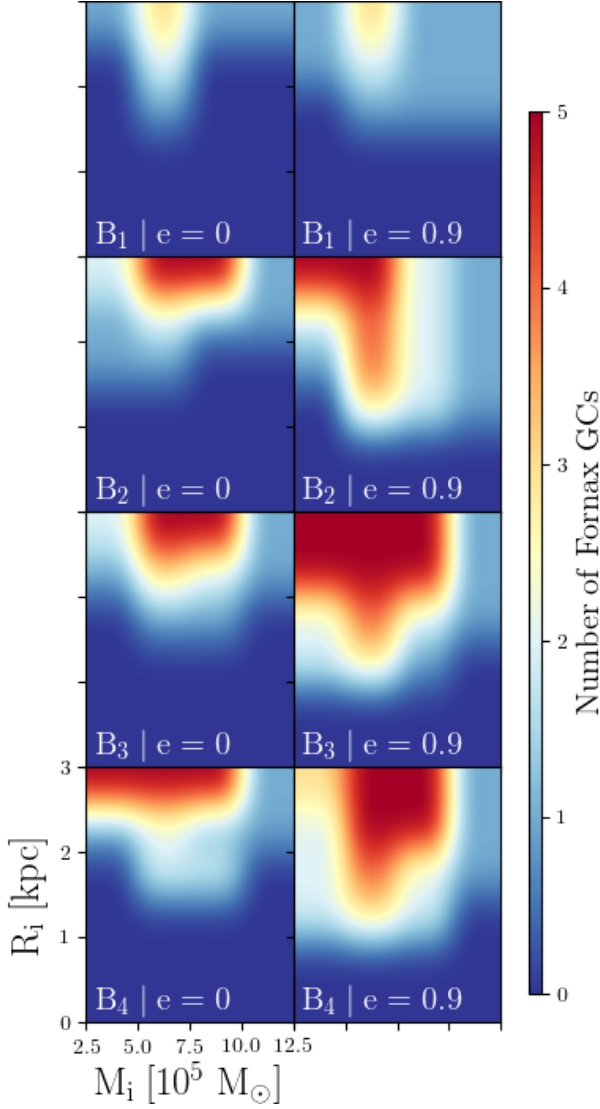


Figure 4.6 – **Cored halo models:** Number of Fornax GCs reproduced by cored halo models B_n with both eccentricity parameters $e = 0$ and 0.9 for our range of initial conditions. The initial parameters are orbital radii $R_i = [1.0, 1.5, 2.0, 2.5, 3.0]$ kpc and GC masses $M_i = [2.5, 5.0, 7.5, 10] \times 10^5 M_\odot$. B_2 , B_3 and B_4 models can reproduce observations for a relevant range of initial cluster orbital radii and masses.

Figure 4.7 – **Cuspy halo models:** Same as Figure 4.6, except for cuspy halo models N_n . N_2 ($r_s = 1$ kpc) model can reproduce GC distributions compatible with observations for both eccentric parameters.

in agreement with survival regions. These figures compare the cored halo models B_n and cuspy halo models N_n for our range of initial cluster orbital radii and masses with an eccentricity parameter $e = 0$ and $e = 0.9$, respectively.

Theoretically, we expect that low initial cluster mass entails that the GCs are destroyed by the tidal field. On the contrary, high initial cluster mass results in the GC spiralling towards the centre. Blue and orange regions represent clearly this expected dynamical behaviour for all halo models. Not surprisingly, we obtain more survival regions compatible with GC observations for $e = 0.9$ than for $e = 0$, because clusters with high eccentric orbit are less affected by dynamical friction and tidal disruption. Indeed, these clusters spend too little time in high density regions. This result is valid for both cored and cuspy halos. For all halo models, we claimed that GCs have to be initially more massive in order to be in agreement with present observations. They need to be about 1.3 to 18 times more massive than the current clusters. We state also that initial orbital radii of clusters have to be at a distance greater than 1 kpc from the centre of Fornax for all halo models. In fact, clusters with $R_i < 1$ kpc are subject to a higher tidal disruption and dynamical friction, because they orbit in a high density region.

B_2 , B_3 and B_4 models hold for the five GCs of Fornax for both eccentric parameters with B_1 model being the sole exception. For $e = 0$ ($e = 0.9$), B_1 model is not valid for GC1 and GC5 (GC1 and GC3). GC1 proves to be the tightest constraint, ruling out B_1 model ($r_c = 0.25$ kpc). In fact, this cluster requires at the same time a weak orbital decay and a very weak or huge mass loss induced by the DM halo. Concerning cuspy halos, simulations predict that N_2 ($r_s = 1$ kpc) model can reproduce GC distributions compatible with observations for both eccentric parameters (see Figure 4.7). Otherwise, GC3 distributions remain a challenge for N_1 , N_3 and N_4 models with our initial mass range. However, we expect that GCs with $M_i > 10 \times 10^5 M_\odot$ could be compatible with GC3 observations for the N_3 ($r_s = 1.5$ kpc) model (see Figures 4.10 and 4.11 for more details). Even if direct dynamical modelling of stellar population [Amorisco et al., 2013; Walker & Peñarrubia, 2011] attest against the presence of a divergent cusp in Fornax, we find a cuspy halo, which can reproduce the observed distributions. Indeed, the NFW profile can be reconciled with observations.

Concerning cored halos, Figure 4.6 imply that B_2 , B_3 and B_4 models can reproduce observations for a relevant range of initial cluster orbital radii and masses. As observed above, B_1 model ($r_c = 0.25$ kpc) cannot reproduce all the observed GCs, especially GC1 in both circular and high eccentric orbits (see Figures 4.8 and 4.9 for more details). In this context, using GC distributions, it is possible to put constraints on the core radius. Thus, we derive a lower limit of $r_c \gtrsim 0.5$ kpc. We ruled out the model with $r_c = 0.25$ kpc, but we did not investigate core sizes between 0.5 and 0.25 kpc. We expect that the true lower limit is in this core size range. Our lower limit ($r_c \gtrsim 0.5$ kpc) is in disagreement with Strigari et al. [2006], who found an upper limit of $r_c \lesssim 0.3$ kpc, based on a constraint on central phase-space density of Fornax. However, Amorisco et al. [2013] showed that Fornax DM halo has a core with $r_c = 1^{+0.8}_{-0.4}$ kpc by exploiting three distinct stellar subpopulations of Fornax. Their limit is totally compatible with our prediction from the B_2 , B_3 and B_4 models (see Table 4.2). According to Walker & Peñarrubia [2011], the slope of the halo mass profile measured in Fornax suggests $r_c \gtrsim 1$ kpc.

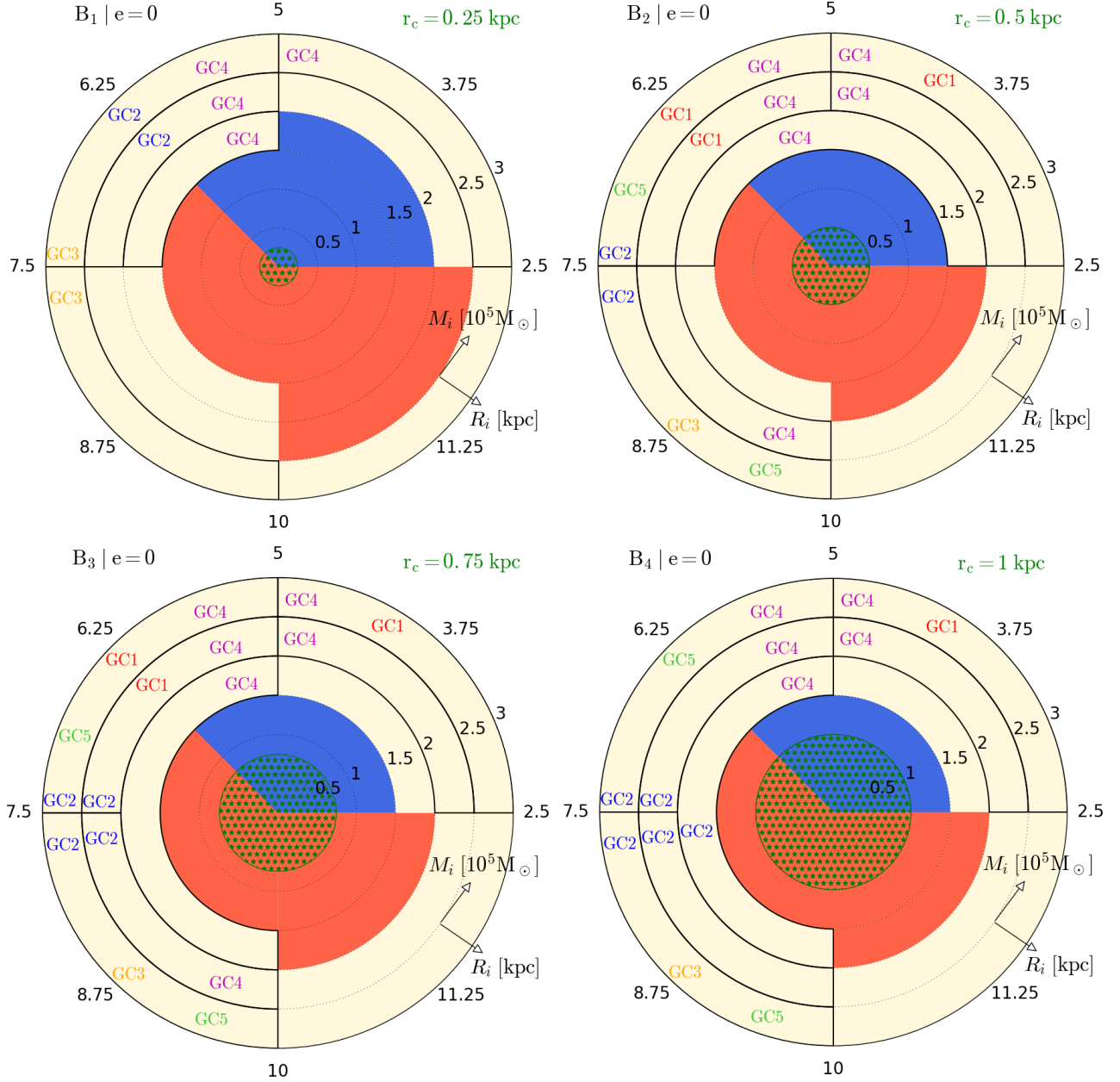


Figure 4.8 – Final states ($T = 10 - 12$ Gyr) for initial GC orbital radii $R_i = [0.5, 1.0, 1.5, 2.0, 2.5]$ kpc and masses $M_i = [2.5, 5.0, 7.5, 10] \times 10^5 M_\odot$ with eccentricity parameter $e = 0$ for cored halo models B_n. Blue (orange) regions represent the initial parameter range, where clusters were destroyed by the tidal field (have suffered from dynamical friction and have sunken to the galactic centre). The beige regions represent the range of initial parameters, where clusters can survive over 10-12 Gyr. Some of these regions are compatible with observed GC distributions. We also represented the core region with green stars. Only B₂, B₃ and B₄ models can reproduce the five GCs. Observed data for GCs and halo parameters are summarized in Table 4.1 and Table 4.2.

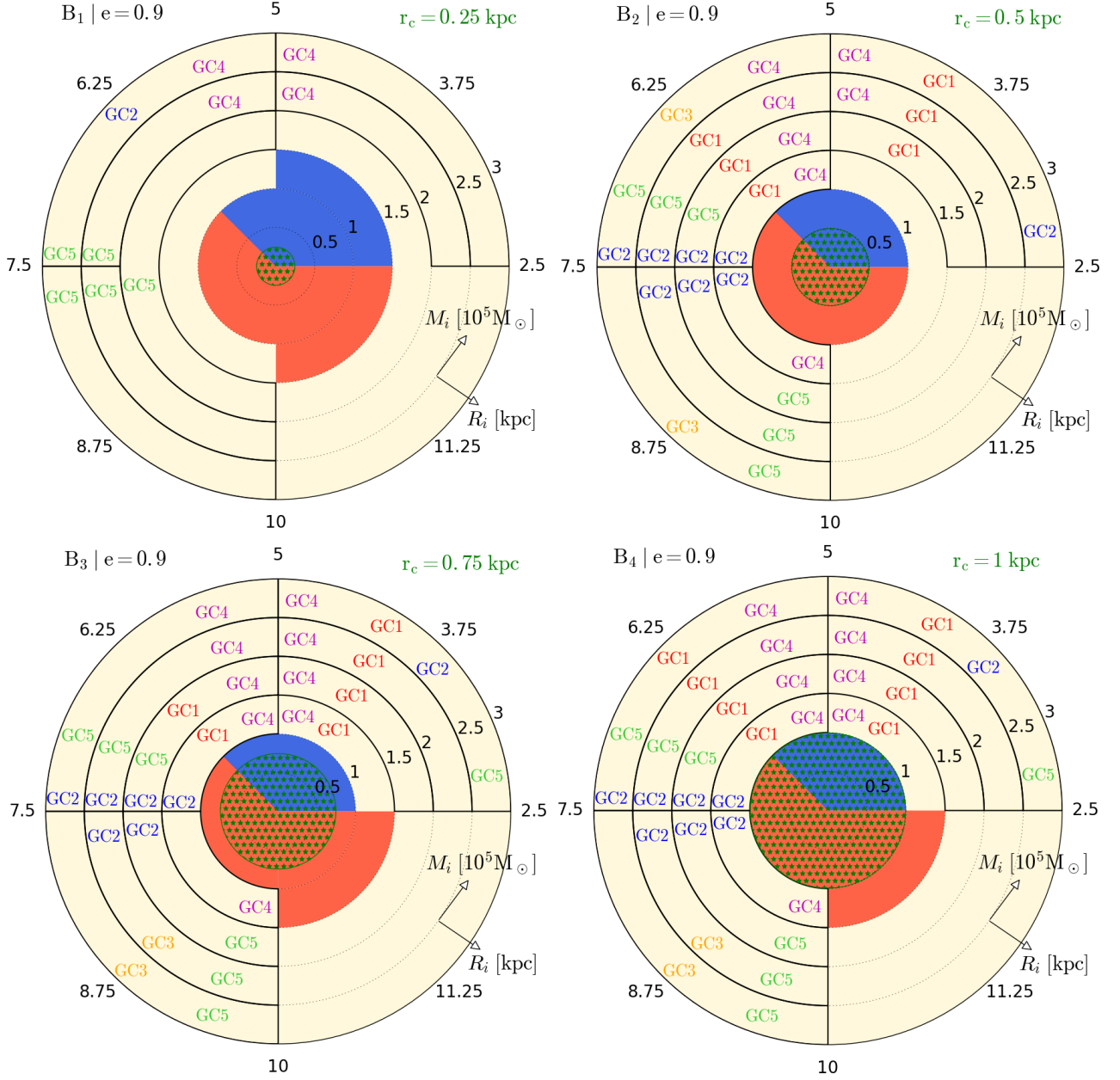


Figure 4.9 – Same as Figure 4.8, except with eccentricity parameter $e = 0$ for cored halo models B_n . Only B_2 , B_3 and B_4 models can reproduce the five GCs. Observed data for GCs and halo parameters are summarized in Table 4.1 and Table 4.2.

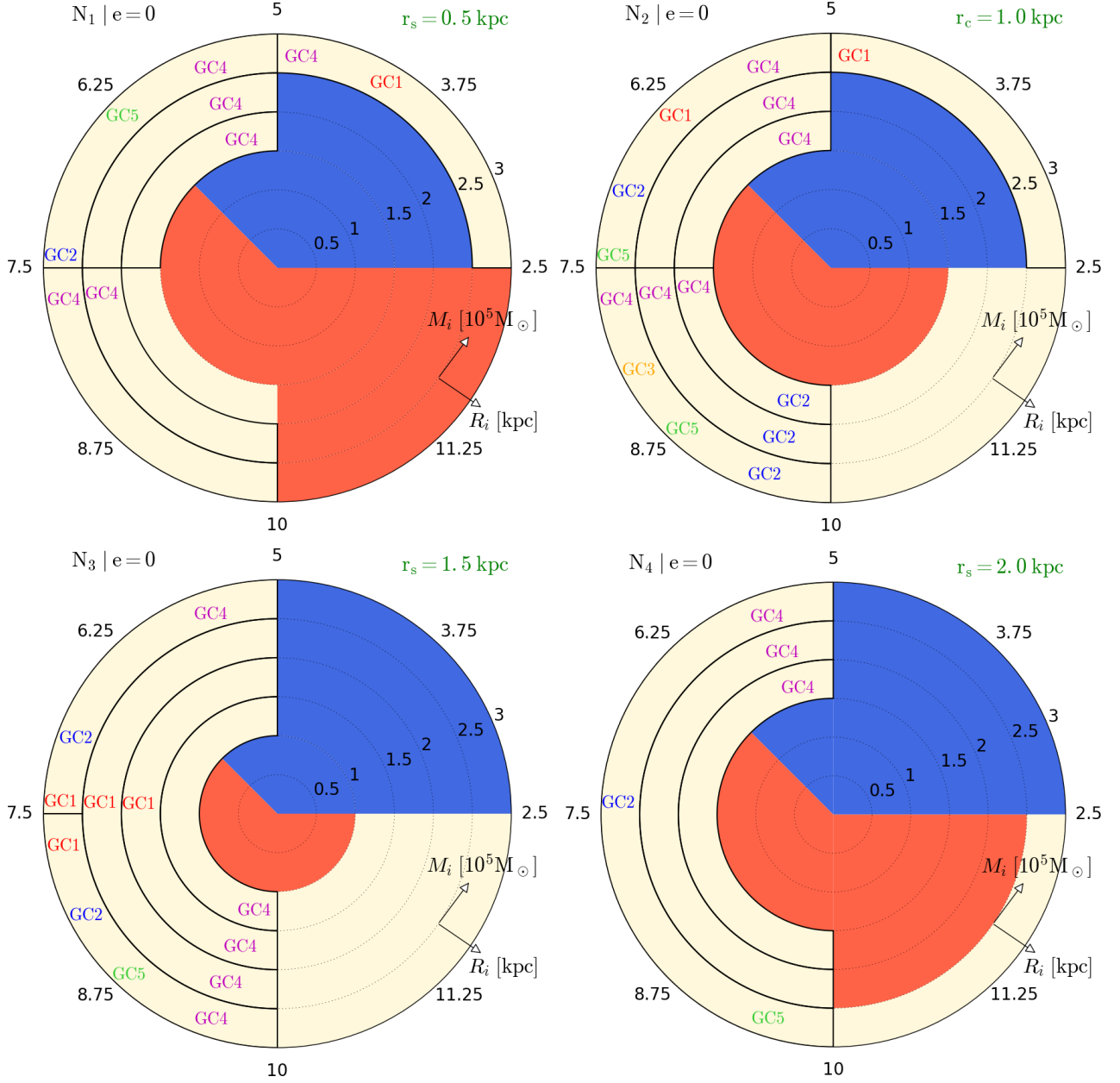


Figure 4.10 – Same as Figure 4.8, except with eccentricity parameter $e=0$ for cuspy halo models N_n . Only N_2 model can reproduce the five GCs. Observed data for GCs and halo parameters are summarized in Table 4.1 and Table 4.2.

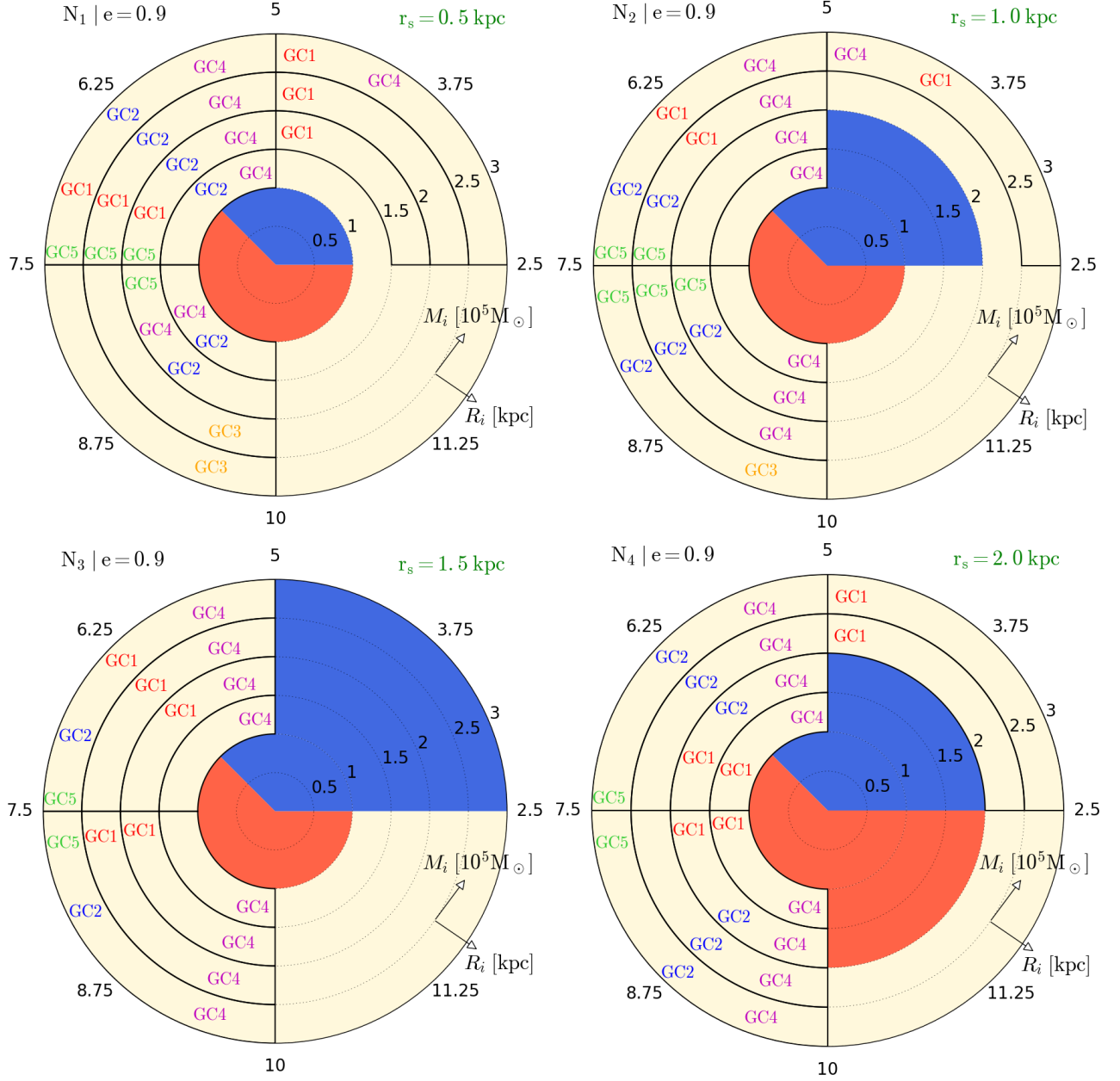


Figure 4.11 – Same as Figure 4.8, except with eccentricity parameter $e = 0.9$ for cuspy halo models N_n . Only N_1 and N_2 models can reproduce the five GCs. Observed data for GCs and halo parameters are summarized in Table 4.1 and Table 4.2.

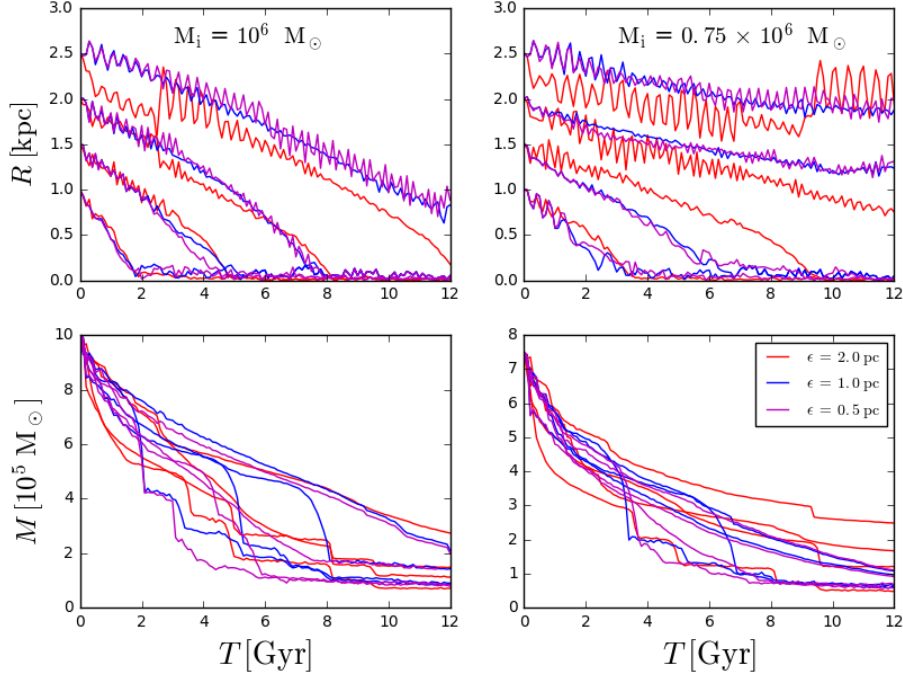


Figure 4.12 – Impact of softening length on the radial and tidal evolutions of GCs on a circular orbit with initial mass $M_i = 0.75$ and $1 \times 10^6 M_\odot$ for B_4 model. Top and bottom panels show the evolution of orbital radius and cluster mass, respectively. We ran simulations with three different softening lengths $\epsilon = [0.5, 1, 2]$ pc in order to ensure that our simulations do not suffer from numerical noise. Our simulations are well converged between 10 and 12 Gyr for $\epsilon = 0.5$ and 1 pc. We chose $\epsilon = 1$ pc as the softening length for all our simulations.

4.2.4 Appendix

Numerical convergence

We assess the impact of a numerical parameter that controls the accuracy of our simulations; the softening length $\epsilon_0 = 1$ pc. To test how the softening length impacts on the radial and tidal evolution of GCs, we ran simulations with three different softening lengths $\epsilon = \epsilon_0/2, \epsilon_0$ and $2\epsilon_0$ in order to ensure that our simulations do not suffer from numerical noise. The evolution of the orbital radius and the mass loss of five clusters moving on a circular orbit in model B_4 (see Table 4.2) is shown in Fig 4.12 for three different softening lengths. It can be seen that orbital and tidal evolutions are very similar for $\epsilon = 0.5$ and 1 pc. However, for $\epsilon = 2$ pc, numerical noise causes artificial decay and enhanced disruption of the cluster. Our simulations are well converged between 10 and 12 Gyr for $\epsilon = 0.5$ and 1 pc. We chose $\epsilon = 1$ pc as the softening length for all our simulations. For all runs, the energy relative error is lower than 5%. We state that the energy of the system is conserved in all our simulations.

MW tidal field

Our host galaxy potential is modelled from Allen & Santillan [1991] consists of a stellar bulge as a Plummer sphere [Plummer, 1911], a disc represented by the potential from [Miyamoto & Nagai, 1975] and a spherical DM halo described by NFW profile [Navarro et al., 1997]. For this model, we used the revised parameters from Irrgang et al. [2013] (see their Table 1). Nevertheless, MW tidal field can have a significant impact on GCs on eccentric orbits. In Figure 4.13, we represented the orbital radius and mass of GCs on an eccentric orbit ($e = 0.9$) with initial mass $M_i = 0.5$ and

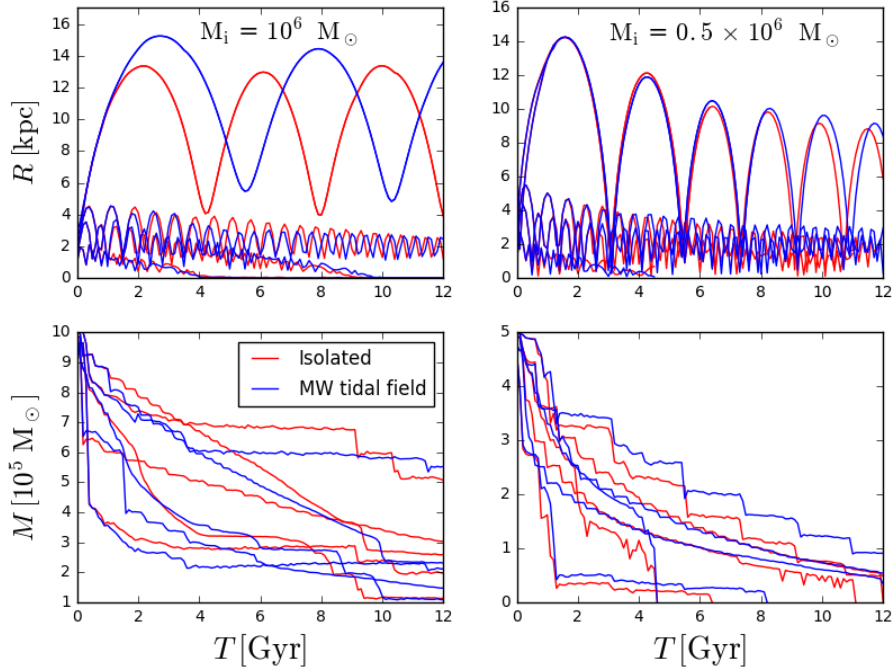


Figure 4.13 – Impact of MW tidal field on the radial and tidal evolution of GCs on a eccentric orbit ($e = 0.9$) with initial mass $M_i = 0.5$ and $1 \times 10^6 M_\odot$ for B_1 model. Top and bottom panels show the evolution of orbital radius and cluster mass, respectively. We ran simulations with and without static potential in order to measure the importance of MW tidal field. MW tidal field was taken into account in our simulations, especially for high eccentric orbit

$1 \times 10^6 M_\odot$ as a function of time for B_1 model. It can be seen in this figure that the orbits tend to be spread by the MW tidal field. In other words, the apocentre and pericentre are increased by the Galactic field. This effect becomes more important as the ratio between the initial orbital radius and the tidal radius increases. Thus, MW tidal field was taken into account in our simulations, especially for high eccentric orbit.

4.3 Embedding GC in DM minihalos

Recent simulations of the Fornax dwarf galaxy found that the observed GCs are not necessarily incompatible with a cuspy DM profile (NFW) and that this depends strongly on GC initial conditions [Boldrini et al., 2019]. However Fornax GCs remain a puzzle for understanding their survival over a Hubble time.

GCs are gravitationally bound groupings of mainly old stars, formed in the early phases of galaxy formation. The origin of GCs is one of the key unsolved astrophysical problems. There are also various unresolved open questions regarding the formation and evolution of GCs during galaxy formation and assembly within a cosmological framework [Forbes et al., 2018]. Despite their relevance to star formation, galaxy evolution and cosmology, there is no clear consensus on the formation of GCs. One can classify all proposed scenarios for old GC formation into two broad categories. Firstly, GCs originated as gravitationally bound gas clouds in the early Universe and are formed inside their present-day host galaxies. This corresponds to a primary in-situ formation process [Kravtsov & Gnedin, 2005; Kruijssen, 2015; Peebles & Dicke, 1968]. Secondly, GCs can be formed around the time of reionization in DM minihalos that later merge to become a part of the present-day host galaxy. It corresponds to a secondary galactic origin in a similar way to formation of dwarf galaxies

[Bromm & Clarke, 2002; Mashchenko & Sills, 2005; Peebles, 1984; Ricotti et al., 2016]. Little star formation can take place during the reionization epoch inside these DM minihalos with virial masses less than $10^8 M_\odot$, as the heated gas can escape [Barkana & Loeb, 1999]. However, the reionization of the Universe can actually trigger star formation in DM minihalos through different reionization-regulated positive feedback mechanisms [Cen, 2001; Ricotti et al., 2002]. While most GCs are old, there are also young GCs such as Terzan 7 and Whiting 1 [Law & Majewski, 2010; Massari et al., 2017], as well as the populations of young GCs in the Magellanic Clouds and many other nearby star-forming galaxies. These GCs could be formed via a different mechanism from that of the old GCs. Here, we focus on the second scenario where GCs are formed at the centres of their own DM minihalos.

Positions and proper motions for GCs in the Galaxy from the second data release of the Gaia mission will offer unique insights into GC dynamics [Gaia Collaboration et al., 2018]. Until now, these DM minihalos have not been detected, but there are GC features and perhaps observational signatures [Sollima et al., 2016]. For instance, an extended diffuse stellar envelope can highlight whether GCs might be embedded in DM minihalos [Kuzma et al., 2016; Olszewski et al., 2009; Peñarrubia et al., 2017]. Also, GCs orbiting in the inner regions of the Galaxy may lose a large fraction of any DM minihalo mass [Bromm & Clarke, 2002].

In this work, we embed GCs in DM minihalos in order to simultaneously resolve the timing and the cusp-core problems in Fornax with the most prevalent initial conditions from the Illustris cosmological simulation [Pillepich et al., 2018]. Our N-body simulations performed on GPU allow us to study the evolution of the DM density profile in the centre of Fornax at high resolution. The Section 4.3 is organized as follows. Subsection 4.3.1 provides a description of the Fornax system and the N-body modelling. In Subsection 4.3.2, we outline details of our numerical simulations. In Subsection 4.3.3, we illustrate our simulation results and discuss the implications of DM minihalos of GCs on the timing and cusp-core problems.

4.3.1 Fornax-GC system

The dSph galaxy Fornax is one of the more DM-rich satellites of the MW Galaxy with a stellar mass of about $10^8 M_\odot$ at a distance of around 147 kpc [de Boer & Fraser, 2016]. We consider only the first five GCs with masses of about $10^5 M_\odot$ and average projected distances of about 1 kpc. In this section, we present the models for Fornax and its GCs that provide the initial conditions for our simulations. A live gravitational system is necessary to capture tidal stripping and dynamical friction. Thus, Fornax has to be modelled as a live galaxy with its GCs, i.e. a self-gravitating system composed of star and DM particles.

It has been shown that simulated GCs formed within Fornax, modelled with a cuspy or cored DM halo, are compatible with observations [Boldrini et al., 2019]. However, the origin of the Fornax DM core remains unsolved. Here, we consider two scenarios to explain the timing problem. We assume that GCs have experienced either early accretion 10-12 Gyr ago ($z=3$) or recent accretion 2-4 Gyr ago ($z=0.36$) by the Fornax galaxy. Fornax GCs are all dominated by an old population (>10 Gyr), which gives an uncertainty in the GC age determinations [de Boer & Fraser, 2016].

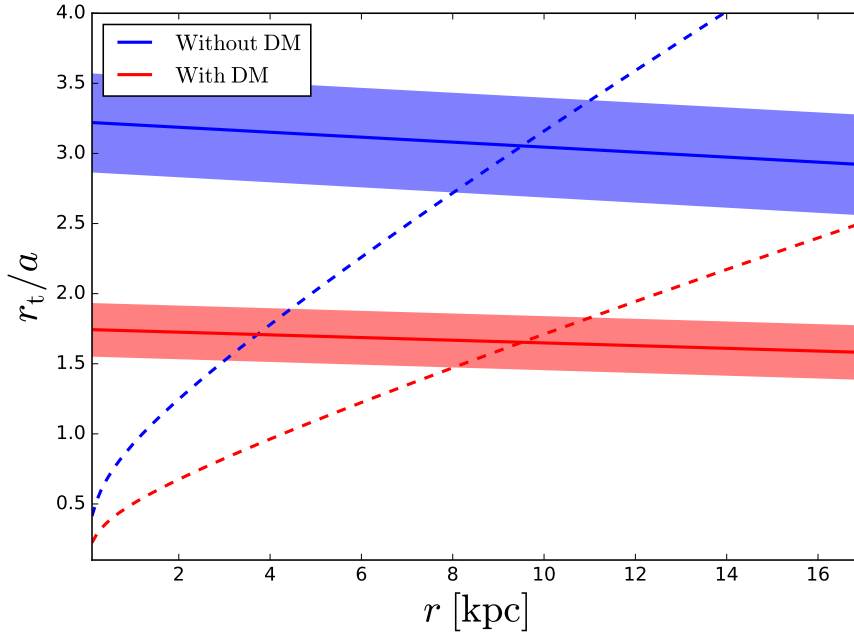


Figure 4.14 – **Tidal impact of MW:** Ratio between the tidal radius and the typical size of GCs as a function of the orbital radius centered on Fornax for GCs with and without a DM minihalo. For GCs composed only of stars, we assume that $a = r_{\text{tmax}}$, where r_{tmax} is the highest initial tidal radius of our GCs in Fornax. However, we set $a = r_{\text{vir}}$, where r_{vir} is the virial radius of the $2 \times 10^7 M_{\odot}$ minihalo for GCs embedded in a DM minihalo. Solid (dashed) line represents the influence of the MW (Fornax) on GCs. For the MW, the error bands are due to the uncertainty on pericentre and apocentre of Fornax [Gaia Collaboration et al., 2018]. The MWG has no major impact on Fornax GCs, because the tidal radius is always higher than the typical size of the GCs at any radii. This is the reason why we assume that tidal disruptions are mostly driven by Fornax and that our dSph model is in isolation.

Fornax galaxy

We construct Fornax as a live galaxy composed of stars and DM particles only, since dSph galaxies contain little or no gas today. The Fornax stellar component is modelled, due to the presence of a stellar core ($r_0 = 0.668 \text{ kpc}$ [Strigari et al., 2010]), by a Plummer profile [Plummer, 1911]:

$$\rho(r) = \frac{3a^2 M_0}{4\pi} (r^2 + a^2)^{-5/2}, \quad (4.7)$$

where $a = r_0(\sqrt{2} - 1)^{-1/2}$ and $M_0 = 3.82 \times 10^7 M_{\odot}$ are the scale parameter and the mass, respectively [de Boer & Fraser, 2016]. For the DM halo of Fornax, we assume a NFW form [Navarro et al., 1996]:

$$\rho(r) = \rho_0 \left(\frac{r}{r_s} \right)^{-1} \left(1 + \frac{r}{r_s} \right)^{-2}, \quad (4.8)$$

with the central density ρ_0 and scale radius r_s . For the simulations, we consider a Fornax-like dSph with mass of $10^9 M_{\odot}$ at redshift z depending on the considered scenario. Given the halo mass and redshift, the scale radius r_s of the Fornax halo was estimated from cosmological N-body simulations [Prada et al., 2012].

Globular Clusters

In our model, GCs with a stellar mass M_* are formed at the centre of DM minihalos with a virial mass M_{mh} . We fix the mass ratio M_*/M_{mh} to 0.05. For the five surviving GCs orbiting in Fornax,

Redshift	Object	r [kpc]	v_x [km/s]	v_y [km/s]	v_z [km/s]	$ v $ [km/s]
$z = 3$	E ₁	2.11	20.22	1.6	8.1	21.8
	E ₂	2.74	16.42	3.28	15.75	22.99
	E ₃	1.1	38.62	15.44	18.94	39.97
	E ₄	1.76	13.46	21.46	26.87	36.94
	E ₅	1.14	32.81	6.93	7.89	34.37
$z = 0.36$	O ₁	5.32	13.9	1.31	14.38	20.04
	O ₂	2.07	9.43	19.05	21.42	30.18
	O ₃	1.95	37.49	4.55	6.21	38.28
	O ₄	2.19	3.51	3.87	34.0	34.39
	O ₅	2.05	19.62	29.8	15.1	38.75

Table 4.3 – Initial conditions for five GCs E_i at $z=3$ (≈ 12 Gyr) and five GCs O_i at $z=0.36$ (≈ 4 Gyr), determined by using Illustris TNG-100 data. We consider two scenarios to explain the timing problem. We assume that GCs have experienced early accretion onto the Fornax galaxy 10-12 Gyr ago, or alternatively have undergone recent accretion 4 Gyr ago ($z=0.36$). This is the reason why we determine the most prevalent positions and velocities of $7.5 \times 10^6 M_\odot$ particles at these two redshifts, which have the same projected distances D_{obs} as Fornax GCs at $z=0$ using multidimensional binned statistics. The Illustris DM mass resolution is of the same order as our minihalo mass.

we assume a two-component model that includes a stellar component and a DM minihalo:

$$M_{\text{model}}(r) = M_*(r) + M_{\text{mh}}(r). \quad (4.9)$$

Our N-body realizations assume a [King \[1962\]](#) stellar density distribution,

$$\rho(r) = \rho_0 \left[\left(1 + \left(\frac{r}{r_k} \right)^2 \right)^{-1/2} - C \right], \quad C = \left[1 + \left(\frac{r_t}{r_k} \right)^2 \right]^{-1/2}, \quad (4.10)$$

where r_k and r_t are the King and tidal radii, respectively. For all the simulations, we chose a King radius $r_k = 1$ pc lower than the observed radius, because it is susceptible to increase through dynamical processes such as mass loss [[Mackey & Gilmore, 2003](#)]. The DM minihalos are distributed in a spherical halo following a NFW profile with a mass of $2 \times 10^7 M_\odot$ (see Equation (7.1)) at redshift $z = 3$ or $z = 0.36$ depending on the accretion scenario. Given the halo mass and redshift, the halo concentration c_{200} of the DM minihalos can be estimated from cosmological N-body simulations [[Prada et al., 2012](#)].

We wish to provide relevant GC initial conditions from cosmological simulations. We found 7395 isolated subhalos with mass of about $10^9 M_\odot$ in the Illustris TNG-100 simulation [[Pillepich et al., 2018](#)]. The mass resolution of TNG-100 is $7.5 \times 10^6 M_\odot$, which is of the same order as our minihalo mass. The current projected distances D_{obs} for the GCs are from 0.24 to 1.6 kpc, which is the minimum distance between GCs and the Fornax centre. In order to determine the GC positions and velocities at these redshifts, we select particles of the isolated subhalos at $z=0$, which have the same projected distances as Fornax GCs at $z=0$ and we find corresponding particles at redshift $z=3$ and $z=0.36$. We subsequently compute multidimensional binned statistics for this 6-dimensional space in order to determine the maximum weights for each dimension. We applied Scott's rule to determine the optimal bin width given by

$$\Delta_b = \frac{3.5\sigma}{n^{1/3}}, \quad (4.11)$$

where σ is the standard deviation of one dimension, and n is the number of points. Our initial conditions for GCs, positions and velocities, calculated with this method are listed in Table 7.1.

MW Galaxy tidal field

As Fornax is a galaxy satellite of the MW, we may expect that the MW tidal field to have an impact on GCs. We estimated this by calculating the theoretical tidal radius of our GCs with and without a DM minihalo in the simulation [Küpper et al., 2010]. The tidal radius marks the distance beyond which stars can escape the GC. For our calculation, we assume that the MW potential, based on the model of Allen & Santillan [1991], consists of a stellar bulge as a Plummer sphere [Plummer, 1911], a disc represented by the potential from Miyamoto & Nagai [1975] and a spherical DM halo described by a NFW profile [Navarro et al., 1997]. For this model, we used the revised parameters from Irrgang et al. [2013] (see their Table 1). The tidal radius is calculated at the mean radius, because it is currently overestimated at the pericentre. Indeed, the variation of the tidal field over time is sufficiently fast that the cluster cannot adapt to the changing environment, but rather behaves as if it experiences a single mean tidal field along its orbit. Fig. 4.14 describes the ratio between the tidal radius and typical size of GCs as a function of the orbital radius centered on Fornax of GCs with and without a DM minihalo. We assume that the size of a GC (with a DM minihalo) corresponds to its initial tidal (virial) radius in Fornax. For GCs composed only of stars, we consider the highest initial tidal radius r_{tmax} of our GCs in Fornax as the typical size a . However, we set the virial radius r_{vir} of the $2 \times 10^7 M_{\odot}$ minihalo as the typical size for GCs embedded in a DM minihalo. For the MW, the error bands are due to the uncertainty in pericentre and apocentre of Fornax [Gaia Collaboration et al., 2018]. We showed that the MW (solid line) has no major impact on Fornax GCs, because the tidal radius is always higher than the typical size of the GCs at any radii. On the contrary, Fornax (dashed line) will give rise to tidal disruptions of the GCs, especially those with DM minihalos. Finally, we assume that this dynamical process is mostly driven by Fornax and that our dSph model is in isolation.

4.3.2 N-body simulations

To generate our live objects, we use the initial condition code magi [Miki & Umemura, 2017a]. We perform our simulations with the high performance collisionless N-body code gothic [Miki & Umemura, 2017b]. We run N-body simulations with five GCs orbiting in Fornax galaxy by adopting a softening length of $\epsilon_0 = 1$ pc and an accuracy control parameter of $A_0 = 2^{-7}$. Considering a softening length similar to the King radius maintain the dynamical stability of an isolated GC (see Fig.s 4.25). We assess the impact of the softening length ϵ on the stellar density profile for an isolated GC with and without a DM minihalo, and the orbital decay and the mass loss of GCs and the evolution of the DM profile of Fornax (see in Fig.s 4.25, 7.7, 4.27 and 4.28). We consider both early and recent accretion of GCs by Fornax. For these two scenarios, we run simulations with five GCs embedded in their own DM minihalo and five GCs composed only of stars as usual. Initially, GCs with and without DM minihalo have the same most prevalent positions and velocities (see in Table 7.1). The halo and the stellar components of Fornax are represented by $N = 10^7$ particles. The mass ratios for these two components determine the particle number for each component. DM minihalos and GC stars are represented by about 10^5 and 10^4 particles, respectively. In fact, we require that the particle masses of all components are set to be equal in order to reduce numerical artifacts. To analyze our data and extract our results, we use a python module toolbox, pnbody 4.0 [Revaz, 2013].

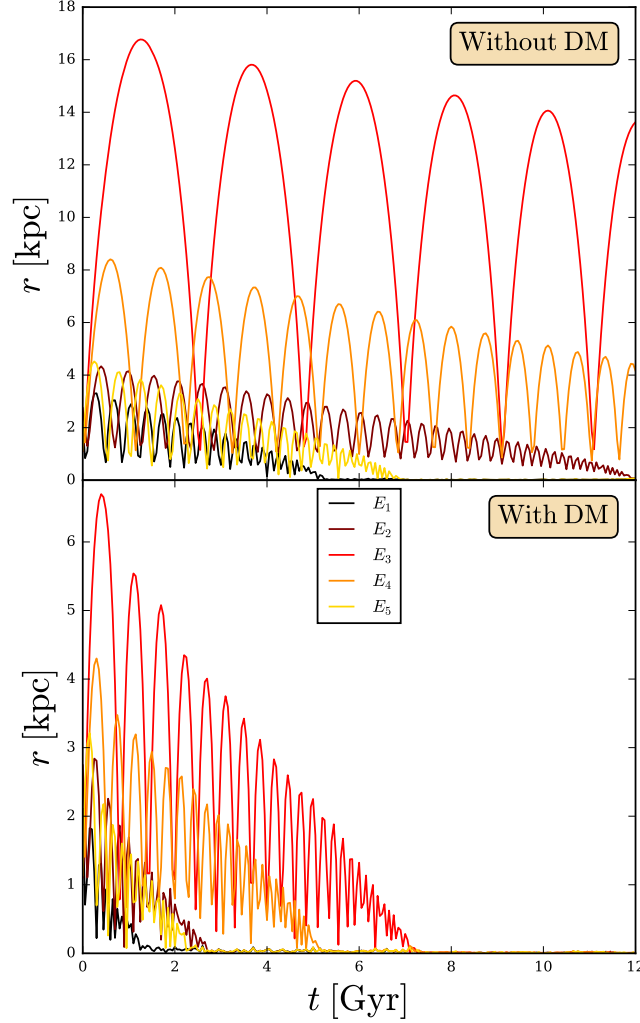


Figure 4.15 – **DM minihalos accelerate GC infall:** Orbital decay of the 5 GCs without (*upper*) and with (*lower panel*) in a $2 \times 10^7 M_\odot$ DM minihalo over 12 Gyr because the Fornax GCs are all dominated by ancient (>10 Gyr) populations of stars [de Boer & Fraser, 2016]. These radii correspond to the distances between each GC mass centre and Fornax mass centre. Initially, $10^6 M_\odot$ GCs with and without DM minihalos have the same most prevalent positions and velocities at $z=3$ from Illustris TNG-100 cosmological simulations (see objects E_i in Table 7.1). Our initial conditions entail an accretion process by the Fornax galaxy with eccentric orbits for all the GCs. The infall of GCs with and without a DM minihalo rules out the early accretion scenario for Fornax GCs as this dSph has five orbiting GCs observed at the present day.

4.3.3 Results

Next, we present and discuss our simulation results. To describe cluster orbital decay, we calculate the distance between the cluster and Fornax mass centres at each snapshot, in order to get the orbital radius. To estimate the GC mass loss, we count only bound particles. The main challenge with the Fornax timing problem is to find a way to delay GC orbital decay in order to observe GCs in orbit today instead of a nuclear star cluster at the centre of the galaxy. The GC infall is due to dynamical friction generated by the Fornax DM field. Compared to stellar GCs, DM minihalos are expected to fall more rapidly towards the galaxy centre due to their higher masses. We consider two scenarios for Fornax GCs, as described in the following sections.

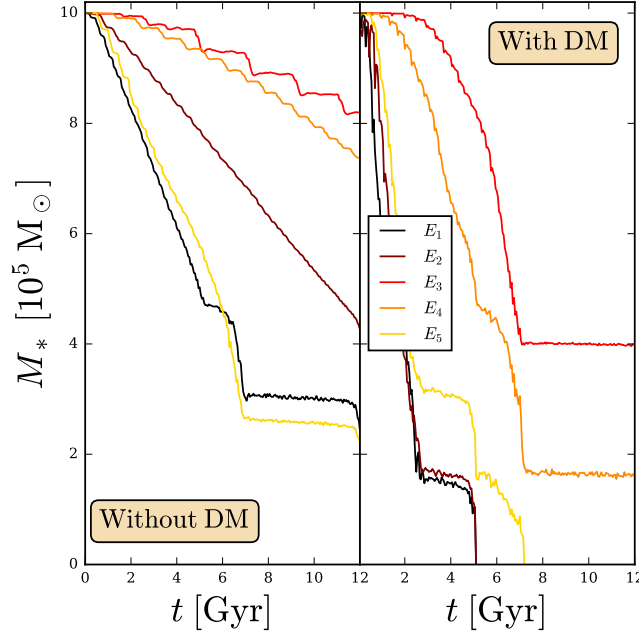


Figure 4.16 – **DM minihalos accelerate tidal stripping:** Evolution of the mass loss of the GC stellar component for the 5 GCs without (*left panel*) and with (*right panel*) a $2 \times 10^7 M_{\odot}$ DM minihalo over 12 Gyr. The initial stellar masses of GCs are $10^6 M_{\odot}$. In order to estimate the GC mass loss, we count only bound particles. GCs with a $2 \times 10^7 M_{\odot}$ DM minihalo lost more stars compared to stellar GCs, because minihalos induce major tidal stripping. All stellar GCs survive in this early accretion scenario. However, we observe that three GCs with a DM minihalo are completely tidally stripped within 8 Gyr.

Early accretion

First, we assume that GCs with and without a DM minihalo were accreted 10-12 Gyr ago by Fornax. Figure 4.15 depicts the orbital decay of five GCs with and without a DM minihalo over 12 Gyr in this scenario. Initially, they have the same most prevalent positions and velocities at $z = 3$ from Illustris TNG-100 cosmological simulation (see objects E_i in Table 7.1). Our initial conditions entail an accretion process by the Fornax galaxy with eccentric orbits for all the GCs. The orbital period is higher for the stellar GCs than for GCs with a DM minihalo. In Figure 4.15, orbital radii confirm that DM minihalos accelerate the infall of the five GCs. The stellar mass loss of all the GCs over 12 Gyr is presented in Figure 4.16. GCs with DM minihalos lose more stars compared to stellar GCs, because minihalos induce major tidal stripping. Indeed, stripping by the Fornax tidal field is more efficient at small radii. We also observe that three GCs with DM minihalos are completely tidally stripped within 8 Gyr.

Fornax is dominated by metal-rich stars whereas GCs are dominated by metal-poor stars. The metal-poor stellar mass in Fornax was estimated to be about $(44.9 \pm 5.3) \times 10^5 M_{\odot}$ [de Boer & Fraser, 2016]. This large quantity of metal-poor stars in Fornax could suggest that each of these four surviving metal-poor GCs has likely lost several times $10^5 M_{\odot}$ due to dynamical processes. GC4 is excluded from this estimate, because this cluster is possibly more metal-rich than the other clusters. Another explanation is that GCs have sunk to the galaxy centre and were destroyed such as our three GCs with DM minihalos. Hence, these metal-poor stars could correspond to relics of destroyed GCs with DM minihalos. This could be also possible for stellar GCs, but this scenario within 12 Gyr is more reliable for DM minihalos as the latter accelerate the tidal stripping (see in Figure 4.16). Fornax observations reveal that Fornax has no NSC at its centre. In order to verify

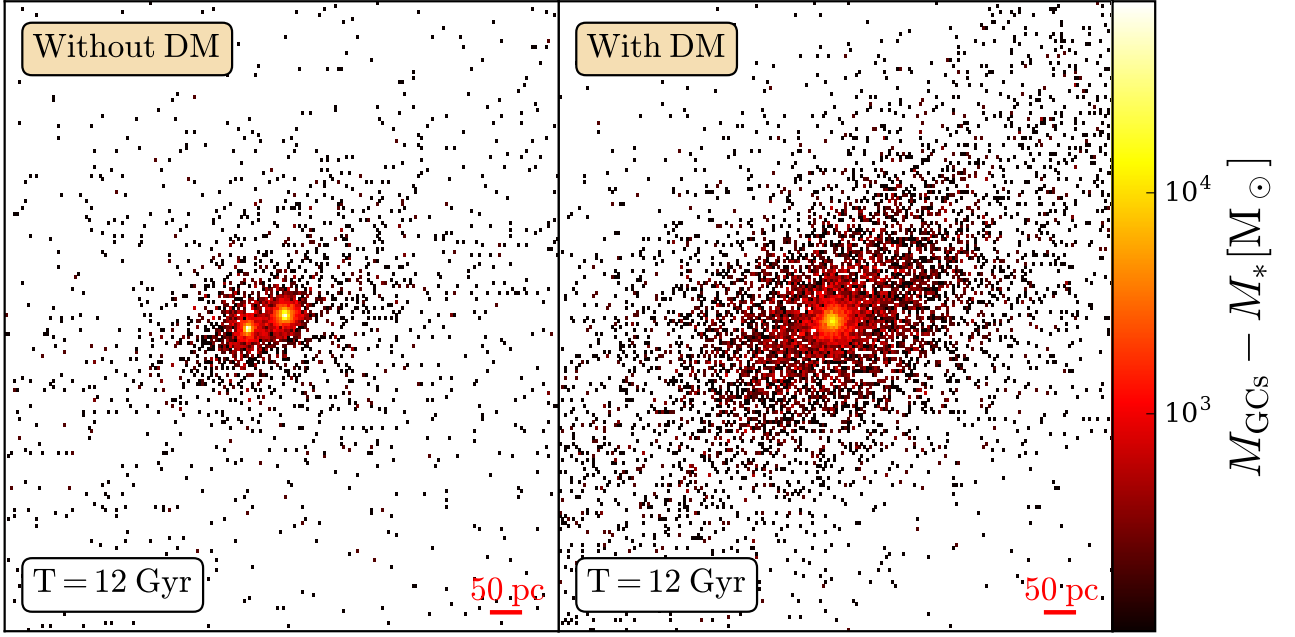


Figure 4.17 – **Formation of a nuclear star cluster (NSC)**: Mass difference between stars of the 5 GCs without (*left panel*) and with (*right panel*) a DM minihalo and Fornax stars at $T = 12$ Gyr. We represented only bins with a size of 5 pc, which have a positive mass difference. The latter allows us to highlight a stellar overdensity induced by GCs at the Fornax centre. This mass difference exhibits the presence of a double nucleus for stellar GCs and single nucleus for GCs with DM minihalo. Infalling GCs, which are not completely tidally stripped, will contribute to the formation of a NSC. As Fornax exhibits the absence of a nuclear star cluster at the centre, the formation of a NSC ruled out the early accretion scenario for Fornax GCs.

that no NSC was formed in our scenario, Figure. 4.17 illustrates the mass difference between stars of the 5 GCs, without and with a DM minihalo, and Fornax stars at $T = 12$ Gyr. We represent only bins with a size of 5 pc, which have a positive mass difference. The latter allows us to highlight an overdensity for stars. In other words, we want to clearly separate a NSC from the stellar component of the galaxy. Figure. 4.17 showed the presence for a double nucleus for stellar GCs and single nucleus for GCs with DM minihalo formed by infalling GCs, which are not completely destroyed by the Fornax tidal field. Thus, we rule out the early accretion scenario for Fornax GCs due to the infall of the five GCs and the formation of a NSC. We point out that stars of GCs with a DM minihalo, which are completely tidally stripped, will not contribute to the formation of a nuclear star cluster at the centre.

Our GPU simulations allow us to also study the impact of GCs with or without a DM minihalo on the evolution of the DM density profile of Fornax. We observe the formation of cores in the cold DM halo of Fornax. As all GCs have eccentric orbits, they can perturb the DM halo of Fornax by their multiple crossings near the Fornax centre (see Figure. 4.15). Initially, the Fornax DM halo assumes a NFW profile. We consider DM particles from both Fornax halo and GCs to determine the DM density profile of Fornax over the time. In order to determine precisely if there is core formation in the Fornax halo, we did a fit for the DM profile. As shown in Figure. 4.18, we found that all our profiles are well fitted by the following five-parameter formula:

$$\rho(r) = \rho_c W(r) + [1 - W(r)]\rho_{\text{NFW}}(r), \quad (4.12)$$

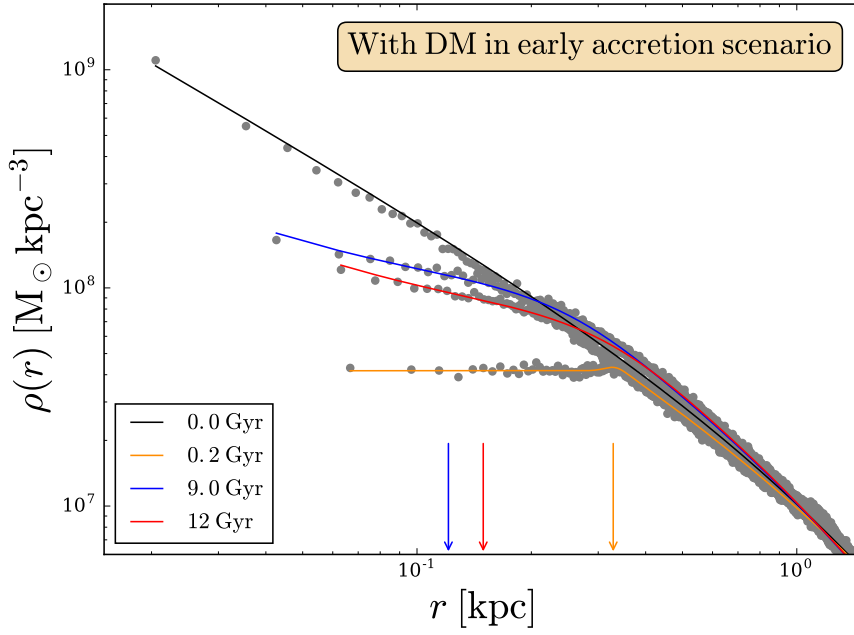


Figure 4.18 – **Heating of the DM central region:** DM density profile of Fornax at different times with its corresponding core radius (marked by arrows). We represent only cored profiles due to the heating by GCs with a DM minihalo in the early accretion scenario. Initially, the Fornax DM halo assumes a NFW profile. We consider DM particles from both Fornax halo and GCs to determine the DM density profile of Fornax. The fitting function described by Equation (4.12) reproduces the simulated density structures and captured the rapid transition from the cusp to the core. We set Poissonian errors for fitting weights. The DM distribution of Fornax halo is divided in bins of groups composed of $N_g = 1024$ particles.

where ρ_c is the core constant density and $W(r)$ is defined as

$$2W(r) = 1 - \operatorname{erf}\left(\frac{r - r_c}{2\delta}\right), \quad (4.13)$$

where r_c is the core radius and δ is a parameter to control the sharpness of the transition from the cusp to the core and the converse. It reproduces the simulated density structures and captured the rapid transition from the cusp to the core (see Figure. 4.18). We set Poissonian errors for fitting weights. The DM distribution of Fornax halo is divided in bins of groups composed of $N_g = 1024$ particles. The smallest core size in the simulations is of the order of 10 pc, which corresponds to our spatial resolution. Thus, we assume that a cusp-to-core transition occurred when the core size r_c becomes greater than our spatial resolution. As the value of the core size depends entirely on the fitted DM profile, we did not use this radius as a constraint on the DM halo core size of Fornax. Figure. 4.19 describes the evolution of the fitted core radius r_c of the Fornax halo over 12 Gyr due to heating by GCs with and without a DM minihalo. We consider the core radii r_c to determine whether a transition appears in our simulation. Non-zero core sizes r_c means that a cusp-to-core transition occurred for the Fornax DM halo. The absence of cores ($r_c = 0$) means that DM halo is cuspy and is still described by a NFW profile. For stellar GCs, the absence of core shows that these $10^6 M_\odot$ orbiting objects can't generate DM cores. The energy transfer is not sufficient to perturb the DM distribution at the centre of the galaxy due to their low mass. However, once they are spiralling into the centre of the galaxy, they induce a cusp-to-core transition. Then, we observe a DM core of about 100-150 pc for the Fornax halo. Contrary to stellar GCs, dynamical heating of the DM field from DM minihalo crossings drives core formation. These core sizes are between 150 and 400 pc, and depend on the frequency of the crossings. Besides, between crossings, the halo can

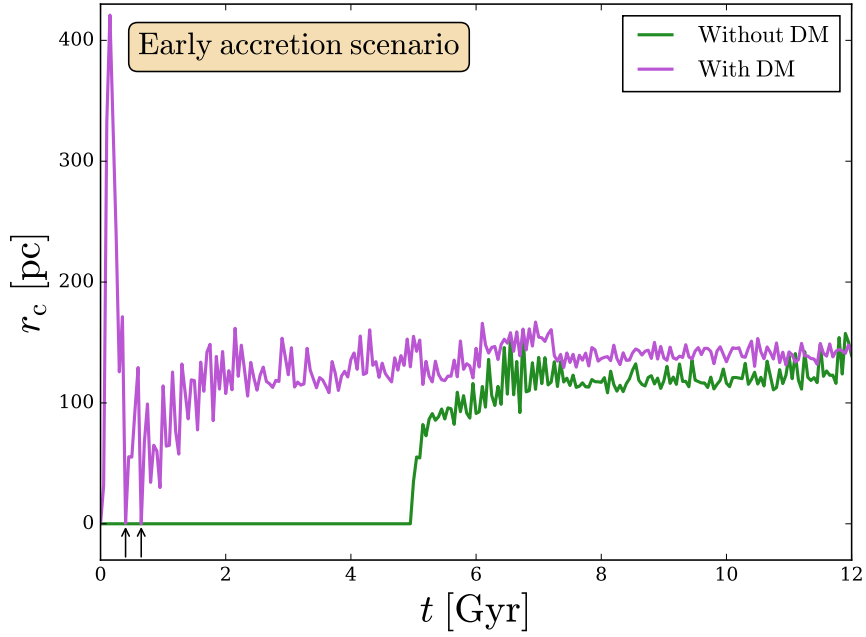


Figure 4.19 – **Fornax DM core in the early accretion scenario:** Fitted core radius r_c of the DM cored halo (see Equation (4.12)) induced by crossings of GCs with (in purple) and without (in green) a DM minihalo as a function of time. $r_c \neq 0$ ($r_c = 0$) means that there is a (no) cusp-to-core transition for the Fornax DM halo. The absence of a core within the first 5 Gyr states that stellar GCs in orbit cannot generate DM cores due to their low mass impact. However, once they are spiralling into the centre of the galaxy, they induce a cusp-to-core transition. Contrary to stellar GCs, dynamical heating of the DM field from DM minihalo crossings drives the core formation. The core sizes depend on the frequency of the crossings. Besides, between crossings, the halo can re-form the cuspy halo owing to the new orbits of DM particles initially at the Fornax centre as they gained energy from the GCs. We observed these reverse transitions (marked by black arrows) of the Fornax DM halo.

re-form the cuspy halo owing to the new orbits of DM particles initially at the Fornax centre as they gained energy from the GCs. Figure 4.19 shows cusp-to-core transitions and the reverse transitions (marked by black arrows) of the Fornax DM halo. In this early accretion scenario, GCs with and without a DM minihalo cannot explain both DM core formation and timing problem. Despite the core formation in cold DM, they are ruled out by the GC infall and consequent NSC formation.

Recent accretion

In this section, we assume that GCs with and without a DM minihalo were accreted 4 Gyr ago by Fornax. Figure 4.20 describes the orbital decay of GCs with and without a DM minihalo over 4 Gyr in this scenario. Initially, they have the same most prevalent positions and velocities at $z=0.36$ from Illustris TNG-100 cosmological simulation (see objects O_i in Table 7.1). According to the initial orbital radii, stellar GCs (*upper panel*) stay in orbit beyond 2 kpc from the centre, whereas GCs with a DM minihalo (*lower panel*) are accreted by Fornax and are falling towards the Fornax centre. But, as all the 5 GCs with a DM minihalo are still orbiting before 3 Gyr, they cannot form a NSC in accordance with observations. Table 7.2 depicts orbital radii and masses of GCs embedded in a DM minihalo at 3 Gyr. For each observed Fornax GC, we propose a GC with a DM minihalo as a candidate in order to reproduce the spatial distribution of observed GCs if GCs were accreted less than 3 Gyr ago. Their orbital radii are higher than the projected distances D_{obs} , which are the minimum distances between observed GCs and the Fornax centre. Concerning the GC observed

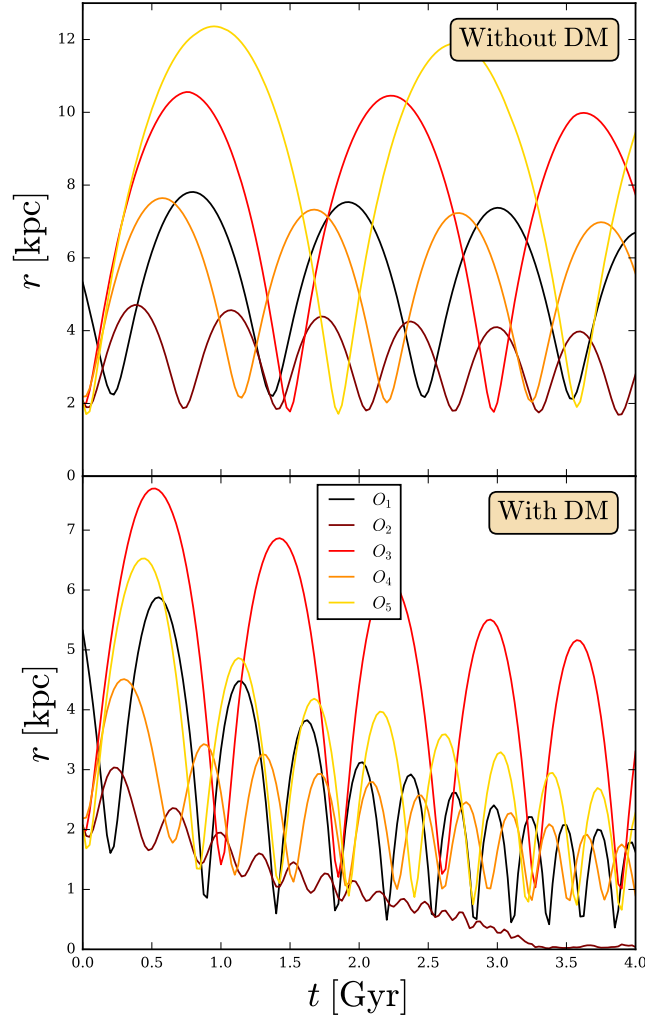


Figure 4.20 – **DM minihalos stay in orbit:** Orbital decay of the 5 GCs without (*upper panel*) and with (*lower panel*) a $2 \times 10^7 M_{\odot}$ DM minihalo over 4 Gyr. These radii correspond to the distances between the mass centre of each GC and Fornax. Initially, $10^6 M_{\odot}$ GCs with and without DM minihalo have the same most prevalent positions and velocities at $z = 0.36$ from Illustris TNG-100 cosmological simulation (see objects O_i in Table 7.1). Our initial conditions entail an accretion process by Fornax galaxy only for GCs with a DM minihalo. Stellar GCs experienced stable eccentric orbits beyond 2 kpc.

mass, we found a higher mass from the simulations for each GC with a DM minihalo. As the GC dynamical evolution is entirely determined by the DM minihalo, we could easily set lower stellar mass limits to the initial GCs in order to reproduce the observed masses. Reducing the stellar mass of GCs could contribute to their survival. Similarly to GCs with a DM minihalo, the spatial distribution of stellar GCs over 4 Gyr is also compatible with observations of Fornax GCs. Thus, both GC types can resolve the Fornax timing problem in this recent accretion scenario.

Nevertheless, Figure 4.21 highlights that there is no cusp-to-core transition for stellar GCs in this scenario. As they stay on orbit beyond 2 kpc, they cannot transfer energy to DM particles at the centre of the galaxy. Moreover, we established previously that their crossings cannot perturb the DM halo due to their low mass compared to DM minihalos. With stellar GCs, the DM profile does not change over time as shown by [Boldrini et al. \[2019\]](#). Concerning GCs with a DM minihalos, we observe a cusp-to-core transition induced by their crossings. More precisely, there are forward and reverse transitions from the cusp to the core. However, most of the time, Fornax is expected to

Object	$M_{\text{obs}}^{(a)}$ [$10^5 M_{\odot}$]	$D_{\text{obs}}^{(b)}$ [kpc]		r [kpc]	M [$10^5 M_{\odot}$]
GC1	0.42 ± 0.10	1.6	O_3	5.38	9.98
GC2	1.54 ± 0.28	1.05	O_5	3.26	9.91
GC3	4.98 ± 0.84	0.43	O_1	2.33	8.57
GC4	0.76 ± 0.15	0.24	O_2	0.28	6.83
GC5	1.86 ± 0.24	1.43	O_4	1.64	9.67

Table 4.4 – **Comparison with GC observations:** The final radii and masses of GCs embedded in DM minihalos at 3 Gyr. We found GC candidates O_i compatible with the observed projected distances D_{obs} . However, we found higher masses for simulated GCs than for those observed. We note that we could set lower stellar mass to the initial GCs in order to reproduce the observed masses. DM minihalo of GCs solve the Fornax timing problem if GCs were accreted less than 3 Gyr ago. References: (a) [de Boer & Fraser \[2016\]](#), (b) [Mackey & Gilmore \[2003\]](#).

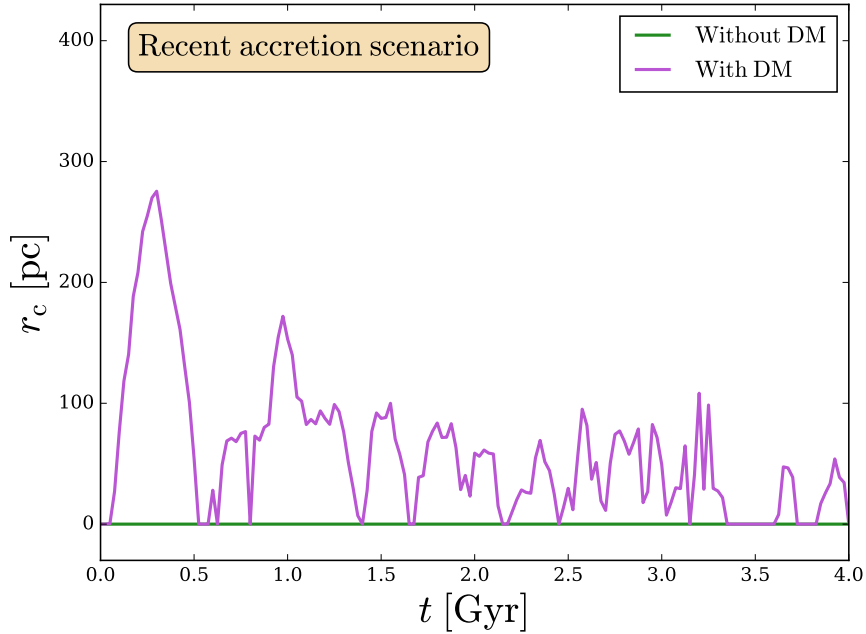


Figure 4.21 – **Fornax DM core in the recent accretion scenario:** Fitted core radius r_c of the DM cored halo induced by crossings of GCs with (in purple) and without (in green) a DM minihalo as a function of time. $r_c \neq 0$ ($r_c = 0$) means that there is a (no) cusp-to-core transition for the Fornax DM halo. In this scenario, the complete absence of core confirms again that stellar GCs on orbit cannot generate DM cores due their low mass impact. Contrary to stellar GCs, dynamical heating of the DM field from DM minihalo crossings entails the core formation.

have a core due to DM minihalo crossings according to our simulation results. In addition, in the recent accretion scenario, we show that only GCs with a DM minihalo can explain both the DM core formation and timing problem in Fornax.

As the recent accretion scenario with GCs with a DM minihalo is compatible with Fornax observations, especially for the DM core formation and GC spatial distribution, we are interested by the mass loss of DM minihalos. Figure. 4.22 illustrates the mass of remnant DM minihalos centered on the stellar component of the five GCs O_i between 2 and 3 Gyr. It is shown that all the DM

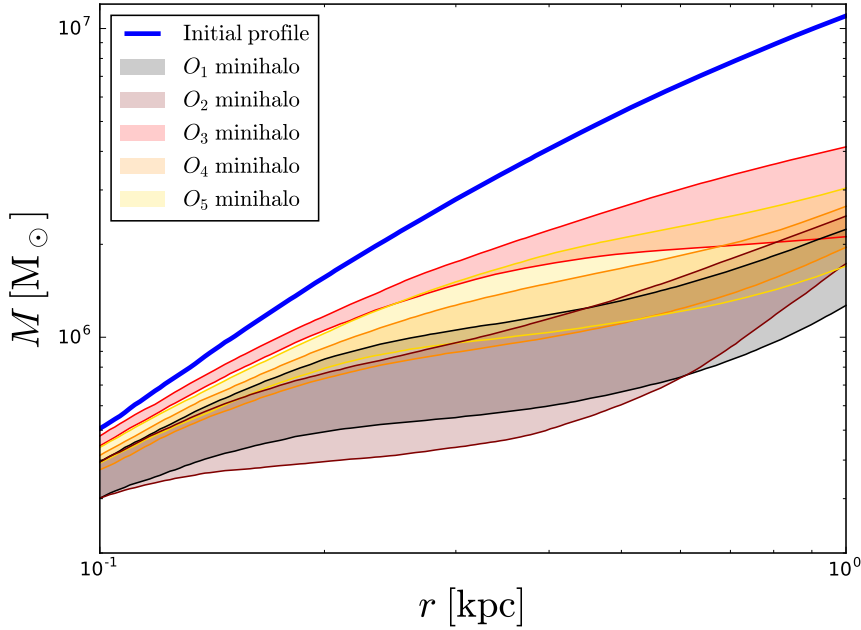


Figure 4.22 – **DM minihalo remnants:** Masses of remnant DM minihalos centered on the stellar component of O_i GCs between 2 and 3 Gyr. The blue dashed line represents the initial distribution of $2 \times 10^7 M_\odot$ minihalo centered on its stellar component. It is shown that all the DM minihalos have been tidally stripped by the tidal field of Fornax. We have found that GCs are embedded in DM minihalos less massive than $10^7 M_\odot$ inside the central 500 pc after 2-3 Gyr, which is in agreement with the observed prediction on a MW GC, NGC 2419 [Baumgardt et al., 2009; Ibata et al., 2013]

minihalos have been tidally stripped by the tidal field of Fornax. Even if GCs are not proven to have a significant amount of DM, this does not preclude them from having been formed originally inside a DM minihalo. Indeed, we showed that our GCs lost a large fraction of their DM minihalos. We have found that GCs are embedded in DM minihalos less massive than $10^7 M_\odot$ inside the central 500 pc after 2-3 Gyr, which is also in agreement with the observed prediction on a MW GC, NGC 2419, based on the observed velocity dispersion [Baumgardt et al., 2009]. We found also good agreement with the prediction of Ibata et al. [2013], who established that the virial mass of the minihalo of NGC2419 cannot exceed $\sim 4 \times 10^6 M_\odot$.

Enhancement of the core formation

For both GCs with and without a DM minihalo, we noticed previously that spiralling GCs at the centre of the galaxy enhance the core formation (see in Figure. 4.15 and 4.19). However, the infall of GCs can entail the formation of a NSC at the centre of the galaxy. For NSC formation, GCs at the centre have to be completely tidally stripped. Thus, the GC tidal stripping needs to be accelerated as in the case of the DM minihalo (see in Figure. 4.16). Adding an infalling GC with a DM minihalo is also motivated by the fact that Fornax has a large quantity of metal-poor stars, which could correspond to relics of destroyed GCs with DM minihalos. In addition, according to its stellar kinematics, Fornax is expected to have a large core [Amorisco & Evans, 2011; Kowalczyk et al., 2019; Pascale et al., 2018; Read et al., 2019; Walker & Peñarrubia, 2011]. Adding a falling GC with a DM minihalo, which is going to be completely disrupted, could contribute to the formation of a larger DM core. We test this hypothesis by running a simulation with the five O_i GCs with a DM minihalo and one additional GC with a DM minihalo. We want to improve the degree of core

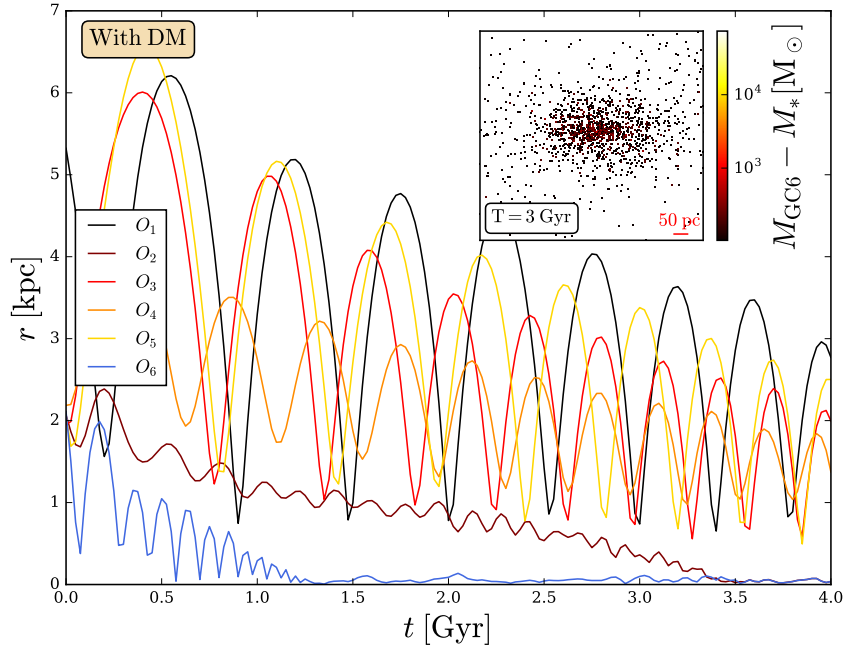


Figure 4.23 – **Infall without forming a NSC:** Orbital decay of the 6 GCs with a $2 \times 10^7 M_\odot$ DM minihalo over 4 Gyr. These radii correspond to the distances between mass centre of each GC and Fornax. The first five GCs have the same initial conditions as in Figure. 4.20. Stellar distribution of the mass difference between the O_6 GC with a DM minihalo and Fornax stellar component (*inset*) highlights that there is no NSC at the centre of the galaxy despite the rapid infall of this additional GC with a DM minihalo. Finally, we establish that Fornax could have more than five 5 GCs. The extra GCs have fallen to the Fornax centre and were destroyed, which is compatible with the large quantity of the metal-poor stars found in Fornax. The absence of NSC on this timescale is only possible because DM minihalos accelerate the tidal stripping.

formation in the recent accretion scenario. Figure. 4.23 describes the orbital decay of the 6 GCs with a $2 \times 10^7 M_\odot$ DM minihalo over 4 Gyr. The first five GCs have the same initial conditions as in Figure. 4.20. We notice that O_6 GC with a DM minihalo spirals to the centre after 1 Gyr. Stellar distribution of the mass difference between the O_6 GC with a DM minihalo and Fornax stellar component (*upper subplot*) highlights that there is no NSC at the centre of the galaxy despite the rapid infall of this additional GC with a DM minihalo. As expected, O_6 GC is completely destroyed after 3 Gyr (see inset in Figure. 4.23). Finally, we establish that Fornax could have more than five 5 GCs. More than one extra GC could have fallen to the Fornax centre a long time ago and could have been destroyed, which is compatible with the large quantity of the metal-poor stars found in Fornax. The absence of NSC on our timescale is only possible because DM minihalos accelerate the tidal stripping. Figure. 4.24 compares the fitted core radius as a function of time for the five O_i GCs with a DM minihalo (in purple) and these five GCs plus one additional GC with a DM minihalo (in blue). We show that the rapid infall of O_6 GC with a DM minihalo enhances the core formation due to crossings of the five GCs with a DM minihalo. Thus, if Fornax had more than five 5 GCs, they could contribute to form a larger core.

As the value of the core size r_c depends entirely on the fitted DM profile, we can't use this radius as a constraint on the DM halo core size of Fornax. However, the DM density at 150 pc of Fornax was estimated to be around $10^8 M_\odot \text{ kpc}^{-3}$ for a virial mass of $\sim 2 \times 10^{10} M_\odot$ by using stellar kinematics [Read et al., 2019]. Assuming a virial mass of $10^9 M_\odot$, we found a similar density at this specific radius in our simulation with 6 GCs embedded in a DM minihalo. As core formation is entirely driven

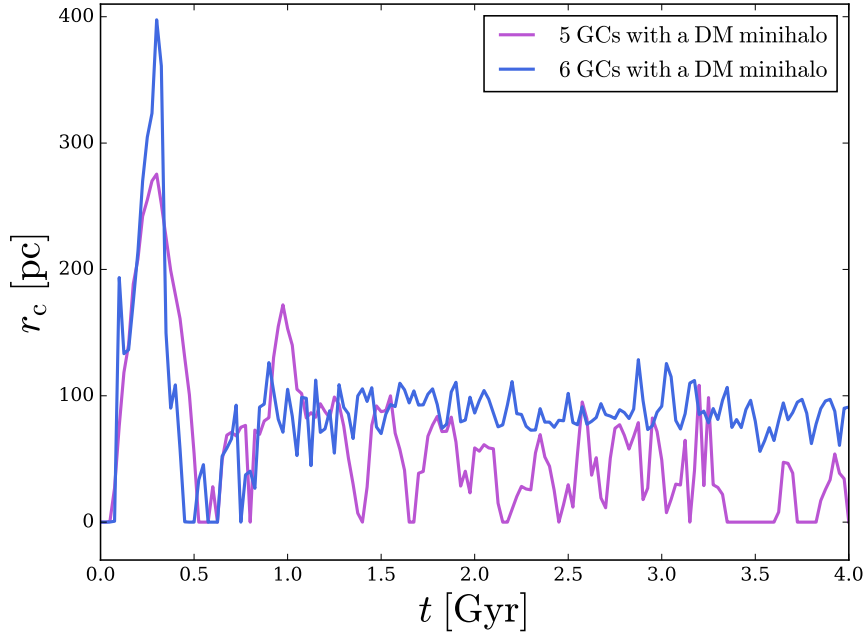


Figure 4.24 – **Enhancement of the core formation:** Fitted core radius r_c of the DM cored halo induced by crossings of the five O_i GCs with a DM minihalo (in purple) plus one additional GC with a DM minihalo (in blue) as a function of time. $r_c \neq 0$ ($r_c = 0$) means that there is a (no) cusp-to-core transition for the Fornax DM halo. In this scenario, the rapid infall of O_6 GC with a DM minihalo enhances the core formation due to crossings of the five GCs with DM minihalos.

by energy transfers via dynamical friction, it will be harder to induce a core with this density at 150 pc for a $10^{10} M_\odot$ halo with only five GCs, because the center of the higher mass halo is less dense. Thus, dynamical friction will be less efficient in these halos. Nevertheless, DM substructures will have the same behaviour as our GCs with a DM minihalo. As the GC dynamical evolution is entirely determined by the DM minihalos, these substructures could have also interacted with Fornax and induced a cusp-to-core transition. In addition to GCs, subhalos could be responsible for the large core formation in Fornax. The dynamics of DM substructures in dwarf galaxies is investigated in Boldrini et al. (in prep.).

4.3.4 Appendix

In this section, we assess the impact of a numerical parameter that controls the accuracy of our simulations; the softening length ϵ . To test how the softening length impacts on the stellar density profile for isolated GCs with and without a DM minihalo, and the orbital radius and the mass loss of GCs with a DM minihalo and the Fornax DM density profile, we ran simulations with three different softening lengths, $\epsilon = 2, 1$ and 0.5 pc, in order to ensure that our simulations do not suffer from numerical noise. We apply these tests to the simulation over 12 Gyr in the early accretion scenario for GCs with a DM minihalo.

As our softening length is similar to the stellar core radius of the GCs, we studied the impact of the softening on the evolution of the stellar density profile over time in Figure. 4.25 for an isolated GC with and without a DM minihalo. Initially, GC stars assume a King profile with a King radius $r_k = 1$ pc. The stellar distribution is divided in bins of groups composed of $N_g = 256$ particles. Figure. 4.25 shows that our mass resolution does not allow us to resolve the 1 pc core radius of GCs.

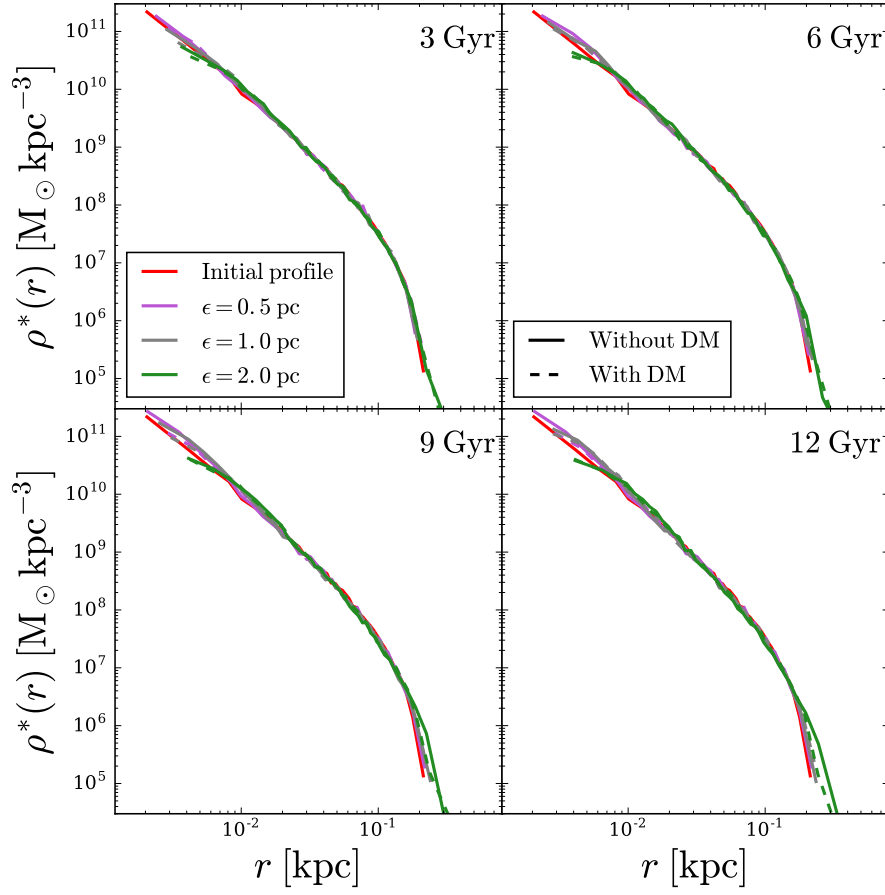


Figure 4.25 – **Impact of softening on GC stellar density profiles:** Stellar density profile of an isolated GC with and without a DM minihalo for different times and three different softening lengths. Initially, GC stars assume a King profile with a King radius $r_k = 1$ pc. The stellar distribution is divided in bins of groups composed of $N_g = 216$ particles. Our mass resolution does not allow us to resolve the 1 pc core radius of GCs. We noticed that the dynamics of GCs is subject to numerical effects for $\epsilon = 2$ pc. Our convergence test states that the stellar density profiles for $\epsilon = 0.5$ and 1 pc are nearly identical.

We noticed that the dynamics of GCs is subject to numerical effects for $\epsilon = 2$ pc. The convergence of the stellar density profiles confirm that it is sufficient to consider a softening length of 1 pc, which is similar to the King radius for our study.

The evolution of the orbital radius of the five clusters in an accretion process with eccentric orbits (see objects E_i in Table 7.1) is shown in Figure 7.7 for three different softening lengths. It can be seen that the orbital decays of GCs are very similar for all the softening lengths. The evolution of the mass loss for the GC stellar component embedded in a DM minihalo is also providing in Figure 4.27 for different softening lengths. Our simulations are well converged for $\epsilon = 0.5$ and 1 pc. However, for $\epsilon = 2$ pc, numerical noise causes enhanced disruption of the clusters as in Figure 4.25.

In order to determine how the DM density profile depends on the softening length, Figure 4.28 presents the evolution of fitted DM core radius over time for three different softening lengths. We observe a deviation of the core radius for a softening of 2 pc compared to the other softening lengths. For 1 and 0.5 pc, we deduce that the softening length do not affect the DM core radius. As our simulations with a numerical parameter of 1 and 0.5 pc are well converged over 12 Gyr, we chose $\epsilon = 1$ pc as the softening length for all our simulations and ensured that our simulations do not suffer from numerical noise.

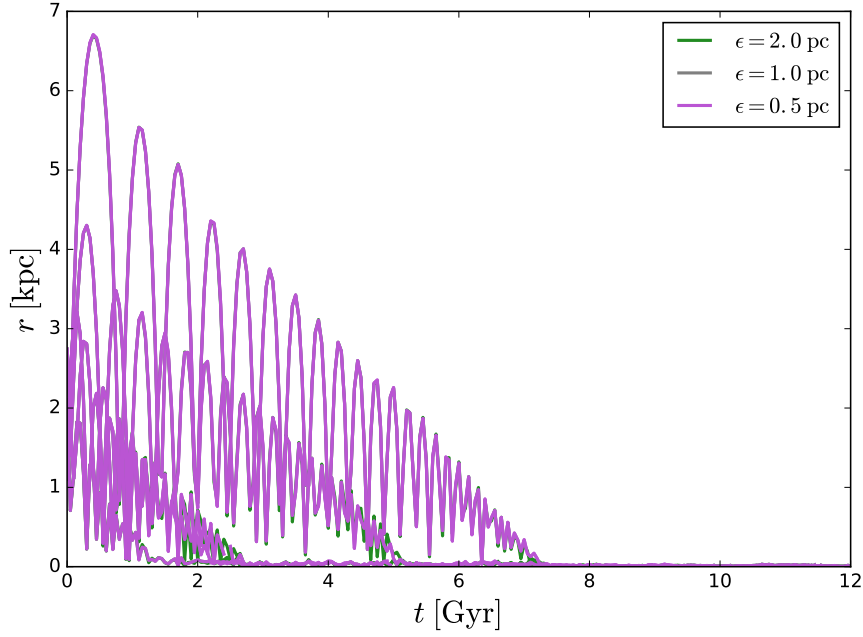


Figure 4.26 – **Impact of softening on orbital decay:** Orbital radius of the five GCs with a DM minihalo in an early accretion process with eccentric orbits (see objects E_i in Table 7.1) as a function of time for three different softening lengths. The orbital decays of GCs are nearly identical for all the softening lengths. As the stellar density profiles for $\epsilon = 0.5$ and 1 pc are very similar (see Figure. 4.25), the orbital radius behaves the same for these softenings.

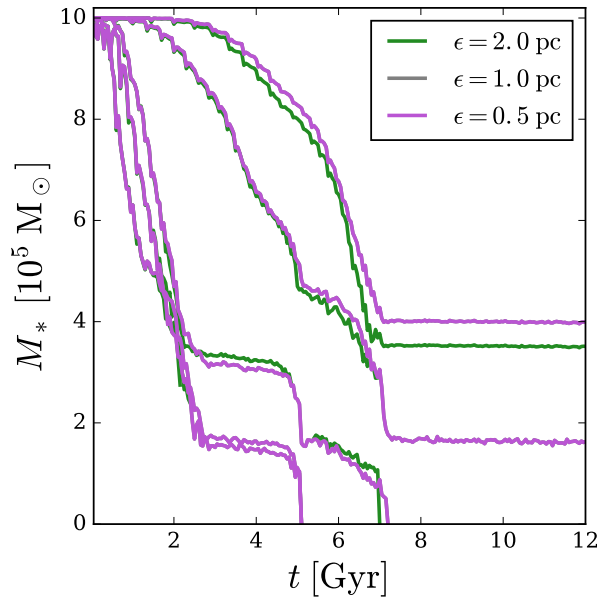


Figure 4.27 – **Impact of softening on mass loss:** Evolution of the mass loss of the stellar component embedded in a DM minihalo over 12 Gyr for three different softening lengths. Our simulations are well converged for $\epsilon = 0.5$ and 1 pc. As the stellar density profiles for $\epsilon = 0.5$ and 1 pc are nearly identical (see Figure. 4.25), the mass loss behaves the same for these softenings.

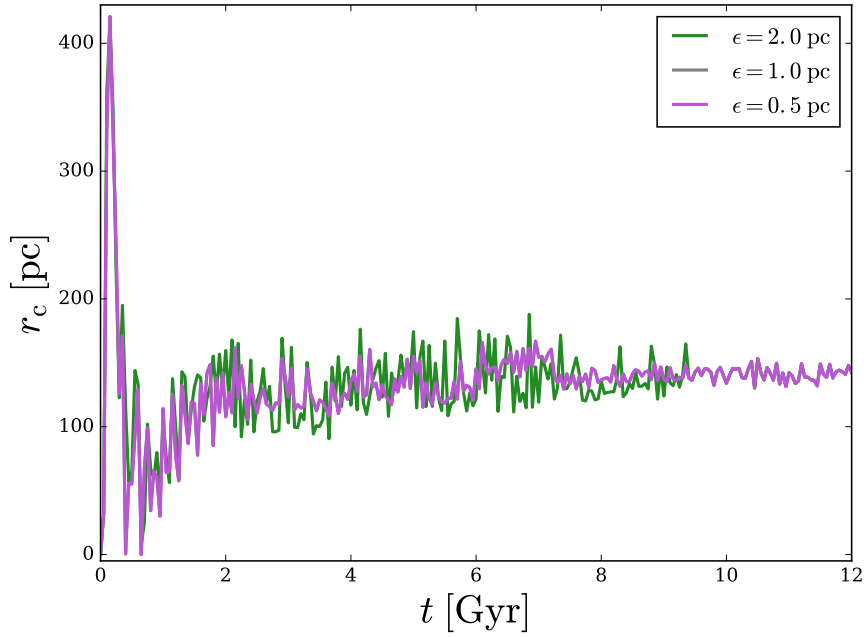


Figure 4.28 – **Impact of softening on DM halo core size:** Fitted DM core radius as a function of time for three different softening lengths. The core formation is due to crossings of GCs with a DM minihalo in the early accretion scenario. We observe a deviation of the core radius for a softening of 2 pc compared to the other softening lengths. For 1 and 0.5 pc, we noticed that the softening length does not affect the DM core radius. As the stellar density profiles for $\epsilon = 0.5$ and 1 pc are nearly identical (see Figure. 4.25), the DM halo core size behaves the same for these softenings.

4.4 References

- Allen C., Santillan A., 1991, , [22](#), [255](#) [58](#), [68](#), [73](#)
- Amorisco N. C., Evans N. W., 2011, [MNRAS](#), [411](#), [2118](#) [81](#)
- Amorisco N. C., Agnello A., Evans N. W., 2013, [MNRAS](#), [429](#), [L89](#) [56](#), [57](#), [63](#)
- Arca-Sedda M., Capuzzo-Dolcetta R., 2016, [MNRAS](#), [461](#), [4335](#) [54](#)
- Arca-Sedda M., Capuzzo-Dolcetta R., 2017, [MNRAS](#), [464](#), [3060](#) [54](#)
- Barkana R., Loeb A., 1999, [ApJ](#), [523](#), [54](#) [70](#)
- Baumgardt H., Côté P., Hilker M., Rejkuba M., Mieske S., Djorgovski S. G., Stetson P., 2009, [MNRAS](#), [396](#), [2051](#) [81](#)
- Boldrini P., Mohayaee R., Silk J., 2019, [MNRAS](#), [485](#), [2546](#) [69](#), [70](#), [79](#)
- Bromm V., Clarke C. J., 2002, [ApJ](#), [566](#), [L1](#) [70](#)
- Burkert A., 1995, [ApJ](#), [447](#), [L25](#) [56](#)
- Cen R., 2001, [ApJ](#), [560](#), [592](#) [70](#)
- Chandrasekhar S., 1943, [ApJ](#), [97](#), [255](#) [54](#)
- Cole D. R., Dehnen W., Read J. I., Wilkinson M. I., 2012, [MNRAS](#), [426](#), [601](#) [54](#), [55](#)
- Da Costa G. S., Armandroff T. E., 1995, [AJ](#), [109](#), [2533](#) [54](#)
- Errani R., Peñarrubia J., Walker M. G., 2018, [MNRAS](#), [481](#), [5073](#) [56](#)
- Fall S. M., Zhang Q., 2001, [ApJ](#), [561](#), [751](#) [58](#)
- Forbes D. A., et al., 2018, [Proceedings of the Royal Society of London Series A](#), [474](#), [20170616](#) [69](#)
- Gaia Collaboration et al., 2018, [A&A](#), [616](#), [A12](#) [57](#), [70](#), [71](#), [73](#)
- GoerdT T., Moore B., Read J. I., Stadel J., Zemp M., 2006, [MNRAS](#), [368](#), [1073](#) [54](#)
- Ibata R., Nipoti C., Sollima A., Bellazzini M., Chapman S. C., Dalessandro E., 2013, [MNRAS](#), [428](#), [3648](#) [81](#)
- Irrgang A., Wilcox B., Tucker E., Schiefelbein L., 2013, [A&A](#), [549](#), [A137](#) [58](#), [68](#), [73](#)
- Jordán A., et al., 2007, [ApJS](#), [171](#), [101](#) [58](#)
- King I., 1962, [AJ](#), [67](#), [471](#) [57](#), [72](#)
- Kowalczyk K., del Pino A., Łokas E. L., Valluri M., 2019, [MNRAS](#), [482](#), [5241](#) [81](#)
- Kravtsov A. V., Gnedin O. Y., 2005, [ApJ](#), [623](#), [650](#) [69](#)
- Kruijssen J. M. D., 2015, [MNRAS](#), [454](#), [1658](#) [69](#)
- Küpper A. H. W., Kroupa P., Baumgardt H., Heggie D. C., 2010, [MNRAS](#), [401](#), [105](#) [73](#)

- Kuzma P. B., Da Costa G. S., Mackey A. D., Roderick T. A., 2016, *MNRAS*, **461**, 3639 70
- Law D. R., Majewski S. R., 2010, *ApJ*, **718**, 1128 70
- Mackey A. D., Gilmore G. F., 2003, *MNRAS*, **340**, 175 56, 72, 80
- Mashchenko S., Sills A., 2005, *ApJ*, **619**, 243 70
- Massari D., Posti L., Helmi A., Fiorentino G., Tolstoy E., 2017, *A&A*, **598**, L9 70
- Miki Y., Umemura M., 2017a, arXiv e-prints, p. [arXiv:1712.08760](https://arxiv.org/abs/1712.08760) 73
- Miki Y., Umemura M., 2017b, *New Astron.*, **52**, 65 73
- Miyamoto M., Nagai R., 1975, *PASJ*, **27**, 533 58, 68, 73
- Navarro J. F., Frenk C. S., White S. D. M., 1996, *ApJ*, **462**, 563 56, 71
- Navarro J. F., Frenk C. S., White S. D. M., 1997, *ApJ*, **490**, 493 58, 68, 73
- Oh K. S., Lin D. N. C., Richer H. B., 2000, *ApJ*, **531**, 727 54
- Olszewski E. W., Saha A., Knezek P., Subramaniam A., de Boer T., Seitzer P., 2009, *AJ*, **138**, 1570 70
- Pascale R., Posti L., Nipoti C., Binney J., 2018, *MNRAS*, **480**, 927 81
- Peñarrubia J., Varri A. L., Breen P. G., Ferguson A. M. N., Sánchez-Janssen R., 2017, *MNRAS*, **471**, L31 70
- Peebles P. J. E., 1984, *ApJ*, **277**, 470 70
- Peebles P. J. E., Dicke R. H., 1968, *ApJ*, **154**, 891 69
- Pillepich A., et al., 2018, *MNRAS*, **473**, 4077 70, 72
- Plummer H. C., 1911, *MNRAS*, **71**, 460 56, 58, 68, 71, 73
- Prada F., Klypin A. A., Cuesta A. J., Betancort-Rijo J. E., Primack J., 2012, *MNRAS*, **423**, 3018 71, 72
- Read J. I., Wilkinson M. I., Evans N. W., Gilmore G., Kleya J. T., 2006a, *MNRAS*, **366**, 429 58
- Read J. I., Goerdt T., Moore B., Pontzen A. P., Stadel J., Lake G., 2006b, *MNRAS*, **373**, 1451 54
- Read J. I., Walker M. G., Steger P., 2019, *MNRAS*, **484**, 1401 81, 82
- Revaz Y., 2013, pNbody: A python parallelized N-body reduction toolbox (ascl:1302.004) 60, 73
- Ricotti M., Gnedin N. Y., Shull J. M., 2002, *ApJ*, **575**, 49 70
- Ricotti M., Parry O. H., Gnedin N. Y., 2016, *ApJ*, **831**, 204 70
- Sadoun R., Mohayaee R., Colin J., 2014, *MNRAS*, **442**, 160 57
- Salucci P., Burkert A., 2000, *ApJ*, **537**, L9 56

- Sánchez-Salcedo F. J., Reyes-Iturbide J., Hernandez X., 2006, *MNRAS*, 370, 1829 54
- Sbordone L., et al., 2015, *A&A*, 579, A104 54
- Smith E. O., Neill J. D., Mighell K. J., Rich R. M., 1996, *AJ*, 111, 1596 56
- Sollima A., et al., 2016, *MNRAS*, 462, 1937 70
- Springel V., 2005, *MNRAS*, 364, 1105 59
- Strigari L. E., Bullock J. S., Kaplinghat M., Kravtsov A. V., Gnedin O. Y., Abazajian K., Klypin A. A., 2006, *ApJ*, 652, 306 63
- Strigari L. E., Frenk C. S., White S. D. M., 2010, *MNRAS*, 408, 2364 56, 71
- Tremaine S. D., 1976, *ApJ*, 203, 345 54
- Tremaine S. D., Ostriker J. P., Spitzer L. J., 1975, *ApJ*, 196, 407 54
- Walker M. G., Peñarrubia J., 2011, *ApJ*, 742, 20 56, 57, 63, 81
- Wang M. Y., et al., 2019, *ApJ*, 875, L13 54
- Webbink R. F., 1985, in Goodman J., Hut P., eds, IAU Symposium Vol. 113, Dynamics of Star Clusters. pp 541–577 56
- de Boer T. J. L., Fraser M., 2016, *A&A*, 590, A35 55, 56, 58, 59, 70, 71, 74, 75, 80

Chapter 5

Primordial black holes as dark matter candidates: a new solution to the cusp-core problem

The work presented in this chapter is based on Boldrini et al. (2020a) ([arXiv:1909.07395](#))

Contents

5.1	Primordial black holes as dark matter candidates	92
5.2	N-body modelling	92
5.3	Results	94
5.3.1	Evidences for core formation from gravitational heating by PBHs	94
5.3.2	Core size and core formation time	97
5.4	References	101

5.1 Primordial black holes as dark matter candidates

The nature of DM is one of the major unsolved problems in astrophysics. The most popular DM candidates include weakly interacting massive elementary particles (WIMPs), such as supersymmetric neutralinos or axions [Bergström, 2000; Bertone et al., 2005; Jungman et al., 1996]. An alternative proposal to explain the nature of DM is that DM could be made of macroscopic compact halo objects (MACHOs) such as primordial black holes (PBHs) (Hawking [1971]; Zel'dovich & Novikov [1967] and more recently Clesse & García-Bellido [2018]; Khlopov [2010]). These PBHs could naturally be produced in the early Universe via cosmic inflation, without the need to appeal to new physics beyond the standard model [Clesse & García-Bellido, 2015; Inomata et al., 2017]. There are currently three allowed mass windows around 4×10^{-17} , 2×10^{-14} and 25 - 100 M_{\odot} [Carr et al., 2017]. PBHs can constitute much or even all of the DM in these mass windows by considering only the most well-established bounds and neglecting those that depend on additional astrophysical assumptions. However, taking into account all of the astrophysical constraints means that the PBH+CDM fraction can still be as much as ~ 0.1 [Carr et al., 2017], and even larger in the lowest mass windows. Despite the fact that there is still no direct evidence for PBHs, the 25 - 100 M_{\odot} mass window is of special interest in view of the recent detection of black-hole mergers by LIGO [Abbott et al., 2016]. Moreover, the observed LIGO detection rates can be explained for a PBH mass fraction of order 0.001 to 0.01 [Kovetz, 2017; Sasaki et al., 2016]. In the future, the Laser Interferometer Space Antenna (LISA) could potentially also detect PBHs in this mass window [Amaro-Seoane et al., 2017].

In collisionless systems, stellar particle encounters lead to the relaxation of particles with similar kinetic energy and drive the system to energy equipartition. Systems comprised of particles of differing masses will also drive mass segregation processes (see Figure 5.1). As an example, massive stars or MACHOs fall towards the center of the potential well and their energy is transferred to the lighter stars, which move away from the center [Chandrasekhar, 1943; Spitzer, 1969]. Consequently, the system can expand and the density profile of the system can change due to this diffusion process [Brandt, 2016; Koushiappas & Loeb, 2017; Zhu et al., 2018].

Here, in the numerical experiments, we explore the consequences of assuming the DM in galaxies consists of both CDM and PBHs. We propose that PBHs, as DM candidates, can induce a cusp-to-core transition in PBH+CDM halos through gravitational heating from two principal mechanisms, dynamical friction by CDM particles on PBHs and two-body relaxation between PBH and CDM. We explore this transition using high performance N-body simulations on GPU to probe the PBH+CDM mass fraction f_m in $10^7 M_{\odot}$ dwarf galaxies. Our simulations allow a mass resolution of 1 M_{\odot} for DM particles. We work with PBHs in the 25-100 M_{\odot} mass window, which is consistent with the LIGO detections. Chapter 5 is organized as follows. Section 5.2 provides a description of N-body modelling and our numerical simulations. In Section 5.3, we show our simulation results and discuss the implications of PBH as a DM candidate.

5.2 N-body modelling

In this work, we consider that a fraction of the DM consists of 25-100 M_{\odot} PBHs. Then, a DM halo is composed of CDM particles and PBHs (DM = PBH + CDM) (see Figure 5.1). We define the PBH+CDM mass fraction as

$$f_m = \frac{M_{\text{PBH}}}{M_{\text{CDM}}}, \quad (5.1)$$

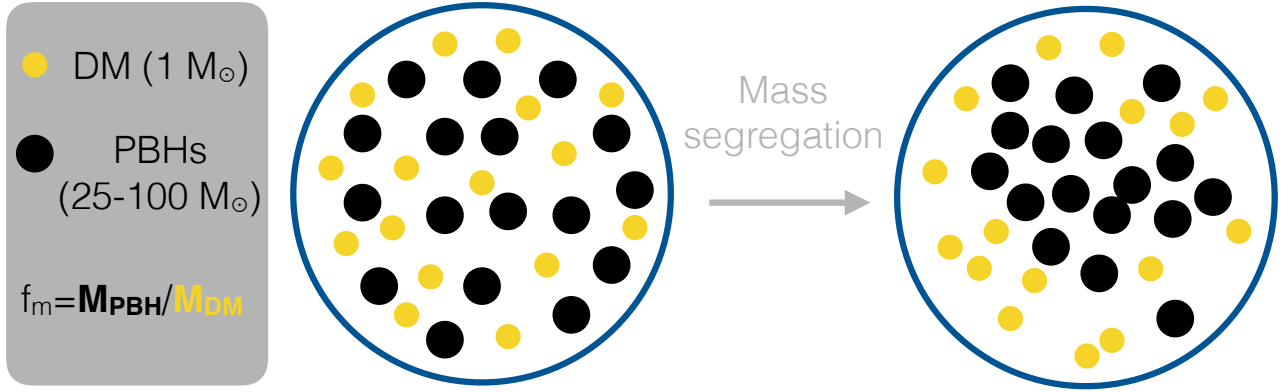


Figure 5.1 – **Mass segregation in a PBH+CDM halo:** Our halo is composed of DM and PBH particles with a total mass of $10^7 M_\odot$. A fraction of the DM consists of 25-100 M_\odot PBHs. Our simulations allow a mass resolution of $1 M_\odot$ for DM particles. This DM halo comprised of particles of differing masses will drive mass segregation processes.

where M_{PBH} and M_{CDM} are the total masses of PBHs and CDM particles. For our halo, we assume the NFW form [Navarro et al., 1996]:

$$\rho(r) = \rho_0 \left(\frac{r}{r_s} \right)^{-1} \left(1 + \frac{r}{r_s} \right)^{-2}, \quad (5.2)$$

with scale density ρ_0 and scale length r_s . The relaxation time is proportional to $N/\ln(N)$, where N is the number of particles. Assuming 100 M_\odot PBHs and $10^7 M_\odot$ halo, the particle relaxation will take between 1 and 12 Gyr depending on f_m considered between 1 and 0.01. In comparison, the relaxation time for 10^8 ($10^9 M_\odot$) halos are 10 (100) times longer than for $10^7 M_\odot$ and longer than the age of the Universe, which is why we focus here on a $10^7 M_\odot$ dwarf galaxy, starting at redshift $z=2$ in the simulations. Given the halo mass and redshift, the halo concentration c_{200} can be estimated from cosmological N-body simulations [Prada et al., 2012]. Our halo is composed of DM and PBH particles with a total mass of $10^7 M_\odot$ (see Figure 5.1).

To generate our NFW halos, we use the initial-condition generator, magi [Miki & Umemura, 2018]. We perform our simulations with the high performance collisionless N-body code, gothic [Miki & Umemura, 2017]. We evolve different PBH+CDM halos composed of 25, 50, 75 and 100 M_\odot PBHs over 11 Gyr by adopting the softening length of $\epsilon_0 = 1.331$ pc and the accuracy control parameter of 2^{-7} . All runs were made with CDM particles of $1 M_\odot$. We explored also PBH+CDM halos with different mass fractions $f_m = [0.01, 0.1, 0.5]$. In our simulations, we assume that the CDM and PBH components of PBH+CDM halos initially follow NFW profiles with the same concentration. We tested two different scale lengths for the profile of the PBH component: $r_s^{\text{PBH}} = r_s^{\text{CDM}}$ and $r_s^{\text{PBH}} = r_s^{\text{CDM}}/2$. The second corresponds to a scenario where the density of PBHs is enhanced in the central region. Indeed, we suppose that mass segregation of PBHs would occur, and this increases the density of PBHs at the centre. This scenario should also enhance the formation of cores due to dynamical heating of the CDM by PBHs. It will also accelerate the two-body relaxation.

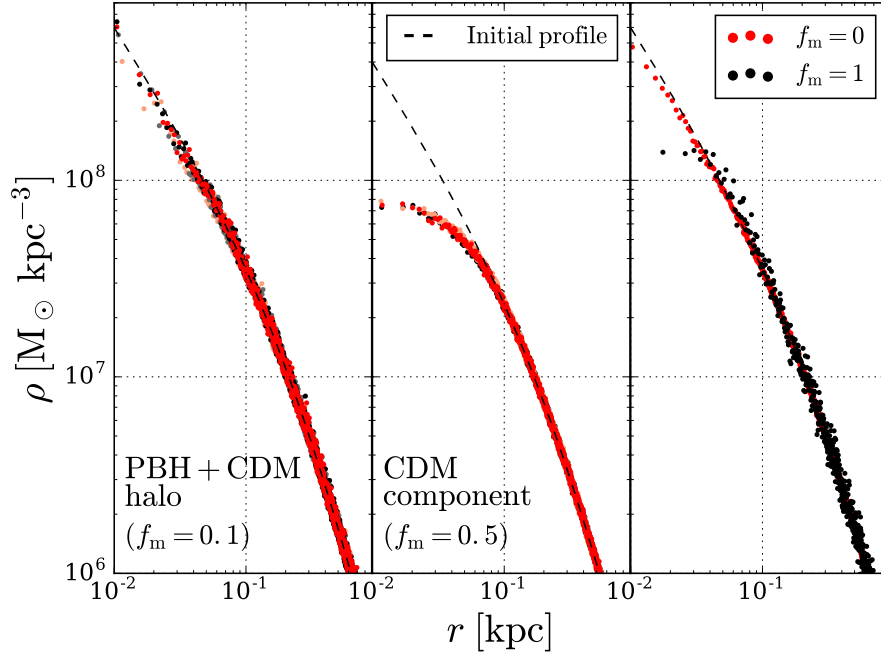


Figure 5.2 – **Tests of numerical accuracy:** Density profiles of a halo composed of $100 M_{\odot}$ PBHs to test the impact of the accuracy control parameter A (*left panel*) and softening length ϵ (*middle panel*) in simulations. We tested the impact of the accuracy control parameters of 2^{-6} (orange points), 2^{-7} (black points), 2^{-8} (grey points) and 2^{-9} (red points) for a halo with $f_m = 0.1$ and $r_s^{\text{PBH}} = r_s^{\text{CDM}}$. Density profiles of PBH+CDM halo (*left panel*) hold the initial distribution for all the different parameter values. The middle panel shows our softening convergence test for the density profiles of the CDM component of $f_m = 0.5$ halo with a softening length $\epsilon = \epsilon_0/2$, ϵ_0 and $2\epsilon_0$, where $\epsilon_0 = 1.331$ pc. Indeed, the core size of the CDM component is independent of the softening length. The right panel describes density profiles of a halo composed only with CDM particles ($f_m = 0$) and a halo composed only with PBH particles ($f_m = 1$). The CDM profiles at the beginning $T = 0$ Gyr (dashed line) and at the end of the simulation $T = 11$ Gyr (red points), which are nearly identical, show the stability of our halo. However, there is core formation for $f_m = 1$ due only to two-body relaxation between PBHs.

5.3 Results

5.3.1 Evidences for core formation from gravitational heating by PBHs

First, we assess the impact on the PBH+CDM halo density profiles in our simulations of the two numerical parameters, which are the accuracy control parameter and the softening length ϵ . We tested 2^{-6} , 2^{-7} , 2^{-8} and 2^{-9} for the accuracy control parameter in a PBH+CDM halo with $f_m = 0.1$ and $m_{\text{PBH}} = 100 M_{\odot}$. The left panel of the Figure 5.2 shows that PBH+CDM density profiles hold the initial distribution for all the different values of the accuracy control parameter. Additional accuracy tests confirmed also that the density profile hold the initial distribution for the considered f_m and m_{PBH} values. To test how the softening length impacts on the density profile of the CDM component and the CDM core size, we ran simulations with three different softening lengths $\epsilon = \epsilon_0/2$, ϵ_0 and $2\epsilon_0$ in order to ensure that our simulations do not suffer from numerical noise. We applied this test on a PBH+CDM halo with $f_m = 0.5$ and $m_{\text{PBH}} = 100 M_{\odot}$ expected to have core formation. The middle panel of Figure 5.2 reveals that softening length (or particle size) does not affect the density profile of CDM component and its core size. Thus, numerical artifacts are not responsible for core formation. We tested also the stability of our halo composed only with CDM particles ($f_m = 0$) over 11 Gyr. We compare our halo profiles at the beginning ($T = 0$ Gyr) and at

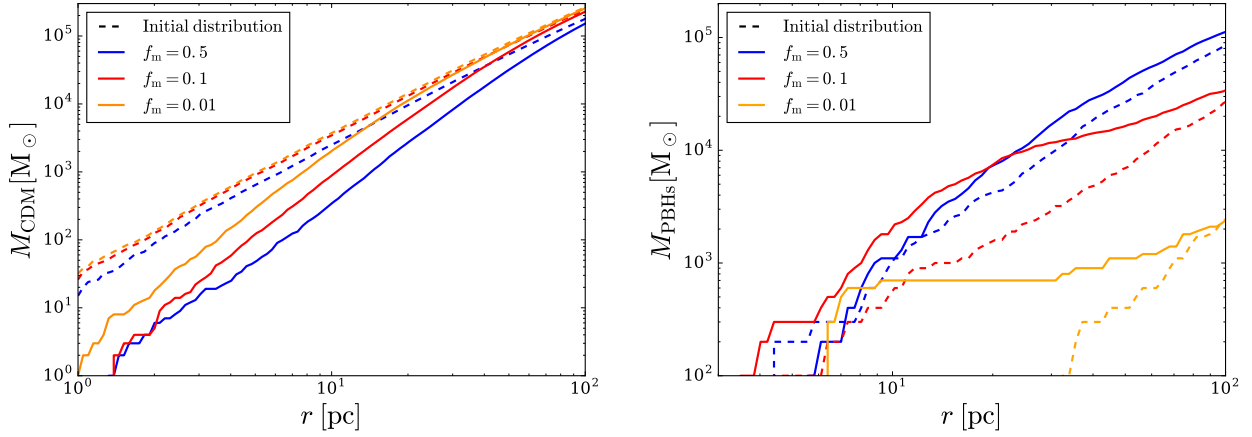


Figure 5.3 – **Auto-redistribution of CDM particles and PBHs:** Comparison between $T = 0$ Gyr (dashed line) and $T = 11$ Gyr (solid line) of the interior mass of the CDM component (*left panel*) and $100 M_{\odot}$ PBHs (*right panel*) as a function of radius for the three different mass fraction f_m and $r_s^{\text{PBH}} = r_s^{\text{CDM}}$. The profiles show that CDM particles moved to outer regions and PBHs felt to the halo center. This phenomenon is due to dynamical friction by the CDM environment on PBHs and to a lesser extent by two-body relaxation between PBHs and CDM.

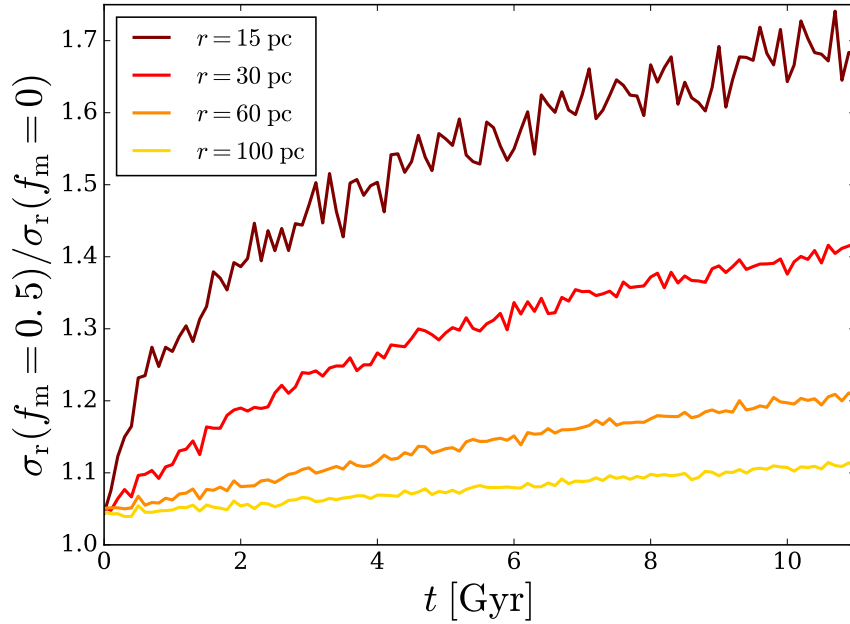


Figure 5.4 – **Heating of the CDM component:** Ratio between CDM radial velocity dispersion for $f_m = 0.5$ and $f_m = 0$ halos as a function of time at different radii. The PBH+CDM halo with $f_m = 0.5$ contains $100 M_{\odot}$ PBHs following an initial NFW profile with $r_s^{\text{PBH}} = r_s^{\text{CDM}}$. Over time, the velocity dispersion ratio increases, especially at the center, due to PBH heating processes, which are two-body relaxation and dynamical friction effect of PBHs. This leads to core formation.

the end ($T=11$ Gyr) of the simulation, which are nearly identical for all radii, on the right panel of Figure 5.2. We added the density profile of a halo composed only with PBHs ($f_m=1$), which highlights core formation due to two-body relaxation between PBHs.

As we show that numerical effects do not initiate core formation, we need to provide evidence

for the dynamical mechanism which will induce the cusp-to-core transition. Figure 5.3 compares the interior mass of the CDM component (*left panel*) and $100 M_{\odot}$ PBHs (*right panel*) as a function of radius for three different mass fractions f_m between $T = 0$ Gyr and $T = 11$ Gyr. Profiles in Figure 5.3 illustrate that contrary to the CDM particles, the number of PBHs increases in the central region. This results in the PBH infalling towards the central region. By falling in, PBHs will transfer energy to the CDM field via dynamical friction. This is the reason why CDM particles move to the outer regions as we see in the left panel of Figure 5.3. Another important dynamical effect is two-body relaxation between PBHs, which enhances the CDM particle migration. The CDM velocity dispersion is sensitive to these energy exchanges between CDM particles and PBHs. Figure 5.4 compared the CDM radial velocity dispersion for $f_m = 0.5$ and $f_m = 0$ halos as a function of time at different distances from the halo center. The PBH+CDM halo with $f_m = 0.5$ contains $100 M_{\odot}$ PBHs following an initial NFW profile with $r_s^{\text{PBH}} = r_s^{\text{CDM}}$. We highlight that the velocity dispersion ratio increases rapidly, especially in the central region over time, due to PBH heating processes, which are two-body relaxation and dynamical friction effect of PBHs. This leads to core formation. In addition, Figure 5.5 shows the evolution of the CDM density profiles and the CDM mass-weighted velocity distribution projected face-on through a 100 pc slice during a cusp-to-core transition for the CDM component in a PBH+CDM halo with $f_m = 0.01, 0.1$ and 0.5 by assuming $100 M_{\odot}$ PBHs and $r_s^{\text{PBH}} = r_s^{\text{CDM}}$. As the CDM velocity increases in the central region, the CDM density profile changes until core formation occurs. This figure demonstrates that core formation goes along with dynamical heating of CDM particles.

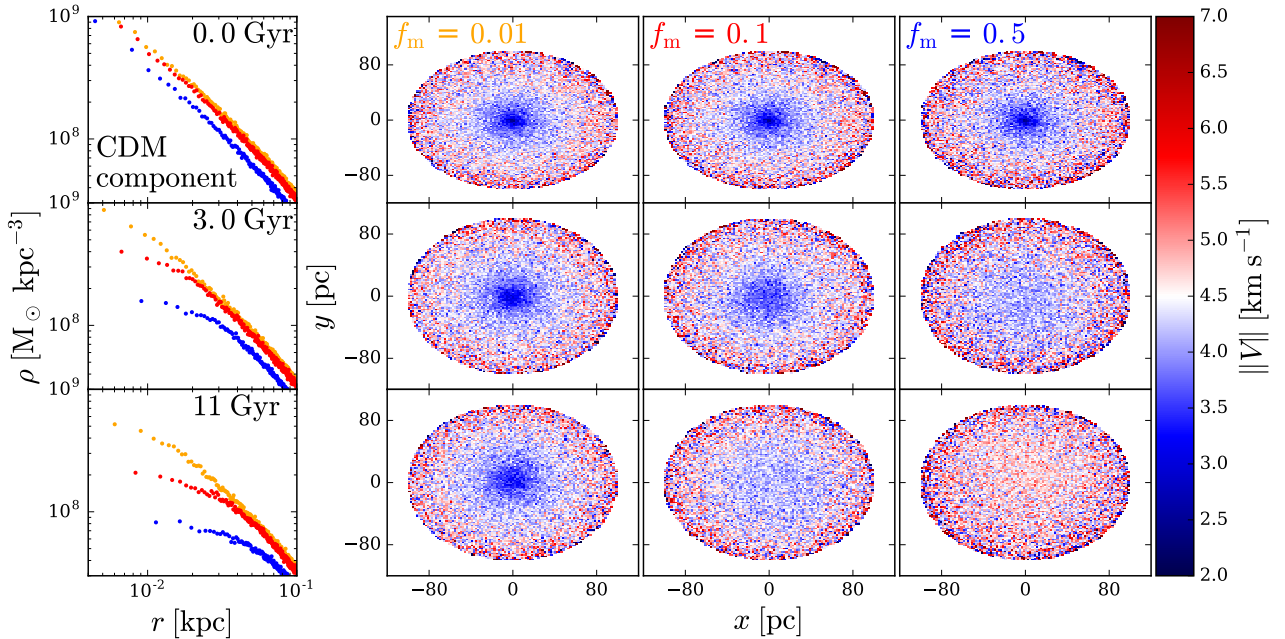


Figure 5.5 – **Cusp-to-core transition due to heating:** Density profiles of the CDM component (*left panels*) for $f_m = 0.01$ (yellow), 0.1 (red) and 0.5 (blue) with $100 M_{\odot}$ PBHs and $r_s^{\text{PBH}} = r_s^{\text{CDM}}$ and their corresponding maps of the CDM mass-weighted velocity distribution projected face-on through a 100 pc (*right panels*) at 0, 3 and 11 Gyr. As the CDM velocity increases in the central region, the CDM density profile changes until core formation occurs. All the maps show that core formation goes with dynamical heating of DM particles.

5.3.2 Core size and core formation time

Figure 5.6 shows the overall density profiles of the PBH+CDM halo and the density profiles of the CDM and PBH components of the PBH+CDM halo separately after $T = 11$ Gyr for different initial mass fractions f_m , initial scale radii for the PBH component r_s^{PBH} and initial PBH masses m_{PBH} . As we expect, two-body relaxation between PBHs and dynamical friction effects from CDM particles modified all the density profiles. In order to determine if there is core formation in our halos, we did a single-component fit for the PBH+CDM profile and separate fits for CDM and PBH profiles. We tested many profiles such as Einasto [Einasto, 1965], Burkert [Burkert, 1995] and Zavala (Eq.(4) in Zavala et al. [2013]) profiles. However, we found that all of our profiles are well fitted by the following five-parameter formula:

$$\rho(r) = \rho_c W(r) + (1 - W(r))\rho_{\text{NFW}}(r), \quad (5.3)$$

where ρ_c is the central core density and $W(r)$ is defined as

$$2W(r) = 1 - \text{erf}\left(\frac{r - r_c}{2\Delta}\right), \quad (5.4)$$

where r_c is the core radius and Δ is a parameter to control the sharpness of the transition from the core to the NFW profile. The error function corresponds to a switching function here. Our fitting formula reproduces the simulated density structures and captures the rapid transition from the cusp to the core. We set Poissonian errors for fitting weights. Our results suggest that it is natural to have multiple cores for a two component halo. Indeed, the core radii of the PBH+CDM halo, the CDM component and the PBH component differ. Based on a reduced chi-squared method, fits of the CDM component of the PBH+CDM halo provide the best-fit values of core radii (see Table 5.1). We consider these core radii to determine whether a transition appears in our simulation. The smallest core size in the simulations is of the order of 10 pc, which corresponds to our spatial resolution. Thus, we assume that a cusp-to-core transition occurred when the core size r_c becomes greater than our spatial resolution. Table 5.1 describes the best fit values for core sizes for the CDM component of the PBH+CDM halo for all our simulation scenarios. In the case where the density of PBHs is enhanced in the central region ($r_s^{\text{PBH}} = r_s^{\text{CDM}}/2$), the dynamical heating by PBHs generate larger core sizes (see also Figure 5.6).

Now, we have the relation between the core radius $r_c(t)$ of the CDM component of the PBH+CDM halo and the time t when the cusp-to-core transition occurs in the simulations. We invert this function in order to calculate the time ratio $T_c(r_c)/T_r(r_c)$, where $T_c(r_c)$ and $T_r(r_c)$ are the core formation time and the relaxation time, respectively. The relaxation time T_r is given by [Binney & Tremaine, 2008]:

$$T_r(r) \simeq \frac{v^3(r)}{8\pi(n_{\text{CDM}}m_{\text{CDM}}^2 + n_{\text{PBH}}m_{\text{PBH}}^2)G^2 \ln\left(\frac{r_{200}}{\epsilon}\right)}, \quad (5.5)$$

where n_{CDM} and m_{CDM} (n_{PBH} and m_{PBH}) are the number-density and mass of CDM (PBH) particles, respectively. v , ϵ and r_{200} represent the velocity, the softening length and the virial radius, respectively.

Figure 5.7 illustrates the time ratio $T_c(r_c)/T_r(r_c)$ as function of the core formation time $T_r(r_c)$ for all the simulation runs where a cusp-to-core transition occurred (see Table 5.1). We notice that the ratio $T_c(r_c)/T_r(r_c)$ is almost constant over the time in most of simulation runs. Furthermore, it does not strongly depend on the fraction f_m , the PBH mass m_{PBH} or the PBH scale radius r_s^{PBH} .

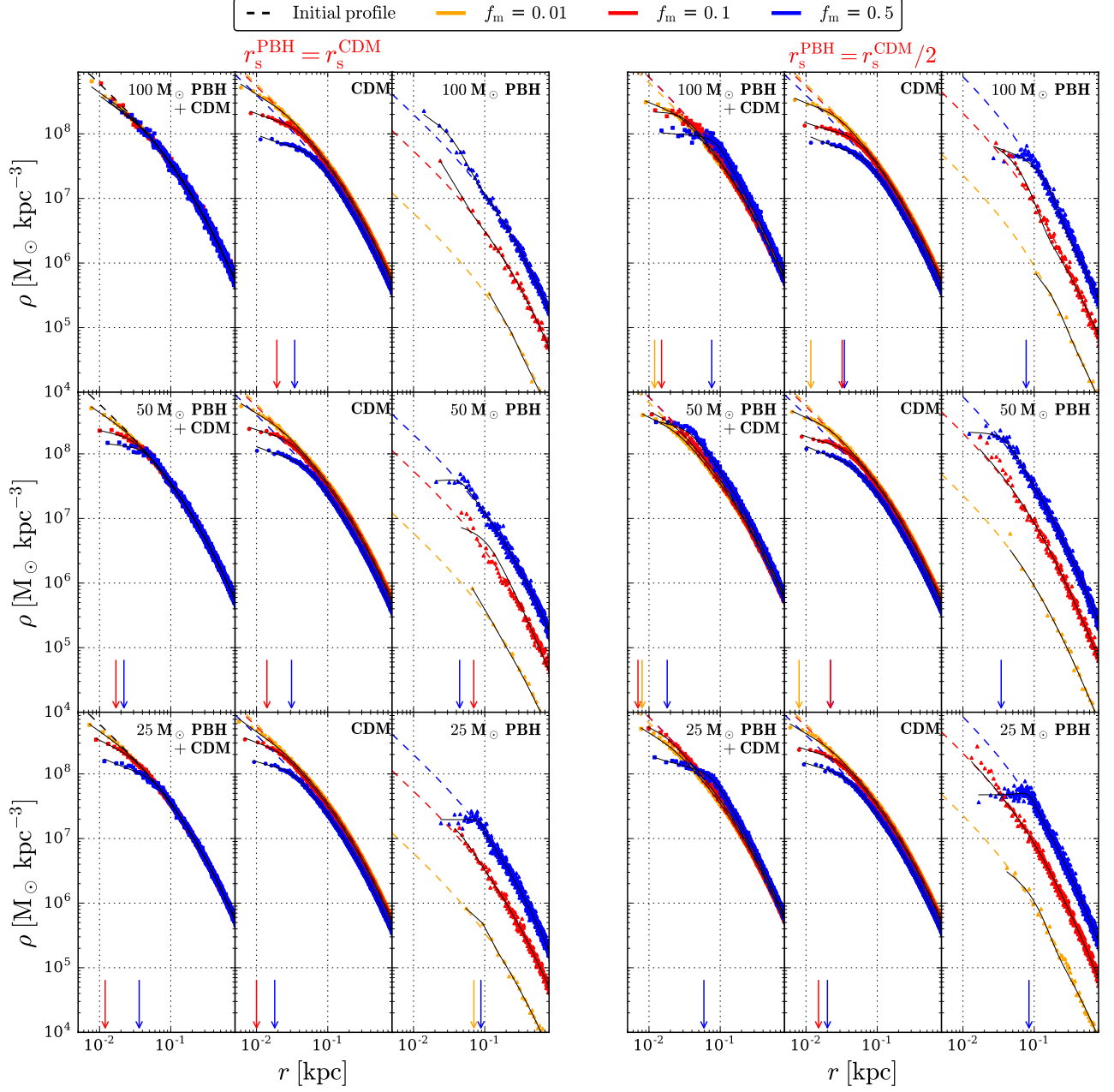


Figure 5.6 – **Cusp-to-core transitions in PBH+CDM halos:** In each subset, the left panel corresponds to the overall density profiles of the PBH+CDM halo, the middle and right panels to the density profiles of the CDM and PBH components of the PBH+CDM halo separately after $T = 11$ Gyr. Initially, the PBH and CDM components of the PBH+CDM halo with a total mass of $10^7 M_\odot$ follow NFW density profiles (dashed lines). We tested two different scale lengths for the profile of the PBH component: $r_s^{\text{PBH}} = r_s^{\text{CDM}}$ (left column) and $r_s^{\text{PBH}} = r_s^{\text{CDM}}/2$ (right column). We explore three different PBH+CDM mass fractions $f_m = [0.01, 0.1, 0.5]$ (see Equation (5.1)). Heating processes between PBH and CDM particles induce a transition from cusp to core in a PBH+CDM halo. In order to determine if there is this transition in our PBH+CDM halo, we did fits (black lines) for the three different density profiles and the size of formed cores are marked by arrows. Our results suggest that it is natural to have multiple cores for a two component halo. Indeed, the core radii of the PBH+CDM halo, the CDM component and the PBH component differ. In the case where the density of PBHs is enhanced in the central region ($r_s^{\text{PBH}} = r_s^{\text{CDM}}/2$), the dynamical heating by PBHs generate larger core sizes (see also Table 5.1).

We derive that a cusp-to-core transition occurred for $T_c(r)/T_r(r) \lesssim 300$. The discrepancy between

f_m	$r_s^{\text{PBH}}/r_s^{\text{CDM}}$	m_{PBH} [M_\odot]	CCT	r_c [pc]	χ^2/ν
0.5	1	25	✓	17.6	1.01
0.5	1	50	✓	31.28	1.02
0.5	1	100	✓	34.32	1.0
0.1	1	25	✓	10.01	1.01
0.1	1	50	✓	14.48	1.0
0.1	1	100	✓	19.33	1.03
0.01	1	25	×	-	-
0.01	1	50	×	-	-
0.01	1	100	×	-	-
0.5	1/2	25	✓	19.7	1.05
0.5	1/2	50	✓	22.48	0.99
0.5	1/2	100	✓	34.63	1.06
0.1	1/2	25	✓	15.1	1.02
0.1	1/2	50	✓	21.55	1.02
0.1	1/2	100	✓	32.23	1.01
0.01	1/2	25	×	-	-
0.01	1/2	50	×	-	-
0.01	1/2	100	✓	11.73	0.99

Table 5.1 – Best fit values for core sizes for the CDM component of the PBH+CDM halo with their corresponding reduced chi-squared χ^2/ν for all our simulation scenarios. From left to right, the columns give: the PBH-CDM mass fraction; the scale length for the PBH component; the PBH mass; if or no cusp-to-core transition (CCT) occurs; the core radius of the CDM component; the reduced chi-squared. All these cores are resolved in simulations based on our resolution of about 10 pc when a cusp-to-core transition (CCT) occurs. In the case where the density of PBHs is enhanced in the central region ($r_s^{\text{PBH}} = r_s^{\text{CDM}}/2$), the dynamical heating by PBHs generate larger core sizes (see Figure 5.6).

the time ratio values is certainly due to our core estimation based only on the CDM component.

Figure 5.8 represents core size and core formation time maps in (f_m, m_{PBH}) space for both for r_s^{CDM} models and $r_s^{\text{CDM}}/2$ models. The core radii were calculated for $T_c = 11$ Gyr. In order to draw these maps, we predict r_c and T_c by setting the time ratio $T_c(r_c)/T_r(r_c)$ at 300 and calculating the relaxation time (see Equation 5.5). Indeed, the white line in top panels of Figure 5.8, which marks the limit of the cusp-to-core transition, is consistent with the shape of the CDM distribution from simulations (triangles and squares) under this latter assumption. As one can see, core radius maps in Figure 5.8 demonstrates that higher PBH mass and mass fraction in PBH+CDM halo generates larger core sizes. Enhancing the density of PBHs in the central region ($r_s^{\text{PBH}} = r_s^{\text{CDM}}/2$) lowers the threshold of the cusp-to-core transition (white line). Moreover, our maps show that at least a mass fraction of 1% is needed to induce cores in PBH+CDM halo depending on the PBH mass and r_s^{PBH} . The core formation time was calculated at $r_c = 10$ pc because we assume that a cusp-to-core transition occurred when the core size r_c becomes greater than our spatial resolution of about 10 pc. These maps (see bottom panels in Figure 5.8) reveal that the cusp-to-core transition takes between 1 and 8 Gyr to occur depending on the fraction f_m , the PBH mass m_{PBH} and the PBH scale radius r_s^{PBH} . Enhancing the density of PBHs in the central region accelerate the formation of cores.

We highlighted that the dynamical heating of the CDM component by PBHs can induce cusp-

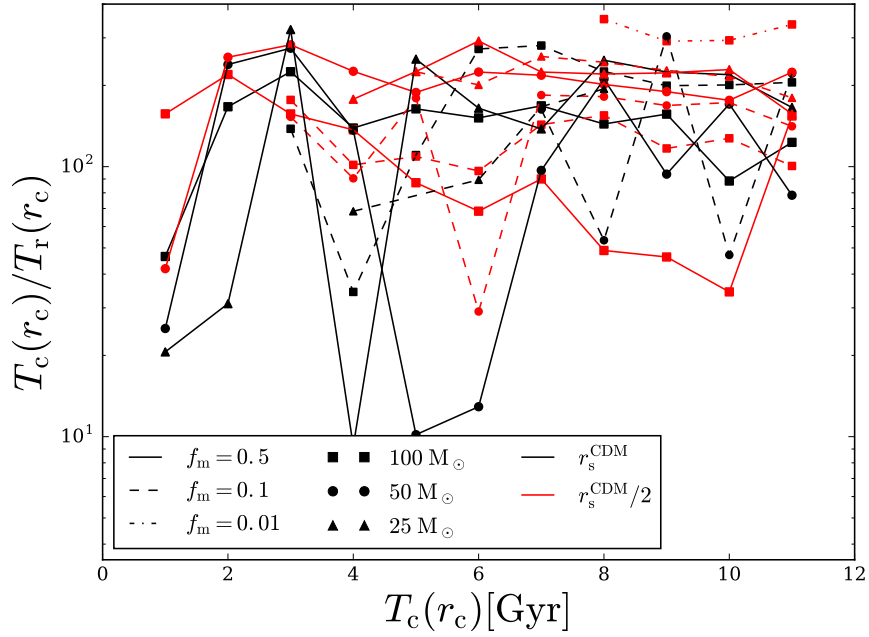


Figure 5.7 – **Estimating core formation time:** Ratio between the core formation time $T_c(r_c)$ and the relaxation time $T_r(r_c)$ as a function of the core formation time $T_c(r_c)$ for all the simulation scenarios where a cusp-to-core transition occurred (see Table 5.1). This ratio is almost constant over the time in most of simulation scenarios and does not strongly depend on the fraction f_m , the PBH mass m_{PBH} or the PBH scale radius r_s^{PBH} . Indeed, we establish that the time ratio is $\mathcal{O}(100)$ for both scale radii of the PBH component r_s^{PBH}

to-core transitions without the presence of baryons and happens automatically in all PBH+CDM halos. Experimentally, annihilation rates from pure CDM halos can prove or prove or disprove this scenario quite clearly [Diemand et al., 2005; Ishiyama et al., 2010]. A baryonic feedback scenario requires starbursts that occur at a particular resonance frequency for a given galaxy potential [Ogiya & Mori, 2011]. A single event blowout, results in a temporary core that quickly reverts back to a cusp. This mechanism shown in this work can work even in such failed cases. In addition, low mass galaxies, such as our PBH+CDM halos, can merge after the cusp-to-core transition in order to form more massive galaxies ($10^8 M_\odot$) with a larger halo cores, which are consistent with observed galaxies. In fact, only a merger of two cored halos yields a cored halo, because a merger of a cuspy halo with a cored halo or a second cuspy halo produces cuspy halo [Boylan-Kolchin & Ma, 2004].

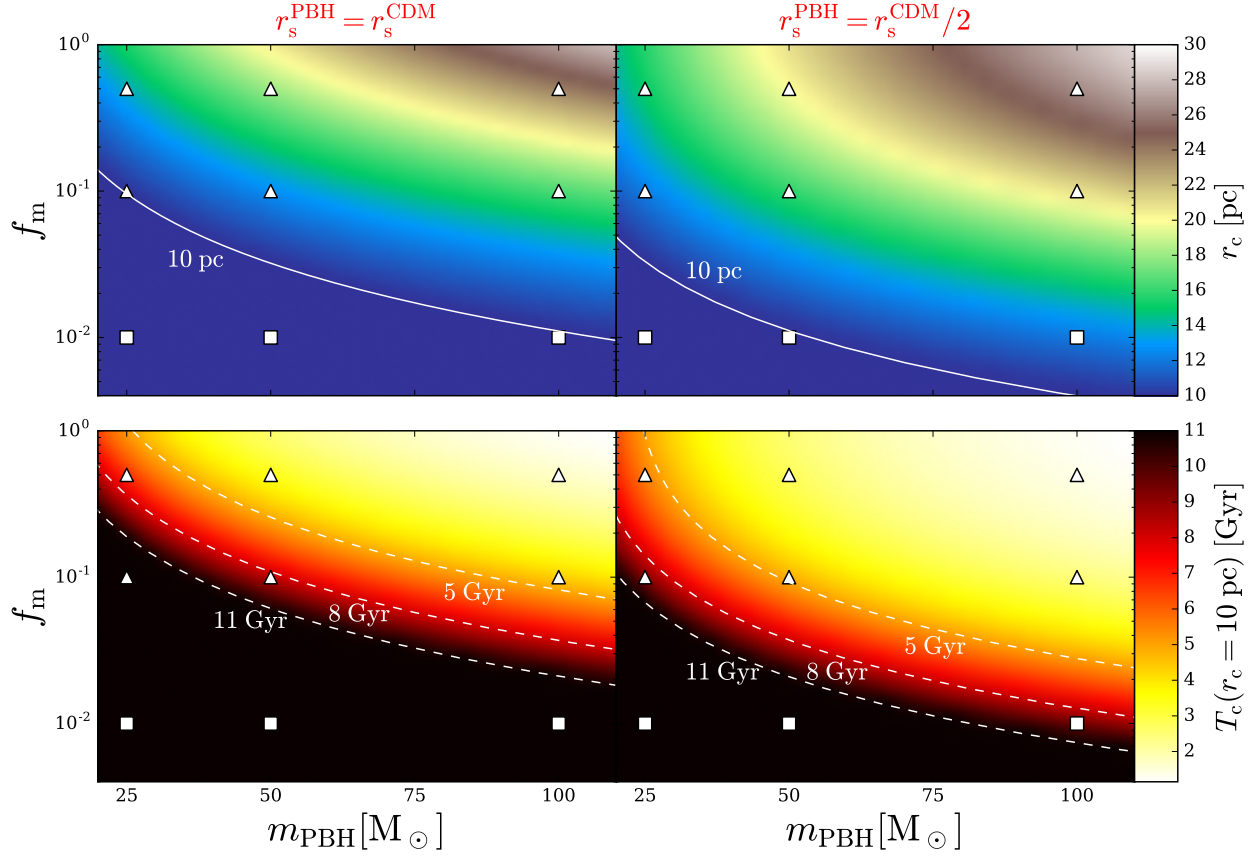


Figure 5.8 – **Core size and core formation time:** Core size (top panels) and core formation time (bottom panels) maps in (f_m, m_{PBH}) space for both for $r_s^{\text{PBH}} = r_s^{\text{CDM}}$ models and $r_s^{\text{PBH}} = r_s^{\text{CDM}}/2$ models. The core radii were calculated for $T_c = 11$ Gyr. Triangles (squares) on maps specify that a PBH+CDM halo for a given f_m and m_{PBH} has a cored (cuspy) profile based on our simulation results. The white line in top panels, which marks the limit of the cusp-to-core transition, is consistent with the shape of the CDM distribution from the simulations (triangles and squares) under this latter assumption. Core radius maps demonstrates that higher PBH mass and mass fraction in PBH+CDM halo generates larger core sizes. Enhancing the density of PBHs in the central region ($r_s^{\text{PBH}} = r_s^{\text{CDM}}/2$) lowers the threshold of the cusp-to-core transition (white line). At least a mass fraction of 1% is needed to induce cores in PBH+CDM halos depending on the PBH mass and r_s^{PBH} . The core formation time maps (bottom panels) reveal that the cusp-to-core transition takes between 1 and 8 Gyr to occur depending on the fraction f_m , the PBH mass m_{PBH} and the PBH scale radius r_s^{PBH} . The core formation time was calculated at $r_c = 10$ pc because we assume that a cusp-to-core transition occurred when the core size r_c becomes greater than our spatial resolution of about 10 pc. Enhancing the density of PBHs in the central region accelerate the formation of cores.

5.4 References

- Abbott B. P., et al., 2016, *Phys. Rev. Lett.*, **116**, 061102 92
- Amaro-Seoane P., et al., 2017, arXiv e-prints, p. arXiv:1702.00786 92
- Bergström L., 2000, *Reports on Progress in Physics*, **63**, 793 92
- Bertone G., Hooper D., Silk J., 2005, *Phys. Rep.*, **405**, 279 92
- Binney J., Tremaine S., 2008, *Galactic Dynamics: Second Edition* 97
- Boylan-Kolchin M., Ma C.-P., 2004, *MNRAS*, **349**, 1117 100

- Brandt T. D., 2016, [ApJ](#), **824**, L31 92
- Burkert A., 1995, [ApJ](#), **447**, L25 97
- Carr B., Raidal M., Tenkanen T., Vaskonen V., Veermäe H., 2017, [Phys. Rev. D](#), **96**, 023514 92
- Chandrasekhar S., 1943, [Reviews of Modern Physics](#), **15**, 1 92
- Clesse S., García-Bellido J., 2015, [Phys. Rev. D](#), **92**, 023524 92
- Clesse S., García-Bellido J., 2018, [Physics of the Dark Universe](#), **22**, 137 92
- Diemand J., Moore B., Stadel J., 2005, [Nature](#), **433**, 389 100
- Einasto J., 1965, Trudy Astrofizicheskogo Instituta Alma-Ata, **5**, 87 97
- Hawking S., 1971, [MNRAS](#), **152**, 75 92
- Inomata K., Kawasaki M., Mukaida K., Tada Y., Yanagida T. T., 2017, [Phys. Rev. D](#), **96**, 043504 92
- Ishiyama T., Makino J., Ebisuzaki T., 2010, [ApJ](#), **723**, L195 100
- Jungman G., Kamionkowski M., Griest K., 1996, [Phys. Rep.](#), **267**, 195 92
- Khlopov M. Y., 2010, [Research in Astronomy and Astrophysics](#), **10**, 495 92
- Koushiappas S. M., Loeb A., 2017, [Phys. Rev. Lett.](#), **119**, 041102 92
- Kovetz E. D., 2017, [Phys. Rev. Lett.](#), **119**, 131301 92
- Miki Y., Umemura M., 2017, [New Astron.](#), **52**, 65 93
- Miki Y., Umemura M., 2018, [MNRAS](#), **475**, 2269 93
- Navarro J. F., Frenk C. S., White S. D. M., 1996, [ApJ](#), **462**, 563 93
- Ogiya G., Mori M., 2011, [ApJ](#), **736**, L2 100
- Prada F., Klypin A. A., Cuesta A. J., Betancort-Rijo J. E., Primack J., 2012, [MNRAS](#), **423**, 3018 93
- Sasaki M., Suyama T., Tanaka T., Yokoyama S., 2016, [Phys. Rev. Lett.](#), **117**, 061101 92
- Spitzer Lyman J., 1969, [ApJ](#), **158**, L139 92
- Zavala J., Vogelsberger M., Walker M. G., 2013, [MNRAS](#), **431**, L20 97
- Zel'dovich Y. B., Novikov I. D., 1967, Soviet Ast., **10**, 602 92
- Zhu Q., Vasiliev E., Li Y., Jing Y., 2018, [MNRAS](#), **476**, 2 92

Chapter 6

Quenching any BH feedback: one consequence of off-center massive black holes

The work presented in this chapter is based on Boldrini et al. (2020c) ([arXiv:2003.02611](#)).

Contents

6.1 Off-center massive black holes	104
6.2 Dark matter subhalos and off-center massive black holes	104
6.2.1 Dwarf galaxy-subhalo simulation	105
6.2.2 Results	106
6.2.3 The cusp-core problem	110
6.3 References	111

6.1 Off-center massive black holes

Most galaxies are known to harbour supermassive black holes (SMBHs), formed within a billion years after the Big Bang. They reside in the centres of present day galaxies with masses of $\sim 10^6 - 10^{10} M_\odot$ based on observations of high-redshift quasars (see [Kormendy & Ho \[2013\]](#) for a review). The radio source Sgr A* the MW Galaxy is an evidence for the presence of a SMBH at its centre [[Issaoun et al., 2019](#)]. Moreover, dwarf galaxies may frequently host massive black holes (MBHs) at their centres according to X-ray observations, among others (see [Greene et al. \[2019\]](#) for a recent review). These MBHs are in the mass range $\sim 10^3 - 10^5 M_\odot$ and are expected to play key roles in SMBH formation scenarios that invoke galaxy mergers.

Intriguingly, some observations of active galactic nuclei (AGN) in dwarf galaxies claim that MBHs are not located at the centers of their host galaxies. This offset varies between tens of parsecs to a few kiloparsecs [[Menezes et al., 2014, 2016](#); [Reines et al., 2020](#); [Shen et al., 2019](#)]. Different scenarios have been proposed to explain these off-center BHs. Plausibly, the offset could be due to the presence of a binary system before the merger (e.g. [Sundararajan et al. \[2010\]](#) and references therein), or via tidal stripping during mergers (see [Tremmel et al. \[2018\]](#) and references therein), the incomplete MBH inspiraling phase of the two merging galaxies [[Barth et al., 2009](#); [Comerford & Greene, 2014](#)], or the recoil of merging BHs [[Komossa, 2012](#); [Loeb, 2007](#); [Merritt & Milosavljević, 2005](#); [Volonteri & Perna, 2005](#)]. Furthermore, recent simulations show that BHs in dwarf galaxies are expected to be wandering around the central regions after the occurrence of mergers or due to tidal stripping [[Bellovary et al., 2010, 2019](#); [Pfister et al., 2019](#)]. The merging mechanism seems important for blue dwarfs, whereas the old dwarfs dominate [[Kado-Fong et al., 2020](#)]. Moreover, major mergers of dwarf galaxies seems also very rare after $z \sim 3$ [[Fitts et al., 2018](#)]. As the frequencies of dwarf galaxy mergers and MBH binaries are uncertain, we propose below an alternative explanation for off-center MBH.

6.2 Dark matter subhalos and off-center massive black holes

The CDM paradigm predicts that a very large number of dark matter substructures exist inside galactic halos [[Diemand et al., 2008](#); [Springel et al., 2008](#)]. Recently, Gaia DR2 data has provided additional evidence for these substructures [[Banik et al., 2019](#)]. DM halos are growing with time, either through mergers with DM halos or by accretion of smaller halos. The latter, considered as DM subhalos, have crossed the virial radius of a larger halo at some point in the past. Subhalos interact gravitationally with all the components of the galaxy before becoming remnants of disrupted halos [[Zavala & Frenk, 2019](#)]. In the central regions, the MBH dominates the central mass content of the galaxy [[Ferrarese & Merritt, 2000](#); [Gebhardt et al., 2000](#)]. This is the reason why passages of subhalos near the central regions of the host galaxy can lead to energy exchange with MBHs in dwarf galaxies.

In this work, we show that subhalo crossings during their infall phase can heat the central regions of dwarf galaxies and kick the central MBH on average out to tens of parsecs from the galaxy centre over a significant fraction of the dwarf history. Assuming average initial conditions for the subhalos, we performed N-body simulations with GPUs, which allow parsec resolution, to study this heating process that naturally creates off-center MBHs in dwarf galaxies. This section is organized as follows. Section 6.2.1 provides a description of the N-body modelling of the dwarf galaxy and its subhalos, along with details of our numerical simulations. In Section 6.2.2, we present our simulation results,

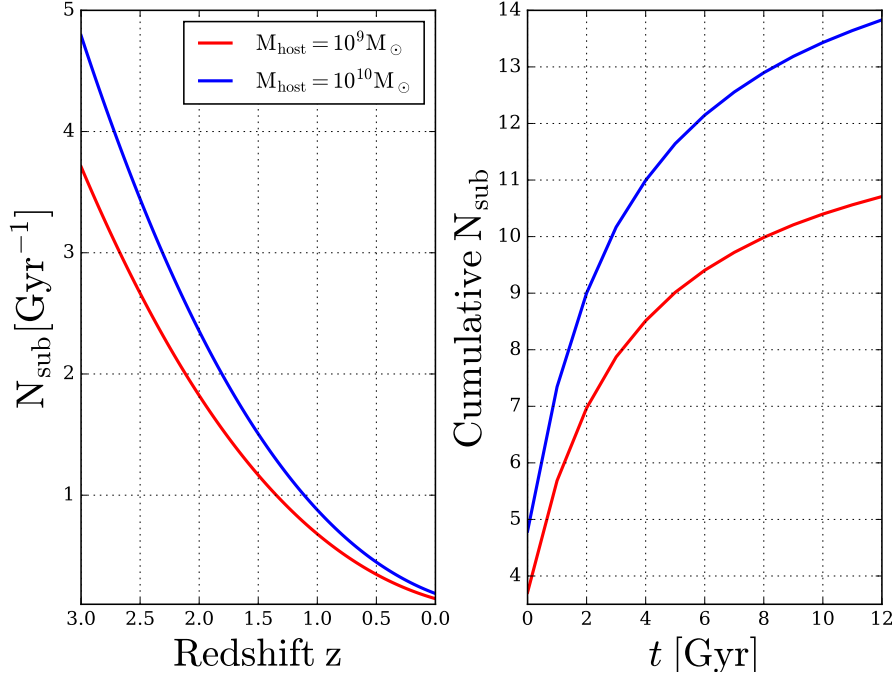


Figure 6.1 – **Subhalo accretions:** Average number of subhalos per Gyr as function of redshift (*left panel*) and cumulative average number of subhalos (*right panel*) as function of time with a mass ratio $10 < M_{\text{host}}/M_{\text{sub}} < 100$ in 10^9 and $10^{10} M_{\odot}$ DM host halos. This estimate is an average of the number of mergers based on the extended Press-Schechter (EPS) formalism [Neistein & Dekel, 2008].

and Section 6.2.3 discusses the implications of off-center BHs for the cusp-core problem.

6.2.1 Dwarf galaxy-subhalo simulation

As our host galaxy, we consider a dwarf galaxy that has accreted DM subhalos with mass ratio $10 < M_{\text{host}}/M_{\text{sub}} < 100$. We construct a live dwarf galaxy composed of a central MBH ($10^5 - 10^6 M_{\odot}$), with only stars and DM particles, since dwarf galaxies contain little or no gas today. The stellar component is modelled by a Plummer profile [Plummer, 1911]:

$$\rho(r) = \frac{3a^2 M_0}{4\pi} (r^2 + a^2)^{-5/2}, \quad (6.1)$$

where a and M_0 are the scale parameter and the mass, respectively. We assume an average half-light radius of 294 pc and a mass of $10^7 M_{\odot}$ for the stellar component of the dwarf galaxy based on Table 1 of Read et al. [2019]. For the host halo and subhalos, we assume a NFW density profile [Navarro et al., 1996]:

$$\rho_{\text{NFW}}(r) = \rho_0 \left(\frac{r}{r_s} \right)^{-1} \left(1 + \frac{r}{r_s} \right)^{-2}, \quad (6.2)$$

with central density ρ_0 and scale-length r_s . For the simulations, we consider DM host halos of $M_{\text{host}} = 10^9$ and $10^{10} M_{\odot}$ at redshift $z = 3$. Given the halo mass and redshift, both halo concentrations c_{200} can be estimated from cosmological N-body simulations [Dutton & Macciò, 2014]. The abundance of subhalo accretion for a specific host halo mass range can be determined by the extended Press-Schechter (EPS) formalism [Bond et al., 1991; Lacey & Cole, 1993]. Fig. 7.2 represents the average number of subhalos per Gyr as function of redshift (*left panel*) and cumulative average number of subhalos (*right panel*) as function of time with mass ratio $10 < M_{\text{host}}/M_{\text{sub}} < 100$ in 10^9 and $10^{10} M_{\odot}$ DM host halos. We determine this rate from analytic merger rates for DM

halos within the EPS formalism [Neistein & Dekel, 2008]. The left panel in Fig. 7.2 shows that a 10^9 (10^{10}) M_\odot host halo has accreted on average 3-4 (4-5) subhalos per Gyr for the adopted mass ratio at $z = 3$ (see Fig. 7.2). Moreover, galaxies continuously accrete smaller halos. Over their history, 10^9 (10^{10}) M_\odot host halos have accreted 10-11 (13-14) subhalos with a mass ratio $10 < M_{\text{host}}/M_{\text{sub}} < 100$ (see *right panel* in Fig. 7.2). In the simulations, the subhalo position was drawn randomly under the requirement that the initial separation between the centre of the galaxy and subhalos is the virial radius of the host halo, r_{vir} . The subhalo orbit has an initial circularity η depending on the host halo mass and redshift. As the orbital distributions of subhalo circularity are given to good approximation by Wetzel [2011], we determine the average circularity $\eta = 0.52$ ($\eta = 0.47$) at $z = 3$ for a 10^9 (10^{10}) M_\odot host halo. Here, the MBH is represented by an additional particle of mass 10^{-4} and $10^{-3} M_{\text{host}}$, placed initially at the center of the dwarf galaxy. We assume also in this study that our dwarf galaxy is in isolation.

To generate our live objects, we use the initial condition code magi [Miki & Umemura, 2018]. We perform our simulations with the high performance collisionless N-body code gothic, which runs entirely on GPUs [Miki & Umemura, 2017]. We evolve the dwarf galaxy-subhalo system over 12 Gyr for 10^9 and $10^{10} M_\odot$ host halos. We performed simulations for 1 and 4 subhalos with mass ratios $M_{\text{host}}/M_{\text{sub}} = 12.5$ and 50, as limiting cases. We set the particle resolution of all the live objects to $100 M_\odot$ and the gravitational softening length to 2 pc. We also assess the impact of numerical effects on BH dynamics by running simulations for three different softening lengths, $\epsilon = 4, 2$ and 1 pc. We apply these tests to the simulation over 12 Gyr for a $10^9 M_\odot$ DM host halo hosting a $10^5 M_\odot$ BH and accreting one DM subhalos with a mass of $8 \times 10^7 M_\odot$. Our simulations are well converged for $\epsilon = 1$ and 2 pc. Our system was centered on the mass center of the stellar component for all our results. The system corresponds to all particles (DM, stars and MBH) in the simulation. The reason why we centered on the stellar component is precisely because observations establish displacements of MBH from the stellar component.

6.2.2 Results

We consider the accretion of DM subhalos by a dwarf galaxy, which hosts a central MBH. Details of all our scenarios are given in Table 7.1. The inset plot in Fig. 7.3 depicts the orbital decays of four subhalos with a mass of $8 \times 10^7 M_\odot$ by a dwarf galaxy embedded in a $10^9 M_\odot$ DM halo over 12 Gyr. These radii correspond to the distance between the subhalo and the centre of the dwarf stellar component. Dynamical friction induced by the DM field is responsible for the infall of these subhalos. As a result, the central region of the galaxy experiences multiple subhalo crossings (see in Fig. 7.3). Indeed, DM subhalos are extended objects following a NFW profile with a scale radius of ~ 600 pc and their outerparts interact with the host galaxy's centre during crossings. Furthermore, subhalos also experience tidal disruptions from the dwarf galaxy. As shown in the inset plot in Fig. 7.3, all subhalos are completely disrupted after 6-8 Gyr.

Subhalo crossings heat the central region and more particularly the MBH via dynamical friction. Indeed, subhalos add energy to the BH, causing it to leave the galaxy centre. Fig. 7.1 illustrates the orbital radius of a $10^5 M_\odot$ MBH, initially at the galaxy centre, over 12 Gyr. This distance corresponds to the distance between the BH and the mass centre of the dwarf stellar component. In the absence of perturbors such as subhalos, the MBH remains at the centre of the dwarf galaxy. This scenario ensures the stability of the BH against numerical effects (black curve in Fig. 7.1). However, taking into account the subhalo interactions results in a kick of the MBH to tens of parsecs from the galaxy centre. Indeed, the MBH has gained kinetic energy via dynamical friction. As subhalos

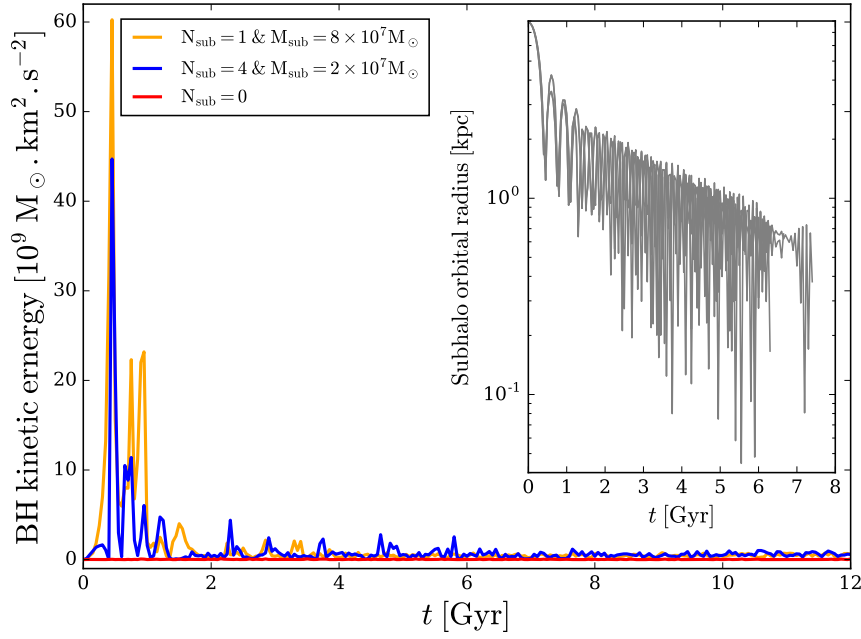


Figure 6.2 – **Energy transfer via dynamical friction:** Kinetic energy over 12 Gyr gained by the MBH in different scenarios (see Table 7.1 for details). As subhalos reach their velocity peak during its first infall in the galaxy, the energy transfer is maximal at their first pericentre of subhalos. Inset figure: Orbital decay of the four subhalos with a mass of $8 \times 10^7 M_{\odot}$ accreted by a dwarf galaxy embedded in a $10^9 M_{\odot}$ host halo over 12 Gyr. These radii correspond to the distance between the subhalo and the centre of the dwarf stellar component. The initial separation between the centres of the galaxy and subhalos is the virial radius of the host halo, r_{vir} . Dynamical friction induced by the DM field is responsible for the infall of these subhalos. Thus, the central region of the galaxy experienced multiple subhalo crossings.

reach their velocity peak during its first infall in the galaxy, the energy transfer is maximal at their first pericentre of subhalos (see Fig. 7.3). Fig. 7.1 also highlights that the displacement of the MBH depends strongly on the number of subhalos and their masses. We assume that the MBH is off-center when its orbital radius is greater than the mean displacement of the MBH calculated over 12 Gyr in the absence of any perturbers ($N_{\text{sub}} = 0$) and this phenomenon is characterized by the offset time T_{offset} . Table 7.1 shows that the MBH is off-center most of the time in all scenarios. We also calculate the time spent by the MBH at $r_{\text{BH}} > 15$ pc. Before kicking the MBH, subhalos need a characteristic time to transfer energy to the central BH, defined to be the heating time T_{heating} . The maximum offset reached by the MBH due to heating from subhalos is between 35 (run12) and 134 pc (run18) depending on the scenarios (see Table 7.1). According to Fig. 7.2, $10^9 M_{\odot}$ DM halos accrete on average 3-4 DM subhalos at redshift $z=3$. Based on run42 and run48, we predict that the MBH will spend on average 1.9-2.5 Gyr beyond 15 pc due the crossings of the four subhalos after the heating time (0.25-0.35 Gyr). Thus, we expect that MBH are off-center for a significant time during the early epochs ($z=1.5-3$) of dwarf galaxies. Furthermore, as the subhalo accretion is a continuous process in galaxies, we expect that most of the time, MBH are offset from the galaxy centre due to repeated heating by subhalo crossings. At low redshift, 1-2 DM subhalos are still be accreted by dwarf galaxies (see Fig. 7.2) and we expect that most of MBHs will be off-center by tens of parsecs even if these substructures are less concentrated at this recent epoch (see run12 and run18 in Table 7.1). However, our mechanism cannot explain the large displacement of MBHs observed for nearby dwarf galaxies [Reines et al., 2020].

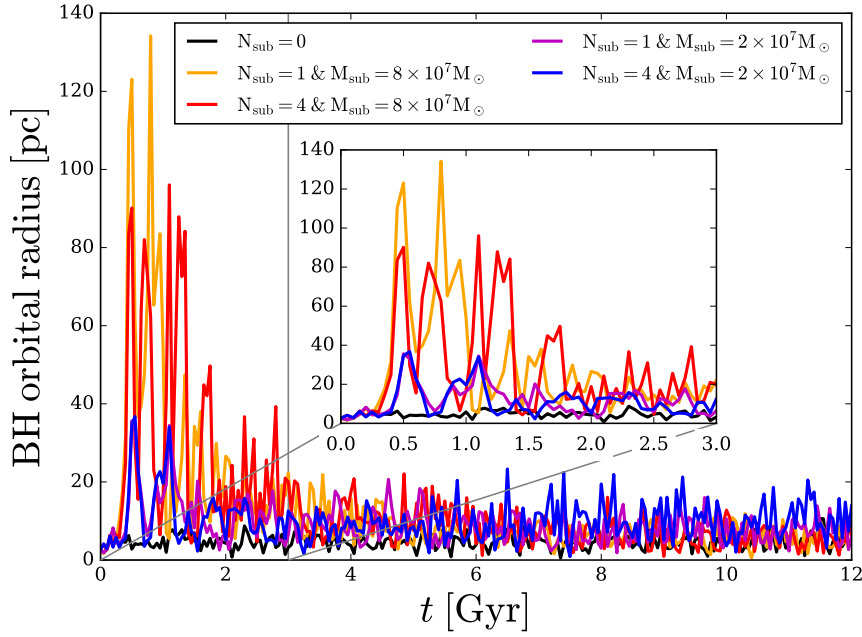


Figure 6.3 – **Off-center MBH:** BH orbital radius over 12 Gyr for different subhalo numbers and masses (see Table 7.1 for details). This radius corresponds to the distance between the BH and the mass centre of the dwarf stellar component. The reason why we centered on the stellar component is precisely because observations establish displacements of MBH from the stellar component. The MBH of mass $10^5 M_\odot$ is initially at the centre of the dwarf galaxy. Subhalo crossings heat the central regions and more particularly affect the MBH via dynamical friction. Indeed, subhalos add energy to the MBH, causing it to leave the galaxy centre. In the absence of perturbers, the MBH remains at the centre of the dwarf galaxy. This scenario ensures the stability of the BH against numerical effects (black curve). However, taking into account the subhalo interactions results in a kick of the MBH to tens of parsecs from the galaxy centre, depending sensitively on the number of subhalos and on their masses. We assume that the MBH is off-center when its orbital radius is greater than the orbital radius of the MBH in the absence of any perturbers ($N_{\text{sub}} = 0$)

According to this scenario, we expect that the host halo and MBH masses play an important role. Indeed, this heating mechanism is based on the efficiency of dynamical friction, which strongly depends on the DM density at the galaxy centre. Run48 and run48b confirm that increasing the BH mass reduces its offset time because more massive objects fall in more rapidly due to dynamical friction (see Table 7.1). We explored the host halo mass impact in Fig. 7.4 by comparing the MBH offset induced by subhalos in $10^9 M_\odot$ and $10^{10} M_\odot$ host halos over 12 Gyr. Fig. 7.4 shows that MBH are off-center for a longer time in higher mass DM hosts. Indeed, the MBH spends on average 3.8 Gyr beyond 15 pc after the heating phase in a $10^{10} M_\odot$ host halo. According to our simulation results, we predict that MBHs are going to be off-center for a longer time in higher mass galaxies. This offset time is directly related to dynamical friction, which strongly depends on the DM density profile. Assuming a NFW profile, we determine the density profiles of DM host halos with different masses at redshift $z = 0$ in Fig. 7.5. Given the halo mass and redshift, both halo concentrations c_{200} can be estimated from cosmological N-body simulations [Dutton & Macciò, 2014]. We show that the density at the centre decreases as the halo mass grows (see Fig. 7.5). At high redshift, the difference between the central density as function of the DM halo mass is reduced but the same trend is respected. Consequently, we predict that off-center BHs are more common in higher mass galaxies because after the kick, dynamical friction on BHs becomes significantly weaker and then BHs take more time to sink towards the centre of these galaxies. Moreover, in high mass galaxies, MBHs are

Simulation	N_{sub}	M_{BH} [M_{\odot}]	M_{sub} [M_{\odot}]	M_{host} [M_{\odot}]	M_{*} [M_{\odot}]	T_{heating} [Gyr]	T_{offset} [Gyr]	$T(r_{\text{BH}} > 15 \text{ pc})$ [Gyr]	$r_{\text{max}}^{\text{BH}}$ [pc]
run42	4	10^5	2×10^7	10^9	10^7	0.35	10.7	1.9	37
run48	4	10^5	8×10^7	10^9	10^7	0.25	9.4	2.5	96
run12	1	10^5	2×10^7	10^9	10^7	0.4	9.95	1.15	35
run18	1	10^5	8×10^7	10^9	10^7	0.3	9.5	2.2	134
run48b	4	10^6	8×10^7	10^9	10^7	0.25	8.25	1.9	92
run48m	4	10^5	8×10^8	10^{10}	10^7	0.3	9.95	3.8	129

Table 6.1 – Simulation parameters for all the scenarios. From left to right, the columns give: the number of subhalos; the MBH mass; the subhalo mass; the DM host halo mass; the stellar mass; the heating time; the offset time; the time spent by the MBH at $r_{\text{BH}} > 15 \text{ pc}$; the maximal distance reached by the MBH. We set the particle resolution of all the live objects to $100 M_{\odot}$ and the gravitational softening length to 2 pc. The maximum offset reached by the MBH due to heating from subhalos is between 35 and 134 pc. MBHs will spend on average 1.9-2.5 Gyr beyond 15 pc due the crossings of the four subhalos after the heating time (0.25-0.35 Gyr). Thus, we expect that MBHs are off-center during a significant time in the early epoch ($z=1.5-3$) of dwarf galaxies.

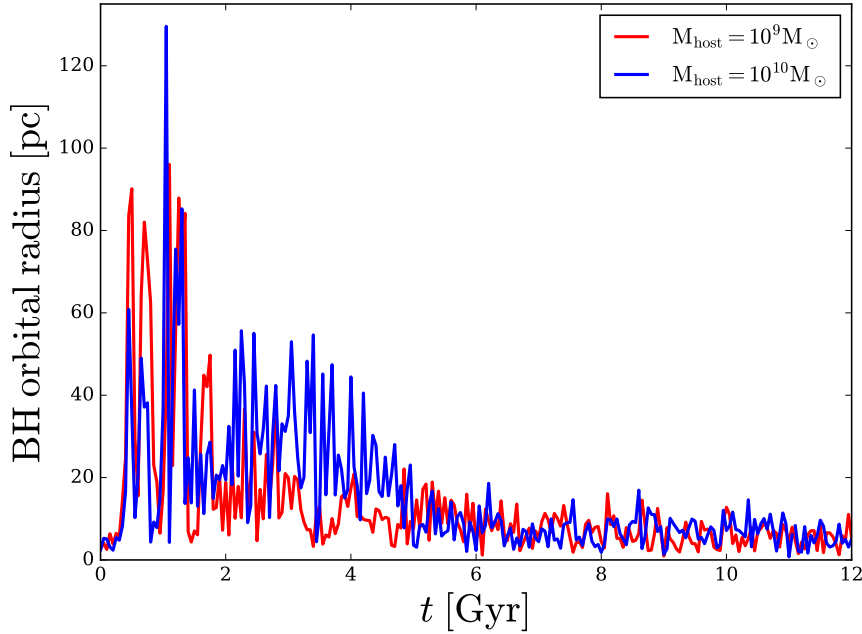


Figure 6.4 – **Host halo mass impact:** BH orbital radius over 12 Gyr in 10^9 and $10^{10} M_{\odot}$ DM host halos accreting four DM subhalos with a mass of $8 \times 10^7 M_{\odot}$. MBHs are off-center more time in higher mass DM host. Indeed, the MBH spent on average 3.8 Gyr beyond 15 pc after the heating phase in a $10^{10} M_{\odot}$ host halo (see Table 7.1). We predict that MBHs are going to be off-center for a longer time in higher mass galaxies.

going to have less inertia due to the lower galaxy potential and thus they will reach farther distances as demonstrated in Fig. 7.4. Our result reinforces our prediction of a population of wandering black holes, particularly in higher mass galaxies [Bellovary et al., 2019; Governato et al., 1994; Islam et al., 2004; Micic et al., 2011; Rashkov & Madau, 2014; Schneider et al., 2002; Volonteri et al., 2003].

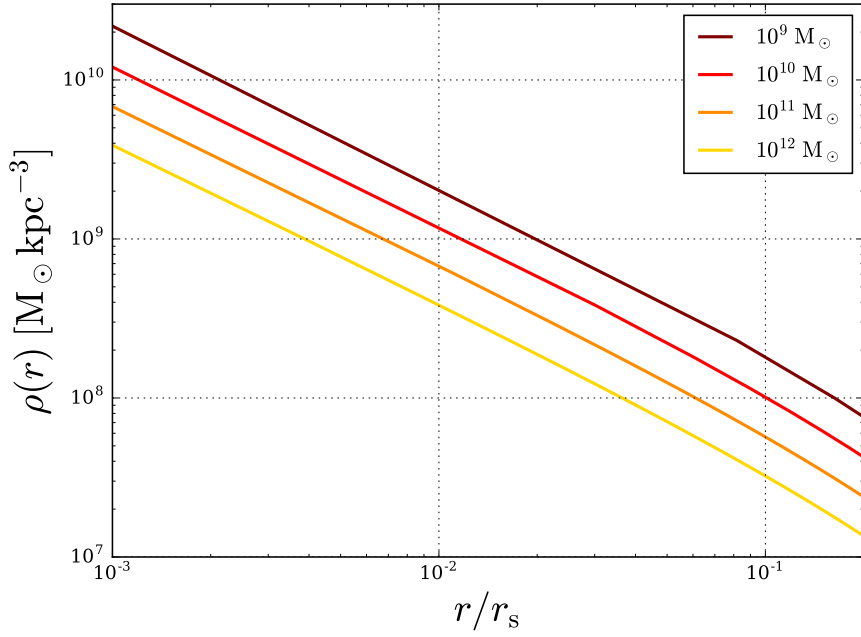


Figure 6.5 – **Dynamical friction in halo centres:** Density profiles of DM host halos with different masses as function of the radius normalized by their scale radius, assuming a NFW profile at redshift $z = 0$. The offset time is related to the efficiency of dynamical friction, which strongly depends on the DM density at the galaxy centre. The density at the centre decreases as the halo mass grows. Consequently, the dynamical friction on BHs becomes significantly weaker and BHs take more time to sink towards the centre of higher mass galaxies after the kick.

6.2.3 The cusp-core problem

Solutions invoking baryonic feedback cycles can potentially reconcile observed dwarf galaxy anomalies with Λ CDM predictions. This challenge at small scales occurs precisely where baryons play an important role, notably through BH feedback that generates significant movements of the gas. BH feedback can expel large amounts of gas from the central of galaxies. A fraction of this gas then cools and returns to the centre, generating repeated cycles of significant outflows which in turn cause rapid fluctuations of the gravitational potential. These potential fluctuations dynamically heat the DM and lead to the formation of a core [e.g. [Martizzi et al., 2013](#); [Peirani et al., 2017](#); [Silk, 2017](#)]. The gradual dispersion of the DM particles away from the center of the halo is ultimately responsible for core creation.

Numerical simulations show that the peak of AGN activity happens between $z \sim 3$ and $z \sim 1.6$. We could be able to observe the flattening of the DM density profile induced by high BH activity. Especially during this early phase of galaxy evolution, we predict that MBHs are off-center according to our simulation results. Due to the heating by subhalos, we have shown that BHs remain on average tens of parsecs away throughout most of the halo's history. However, BHs accrete gas inefficiently away from the galaxy centre as gas clumps are centrally located [[Smith et al., 2018](#)]. Then, the conditions required to alter the deep potential of galaxies appear to be missing. Without BH feedback, the inner density profiles of DM halos will remain cuspy. In addition, off-center BHs entail the quenching of BH feedback in dwarf galaxies. Consequently, it seems difficult to induce DM core formation in dwarfs from BH feedback. Baryonic feedback cycles are the preferred option [[Pontzen & Governato, 2012](#)].

6.3 References

- Banik N., Bovy J., Bertone G., Erkal D., de Boer T. J. L., 2019, arXiv e-prints, p. [arXiv:1911.02662](#) 104
- Barth A. J., Strigari L. E., Bentz M. C., Greene J. E., Ho L. C., 2009, [ApJ](#), 690, 1031 104
- Bellovary J. M., Governato F., Quinn T. R., Wadsley J., Shen S., Volonteri M., 2010, [ApJ](#), 721, L148 104
- Bellovary J. M., Cleary C. E., Munshi F., Tremmel M., Christensen C. R., Brooks A., Quinn T. R., 2019, [MNRAS](#), 482, 2913 104, 109
- Bond J. R., Cole S., Efstathiou G., Kaiser N., 1991, [ApJ](#), 379, 440 105
- Comerford J. M., Greene J. E., 2014, [ApJ](#), 789, 112 104
- Diemand J., Kuhlen M., Madau P., Zemp M., Moore B., Potter D., Stadel J., 2008, [Nature](#), 454, 735 104
- Dutton A. A., Macciò A. V., 2014, [MNRAS](#), 441, 3359 105, 108
- Ferrarese L., Merritt D., 2000, [ApJ](#), 539, L9 104
- Fitts A., et al., 2018, [MNRAS](#), 479, 319 104
- Gebhardt K., et al., 2000, [ApJ](#), 539, L13 104
- Governato F., Colpi M., Maraschi L., 1994, [MNRAS](#), 271, 317 109
- Greene J. E., Strader J., Ho L. C., 2019, arXiv e-prints, p. [arXiv:1911.09678](#) 104
- Islam R. R., Taylor J. E., Silk J., 2004, [MNRAS](#), 354, 427 109
- Issaoun S., Johnson M. D., Blackburn L., Mościbrodzka M., Chael A., Falcke H., 2019, [A&A](#), 629, A32 104
- Kado-Fong E., Greene J. E., Greco J. P., Beaton R., Goulding A. D., Johnson S. D., Komiyama Y., 2020, [AJ](#), 159, 103 104
- Komossa S., 2012, [Advances in Astronomy](#), 2012, 364973 104
- Kormendy J., Ho L. C., 2013, [ARA&A](#), 51, 511 104
- Lacey C., Cole S., 1993, [MNRAS](#), 262, 627 105
- Loeb A., 2007, [Phys. Rev. Lett.](#), 99, 041103 104
- Martizzi D., Teyssier R., Moore B., 2013, [MNRAS](#), 432, 1947 110
- Menezes R. B., Steiner J. E., Ricci T. V., 2014, [ApJ](#), 796, L13 104
- Menezes R. B., Steiner J. E., da Silva P., 2016, [ApJ](#), 817, 150 104
- Merritt D., Milosavljević M., 2005, [Living Reviews in Relativity](#), 8, 8 104

- Micic M., Holley-Bockelmann K., Sigurdsson S., 2011, [MNRAS](#), **414**, 1127 109
- Miki Y., Umemura M., 2017, [New Astron.](#), **52**, 65 106
- Miki Y., Umemura M., 2018, [MNRAS](#), **475**, 2269 106
- Navarro J. F., Frenk C. S., White S. D. M., 1996, [ApJ](#), **462**, 563 105
- Neistein E., Dekel A., 2008, [MNRAS](#), **388**, 1792 105, 106
- Peirani S., et al., 2017, [MNRAS](#), **472**, 2153 110
- Pfister H., Volonteri M., Dubois Y., Dotti M., Colpi M., 2019, [MNRAS](#), **486**, 101 104
- Plummer H. C., 1911, [MNRAS](#), **71**, 460 105
- Pontzen A., Governato F., 2012, [MNRAS](#), **421**, 3464 110
- Rashkov V., Madau P., 2014, [ApJ](#), **780**, 187 109
- Read J. I., Walker M. G., Steger P., 2019, [MNRAS](#), **484**, 1401 105
- Reines A. E., Condon J. J., Darling J., Greene J. E., 2020, [ApJ](#), **888**, 36 104, 107
- Schneider R., Ferrara A., Natarajan P., Omukai K., 2002, [ApJ](#), **571**, 30 109
- Shen Y., Hwang H.-C., Zakamska N., Liu X., 2019, [ApJ](#), **885**, L4 104
- Silk J., 2017, [ApJ](#), **839**, L13 110
- Smith B. D., Regan J. A., Downes T. P., Norman M. L., O'Shea B. W., Wise J. H., 2018, [MNRAS](#), **480**, 3762 110
- Springel V., et al., 2008, [MNRAS](#), **391**, 1685 104
- Sundararajan P. A., Khanna G., Hughes S. A., 2010, [Phys. Rev. D](#), **81**, 104009 104
- Tremmel M., Governato F., Volonteri M., Pontzen A., Quinn T. R., 2018, [ApJ](#), **857**, L22 104
- Volonteri M., Perna R., 2005, [MNRAS](#), **358**, 913 104
- Volonteri M., Haardt F., Madau P., 2003, [ApJ](#), **582**, 559 109
- Wetzel A. R., 2011, [MNRAS](#), **412**, 49 106
- Zavala J., Frenk C. S., 2019, [Galaxies](#), **7**, 81 104

Chapter 7

Andromeda galaxy (M31): a test case

The work presented in this chapter is based on Boldrini (2020d) ([arXiv:2007.03010](#)) and Boldrini et al. (2020e) ([arXiv:2002.12192](#)).

Contents

7.1 A dark matter core in M31	114
7.1.1 Andromeda galaxy (M31)	114
7.1.2 Observation: Giant stellar stream and shell-like features of M31	115
7.1.3 Simulation: High resolution fully GPU code	118
7.1.4 Tests of the models with M31 observations	118
7.1.5 Results: A model-independent cusp-to-core transition in M31	119
7.2 The origin of the black hole offset in M31	123
7.2.1 High-resolution fully GPU N-body simulation	124
7.2.2 Results	124
7.3 References	128

7.1 A dark matter core in M31

7.1.1 Andromeda galaxy (M31)

Due to its proximity, the Andromeda galaxy (M31) provides a wealth of high precision observational data for understanding the history of M31 and the Local Group, and more generally, galaxy formation models in a cold dark matter-dominated universe. M31 exhibits challenging features on different scales ranging from the double nucleus at its centre on a scale of a few parsecs [Kormendy & Bender, 1999; Tremaine, 1995] to the giant stellar stream (GSS) in its outskirts which extends to tens of kiloparsecs [Ibata et al., 2001].

It is widely believed that the phase structures of M31, namely its giant stream and its shell-like features, are results of the accretion of a satellite galaxy [Fardal et al., 2006, 2007; Font et al., 2006; Ibata et al., 2004]. The mass, radial velocity and distance to the stream are observed with good accuracy. The accretion scenario has been simulated with high resolution and the high quality data on the stream and the shell-like features have been used to strongly limit the initial parameter space. In a previous work, we ran high resolution simulations of a live M31 and an infalling satellite, and showed that in the cosmological scenario, the infalling satellite traced a highly eccentric orbit after reaching its turn-around radius, and then fell towards the centre of M31 [Sadoun et al., 2014]. The satellite was disrupted by M31, formed the giant stream and its subsequent passages through the centre of M31 led to the formation of the shell-like features that we observe today. Our work showed that the infalling satellite was dark matter-rich and in the same plane as most of the present-day satellites of M31.

In this work, we show yet another consequence of the satellite accretion in a Λ CDM Universe and show that the density profile of M31 could have been strongly influenced by this mechanism. We demonstrate that the passage of the satellite, which is at the origin of the giant stream, the shells and the warp of the disc of M31, should have also caused a cusp-to-core transition at the centre of the DM distribution in M31. A more general consequence of our work is that accreting satellites on highly eccentric orbits can induce a cusp-to-core transition in CDM haloes. These cores are a common feature of many DM haloes that have been initially cuspy but have accreted subhaloes on highly eccentric orbits. In most cosmological simulations, we expect to see this effect only for DM haloes with masses higher than $10^{12} M_{\odot}$ by assuming they have a sufficient resolution to determine the shapes of DM density profiles [Gao & White, 2007; Laporte & White, 2015; Ma & Boylan-Kolchin, 2004]. The DM density profile of the Aquarius simulation revealed that density profiles become shallower inwards down to the innermost resolved radius [Navarro et al., 2010]. This slight deviation from the NFW model could be evidence for the proposed cusp-to-core mechanism [El-Zant et al., 2001; Ma & Boylan-Kolchin, 2004]. Indeed, most haloes have suffered multiple subhalo mergers, especially at early epochs ($z \sim 2-3$) [Neistein & Dekel, 2008]. However, the cusp can regenerate itself. As such the cuspy profiles are more common in recent epochs, which could explain the presence of transient cores (see Boldrini et al. [2020]; Dekel et al. [2003]; Laporte & Penarrubia [2015])

In this work, we perform high resolution N-body simulations with GPUs, which allow parsec resolution, to study the effect of the accretion of a satellite on the central density profile of the DM halo of M31. The initial conditions of our simulations are determined by observations of the mass, density profile, radial velocities and distances of the giant stream which provide high precision tests of our model. We consider infalling satellite scenarios from Sadoun et al. [2014] and Fardal et al. [2007]. By analysing the density profile of the halo of M31, we see that the initial cuspy profile becomes shallower as the DM particles are heated during the satellite passage and some

The host galaxy

	Component	Profile	a [kpc]	r_{200} [kpc]	Mass [$10^{10}M_{\odot}$]	(x_0, y_0, z_0) [kpc]
M31	DM halo	NFW	7.63	195	88	0
	Bulge	Hernquist	0.61	-	3.24	0
	Disk	Exponential	$R_d = 5.4$	-	3.66	0
		disk	$z_d = 0.6$	-	-	-

The infalling
satellite

Scenario

Sadoun et al. [2014]						
$(M_{DM}/M_*)_{sat} = 20$	DM halo	Hernquist	12.5	20	4.18	$(-84.41, 152.47, -97.08)$
	Stars	Plummer	1.03	-	0.22	$(-84.41, 152.47, -97.08)$
						(v_{x0}, v_{y0}, v_{z0}) [km.s ⁻¹] (0,0,0)
Fardal et al. [2007]						
$(M_{DM}/M_*)_{sat} = 0$	Stars	Plummer	1.03	-	0.22	$(-34.75, 19.37, -13.99)$
						(v_{x0}, v_{y0}, v_{z0}) [km.s ⁻¹] (67.34, -26.12, 13.5)

Table 7.1 – **Simulation parameters:** From left to right, the columns give for each component: the initial density profile; the scale length; the virial radius; the mass; the initial positions in a reference frame centered on M31 with the x-axis pointing east, the y-axis pointing north and the z-axis corresponding to the line-of-sight direction; the velocities in this reference frame. We set the particle resolution of all the live objects to $4.4 \times 10^4 M_{\odot}$ and the gravitational softening length to 10 pc for all components.

migrate outwards from the central region of M31. As the cusp-to-core transition occurs for these two different minor merger scenarios and we expect that increasing satellite mass would only enhance this effect (i.e. for major merger scenarios), we propose that the central DM core of M31 could form irrespective of different models.

This work is organized as follows. In Section 7.1.2 we present a brief summary of observational data. Section 7.1.3 provides a description of the N-body modelling of M31 and its satellite, along with details of our numerical simulations. Then, we assess our model by making a detailed comparison with M31 observations in Section 7.1.4. In Section 7.1.5, we present the results from simulations and discuss the implications for the cusp-core problem.

7.1.2 Observation: Giant stellar stream and shell-like features of M31

A significant fraction of observed galaxies exhibit tidal features such as tidal tails, streams and shells [Malin & Carter, 1980, 1983]. These features are widely believed to be the products of merger events [Hernquist & Quinn, 1988, 1989]. The observations of tidal structures that could arise during mergers of galaxies – as shown by numerical simulations – have been used to put bounds on various

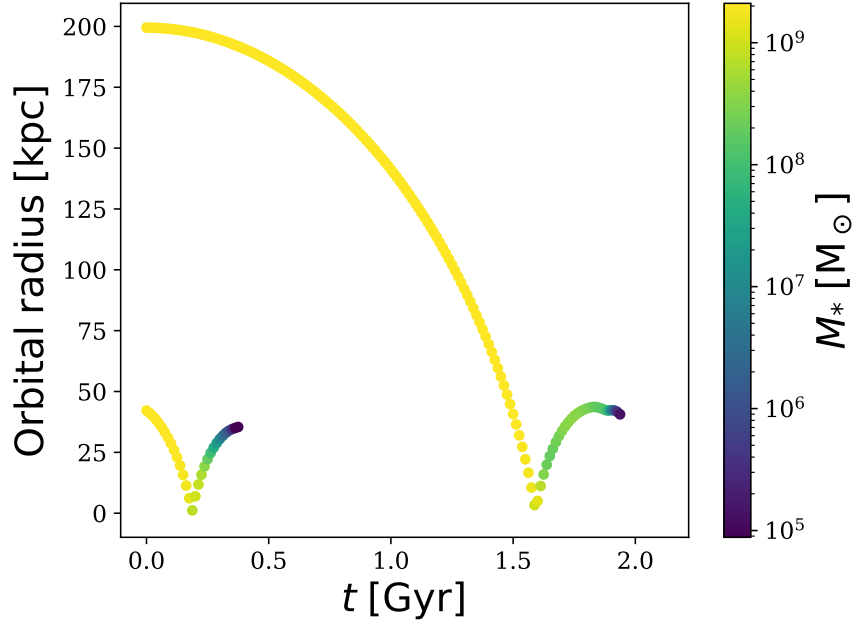


Figure 7.1 – **Orbital evolution of satellite:** Orbital radius as function of time in both Fardal and Sadoun scenarios (see Table 7.1). The orbital radius is colour coded according to the bound stellar mass in the satellite at each time. Satellites with $(M_{\text{DM}}/M_*)_{\text{sat}} = 0$ and 20 have reached their pericentre at 0.18 and 1.6 Gyr and were completely tidally stripped within 0.37 and 1.93 Gyr, respectively.

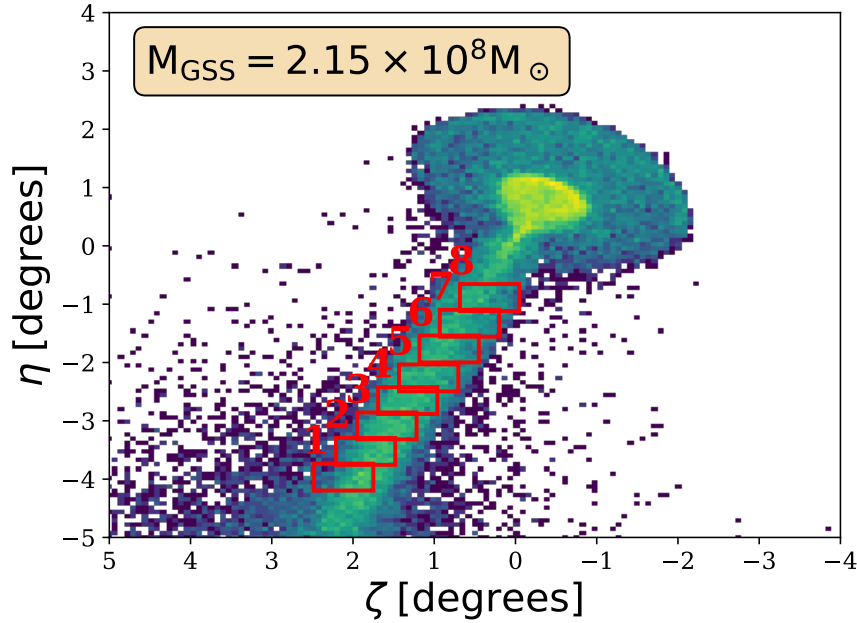


Figure 7.2 – **Giant southern stream of M31:** Simulated stellar density maps in standard sky coordinates corresponding to stars of the satellite at 2.1 Gyr. We represent the observed stellar fields by black boxes [McConnachie et al., 2003]. We find $M_{\text{GSS}} = 2.15 \times 10^8 M_{\odot}$ in good agreement with the value of $2.4 \times 10^8 M_{\odot}$ derived from observations with a mass-to-light ratio of 7 [Fardal et al., 2006; Ibata et al., 2001]

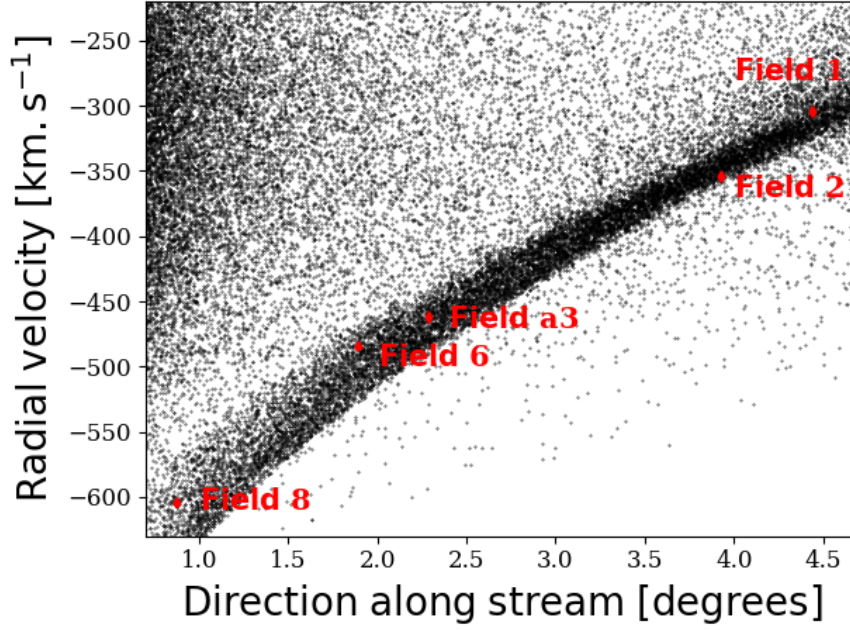


Figure 7.3 – **Comparison with kinematic data of the observed GSS:** Simulated radial velocity of satellite particles as a function of the distance along the stream at 2.1 Gyr. We represent the radial velocity measurements in five fields by red points with error-bars [Fardal et al., 2006; Ibata et al., 2004]. A good agreement with observations for the radial velocity measurement is shown.

parameters, such as the orbital parameters and the masses of the host galaxies and their satellites.

In this work, we consider M31 which is an example of a spiral galaxy that exhibits tidal features, such as streams and shells. The Andromeda galaxy contains two rings of star formation off-centred from the nucleus [Block et al., 2006, and references therein] and most notably a Giant Southern Stream (GSS) [Bellazzini et al., 2003; Brown et al., 2006; Ferguson et al., 2002; Ibata et al., 2001, 2005, 2007; McConnachie et al., 2009; Richardson et al., 2008; Zucker et al., 2004]. The GSS is a faint stellar tail located at the southeast part of M31. It extends radially outwards of the central region of M31 for approximately 5° , corresponding to a projected radius of about 68 kpc on the sky. The stream luminosity is $3.4 \times 10^7 L_\odot$ corresponding to a stellar mass of $2.4 \times 10^8 M_\odot$ for a mass-to-light ratio of 7 [Fardal et al., 2006; Ibata et al., 2001]. In the follow-up observations of the GSS, two other structures corresponding to stellar overdensities, which are now believed to be two shells, have been discovered [Fardal et al., 2007, 2012; Ferguson et al., 2002; Tanaka et al., 2010]. The colour–magnitude diagram of the north-eastern shelf is similar to that of the GSS [Ferguson et al., 2005; Richardson et al., 2008]. This similarity has been a strong argument in favour of models which predict that both the GSS and the NE are the results of a single merger event between M31 and a satellite galaxy [Fardal et al., 2007; Font et al., 2006; Ibata et al., 2004].

An empirical minor merger scenario has been studied extensively in which a satellite galaxy falls on to M31 from a distance of a few tens of kpc, on a highly radial orbit (of pericentre of a few kpc) less than one billion years ago. The satellite is tidally disrupted at the pericentre passage and forms the observed M31 stream and the two shell-like features [Fardal et al., 2006, 2007]. Although this empirical model provide good fits to the observations it suffers from simplifications. First, M31 is not modelled as a live galaxy but is only represented by a static potential, and consequently the effects of dynamical friction are not properly taken into account. Secondly, there is no DM in the progenitor satellite whereas a good fraction of satellite galaxies in the Local Group seems to be DM-

rich. Finally, the origin of the infalling satellite and its trajectory in the past has been overlooked. It is highly implausible that a satellite on a highly radial orbit could have survived to arrive within easy reach of M31.

We have proposed an alternative cosmologically-plausible scenario for the origin of the giant stream and also the warped structure of the M31 disc itself [Sadoun et al., 2014]. In our model, a dark-matter-rich satellite is accreted and falls from its first turnaround radius on an eccentric orbit onto M31. The best agreement with the observational data is obtained when the satellite lies on the same plane that contains many of the present dwarfs of M31 [Conn et al., 2013; Ibata et al., 2013]. Unlike the previous model, the disc of M31 is perturbed by the infall of the massive satellite in our model and becomes warped. A major merger scenario, dating back to a few Gyr, from which M31, its giant stream, and many of its dwarf galaxies emerged, has also been proposed [D'Souza & Bell, 2018; Hammer et al., 2010, 2013, 2018].

In this paper, we use this cosmologically-motivated scenario to set up our simulations. To show that our results are universal and hold for a wide range of initial conditions, we also run simulations for the model proposed by Fardal et al. [2007] in which the satellite is DM poor and starts its infall from a much closer distance to the centre of M31.

Here we gain in mass resolution by a factor of 100 by using a fully GPU-scaled code which allows us to study the impact of the infalling satellite not just on the outer parts of M31 but also on the DM distribution at its centre. The rich observational data on the giant stream and shells of M31 provide rather demanding tests of our model. In the following section we discuss the details of our numerical simulations.

7.1.3 Simulation: High resolution fully GPU code

The initial conditions for the M31 satellite are taken from Sadoun et al. [2014] and Fardal et al. [2007] (see details in Table. 7.1). To generate our live objects, we use the initial condition code magi [Miki & Umemura, 2018]. Adopting a distribution-function-based method, it ensures that the final realization of the galaxy is in dynamical equilibrium [Miki & Umemura, 2018]. We perform our simulations with the high performance collisionless N-body code gothic [Miki & Umemura, 2017]. This gravitational octree code runs entirely on GPU and is accelerated by the use of hierarchical time steps in which a group of particles has the same time step [Miki & Umemura, 2017]. We evolve the M31 galaxy-satellite system over 3 Gyr in each scenario. We set the particle resolution of all the live objects to $4.4 \times 10^4 M_{\odot}$ and the gravitational softening length to 10 pc. Softening value was estimated using the following criterion: $\epsilon \sim a/N^{1/3}$, where N and a are the number of particles and the scale length of the component, respectively. As all components in our simulations share the same softening, we set the smaller one, which is given by the stellar component of the satellite. As in Gadget-2 [Springel, 2005], the acceleration Multipole Acceptance Criterion is employed in our GPU code [Miki & Umemura, 2017]. The time-step parameter η is set to 0.5.

7.1.4 Tests of the models with M31 observations

We consider these two common scenarios for the formation of the giant stream of M31. The original empirical scenario in which the satellite has no DM [Fardal et al., 2007] and the cosmological motivated scenario in which the satellite is DM-rich [Sadoun et al., 2014] (see Table 7.1). Figure 7.1 depicts the orbital evolution of satellites in these two scenarios up to their passages through the centre of M31 and their subsequent disruptions. The orbital radius is colour coded according to the bound stellar mass in the satellite at each time. We follow the iterative method of Baumgardt

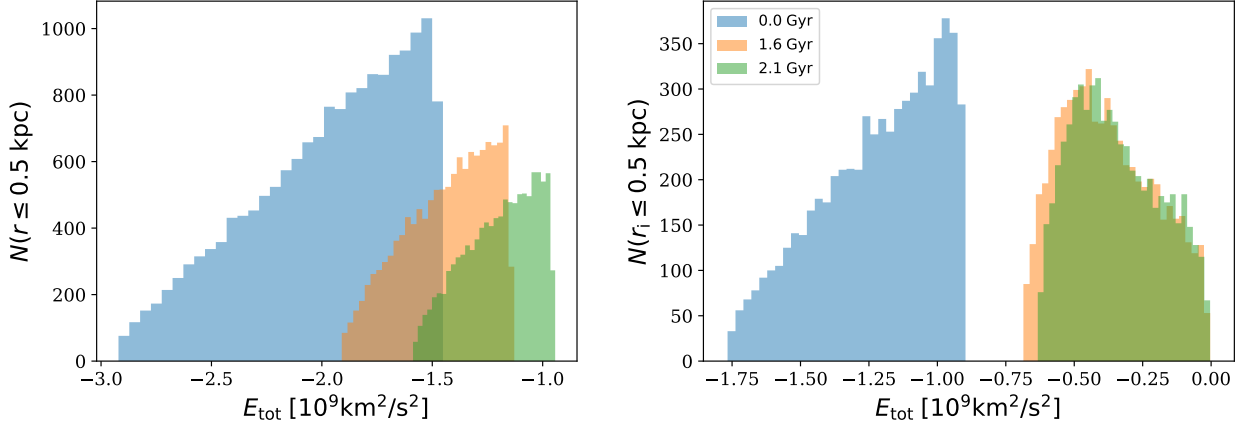


Figure 7.4 – **Energy transfer via dynamical friction:** In the left panel we show the evolution of the energy distribution for DM particles of M31 within a fixed radius of 500 pc in the Sadoun scenario (see Table 7.1). The time for the snapshots are chosen because the pericentre passage occurs at about 1.6 Gyr and the simulation is stopped at 2.1 Gyr when the best agreements with observations are achieved. The figure confirms that not only the DM particles that remain within the 500 pc have gained in energy but also some of them have migrated out of this region. In the right panel, we follow the DM particles which were initially inside the 500 pc radius and show the evolution of the distribution of the energy at the same time intervals as the left panel. Hence in this figure unlike the left panel the number of DM particles is fixed. The histogram clearly shows that most of the particles that were initially inside the 500 pc radius, whether migrated or not, have heated up which could be the mechanism for the core formation.

& Makino [2003] to determine the number of bound particles over time. Satellite galaxies with $(M_{\text{DM}}/M_*)_{\text{sat}} = 0$ and 20 have reached their pericentre at 0.18 and 1.6 Gyr and were completely tidally stripped within 0.37 and 1.93 Gyr, respectively. These two scenarios will naturally lead to the formation of the phase structures of M31.

We confirm our model by making a detailed comparison with M31 observations in the Sadoun scenario (see Table 7.1). Figure 7.2 shows the stellar density maps in standard sky coordinates corresponding to stars of the satellite at 2.1 Gyr. We represent the observed stream fields as solid rectangles with proper scaling. We note that the simulated stream is in good agreement with the observations regarding the morphology and spatial extent of the GSS. We find $M_{\text{GSS}} = 2.15 \times 10^8 M_{\odot}$ in excellent agreement with the value of $2.4 \times 10^8 M_{\odot}$ derived from observations [Fardal et al., 2006; Ibata et al., 2001]. Furthermore, we test the Sadoun model against kinematic data. Figure 7.3 shows radial velocities of satellite particles as a function of the distance along the stream. We obtain a good agreement with observations of the radial velocity measurement in the five fields [Fardal et al., 2006; Ibata et al., 2004].

Although these tests have previously been carried out in Sadoun et al. [2014] using nbodygen for initial conditions and gadget-2, here we test the same model using our fully GPU code gothic and magi as the initial condition generator, which allows us to achieve 100 times higher mass resolution. This higher resolution enables us to study the impact of the satellite on the central DM density profile of M31.

7.1.5 Results: A model-independent cusp-to-core transition in M31

Heating and migration of dark matter in M31

Our GPU simulations enable us to study the impact of the accretion of a DM-rich satellite on the DM distribution in the central regions of M31. We use the method of Power et al. [2003] to determine

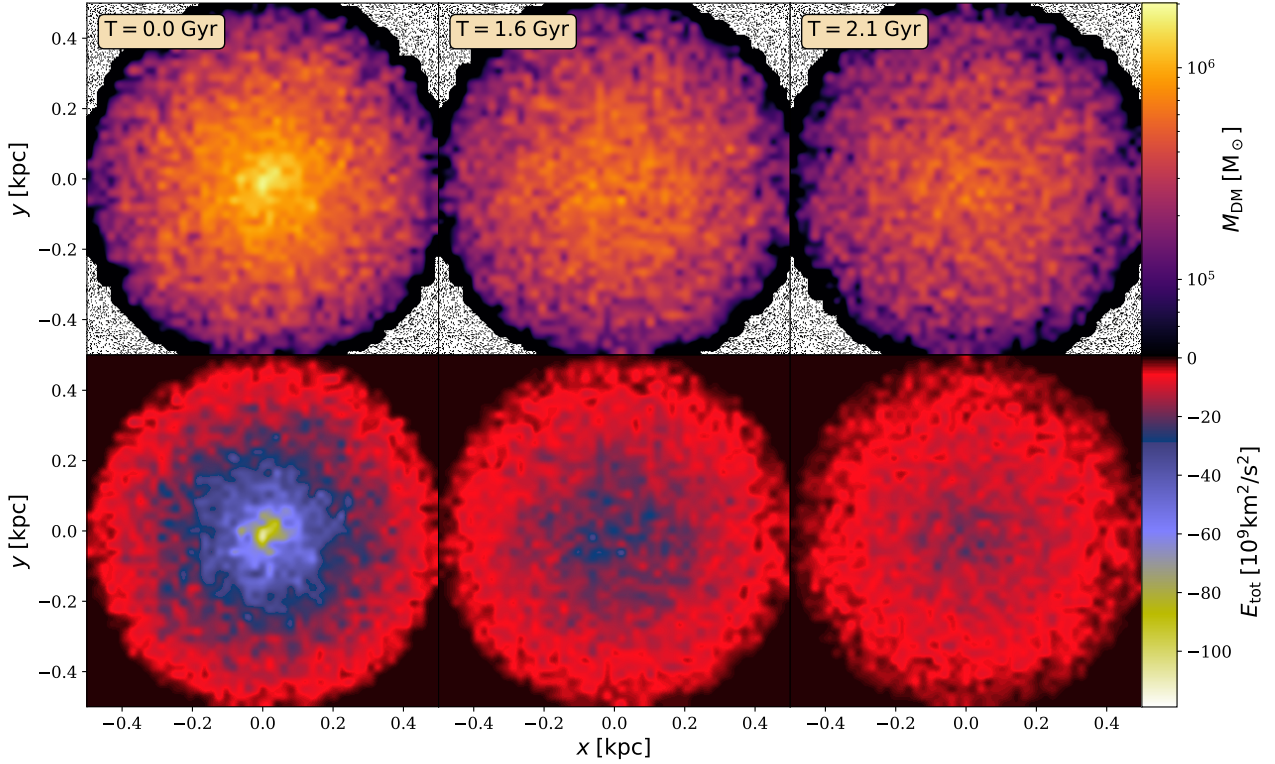


Figure 7.5 – **Migration and heating of dark matter in the central region of M31 during the passage of satellite:** Density-weighted projected mass (top panel) and total energy maps (bottom panel) for M31 DM particles at different times in Sadoun scenario (see Table 7.1). Top panel show the migration of DM particles in the central region of M31, especially after the pericentre passage of the satellite (1.6 Gyr). The bottom panel shows the heating of the DM particles that remains within the 500 pc radius central region.

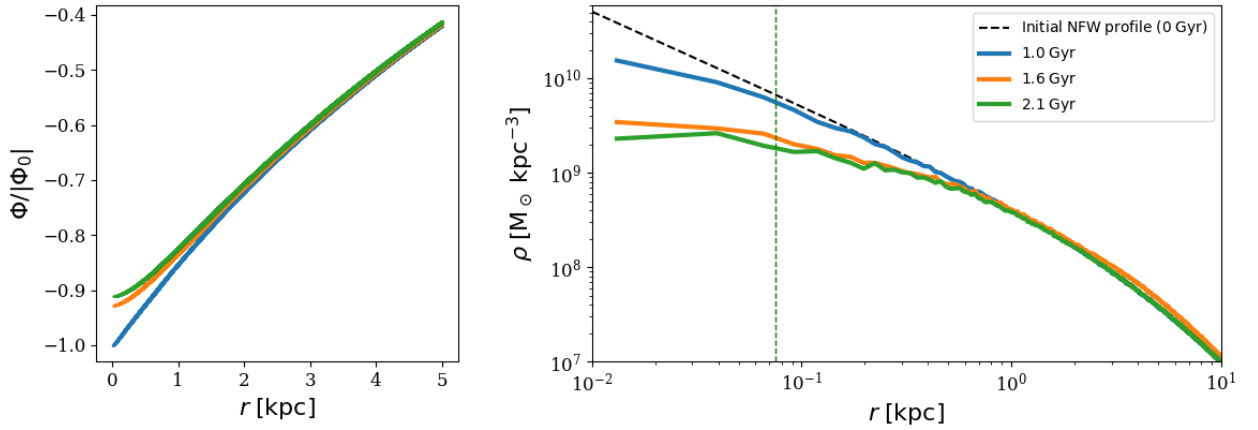


Figure 7.6 – **Change in the potential profile and flattening of the density profile of M31:** Profile of the DM potential of M31 normalized by the norm of its initial central value $|\Phi_0|$ at different times in Sadoun scenario (see Table 7.1) is shown in the left panel. Spherically averaged DM density profile of M31 in Sadoun scenario in 26 pc thick radial shells at different times is shown in the right panel. Initially, the M31 DM halo assumes a NFW profile (black dashed curve). The convergence radius of 73 pc for the M31 DM halo is shown by the vertical dashed green line below which the simulations cannot be considered to be fully converged according to the criterion of Power et al. [2003]. Beyond this region, the flattening of the cusp over almost one decade is evident. The time for the snapshots are chosen because the pericentre passage occurs at about 1.6 Gyr and the simulation is stopped at 2.1 Gyr when the best agreements with observations are achieved. Both panels demonstrate the gradual flattening of the initial cuspy profile.

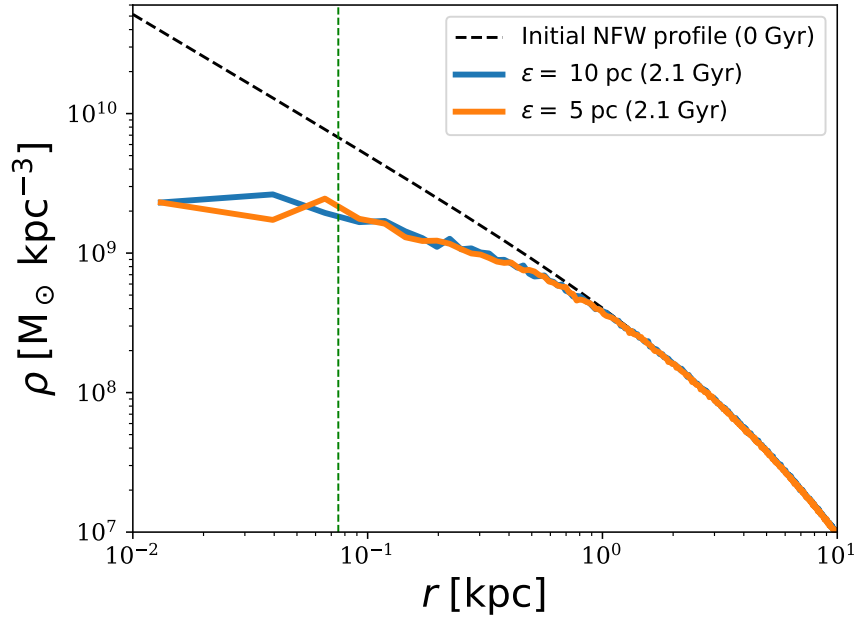


Figure 7.7 – **Impact of softening on M31 DM core:** DM density profile of M31 halo for $\epsilon = 10$ and 5 pc in Sadoun scenario (see Table 7.1). As the softening length ϵ does not affect the DM density profile, our simulation results are thus free from such numerical artifacts.

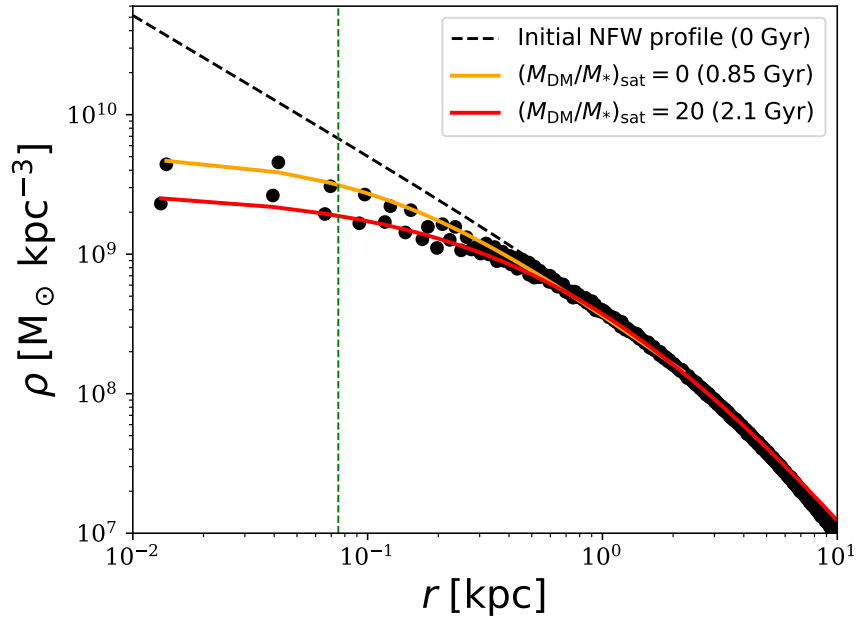


Figure 7.8 – **Model-independent DM core in M31:** Spherically averaged DM density profile for $(M_{\text{DM}}/M_*)_{\text{sat}} = 0$ (Fardal model) and 20 (Sadoun model) in 26 pc thick radial shells. Initially, the M31 DM halo assumes a NFW profile (black dashed line). We consider DM particles from both the M31 and satellite haloes to determine the DM density profile of M31. The fitting function described by Equation (7.1) reproduces the simulated density structures and captures the rapid transition from the cusp to the core. We set Poissonian errors for fitting weights. We stress that our best-fit core radii are larger than the numerical convergence radius. We observe a DM core of about 1.1 (0.59) kpc for the M31 halo in the Sadoun (Fardal) scenario (see Table 7.1).

the halo centre. We apply the shrinking sphere method to the M31 (DM halo and the satellite), the M31 halo and the M31 bulge and have found similar centres of mass at each time. We have further checked our result against this method by finding particles with the lowest potential as the center of the halo in order to have a robust determination of the center.

As the satellite has a radial orbit, its crossings near the centre perturb the M31 halo by heating its DM particles via dynamical friction. The pericentre passage of the Sadoun satellite occurs at 1.6 Gyr. Figure 7.4 depicts the total energy distribution for DM particles of M31, which are within the 500 pc (*left panel*) and in the *right panel* we follow the particles that were initially within the 500 pc at different times in the Sadoun scenario. As the number of particles is not conserved in the left panel of Figure 7.4, it confirms that some DM particles have gained in energy and have migrated outwards from the central region of M31. The right panel demonstrates that the particles that were initially within 500 pc have gained in energy.

To further confirm the mechanism of migration and heating behind the core formation, we also show density-weighted projected mass maps in Figure 7.5. The top panel of this figure clearly demonstrates the migration from the central region as the mass within the 500 pc radius decreases after the pericentre passage of the satellite at 1.6 Gyr. Not only the migrated DM particles but also those that remain within the 500 pc have gained in energy through dynamical friction which slows down the satellite.

The heating and particle migration in the central region of M31 is expected to lead to the flattening of DM density profile. In Figure 7.6, we demonstrate the change in the potential (left panel) and the flattening of the cuspy initial density profile of M31 after the passage of the satellite (at 1.6 Gyr). Initially, the M31 DM halo assumes a NFW profile. We consider DM particles from both M31 and satellite haloes to determine the spherically averaged DM density profile of M31 in 26 pc thick radial shells over the time. We have conservatively applied the Power et al. [2003] criterion to our DM haloes to estimate the radius within which the two-body relaxation time is shorter than the simulation time. We find a convergence radius of 73 pc for the M31 DM halo. The green dashed line marks this region where the simulations are not fully converged according to the criterion of Power et al. [2003]. Beyond this region, Figure 7.6 clearly demonstrates the flattening of the cusp over almost one decade.

The profile of the potential of M31 plotted in the left panel of Figure 7.6 is determined by computing the gravitational potential at different radii using all DM particles. The potential at a specified position is obtained by summing all interactions with the surrounding point masses. However, the softening factor models the interaction between two Plummer point masses. In order to test and assure that our simulation results are robust and reliable, we have performed softening tests. Figure 7.7 shows the DM density profile for a set of simulations that only differ in the value of the softening length ϵ . This figure demonstrates that our simulations are robust to changes in ϵ , and subsequently our results are free from this numerical artifact.

In the next subsection, we provide the fit to the new flattened profile and study the same migration and heating mechanism in other models of formation of giant stream in M31.

Model-independent dark matter core in M31

We consider DM particles from both M31 and satellite haloes to determine the spherically averaged DM density profile. As shown in Figure 7.8, we find that our profile is well-fitted by the following four-parameter formula: [Dehnen, 1993; Hernquist, 1990; Saha, 1992; Zhao, 1996]:

$$\rho(r) = \frac{\rho_c}{(1 + (r/r_c)^{1/\beta})^\gamma}, \quad (7.1)$$

where ρ_c is the core constant density and r_c is the core radius which we find to be about 1.1 kpc for the M31 halo in the Sadoun scenario (see Table 7.1). We stress that our best-fit core radii are larger than the numerical convergence radius and persist over almost one decade. However, as the value of the core size depends on the fitted DM profile, we defer from imposing the precise value of the radius as a constraint on the M31 core and here we wish to only demonstrate that a minor merger can indeed flatten the central density profile and the resulting profile is well-fitted by a DM core.

In order to affirm the model-independent nature of the cusp-to-core transition in M31, we also study the Fardal model [Fardal et al., 2007] for the formation of the giant stream whose precised parameters are given in Table 7.1 and described in Section 2. Using the same numerical precision and constraints, in Figure 7.8 we also show the density profile at the end of the simulation for the Fardal model, which is at 0.85 Gyr when the best-match with observations is once again obtained. In spite of the satellite being far less massive in this scenario still a core profile shows a good fit to the data. However, the core size is relatively smaller as it is expected because the heating and migration mechanisms are less effective for the low-mass satellite.

As the satellite in Sadoun model is 20 times more massive than that in the Fardal model, the core size is larger in the former scenario. However, in both scenarios, the cusp-to-core transition takes place, which highlight the formation of a model-independent core in CDM Universe. It was also pointed out that a major merger scenario could also explain the phase features of M31 [D'Souza & Bell, 2018; Hammer et al., 2010, 2018]. This scenario was not investigated here as it is necessary to invoke hydrodynamics due to the presence of gaseous disk. However, we have demonstrated that a minor merger with M31 is sufficient to form a DM core. Consequently, a major merger scenario with a satellite on highly eccentric orbit should also trigger a cusp-to-core formation for M31 halo. Besides, the resulting DM core is expected to be larger as larger perturber masses lead to larger constant density central region [Goerdt et al., 2010]. Furthermore, we have considered a ratio $(M_{\text{DM}}/M_*)_{\text{sat}} = 20$ for the DM-rich scenario. Interestingly, this implies that the satellite lies below the stellar to halo mass relation as galaxies in this mass range should have a mean halo mass of $\simeq 2 \times 10^{11} M_\odot$ [Behroozi et al., 2010; Henriques et al., 2015; Moster et al., 2013].

To confirm with this present observation of dwarf galaxies, we have also run a simulation for a ratio $(M_{\text{DM}}/M_*)_{\text{sat}} = 100$ for the satellite by keeping $10^9 M_\odot$ for the stellar component as the mass of the giant stream is well constrained by the observations. We find that the DM in the satellite prevents the stellar component to be tidally stripped after the first pericentre passage and consequently the resulting giant stream is far less massive than required by the observations. Subsequent passages will be necessary to completely strip the satellite but which once again fail to reproduce the observed tidal features of M31.

7.2 The origin of the black hole offset in M31

It was pointed out that the majority of off-centered BHs are present in host galaxies showing signs of interactions/mergers [Reines et al., 2020]. One of the most striking features of the Andromeda galaxy is the presence of a doubled-peak nucleus in the central region. These two peaks, P1 and P2, are separated by $0''.49$ corresponding to a projected distance of 1.8 pc at the distance of M31 [Kormendy & Bender, 1999; Lauer et al., 1993]. The optically faint peak P2 has been identified as hosting a MBH of mass $1.5 \times 10^8 M_\odot$. [Gültekin et al., 2009; Kormendy & Bender, 1999; Kormendy & Richstone, 1995]. It was shown that the M31 BH is offset by 0.26 pc from P2 considered as the

centre of the galaxy [Kormendy & Bender, 1999]. As there are several strong indications of a recent merger activity in M31, we propose below a new explanation for this off-centre MBH.

M31 is predicted to arise from the merger and accretion of many smaller sub-systems [White & Frenk, 1991; White & Rees, 1978]. This hypothesis is supported by the discovery of tidal features such as giant stellar stream (GSS) to its south as well as giant stellar shells to the east and west of its centre [Ferguson et al., 2002; Guhathakurta et al., 2006; Ibata et al., 2001, 2004, 2005; Koch et al., 2008; McConnachie et al., 2003]. It is widely believed that the phased features of M31 result from the accretion of a satellite galaxy [Fardal et al., 2006, 2007; Font et al., 2006; Ibata et al., 2004]. After examining the orbits and the mass of an accreting satellite galaxy, numerous high-resolution N-body simulations have been extremely successful in reproducing these structures [Fardal et al., 2006, 2007, 2013; Font et al., 2006; Hammer et al., 2010; Kirihaara et al., 2014, 2017; Miki et al., 2014, 2016; Mori & Rich, 2008; Sadoun et al., 2014].

In this work, we show that the accreting satellite, as the origin of the GSS and stellar shells, heated the central region of M31 and kicked the central MBH from the galaxy centre. Assuming the cosmologically plausible scenario from Sadoun et al. [2014] for the satellite, we performed state-of-the-art N-body simulations with GPUs, which allow parsec resolution, to study this heating process that naturally explains the present BH offset in M31. The section is organized as follows. Section 7.2.1 provides a description of the N-body modelling of M31 and its satellite, along with details of our numerical simulations. In Section 7.2.2, we present our simulation results and discuss the origin of the BH offset in M31.

7.2.1 High-resolution fully GPU N-body simulation

The initial conditions for the M31 satellite are taken from Sadoun et al. [2014] (see details in Table 7.2). The dark matter rich satellite starts at its first turnaround radius at $(x_0, y_0, z_0) = (-84.41, 152.47, -97.08)$ with a null velocity in a reference frame centered on M31 with the x-axis pointing east, the y-axis pointing north and the z-axis corresponding to the line-of-sight direction. We add a massive BH with a mass of $1.5 \times 10^8 M_\odot$ as a point mass in the center of M31 [Gültekin et al., 2009]. To generate our live objects, we use the initial condition code magi [Miki & Umemura, 2018]. Adopting a distribution-function-based method, it ensures that the final realization of the galaxy is in dynamical equilibrium [Miki & Umemura, 2018]. We perform our simulations with the high performance collisionless N-body code gothic [Miki & Umemura, 2017]. This gravitational octree code runs entirely on GPU and is accelerated by the use of hierarchical time steps in which a group of particles has the same time step [Miki & Umemura, 2017]. We evolve the M31 galaxy-satellite system over 2.5 Gyr in each scenario. We set the particle resolution of all the live objects to $4.4 \times 10^4 M_\odot$ and the gravitational softening length to 2 pc.

7.2.2 Results

We consider the accretion of a dark matter rich satellite by M31, which hosts a central MBH (see details in Table 7.2). Dynamical friction induced by the dark matter (DM) field of M31 is responsible for the infall of the satellite. As a result, the central region of the galaxy experiences multiple satellite crossings. The latter heat the central region and more particularly the MBH via dynamical friction. After the first pericentric passage, the dark matter rich satellite adds energy to the BH, causing it to leave the galaxy centre. Fig. 7.9 illustrates the orbital radius of a $1.5 \times 10^8 M_\odot$ MBH, initially at the galaxy centre, over 2.2 Gyr. This radius corresponds to the distance between the BH and the mass centre of the M31 stellar component. In the absence of satellite, the MBH should remain at the

Component	Profile	a [kpc]	r_{200} [kpc]	Mass [$10^{10}M_{\odot}$]
M31 halo	NFW	7.63	195	88
M31 bulge	Hernquist	0.61	-	3.24
M31 disk	Exponential disk	$R_d = 5.4$ $z_d = 0.6$	-	3.66
M31 black hole	Point mass	-	-	0.015
Satellite halo	Hernquist	12.5	20	4.18
Satellite stars	Plummer	1.03	-	0.22

Table 7.2 – **Simulation parameters:** From left to right, the columns provide for each component: the density profile, the scale length, the virial radius, the mass. We set the initial positions in a reference frame centered on M31 with the x-axis pointing east, the y-axis pointing north and the z-axis corresponding to the line-of-sight direction. We consider an infalling scenario of a dark matter rich satellite [Sadoun et al., 2014] where the satellite starts at its first turnaround radius at $(x_0, y_0, z_0) = (-84.41, 152.47, -97.08)$ with a null velocity. We set the particle resolution of all the live objects to $4.4 \times 10^4 M_{\odot}$ and the gravitational softening length to 2 pc. We also add a massive BH as a point mass in the center of M31 with a mass of $1.5 \times 10^8 M_{\odot}$ [Gültekin et al., 2009].

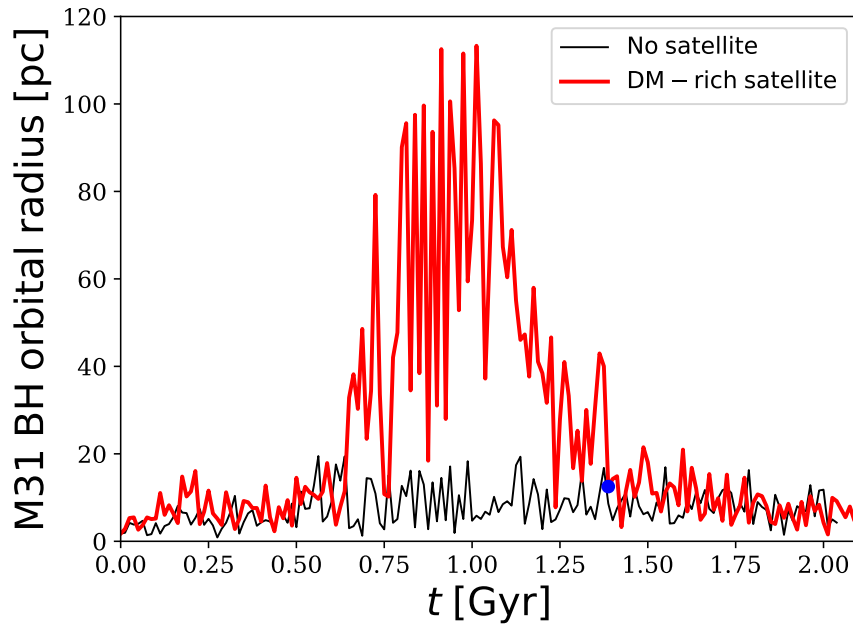


Figure 7.9 – **Off-centered MBH:** M31 BH orbital radius over 2.1 Gyr. This radius corresponds to the distance between the BH and the mass centre of the M31 stellar component. The MBH of mass $1.5 \times 10^8 M_{\odot}$ is initially at the centre of M31. The first passage of the satellite heat the central region and more particularly affect the MBH via dynamical friction. Indeed, the dark matter rich (DM-rich) satellite adds energy to the MBH, causing it to leave the galaxy centre. In the absence of satellite, the MBH remains at the centre of the dwarf galaxy. This scenario ensures the stability of the BH against numerical effects (black curve). However, the first pericentric passage of the satellite in M31 results in a kick of the MBH to hundreds of parsecs from the galaxy centre (red curve)

centre of the dwarf galaxy. With a particle resolution of $4.4 \times 10^4 M_{\odot}$ and a softening length of 2 pc, we cannot resolve properly the BH dynamics below 2 pc. Numerical artifacts amplify the expected

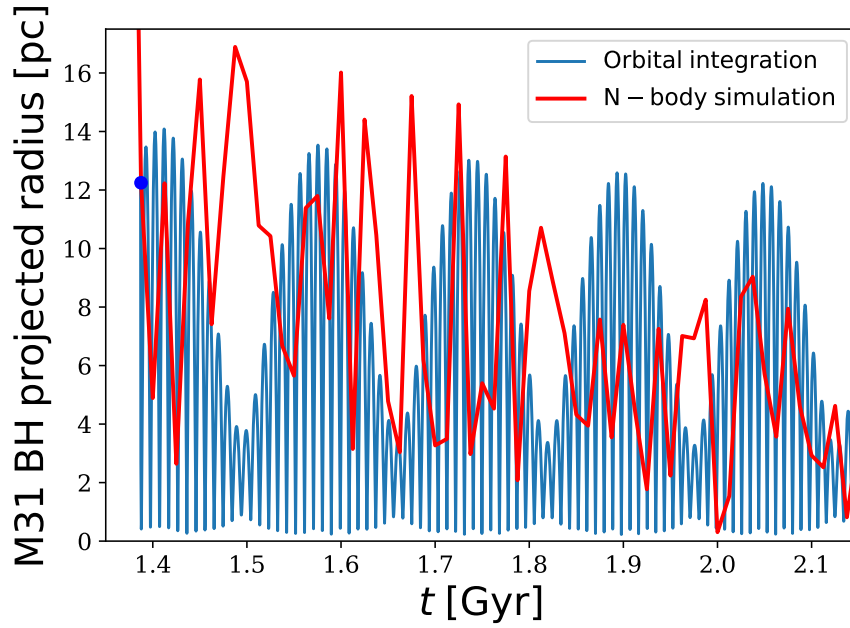


Figure 7.10 – **Zoom on the BH offset:** M31 BH projected radius from simulation and orbit integration between 1.35 and 2.15 Gyr. We take initial conditions for the MBH at resolved scales (above 10 pc) from the simulation in order to reduce our numerical noise. For our calculation, we considered all M31 components detailed in Table 7.2. The MBH is still offset and is orbiting with a mean projected pericentre of 0.45 pc, which is similar to the value of 0.26 pc derived from observations [Kormendy & Bender, 1999]. As shown before, the best match between the observed and simulated stream is obtained at 2.1 Gyr, which corresponds to a BH projected pericentre of 0.39 pc for orbital integrations from $t_0 = 1.38$ Gyr.

Brownian motion of the MBH at the M31 centre (black curve) [Merritt et al., 2007]. However, the first pericentric passage of the satellite in M31 results in a kick of the MBH to hundreds of parsecs from the galaxy centre (red curve), where the BH dynamic is resolved in our simulation.

After having reached its maximum offset, the MBH sinks towards the M31 centre due to dynamical friction. Near the M31 centre, Fig. 7.9 depicts a stalling behaviour of the MBH due to numerical effects. As M31 BH is currently offset by 0.26 pc, we want to determine the BH fate in the centre of galaxy (below 2 pc). That is the reason why we integrate the orbits of the MBH forward in time using the galpy package [Bovy, 2015] by taking into account dynamical friction. Via this semi-analytical approach, we avoid numerical effects due to a lack of particle resolution and a softening length. We employ initial conditions at $t_0 = 1.38$ Gyr for the MBH at resolved scales (above 10 pc) from the simulation with a satellite in order to reduce our numerical noise. For our calculation, we considered all M31 components detailed in Table 7.2. Fig. 7.10 compares the M31 BH projected radius from simulation and orbit integrations between 1.35 and 2.15 Gyr. We have tested different initial times t_0 for the orbital integrations of the MBH. According to Figure 7.10, the MBH is still offset and is orbiting with a mean projected pericentre of 0.45 pc, which is similar to the value of 0.26 pc derived from observations [Kormendy & Bender, 1999]. As shown before, the best match between the observed and simulated stream is obtained at 2.1 Gyr, which corresponds to a BH projected pericentre of 0.39 pc for orbital integrations from $t_0 = 1.38$ Gyr. The discrepancy between our estimation and observation could be explained by the unavoidable numerical artifacts highlighted previously. Moreover, our result suggests that the MBH is still orbiting at M31 centre and is currently observed at its pericentre if the accreting satellite is responsible for the BH offset. Despite a recent merger with a dark matter rich satellite, we demonstrate that the MBH had suffi-

cient time to come back to M31 centre. Thus, we establish that the infall of the accreting satellite in M31 naturally explains a BH offset by sub-parsecs. At the same time, we also ruled out the Brownian motion of the MBH as the origin of this offset.

7.3 References

- Baumgardt H., Makino J., 2003, *MNRAS*, **340**, 227 118
- Behroozi P. S., Conroy C., Wechsler R. H., 2010, *ApJ*, **717**, 379 123
- Bellazzini M., Cacciari C., Federici L., Fusi Pecci F., Rich M., 2003, *A&A*, **405**, 867 117
- Block D. L., et al., 2006, *Nature*, **443**, 832 117
- Boldrini P., Mohayaee R., Silk J., 2020, *MNRAS*, **492**, 3169 114
- Bovy J., 2015, *ApJS*, **216**, 29 126
- Brown T. M., Smith E., Ferguson H. C., Rich R. M., Guhathakurta P., Renzini A., Sweigart A. V., Kimble R. A., 2006, *ApJ*, **652**, 323 117
- Conn A. R., et al., 2013, *ApJ*, **766**, 120 118
- D'Souza R., Bell E. F., 2018, *Nature Astronomy*, **2**, 737 118, 123
- Dehnen W., 1993, *MNRAS*, **265**, 250 122
- Dekel A., Devor J., Hetzroni G., 2003, *MNRAS*, **341**, 326 114
- El-Zant A., Shlosman I., Hoffman Y., 2001, *ApJ*, **560**, 636 114
- Fardal M. A., Babul A., Geehan J. J., Guhathakurta P., 2006, *MNRAS*, **366**, 1012 114, 116, 117, 119, 124
- Fardal M. A., Guhathakurta P., Babul A., McConnachie A. W., 2007, *MNRAS*, **380**, 15 114, 115, 117, 118, 123, 124
- Fardal M. A., et al., 2012, *MNRAS*, **423**, 3134 117
- Fardal M. A., et al., 2013, *MNRAS*, **434**, 2779 124
- Ferguson A. M. N., Irwin M. J., Ibata R. A., Lewis G. F., Tanvir N. R., 2002, *AJ*, **124**, 1452 117, 124
- Ferguson A. M. N., Johnson R. A., Faria D. C., Irwin M. J., Ibata R. A., Johnston K. V., Lewis G. F., Tanvir N. R., 2005, *ApJ*, **622**, L109 117
- Font A. S., Johnston K. V., Guhathakurta P., Majewski S. R., Rich R. M., 2006, *AJ*, **131**, 1436 114, 117, 124
- Gao L., White S. D. M., 2007, *MNRAS*, **377**, L5 114
- Goerdt T., Moore B., Read J. I., Stadel J., 2010, *ApJ*, **725**, 1707 123
- Guhathakurta P., et al., 2006, *AJ*, **131**, 2497 124
- Gültekin K., et al., 2009, *ApJ*, **698**, 198 123, 124, 125
- Hammer F., Yang Y. B., Wang J. L., Puech M., Flores H., Fouquet S., 2010, *ApJ*, **725**, 542 118, 123, 124

- Hammer F., Yang Y., Fouquet S., Pawlowski M. S., Kroupa P., Puech M., Flores H., Wang J., 2013, *MNRAS*, **431**, 3543 118
- Hammer F., Yang Y. B., Wang J. L., Ibata R., Flores H., Puech M., 2018, *MNRAS*, **475**, 2754 118, 123
- Henriques B. M. B., White S. D. M., Thomas P. A., Angulo R., Guo Q., Lemson G., Springel V., Overzier R., 2015, *MNRAS*, **451**, 2663 123
- Hernquist L., 1990, *ApJ*, **356**, 359 122
- Hernquist L., Quinn P. J., 1988, *ApJ*, **331**, 682 115
- Hernquist L., Quinn P. J., 1989, *ApJ*, **342**, 1 115
- Ibata R., Irwin M., Lewis G., Ferguson A. M. N., Tanvir N., 2001, *Nature*, **412**, 49 114, 116, 117, 119, 124
- Ibata R., Chapman S., Ferguson A. M. N., Irwin M., Lewis G., McConnachie A., 2004, *MNRAS*, **351**, 117 114, 117, 119, 124
- Ibata R., Chapman S., Ferguson A. M. N., Lewis G., Irwin M., Tanvir N., 2005, *ApJ*, **634**, 287 117, 124
- Ibata R., Martin N. F., Irwin M., Chapman S., Ferguson A. M. N., Lewis G. F., McConnachie A. W., 2007, *ApJ*, **671**, 1591 117
- Ibata R. A., et al., 2013, *Nature*, **493**, 62 118
- Kirihara T., Miki Y., Mori M., 2014, *PASJ*, **66**, L10 124
- Kirihara T., Miki Y., Mori M., Kawaguchi T., Rich R. M., 2017, *MNRAS*, **464**, 3509 124
- Koch A., et al., 2008, *ApJ*, **689**, 958 124
- Kormendy J., Bender R., 1999, *ApJ*, **522**, 772 114, 123, 124, 126
- Kormendy J., Richstone D., 1995, *ARA&A*, **33**, 581 123
- Laporte C. F. P., Penarrubia J., 2015, *MNRAS*, **449**, L90 114
- Laporte C. F. P., White S. D. M., 2015, *MNRAS*, **451**, 1177 114
- Lauer T. R., et al., 1993, *AJ*, **106**, 1436 123
- Ma C.-P., Boylan-Kolchin M., 2004, *Phys. Rev. Lett.*, **93**, 021301 114
- Malin D. F., Carter D., 1980, *Nature*, **285**, 643 115
- Malin D. F., Carter D., 1983, *ApJ*, **274**, 534 115
- McConnachie A. W., Irwin M. J., Ibata R. A., Ferguson A. M. N., Lewis G. F., Tanvir N., 2003, *MNRAS*, **343**, 1335 116, 124
- McConnachie A. W., et al., 2009, *Nature*, **461**, 66 117

- Merritt D., Berczik P., Laun F., 2007, *AJ*, 133, 553 126
- Miki Y., Umemura M., 2017, *New Astron.*, 52, 65 118, 124
- Miki Y., Umemura M., 2018, *MNRAS*, 475, 2269 118, 124
- Miki Y., Mori M., Kawaguchi T., Saito Y., 2014, *ApJ*, 783, 87 124
- Miki Y., Mori M., Rich R. M., 2016, *ApJ*, 827, 82 124
- Mori M., Rich R. M., 2008, *ApJ*, 674, L77 124
- Moster B. P., Naab T., White S. D. M., 2013, *MNRAS*, 428, 3121 123
- Navarro J. F., et al., 2010, *MNRAS*, 402, 21 114
- Neistein E., Dekel A., 2008, *MNRAS*, 388, 1792 114
- Power C., Navarro J. F., Jenkins A., Frenk C. S., White S. D. M., Springel V., Stadel J., Quinn T., 2003, *MNRAS*, 338, 14 119, 120, 122
- Reines A. E., Condon J. J., Darling J., Greene J. E., 2020, *ApJ*, 888, 36 123
- Richardson J. C., et al., 2008, *AJ*, 135, 1998 117
- Sadoun R., Mohayaee R., Colin J., 2014, *MNRAS*, 442, 160 114, 115, 118, 119, 124, 125
- Saha P., 1992, *MNRAS*, 254, 132 122
- Springel V., 2005, *MNRAS*, 364, 1105 118
- Tanaka M., Chiba M., Komiyama Y., Guhathakurta P., Kalirai J. S., Iye M., 2010, *ApJ*, 708, 1168 117
- Tremaine S., 1995, *AJ*, 110, 628 114
- White S. D. M., Frenk C. S., 1991, *ApJ*, 379, 52 124
- White S. D. M., Rees M. J., 1978, *MNRAS*, 183, 341 124
- Zhao H., 1996, *MNRAS*, 278, 488 122
- Zucker D. B., et al., 2004, *ApJ*, 612, L117 117

Chapter 8

Conclusion & Prospects

On scales of galaxies and above, the cold dark matter paradigm successfully explains various observations over a large range of epochs. The frontier in this field has shifted to relatively unexplored sub-galactic scales, the domain of the central regions of halos, and especially for dwarf galaxies where unresolved issues remain independently of baryons. Dwarf galaxies, which are among the most dark matter-dominated galaxies in the Universe, provide an excellent laboratory for studying dark matter in the context of galaxy formation and evolution. My doctoral research focuses on the inconsistency of inner DM density profiles in dwarf galaxies, known as the cusp-core problem, detailed in Chapter 2.

Pathways to contribute towards solving these problems include the use of high resolution collisionless N-body simulations, a particularly useful technique to investigate the internal dynamics of dwarf galaxies. My GPU-based approach allows simulations of live galaxies containing live globular clusters and substructures, providing new insights into cores and cusps. This thesis uses the non-public code, GOTHIC as its base N-body code, presented in Chapter 3. This gravitational oct-tree code runs entirely on GPU with adaptive time steps.

In Chapter 4, we have revisited the cusp-core problem applied to Fornax. For the first time, the Fornax globular system has been modeled with live objects, i.e. self-gravitating systems only composed of star and DM particles, in order to properly implement dynamical friction and tidal effects between Fornax and GCs. We have performed N-body simulations for cored and cuspy halos in MW tidal field modeled by a static potential. Using constraints from GC spatial and mass distributions, we showed that Fornax can have either a cored or a cuspy halo. More precisely, our results have revealed a lower limit of a core size of $r_c \gtrsim 500$ pc for Fornax cored halo. Even if many studies attest against the presence of a divergent cusp in Fornax, we show also that, from our GC constraints, Fornax can have a cuspy halo. Recently, [Meadows et al. \[2020\]](#) stated also that a DM cusp in Fornax cannot be ruled out by the spatial distribution of GCs. Apart from CDM, all variant DM theories, including warm DM, fuzzy DM, and self-interacting DM are apparently in favour of cored halos. Future work could investigate the dynamical behaviour of GCs in these theories, in particular the impact on dynamical friction. Recently, [Lancaster et al. \[2020\]](#) established that the Fornax timing problem is no longer resolved in fuzzy DM.

In Chapter 4, we have also studied the motion of GCs embedded in DM minihalos inside the CDM halo of Fornax in order to deal with the timing problem. We have considered an early and a recent accretion scenario of GCs by Fornax with the most prevalent initial conditions taken from Illustris TNG-100 cosmological simulations. We proposed a new mechanism to resolve the cusp-core problem. First, the infall of GCs and the formation of a nuclear star cluster rules out the early accretion scenario for GCs with and without a DM minihalo. However, we showed that GC crossings near the Fornax centre induce a cusp-to-core transition of the DM halo. Secondly, we demonstrated that DM minihalos, as a new component of GCs, resolve both the timing and cusp-core problems in Fornax if the five GCs were accreted recently, less than 3 Gyr ago, by Fornax. Under these assumptions, the infall of these GCs does not occur and no star cluster forms in the centre of Fornax in accordance with observations. Crossings of GCs with a DM minihalo near the Fornax centre induce a cusp-to-core transition of the DM halo and hence resolve the cusp-core problem in this dwarf galaxy. The DM core size depends strongly on the frequency of GC crossings. We subsequently highlighted that an infalling GC with a DM minihalo enhances core formation without forming a nuclear star cluster at the Fornax centre. Moreover, we are in good agreement with the constraints on the DM mass of GCs as our clusters lost a large fraction of their DM minihalos. All of these aspects provide strong evidence for the existence of DM halos in GCs. Our simulations clearly show that between central passages, the DM halo can regenerate its cusp. [Read et al. \[2019\]](#) found that dwarf galaxies can be separated into two distinct classes, those with cold DM cusps and DM cores. Fornax favours a DM core, whereas Carina, Sextant, and Draco favour a

DM cusp. The transient phenomenon that we have found could explain this diversity of DM halo profiles. GCs embedded in DM minihalos, which are eventually completely stripped, could have induced such cup-core transitions by past infall. However, we regard this as unlikely since GCs do not appear to be ubiquitous in dwarf galaxies. Moreover, past mergers seem necessary to explain the spatial distribution of stellar populations in Fornax [del Pino et al., 2015]. In addition to GCs in DM minihalos, these events could help to trigger the formation of the DM in Fornax. Leung et al. [2020] showed that Fornax needs to have undergone a major merger with a mass ratio between 0.2 and 0.5 in order to reproduce the GC and stellar properties.

In Chapter 5, we addressed the cusp-core problem in $10^7 M_\odot$ halos such as low-mass dwarf galaxies by considering the possibility that a fraction of the DM is made of PBHs. We show that the dynamical heating of the CDM component through PBH infall and two-body relaxation between PBHs induce the formation of cores in PBH+CDM halos. Using N-body simulations, we confirmed that PBHs as DM candidates can initiate a cusp-to-core transition in these low-mass galaxies. Our results suggest also that it is natural to have multiple cores for a two-component halo. Then, we test the PBH+CDM mass fraction f_m and PBH mass m_{PBH} . We work with PBHs in the 25-100 M_\odot mass window, which is consistent with the LIGO detections. Our simulations allow a mass resolution of 1 M_\odot for CDM particles. Finally, we derive a criterion based on the relaxation time in order to determine if a cusp-to-core transition occurred. Based on our criterion, we set the lower limit on the PBH+CDM mass fraction to be 1% of the total DM content to induce cores in PBH+CDM halo depending on the PBH mass and r_s^{PBH} . Here, we have shown that this scenario works even for a small fraction of PBHs. We determined that the cusp-to-core transition takes between 1 and 8 Gyr to appear, depending on the fraction f_m , the PBH mass m_{PBH} and the PBH scale radius r_s^{PBH} . After a transition, the major impact of the PBH+CDM mass fraction and PBH mass is on the core size. Indeed, a larger PBH fraction and PBH mass will induce a larger core radius. As cores occur naturally in PBH+CDM halos without the presence of baryons, there is no cusp-core problem in this alternative theory. As low mass galaxies require less than 8 Gyr to form cores, higher mass galaxies with larger cores as observed can form in the hierarchical scenario. The existence of PBHs in the mass range studied here, 25 - 100 M_\odot , can possibly be confirmed by the LISA mission. As this DM theory is characterized by a single parameter, f_m , Future work could apply Jeans analysis assuming a NFW profile predicted by CDM for the DM component and a core profile for the PBH component to the kinematic data of eight classical dwarf galaxies so as to constrain this mass fraction.

In Chapter 6, we have shown that the heating of the central region in dwarf galaxies by subhalos via dynamical friction entails the offset of MBHs, especially at early epochs ($z=1.5-3$). Indeed, at redshift $z=3$, the average number of subhalo accretions is high (~ 4 per Gyr) and then the sinking of subhalos transfers energy to the galaxy centre and especially to the MBH, causing it to leave the central region. The heating by subhalos and the subsequent kick to the central MBH provides a new mechanism that contributes to explain observed off-center BHs in dwarf galaxies. We have also predicted that off-center BHs are more common in higher mass galaxies because, after the kick, dynamical friction on BHs becomes significantly weaker, and then BHs take more time to sink towards the centre of these galaxies. As BH feedback consists of energy injection into halos, this latter is commonly invoked as a mechanism for core formation. Indeed, BH feedback can induce a cusp-to-core transition for the DM halo. Here, we have argued that the main consequence of off-center BHs during early epochs of dwarf galaxies is the quenching of BH feedback and then the absence of DM core formation by this mechanism. Thus, pinning the BH to the halo centre can result in unrealistic galactic evolution in some cosmological simulations [Schaye et al., 2015; Sijacki et al., 2015; Taylor & Kobayashi, 2014]. Dynamical perturbations induced by subhalo crossings, causing MBHs to vacate the galaxy center, can also modify the spatial distribution of the other

galaxy components such as stars and DM particles. Stars heated by subhalos can contribute to populating the stellar halo as an alternative to star formation in gas outflows that are associated with starburst activity [Gallagher et al., 2019; Maiolino et al., 2017; Rodríguez del Pino et al., 2019; Yu et al., 2020]. A notable difference between these scenarios will be the age distribution of the ejected stars.

In Chapter 7, we reaffirmed that the accretion of a dark-matter-rich satellite reproduces successfully the tidal features such as the giant stellar stream and the two shells in M31. We have mainly studied the model proposed by Sadoun in 2014 in which the Satellite is dark-matter rich and falls from its turnaround radius onto M31. However, we have increased the resolution of the previous simulations by using a fully GPU code. The substantial gain of 100 in mass resolution has enabled us to here study the impact of such an accretion event on the spatial distribution of dark matter in the central regions of M31. Our simulations show that as the satellite falls onto M31, it is slowed down by dynamical friction and its energy is transferred to the host halo. The dark matter particles in the central regions of M31 are heated and migrate outwards. Here we have shown that in this process the initial cusp shallows down for over almost a decade and is well-fitted by a core profile. To explore the model-independent aspect of our results we have also studied the Fardal model, in which the satellite contains no dark matter and starts its orbit close to the centre of M31. Also in this scenario, we observe a cusp-to-core transition. We infer that merger events in which satellites fall on highly eccentric orbits onto their host haloes can provide a general mechanism for core formation in a Λ CDM Universe where haloes have cuspy profiles. It has been reported that satellites in host haloes with larger mass ratios have slightly more eccentric orbits with lower angular momentum and moreover, satellites around more massive haloes seem to be on more radial orbits at fixed mass ratio [Jiang et al., 2015; Tormen, 1997; Wetzel, 2011]. Hence, we expect that a noticeable fraction of galaxies in Λ CDM Universe to harbour cores that have been formed during merger and accretion events. Moreover, we have shown that the heating of the central region of M31 by this dark matter rich satellite via dynamical friction entails a significant MBH offset after the first pericentric passage by using a fully GPU state-of-the-art N-body simulation. Using orbital integrations, we highlighted the sinking of the BH towards the parsec scale in M31. The heating by the satellite and the subsequent kick to the central MBH naturally explains a present BH offset by sub-parsecs in M31, detected by Kormendy & Bender [1999]. Our result reinforces the prediction of Boldrini et al. [2020] concerning the furthest distance reached by MBHs in high mass galaxies. Indeed, they pointed out that MBHs are going to have less inertia due to the lower potential in these galaxies.

8.1 References

- Boldrini P., Mohayaee R., Silk J., 2020, *MNRAS*, **495**, L12 134
- Gallagher R., Maiolino R., Belfiore F., Drory N., Riffel R., Riffel R. A., 2019, *MNRAS*, **485**, 3409 134
- Jiang L., Cole S., Sawala T., Frenk C. S., 2015, *MNRAS*, **448**, 1674 134
- Kormendy J., Bender R., 1999, *ApJ*, **522**, 772 134
- Lancaster L., Giovanetti C., Mocz P., Kahn Y., Lisanti M., Spergel D. N., 2020, *J. Cosmology Astropart. Phys.*, **2020**, 001 132
- Leung G. Y. C., Leaman R., van de Ven G., Battaglia G., 2020, *MNRAS*, **493**, 320 133
- Maiolino R., et al., 2017, *Nature*, **544**, 202 134
- Meadows N., Navarro J. F., Santos-Santos I., Benítez-Llambay A., Frenk C., 2020, *MNRAS*, **491**, 3336 132
- Read J. I., Walker M. G., Steger P., 2019, *MNRAS*, **484**, 1401 132
- Rodríguez del Pino B., Arribas S., Piqueras López J., Villar-Martín M., Colina L., 2019, *MNRAS*, **486**, 344 134
- Schaye J., et al., 2015, *MNRAS*, **446**, 521 133
- Sijacki D., Vogelsberger M., Genel S., Springel V., Torrey P., Snyder G. F., Nelson D., Hernquist L., 2015, *MNRAS*, **452**, 575 133
- Taylor P., Kobayashi C., 2014, *MNRAS*, **442**, 2751 133
- Tormen G., 1997, *MNRAS*, **290**, 411 134
- Wetzel A. R., 2011, *MNRAS*, **412**, 49 134
- Yu S., et al., 2020, *MNRAS*, **494**, 1539 134
- del Pino A., Aparicio A., Hidalgo S. L., 2015, *MNRAS*, **454**, 3996 133